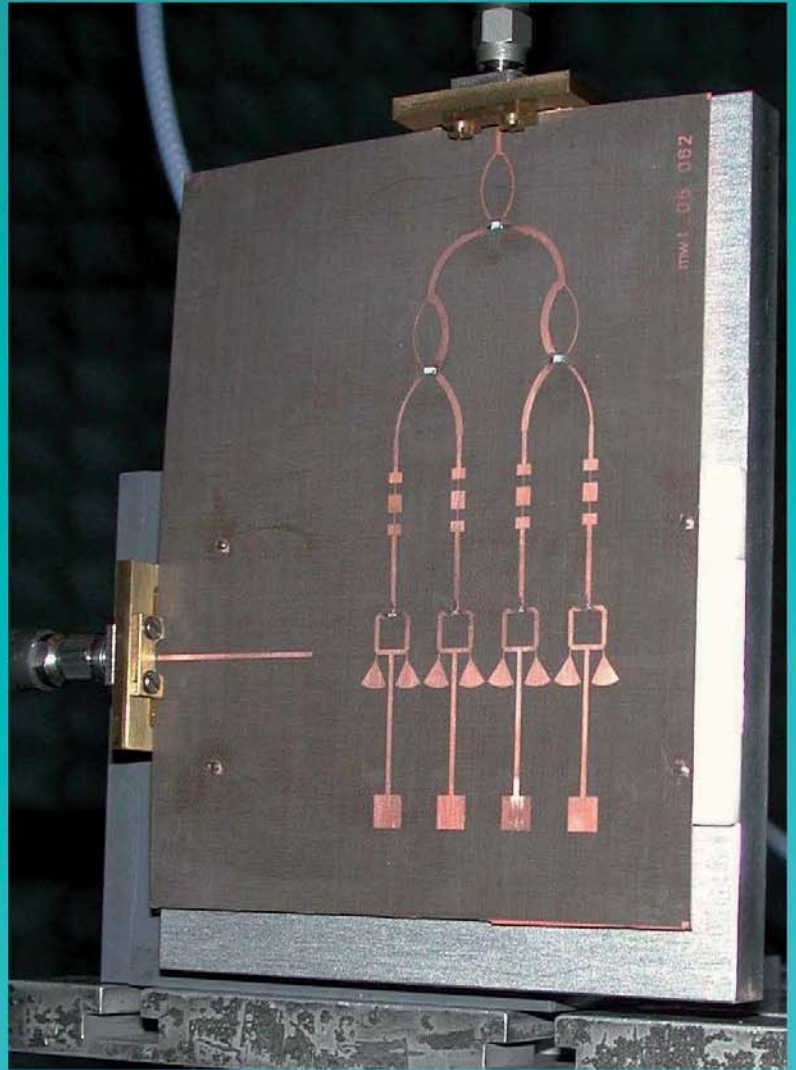
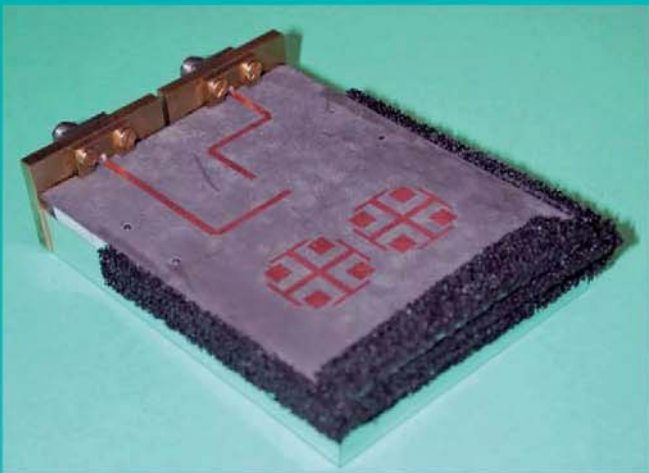
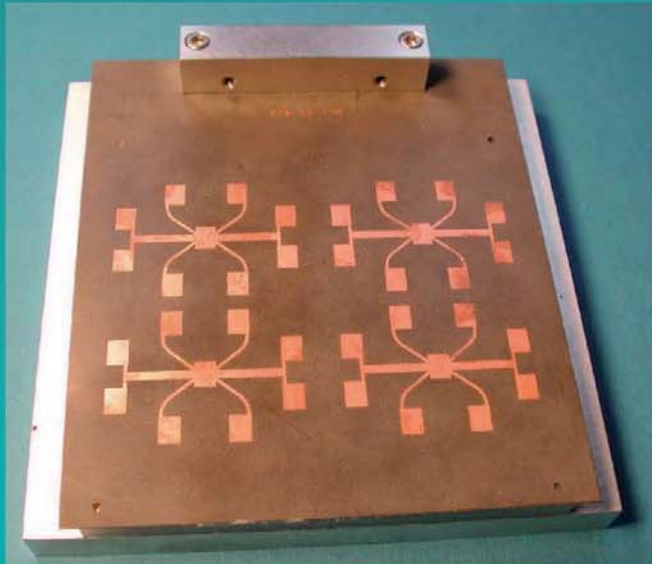


**Ulf Schmid**

**Planar Antenna Arrays Using Feed Networks  
with Nonradiative Dielectric (NRD) Waveguide**



Cuvillier Verlag Göttingen





# **Planar Antenna Arrays Using Feed Networks with Nonradiative Dielectric (NRD) Waveguide**

DISSERTATION

zur Erlangung des akademischen Grades eines

**DOKTOR-INGENIEURS**  
(Dr.-Ing.)

der Fakultät für Ingenieurwissenschaften  
und Informatik der Universität Ulm

von

**ULF SCHMID**

aus Calw

Gutachter: Prof. Dr.-Ing. Wolfgang Menzel  
Prof. Dr. Ke Wu  
Amtierender Dekan: Prof. Dr.-Ing. Michael Weber

Ulm, 21. Juni 2010

Bibliografische Information der Deutschen Nationalbibliothek

Die Deutsche Nationalbibliothek verzeichnet diese Publikation in der Deutschen Nationalbibliografie; detaillierte bibliografische Daten sind im Internet über <http://dnb.d-nb.de> abrufbar.

1. Aufl. - Göttingen: Cuvillier, 2011

Zugl.: Ulm, Univ., Diss., 2010

978-3-86955-898-1

© CUVILLIER VERLAG, Göttingen 2011

Nonnenstieg 8, 37075 Göttingen

Telefon: 0551-54724-0

Telefax: 0551-54724-21

[www.cuvillier.de](http://www.cuvillier.de)

Alle Rechte vorbehalten. Ohne ausdrückliche Genehmigung des Verlages ist es nicht gestattet, das Buch oder Teile daraus auf fotomechanischem Weg (Fotokopie, Mikrokopie) zu vervielfältigen.

1. Auflage, 2011

Gedruckt auf säurefreiem Papier

978-3-86955-898-1

# Acknowledgments

The work underlying this dissertation has been carried out during my employment as a research assistant at the Institute of Microwave Techniques at the University of Ulm.

I am heartily thankful to Prof. Dr. Wolfgang Menzel for supervision and many valuable suggestions and support during the genesis of this thesis. He sparked my interest in microwave technology and antenna design and gave me the opportunity to work in his research group. Thanks to him, I became acquainted with other experts in the field at a very early stage, and later on even worked with some of them.

I am grateful to Prof. Dr. Ke Wu from the École Polytechnique Montréal, Canada, for serving as a second examiner. It was both a great honor and a great pleasure for me that he came to Ulm especially for the defense of my thesis.

I would also like to thank all colleagues and staff members at the Institute of Microwave Techniques. The open and pleasant atmosphere was the basis for a great friendship to many of them. My special thanks go to Dr. Frank Bögelsack for many fruitful discussions and for carefully proofreading this dissertation.

Finally, I would like to thank my wife Karen and my daughter Rebecca for backing and encouragement in spite of countless late hours and many weekends of absence, as well as my parents Kurt and Christel who have supported me on my way.

Ulm, June 2010  
Ulf Schmid



# Contents

<b>1</b>	<b>Introduction</b>	<b>1</b>
<b>2</b>	<b>Propagation in the Nonradiative Dielectric Waveguide (NRD-guide)</b>	<b>7</b>
2.1	Longitudinal Section Electric (LSE) Modes . . . . .	10
2.1.1	Even LSE Modes . . . . .	11
2.1.2	Odd LSE Modes . . . . .	13
2.2	Longitudinal Section Magnetic (LSM) Modes . . . . .	15
2.2.1	Even LSM Modes . . . . .	16
2.2.2	LSM Odd Modes . . . . .	17
2.3	Field Solutions for the Fundamental Modes . . . . .	17
2.4	A Graphical Method for Solutions of the Eigenvalue Equations and Determination of Cutoff-Frequencies . . . . .	20
2.5	Loss Calculation . . . . .	25
2.5.1	Time-Average Power Flow . . . . .	26
2.5.2	Transmission Loss due to Imperfect Conductors . . . . .	27
2.5.3	Transmission Loss due to Imperfect Dielectrics . . . . .	30
<b>3</b>	<b>Fixed Beam Antenna for Point-to-Point Applications</b>	<b>39</b>
3.1	Antenna Design . . . . .	40
3.2	Design and Simulation of Components . . . . .	42
3.2.1	Configurations for Excitation of an NRD-guide . . . . .	42
3.2.2	Feeding Network . . . . .	47
3.2.3	T-junctions . . . . .	48
3.2.4	Sub Arrays . . . . .	50
3.3	Complete Antenna Array . . . . .	52
<b>4</b>	<b>Dual Polarization Antennas</b>	<b>57</b>
4.1	Dual Polarization Antenna Fed by a Dual Mode SINRD-guide . . . . .	59
4.1.1	Design and Characterization of a Dual Mode Transition . . . . .	62
4.1.2	Design and Simulation of a Transition from Dual Mode NRD-guide to Crossed Microstrip Lines . . . . .	68
4.1.3	Design of the Dual Polarization Radiating Element . . . . .	72
4.1.4	Measurements on the Dual Polarization Antenna . . . . .	73

4.1.5	A Transition Microstrip Line to NRD-guide for Simultaneous Excitation of Both Modes . . . . .	78
4.2	Dual Polarization Antenna Array with Optimized Feeding Network	79
4.2.1	NRD-guide Circuit Elements . . . . .	81
4.2.2	Measurements of Dual Mode NRD-guide Test Circuits . .	92
4.2.3	Measurements of the Linear Array of 2×2 Sub Arrays . .	100
<b>5</b>	<b>A Low Cost Low Profile Scanning Receiver Array</b>	<b>107</b>
5.1	Introduction . . . . .	107
5.1.1	Motivation for Automotive Sensors . . . . .	107
5.1.2	Comparison of Sensor Types . . . . .	107
5.1.3	Applications of Radar Sensors . . . . .	108
5.1.4	System Requirements . . . . .	108
5.1.5	Beam Switching and Steering Approaches with Increased Angular Resolution . . . . .	109
5.2	Antenna Design . . . . .	114
5.3	Design and Simulations of the Components . . . . .	115
5.3.1	Design and Simulations of Hybrid Couplers . . . . .	115
5.3.2	Design of a Balanced Mixer with an NRD-guide LO Feed	121
5.4	Performance of the Scanning Receiver Array . . . . .	125
5.5	Two-path Band-pass Filters for a Steeper Phase Increment . . . .	127
<b>6</b>	<b>Summary</b>	<b>131</b>
<b>A</b>	<b>Appendix</b>	<b>135</b>
A.1	Design Details on the Components of the Dual Polarization Antenna	135
A.1.1	Dual Mode Transition from NRD-guide to Microstrip Line	135
A.1.2	Dual Mode NRD-guide T-junction . . . . .	137
A.1.3	Dual Mode Transition from NRD-guide to Crossed Microstrip Lines . . . . .	138
A.2	Layouts of the NRD-guide Fed Antennas . . . . .	139
	<b>Bibliography</b>	<b>143</b>



# Symbols and Abbreviations

## Symbols

$\vec{A}$	Magnetic vector potential . . . . .	9
$\vec{F}$	Electric vector potential . . . . .	9
$\vec{H}$	Magnetic field strength vector . . . . .	9
$h$	Height of a geometric structure . . . . .	7
$l$	Length of a geometric structure . . . . .	72
$w$	Width of a geometric structure . . . . .	7
$d$	Diameter or distance between two geometric structures . . . . .	61
$\vec{E}$	Electric field strength vector . . . . .	7
$\vec{M}$	Magnetic current density vector . . . . .	7
$\vec{J}$	Electric current density vector . . . . .	7
$G$	Antenna gain . . . . .	56
$\eta$	Antenna aperture efficiency . . . . .	56
$\varepsilon_0$	Permittivity of free space . . . . .	7
$\varepsilon_r$	Dielectric constant, relative permittivity . . . . .	9
$\mu_0$ ,	Permeability of free space . . . . .	7
$\kappa$	Electrical conductivity . . . . .	7
$\omega$	Angular frequency . . . . .	7
$\Psi$	Scalar potential, solution of Maxwell's equations . . . . .	10
$R_s$	Surface resistance . . . . .	27
$k$	Wave number . . . . .	9
$Z_F$	Wave impedance . . . . .	13
$s_{ij}$	Scattering parameter . . . . .	13
$t$	Time . . . . .	7
$\lambda$	Wavelength . . . . .	132
$x, y, z$	Cartesian coordinates in space domain . . . . .	7
$\alpha_c$	Attenuation due to ohmic losses in the conductor . . . . .	29
$\alpha_d$	Attenuation due to dielectric losses . . . . .	32

**Symbols**

$\tan\delta$	Dissipation factor . . . . .	47
--------------	------------------------------	----

**Indices**

t	Index for tangential field components . . . . .	13
even	Property of a wave pattern, being an even function in $x$ with respect to the electric field . . . . .	10
odd	Property of a wave pattern, being an odd function in $x$ with respect to the electric field . . . . .	10

**Abbreviations**

ACC	Adaptive (or active) cruise control . . . . .	108
CW	Continuous wave . . . . .	111
NRD	Nonradiative dielectric waveguide . . . . .	2
SINRD	Substrate integrated nonradiative dielectric waveguide . .	4
ENRD	Engraved nonradiative dielectric waveguide . . . . .	4
$LSE_{mn}$	Longitudinal section electric mode with rank $m$ and order $n$ . . . . .	10
$LSM_{mn}$	Longitudinal section magnetic mode with rank $m$ and order $n$ . . . . .	10
MEMS	Microelectromechanical systems . . . . .	112
LCA	Lane change assistant . . . . .	108
LRR	Long range radar . . . . .	108
Radar	Radio detection and ranging . . . . .	107
SRR	Short range radar . . . . .	108
TE	Transverse electric mode or field . . . . .	9
TM	Transverse magnetic mode or field . . . . .	9
PP	Parallel plate wave . . . . .	87
FM	Frequency modulation . . . . .	111
LO	Local oscillator . . . . .	113
RF	Radio frequency . . . . .	113
TMM	Thermoset microwave material . . . . .	61
PMI	Polymethacrylimide . . . . .	79

# 1 Introduction

For advanced communication and sensor applications, antennas with low profile, low loss, and low production cost are required. While planar antennas are very well-suited with respect to antenna depth and cost, they suffer from high losses due to the feeding network, especially for narrow beamwidths [1, 2]. In the case of a microstrip array with corporate microstrip feeding network, the losses increase strongly with the overall size of the antenna array, Fig. 1.1 and [3]. If an element spacing of half a free space wavelength and a microstrip transmission line loss of 0.15 dB per guide wavelength are assumed, maximum gain is in the range of 30 dBi to 35 dBi. With increasing antenna size beamwidth still decreases, but gain decreases, too. With a series feeding the feed network loss can be reduced, but only at the cost of bandwidth. Another issue with series feeding is the specific beam tilt over frequency, which is problematic especially

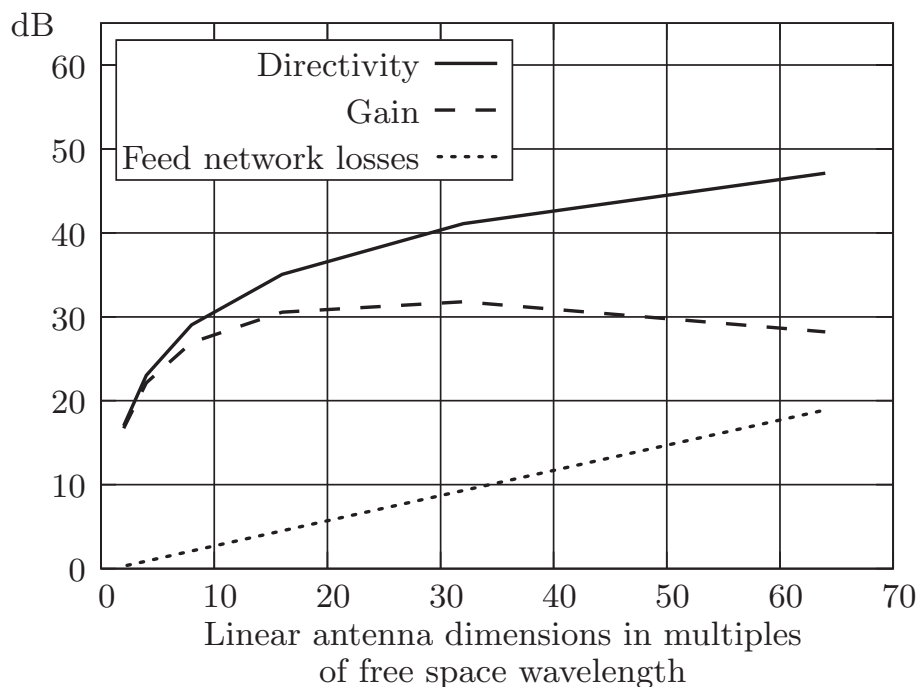


**Fig. 1.1:** Feed network losses, directivity and gain of a microstrip array with corporate microstrip feed network.

for high gain pencil beam antennas with extremely narrow beamwidths. Arrays of horn antennas with a waveguide feed network [4] or waveguide slotted arrays [5–7] which are typically based on a series feeding, are lower in loss, but partly narrow band and usually complicated in design, and they do not readily lend themselves to low cost fabrication. In a former project some work was reported on the fabrication of waveguide networks and antennas [8] as well as waveguide filters and diplexers [9] using plastic injection molding and electroplating, but the authors reported significant reduction of gain compared to the results achieved with a prototype machined from solid aluminum [4]. Printed reflectarrays are known to be an alternative solution leading to high gain and low loss antennas [10], but for some communication applications, the antenna depth even with a folding approach [11] is still too big. Another approach combines microstrip antenna arrays with a waveguide feed network [12–15] for the reduction of feed network losses. Again, the waveguide network may be fabricated using plastic injection molding and electroplating to reduce fabrication cost. Nevertheless, waveguide is still quite bulky and provides some difficulties in designing and assembling the feed network for a restricted space behind the antenna.

In this work an alternative waveguide, the nonradiative dielectric (NRD) waveguide, has been investigated for feeding planar mm-wave antennas. This approach combines the low loss behavior of the NRD-guide feeding network with low profile and low production cost of planar antennas (e.g. microstrip arrays).

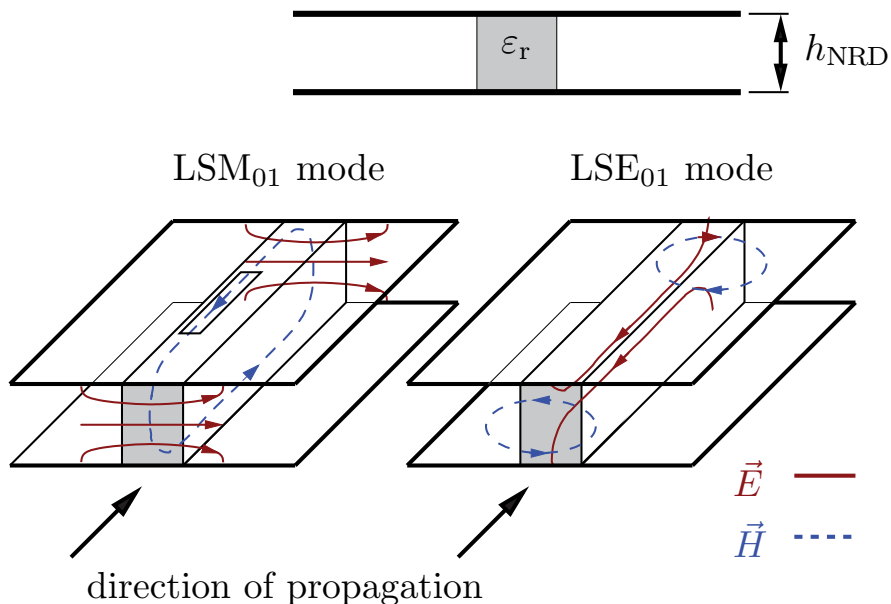
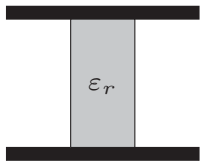


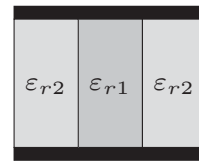
**Fig. 1.2:** Fundamental modes on the NRD-guide.

The NRD-guide, according to Fig. 1.2, consists of a dielectric strip sandwiched between two metal plates with a spacing  $h_{\text{NRD}}$  smaller than a half of free space wavelength. Assuming the same potential for both metal plates, i.e. a symmetry of the electromagnetic fields with a magnetic wall in the plane at half the NRD-guide height, assures that all modes are guided by the dielectric strip. As a result, radiation can only be caused by asymmetries along the NRD-guide height generating the parallel plate mode which is not guided by the dielectric strip. Thus it is feasible to design a group of non-radiative building blocks including bends, curves, and T-junctions, required for complex parallel or series feeding networks. The wave is guided by the dielectric strip in the form of longitudinal section electric (LSE) and longitudinal section magnetic (LSM) waves.

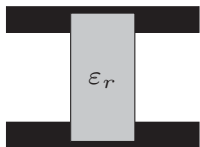
In practical applications, especially in the microwave and mm-wave range, more complicated feeding structures based on the ideal NRD-guide are difficult to implement due to alignment problems. In order to circumvent these problems, different forms of implementations indicated in Fig. 1.3 have been presented in the past.



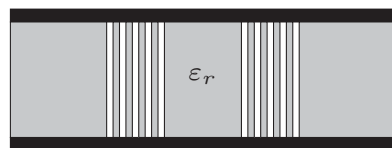
Ideal NRD-guide



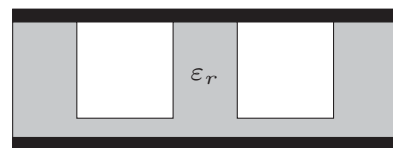
Channelized NRD-guide  
( $\epsilon_{r2} < \epsilon_{r1}$ )



Groove NRD-guide



Synthesized NRD-guide



Engraved NRD(ENRD)-guide

Substrate integrated (SI)NRD-guide

**Fig. 1.3:** Nonradiative dielectric waveguide (NRD-guide) and several alternative setups.

The channelized NRD-guide [16] consists of two materials with different values of  $\epsilon_r$ , where the material with the lower relative dielectric constant  $\epsilon_{r2}$  serves for alignment and might be a type of foam with electrical properties similar to air.

The groove NRD-guide [17–19] features a groove milled into the metal ground planes which makes alignment of the guiding strip easier and more precise. In the synthesized NRD-guide, or substrate integrated NRD (SINRD) waveguide [20–22], the transmission line is defined by a set of holes along the wave guiding area, implementing the low dielectric region as compared to the channelized NRD-guide. The engraved NRD(ENRD)-guide [23] is milled out of a solid block of dielectric material which again avoids tolerance problems.

This work includes three different types of antennas which all consist of a planar antenna part and a feeding network made of one of the above described implementations of the NRD-guide.

The antennas investigated in this thesis are implemented in the K-band (18 GHz–26.5 GHz) as for this frequency range measurement facilities and power amplifiers were readily available, but actually they lend themselves for applications in the millimeter-wave range where the low loss characteristic of the NRD-guide is even more pronounced, e.g. for point-to-point or point-to-multipoint communication links, radiometry, and for radar sensors.

**Chapter 2** of this thesis deals first with the derivation of the eigenvalue equations for the propagation constants of all solutions in the NRD-guide structure assuming the loss-free case. Solving these eigenvalue equations leads to characteristic values including propagation constants, cutoff-frequencies, and single mode propagation bandwidth. In a second step the equations for the attenuation constants according to different loss mechanisms are derived under the assumption of low loss nature with the electromagnetic fields similar to the loss-free case, and by applying a perturbational method. Those equations are then used to choose the proper dimensions of the NRD-guide structure for specific applications described in the following chapters.

The first type of antenna introduced in **Chapter 3** is an antenna for point-to-point or point-to-multipoint applications with low loss, low profile and low production cost. A corporate network of NRD-guides made of low loss high density polyethylene (HDPE) dielectric material serves as feed for planar microstrip patch antenna sub arrays. Smaller sub arrays of microstrip patches are used where losses still are low. The sub arrays are coupled to the back side NRD-guide network via coupling slots in the ground plane of the planar structure. The total height of this antenna is 6.3 mm only. Such a low profile can otherwise only be achieved with purely planar techniques like microstrip antennas fed by a microstrip line feeding network, but then at the cost of increased loss and reduced efficiency.

---

In the second type of antenna introduced in **Chapter 4** the multimode characteristic of the NRD-guide is used to implement a feeding network of a dual polarization antenna. The NRD-guide is used for the first time as a dual mode waveguide. The longitudinal section electric (LSE) and the longitudinal section magnetic (LSM) mode are excited independently by separate transitions from microstrip line to NRD-guide. Each of the modes causes the planar patch arrays to radiate in one linear polarization. Based on these investigations a dual polarization antenna was implemented using a  $2 \times 2$  array of microstrip patch antenna elements with a small microstrip feeding network, and a substrate integrated NRD-guide feed to avoid alignment problems. In an alternative implementation the ideal NRD-guide is used as a feeding network, and independent matching of LSM and LSE modes is conducted by a step in the NRD-guide width, acting as a highly reflective stub for the LSM mode only. This matching technique is the subject of a patent application.<sup>†</sup> Based on this technique a dual polarization antenna array consisting of two  $2 \times 2$  sub arrays has been implemented.

The third type of antenna described in **Chapter 5** is a low cost low profile scanning receiver array with an NRD-guide feeding network. A possible solution for low loss and low cost antennas with electronic scanning facilities is the use of frequency scanned arrays. In this work mixers are used with a frequency sweep in the local oscillator (LO) path. The radio frequency (RF) can be kept constant, and bandwidth can be fully exploited for other purposes like communication or full range resolution in a frequency modulated continuous wave (FM/CW) radar sensor. The RF signal is received by four microstrip antenna elements. Each antenna element is connected to a mixer. The LO signal is distributed via a serial NRD-guide feeding providing the frequency dependent phase shift for beam scanning. In the mixers the RF signals are down-converted in the intermediate frequency (IF) band including the phase shift. A Wilkinson power combiner adds the IF signals in phase. In this scanning receiver array an LO frequency sweep from 22.8 GHz to 24.8 GHz was necessary for a scan range of  $35^\circ$ .

---

<sup>†</sup>The transitions and T-junctions described in Section 4.2 are the subject of a patent application at the German Patent and Trade Mark Office entitled “Anordnung für einen nichtstrahlenden dielektrischen Rechteckwellenleiter zur unabhängigen Nutzung zweier oder mehrerer Moden zur Signal-Übertragung” with application number AZ 10 2011 107 128.1 and date of filing July 12, 2011.





## 2 Propagation in the Nonradiative Dielectric Waveguide (NRD-guide)

As mentioned before, the NRD-guide is a multimode transmission line. Each mode can be described by an eigenvalue equation for the propagation constants, depending on the geometry and the material constants of the NRD-guide. The knowledge of these eigenvalue equations helps to find the characteristic values like cutoff-frequency, propagation constant, single mode propagation bandwidth, and coupling coefficient between parallel NRD-guides. Once the eigenvalue equations are solved, the field patterns of the modes can be calculated and visualization of the field patterns can lead to a deeper understanding about the interaction between different modes, e.g. concerning symmetry characteristics and mode conversion at certain classes of asymmetries [24].

In the first two sections of this chapter, the eigenvalue equations of the different modes are derived from the wave equations and boundary conditions, assuming the loss-free case. In the third section, the field patterns of the fundamental modes are given. In the fourth section, an interpretation of the eigenvalue equations in form of a set of design curves helps in finding the optimum choice of material constants and geometries for a desired center frequency and bandwidth. In section five, different loss mechanisms are investigated and the attenuation constants for the fundamental modes are derived based on a perturbational method.

Figure 2.1 defines the material properties and the geometric dimensions of the NRD-guide assuming infinite extension in the  $z$ -direction, which is the direction of propagation. Index 1 is assigned to parameters inside the dielectric strip with higher dielectric constant as compared to the dielectric constant of the surrounding matter. Index 2 defines parameters outside the dielectric strip. The eigenvalue equations are derived from Maxwell's equations for time harmonic electromagnetic fields ( $\propto e^{j\omega t}$ ), in partial homogeneous ( $\hat{\epsilon}, \hat{\mu}, \hat{\kappa} \neq f(\vec{r})$ ), and isotropic ( $\hat{\epsilon}, \hat{\mu}, \hat{\kappa}$  are scalar functions) media [25]:

$$\nabla \times \vec{E} = -j\omega \hat{\mu} \vec{H} - \vec{M}_i, \quad (2.1)$$

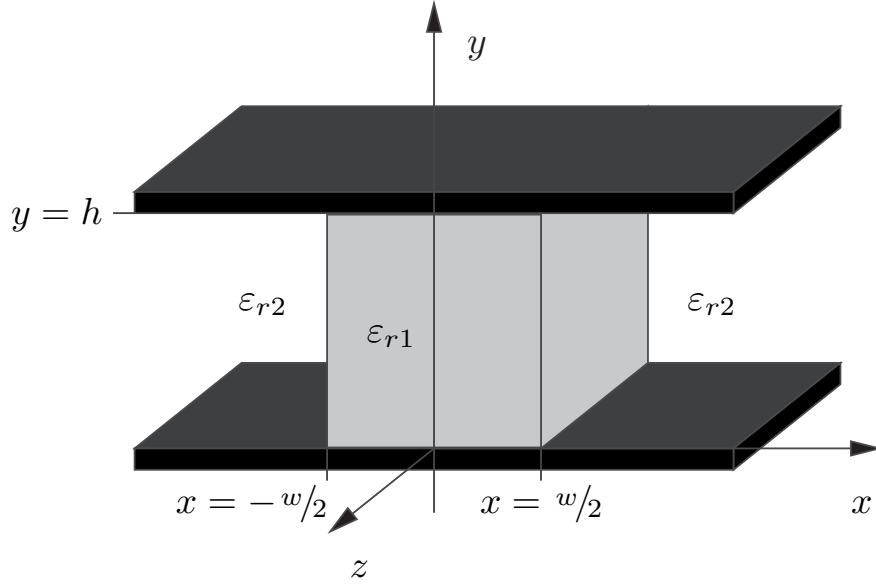


**Fig. 2.1:** Dimensions of the nonradiative dielectric waveguide (NRD-guide).

$$\nabla \times \vec{H} = j\omega\hat{\epsilon}\vec{E} + \vec{J}_c + \vec{J}_i, \quad (2.2)$$

where the term  $\vec{J}_c = \hat{\kappa}\vec{E}$  is called conduction current. Assuming linear matter in the general sense [25],  $\hat{\epsilon}$ ,  $\hat{\mu}$ ,  $\hat{\kappa}$  might all be complex functions of frequency. In this section, assuming the loss-free case, permittivity  $\epsilon$ , permeability  $\mu$ , and conductivity  $\kappa$  are all considered real values which are constant with frequency. In Eqs. (2.1) and (2.2) impressed magnetic current density  $\vec{M}_i$  and impressed electric current density  $\vec{J}_i$  are used to represent sources that are independent of the field. Here, the media are considered to be free of sources, so both impressed current densities are zero. Combining the two first order coupled differential equations leads to the second order differential Helmholtz equations:

$$\nabla \times \nabla \times \vec{E} - (\omega^2\hat{\mu}\hat{\epsilon} - j\omega\hat{\mu}\hat{\kappa})\vec{E} = \vec{0}, \quad (2.3)$$

$$\nabla \times \nabla \times \vec{H} - (\omega^2\hat{\mu}\hat{\epsilon} - j\omega\hat{\mu}\hat{\kappa})\vec{H} = \vec{0}. \quad (2.4)$$

Considering now the case of perfect, non-magnetic ( $\hat{\mu} = \mu_0$ ) and loss-free ( $\hat{\kappa} = 0$ ,  $\hat{\epsilon} = \epsilon' = \epsilon_0\epsilon_r$ ) dielectrics, and taking advantage of the divergence-less character of  $\vec{E}$  and  $\vec{H}$ , simplifies the second order differential Helmholtz equations considerably:

$$\Delta\vec{E} + \omega^2\mu_0\epsilon'\vec{E} = \vec{0}, \quad (2.5)$$

$$\Delta\vec{H} + \omega^2\mu_0\epsilon'\vec{H} = \vec{0}. \quad (2.6)$$

---

A common approach to this problem makes use of the fact that any vector fields (here  $\vec{E}$  and  $\vec{H}$ ) can be represented by two vector potentials, an electric vector potential  $\vec{F}$  and a magnetic vector potential  $\vec{A}$ . An arbitrary field in a homogeneous source-free region can be expressed as the superposition of a transverse magnetic (TM) field and transverse electric (TE) field [25]. The TM field can be fully described by a magnetic vector potential  $\vec{A}=\vec{c}\psi^a$ , the TE field by an electric vector potential  $\vec{F}=\vec{c}\psi^f$ , where  $\vec{c}$  is an arbitrary, yet constant vector independent of the coordinate system. Without loss of generality,  $\vec{c}$  can be defined by one of the three unit vectors in the Cartesian coordinate system  $\vec{e}_x, \vec{e}_y, \vec{e}_z$ . In other words,  $\vec{A}$  and  $\vec{F}$  can be chosen in such a way that e.g. in the Cartesian coordinate system, they consist of one component only and point into the same direction  $x, y$  or  $z$ . These two vector potentials fully describe all solutions in loss-free matter and the respective field patterns can be directly calculated with:

$$\vec{E} = -\nabla \times \vec{F} + \frac{1}{j\omega\epsilon'} \nabla \times \nabla \times \vec{A}, \quad (2.7)$$

$$\vec{H} = \nabla \times \vec{A} + \frac{1}{j\omega\mu_0} \nabla \times \nabla \times \vec{F}, \quad (2.8)$$

applying vector operations.

Both vector potentials must satisfy the Helmholtz equation:

$$\Delta \begin{pmatrix} \vec{A} \\ \vec{F} \end{pmatrix} + \omega^2 \epsilon' \mu_0 \begin{pmatrix} \vec{A} \\ \vec{F} \end{pmatrix} = \vec{0}, \quad (2.9)$$

with  $k=\omega\sqrt{\epsilon'\mu_0}=\omega\sqrt{\epsilon_r\epsilon_0\mu_0}$  being the wave number. The wave equations for  $\vec{A}$  and  $\vec{F}$  can be separated in three independent differential equations according to the components of the Cartesian coordinate system, and

$$k^2 = \epsilon_r k_0^2 = k_x^2 + k_y^2 + k_z^2 \quad (2.10)$$

relates the separation coefficients. Assuming loss-free harmonic wave propagation along the NRD-guide in the  $z$ -direction ( $\propto e^{-jk_z z}$ ), the wave number  $k_z$  is equal to the phase constant  $\beta$  and must be the same inside and outside the dielectric strip. This leads to:

$$k_z^2 = \epsilon_{r1} k_0^2 - k_{x1}^2 - k_y^2, \quad (2.11)$$

$$k_z^2 = \epsilon_{r2} k_0^2 - k_{x2}^2 - k_y^2, \quad (2.12)$$

$$(\epsilon_{r1} - \epsilon_{r2}) k_0^2 = k_{x1}^2 - k_{x2}^2. \quad (2.13)$$

Assuming the ideal structure in Fig. 2.1 with dependency of the physical properties of the dielectric parts only in one transverse direction (the  $x$ -direction), the solutions get much less complex and the fundamental and higher order modes may be fully described by one vector potential with one component only in the  $x$ -direction. Choosing the electrical vector potential  $\vec{F} = F_x \vec{e}_x$  leads to one set of solutions of the structure. According to Eq. (2.7) and the fact that  $\vec{F}$  has only a component in the  $x$ -direction, the electric field  $\vec{E}$  has no  $x$  component; this is why all these solutions are called longitudinal section electric (LSE) modes. Accordingly, choosing the magnetic vector potential  $\vec{A} = A_x \vec{e}_x$  leads to the other set of solutions with the magnetic field  $\vec{H}$  having no  $x$  component, thus being called longitudinal section magnetic (LSM) modes.

In the following two sections first the equations for the vector potentials and the field vectors are stated. Using the even and odd symmetry condition and the boundary conditions in the two metal plates leads then to the eigenvalue equations for the propagation constants.

## 2.1 Longitudinal Section Electric (LSE) Modes

The inherent symmetry of the problem with respect to the  $y$ - $z$ -plane enables the resulting solutions to be grouped into two types, either even or odd modes, depending on whether the  $y$  component of the electric field  $E_y$  is an even or an odd function of  $x$ . The suffixes in the nomenclature LSE $_{mn}$  refer to the rank and order  $m$  and  $n$  in  $x$ - and  $y$ -directions, respectively. As stated before, the LSE modes in the NRD-guide can be fully described by one electric vector potential  $\vec{F}$  having a component in  $x$ -direction only:

$$\vec{F} = F_x \vec{e}_x = \Psi^H \vec{e}_x, \quad (2.14)$$

$$\vec{E} = -\nabla \times \vec{F}, \quad (2.15)$$

$$\vec{H} = \frac{1}{j\omega\mu_0} \nabla \times \nabla \times \vec{F}. \quad (2.16)$$

Taking into account the simple form of the electric vector potential  $\vec{F}$ , and applying the differential operators in the Cartesian coordinate system, formulae for the electric and the magnetic field vectors can be expressed as follows:

$$\vec{E} = \begin{pmatrix} 0 \\ -\frac{\partial}{\partial z}\Psi^H \\ \frac{\partial}{\partial y}\Psi^H \end{pmatrix}, \quad (2.17)$$

$$\vec{H} = \frac{1}{j\omega\mu_0} \begin{pmatrix} -\left(\frac{\partial^2}{\partial y^2} + \frac{\partial^2}{\partial z^2}\right)\Psi^H \\ \frac{\partial^2}{\partial x\partial y}\Psi^H \\ \frac{\partial^2}{\partial x\partial z}\Psi^H \end{pmatrix}, \quad (2.18)$$

with  $\frac{\partial}{\partial z} = -jk_z$  according to the harmonic propagation of the wave pattern along the  $z$ -axis.

To simplify matters the even and odd modes with respect to the  $y$ - $z$ -plane (index  $m$ ) are calculated separately.

### 2.1.1 Even LSE Modes

The even and odd mode naming convention is related to the rank of the solution in  $x$ -direction. As such the rank  $m$  of even LSE modes ( $LSE_{0n}$ ,  $LSE_{2n}$ , ...) is an even number. The above definition that  $E_y$  must be an even function of  $x$  implies that the symmetry can be described by the  $y$ - $z$ -plane being a magnetic wall ( $\vec{n} \cdot \vec{E} = 0$ , with  $\vec{n}$  being the vector with unit length and orthonormal to the  $y$ - $z$ -plane).

In the following equations the index numbers 1 and 2 designate the core medium of the waveguide (dielectric strip) and the surrounding medium (with lower permittivity, e.g. air), respectively. The boundary conditions for the even LSE modes are the following:

According to the symmetry condition with a magnetic wall at  $x=0$ , the  $x$  component of the electric field must vanish:

$$E_x|_{x=0} = 0. \quad (2.19)$$

At the top and bottom metal plates the electric field is perpendicular to the surface, hence:

$$E_x|_{y=0} = E_z|_{y=0} = 0, \quad (2.20)$$

$$E_x|_{y=h} = E_z|_{y=h} = 0. \quad (2.21)$$

According to the continuity condition for the tangential components of the electric and magnetic fields at surfaces between distinct dielectric media, the following equations can be stated at the boundary surface ( $x=\pm\frac{w}{2}$ ) between the wave guiding dielectric strip and the surrounding material with lower permittivity, e.g. air:

$$E_{t1}|_{x=\frac{w}{2}} = E_{t2}|_{x=\frac{w}{2}}, \quad (2.22)$$

$$H_{t1}|_{x=\frac{w}{2}} = H_{t2}|_{x=\frac{w}{2}}, \quad (2.23)$$

with either  $t=y$  or  $t=z$ . With the boundary conditions the number of parameters in the equation for general solutions can be limited. According to the Eqs. (2.20) and (2.21) the  $y$  dependency of any solution  $\Psi$  must be of the form  $\cos(k_y y)$  with  $k_y = \frac{n\pi}{h}$  for  $E_x$  to vanish at  $y=0$  and  $y=h$ . Due to the fact that the wave shall be guided along medium 1 and that the electric field pattern shall be symmetric with respect to the  $y$ - $z$ -plane, the  $x$  dependency must be of the form  $\cosh(jk_{x1}x)$  within medium 1. Outside medium 1 the electromagnetic fields shall decay and thus are of the form  $e^{-jk_{x2}|x|}$ . In conclusion, solutions will be of the form:

$$\Psi_1^H = C \cosh(jk_{x1}x) \cos(k_y y) e^{-jk_z z}, \quad (2.24)$$

$$\Psi_2^H = D e^{-jk_{x2}x} \cos(k_y y) e^{-jk_z z}. \quad (2.25)$$

Applying Eqs. (2.24) and (2.25) in the equations for the electric vector potential (2.17) and (2.18) results in:

$$\vec{E}_1 = C \begin{pmatrix} 0 \\ jk_z & \cosh(jk_{x1}x) & \cos(k_y y) \\ -k_y & \cosh(jk_{x1}x) & \sin(k_y y) \end{pmatrix} e^{-jk_z z}, \quad (2.26)$$

$$\vec{E}_2 = D \begin{pmatrix} 0 \\ jk_z & e^{-jk_{x2}x} & \cos(k_y y) \\ -k_y & e^{-jk_{x2}x} & \sin(k_y y) \end{pmatrix} e^{-jk_z z}, \quad (2.27)$$

$$\vec{H}_1 = \frac{C}{j\omega\mu_0} \begin{pmatrix} (k_y^2 + k_z^2) & \cosh(jk_{x1}x) & \cos(k_y y) \\ -jk_{x1}k_y & \sinh(jk_{x1}x) & \sin(k_y y) \\ k_{x1}k_z & \sinh(jk_{x1}x) & \cos(k_y y) \end{pmatrix} e^{-jk_z z}, \quad (2.28)$$

$$\vec{H}_2 = \frac{D}{j\omega\mu_0} \begin{pmatrix} (k_y^2 + k_z^2) & e^{-jk_{x2}x} & \cos(k_y y) \\ jk_{x2}k_y & e^{-jk_{x2}x} & \sin(k_y y) \\ -k_{x2}k_z & e^{-jk_{x2}x} & \cos(k_y y) \end{pmatrix} e^{-jk_z z}, \quad (2.29)$$

with  $k_y = \frac{n\pi}{h}$ , enforcing vanishing tangential components of the electric field in the metal plates according to Eqs. (2.22) and (2.23).

Application of the Eqs. (2.26) to (2.29) with the boundary conditions for the tangential electric and magnetic field components (2.22) and (2.23), results in the following two equations:

$$E_t : \quad C \cosh\left(jk_{x1} \frac{w}{2}\right) = D e^{-jk_{x2} \frac{w}{2}}, \quad (2.30)$$

$$H_t : \quad C k_{x1} \sinh\left(jk_{x1} \frac{w}{2}\right) = -D k_{x2} e^{-jk_{x2} \frac{w}{2}}. \quad (2.31)$$

Division of the last two formulae leads to the eigenvalue equations for the propagation constants of the even LSE modes:

$$\rightsquigarrow k_{x1} \tan\left(k_{x1} \frac{w}{2}\right) = jk_{x2}. \quad (2.32)$$

With Eqs. (2.26) and (2.28) or (2.27) and (2.29) an expression for the characteristic impedance can be found:

$$Z_{F,LSE} = -\frac{E_y}{H_x} = \frac{\omega\mu_0 k_{z,LSE}}{k_y^2 + k_{z,LSE}^2}. \quad (2.33)$$

### 2.1.2 Odd LSE Modes

The above definition that for the odd LSE mode  $E_y$  must be an odd function of  $x$  implies that the symmetry can be described by the  $y$ - $z$ -plane being an electric wall ( $\vec{n} \times \vec{E} = \vec{0}$ ), i.e.:

$$E_y|_{x=0} = E_z|_{x=0} = 0. \quad (2.34)$$

All other boundary conditions are identical to the boundary conditions given for the even LSE modes Eqs. (2.20) to (2.23) and thus also the respective implications on the solution are the same. With the electric wall at  $x=0$  also the scalar potential  $\Psi^H$  must be an odd function of  $x$  within medium 1, i.e.  $\sinh(jk_{x1}x)$ , and again, outside medium 1 the electromagnetic fields shall decay and thus are of the form  $e^{-jk_{x2}|x|}$ . In conclusion, solutions will be of the form:

$$\Psi_1^H = C \sinh(jk_{x1}x) \cos(k_y y) e^{-jk_z z}, \quad (2.35)$$

$$\Psi_2^H = D e^{-jk_{x2}x} \cos(k_y y) e^{-jk_z z}. \quad (2.36)$$

Applying Eqs. (2.35) and (2.36) in the equations for the electric vector potential (2.17) and (2.18) results in:

$$\vec{E}_1 = C \begin{pmatrix} 0 \\ jk_z & \sinh(jk_{x1}x) & \cos(k_y y) \\ -k_y & \sinh(jk_{x1}x) & \sin(k_y y) \end{pmatrix} e^{-jk_z z}, \quad (2.37)$$

$$\vec{E}_2 = D \begin{pmatrix} 0 \\ jk_z & e^{-jk_{x2}x} & \cos(k_y y) \\ -k_y & e^{-jk_{x2}x} & \sin(k_y y) \end{pmatrix} e^{-jk_z z}, \quad (2.38)$$

$$\vec{H}_1 = \frac{C}{j\omega\mu_0} \begin{pmatrix} (k_y^2 + k_z^2) & \sinh(jk_{x1}x) & \cos(k_y y) \\ -jk_{x1}k_y & \cosh(jk_{x1}x) & \sin(k_y y) \\ k_{x1}k_z & \cosh(jk_{x1}x) & \cos(k_y y) \end{pmatrix} e^{-jk_z z}, \quad (2.39)$$

$$\vec{H}_2 = \frac{D}{j\omega\mu_0} \begin{pmatrix} (k_y^2 + k_z^2) & e^{-jk_{x2}x} & \cos(k_y y) \\ jk_{x2}k_y & e^{-jk_{x2}x} & \sin(k_y y) \\ -k_{x2}k_z & e^{-jk_{x2}x} & \cos(k_y y) \end{pmatrix} e^{-jk_z z}, \quad (2.40)$$

with  $k_y = \frac{n\pi}{h}$ , according to Eqs. (2.22) and (2.23).

Application of the Eqs. (2.37) to (2.40) with the continuity conditions for the tangential electric and magnetic field components, Eqs. (2.22) and (2.23), results in the following two equations:

$$E_t : \quad C \sinh\left(jk_{x1} \frac{w}{2}\right) = D e^{-jk_{x2} \frac{w}{2}}, \quad (2.41)$$

$$H_t : \quad C k_{x1} \cosh\left(jk_{x1} \frac{w}{2}\right) = -D k_{x2} e^{-jk_{x2} \frac{w}{2}}. \quad (2.42)$$

Division of the last two formulae leads to the eigenvalue equations for the propagation constants of the odd LSE modes:

$$\rightsquigarrow k_{x1} \cot\left(k_{x1} \frac{w}{2}\right) = -jk_{x2}. \quad (2.43)$$

In practical applications the propagation characteristics of the first longitudinal section electric odd mode LSE<sub>11</sub> is of great interest as it limits the operational bandwidth of the fundamental longitudinal section magnetic LSM<sub>01</sub> mode.



## 2.2 Longitudinal Section Magnetic (LSM) Modes

For some time the fundamental longitudinal section magnetic (LSM<sub>01</sub>) mode was considered the wanted mode as it usually provides lower attenuation characteristics compared to the LSE<sub>01</sub> mode. Another reason was certainly that interconnects between rectangular waveguide and NRD-guide can be implemented in a simple manner due to the field pattern similarity between the LSM<sub>01</sub> mode and the TE<sub>10</sub> mode in the rectangular waveguide. The LSM modes in the NRD-guide can be fully described by one magnetic vector potential  $\vec{A}$  having a component in  $x$ -direction only:

$$\vec{A} = A_x \vec{e}_x = \Psi^E \vec{e}_x, \quad (2.44)$$

$$\vec{H} = \nabla \times \vec{A}, \quad (2.45)$$

$$\vec{E} = \frac{1}{j\omega\varepsilon'} \nabla \times \nabla \times \vec{A}. \quad (2.46)$$

Taking into account the simple form of the magnetic vector potential  $\vec{A}$ , and applying the differential operators in the Cartesian coordinate system, formulae for the electric and the magnetic field vectors can be expressed as follows:

$$\vec{H} = \begin{pmatrix} 0 \\ \frac{\partial}{\partial z} \Psi^E \\ -\frac{\partial}{\partial y} \Psi^E \end{pmatrix}, \quad (2.47)$$

$$\vec{E} = \frac{1}{j\omega\varepsilon'} \begin{pmatrix} -\left(\frac{\partial^2}{\partial y^2} + \frac{\partial^2}{\partial z^2}\right) \Psi^E \\ \frac{\partial^2}{\partial x \partial y} \Psi^E \\ \frac{\partial^2}{\partial x \partial z} \Psi^E \end{pmatrix}, \quad (2.48)$$

with  $\frac{\partial}{\partial z} = -jk_z$  according to the harmonic propagation of the wave pattern along the  $z$ -direction.

To simplify matters the even and odd modes with respect to the  $y$ - $z$ -plane (index  $m$ ) are again calculated separately.

### 2.2.1 Even LSM Modes

In analogy to the above definition, for the even LSM modes  $H_y$  must be an even function of  $x$ . This implies that the symmetry can be described by the  $y$ - $z$ -plane being an electric wall ( $\vec{n} \times \vec{E} = \vec{0}$ ), i.e.:

$$E_y|_{x=0} = E_z|_{x=0} = 0. \quad (2.49)$$

All other boundary conditions are identical to the boundary conditions given for the even LSE modes (2.20) to (2.23), and thus, also the respective implications on the solution are the same. With the electric wall at  $x=0$  also the scalar potential must be an even function of  $x$  within medium 1, i.e.  $\cosh(jk_{x1}x)$ , and again, outside medium 1 the electromagnetic fields shall decay and thus are of the form  $e^{-jk_{x2}|x|}$ . In conclusion solutions will be of the form:

$$\Psi_1^E = C \cosh(jk_{x1}x) \sin(k_y y) e^{-jk_z z}, \quad (2.50)$$

$$\Psi_2^E = D e^{-jk_{x2}x} \sin(k_y y) e^{-jk_z z}. \quad (2.51)$$

Applying Eqs. (2.50) and (2.51) in the equations for the magnetic vector potential (2.47) and (2.48) results in

$$\vec{E}_1 = \frac{C}{j\omega\epsilon_0\epsilon_{r1}} \begin{pmatrix} (k_y^2 + k_z^2) & \cosh(jk_{x1}x) & \sin(k_y y) \\ jk_{x1}k_y & \sinh(jk_{x1}x) & \cos(k_y y) \\ k_{x1}k_z & \sinh(jk_{x1}x) & \sin(k_y y) \end{pmatrix} e^{-jk_z z}, \quad (2.52)$$

$$\vec{E}_2 = \frac{D}{j\omega\epsilon_0\epsilon_{r2}} \begin{pmatrix} (k_y^2 + k_z^2) & e^{-jk_{x2}x} & \sin(k_y y) \\ -jk_{x2}k_y & e^{-jk_{x2}x} & \cos(k_y y) \\ -k_{x2}k_z & e^{-jk_{x2}x} & \sin(k_y y) \end{pmatrix} e^{-jk_z z}, \quad (2.53)$$

$$\vec{H}_1 = C \begin{pmatrix} 0 \\ -jk_z & \cosh(jk_{x1}x) & \sin(k_y y) \\ -k_y & \cosh(jk_{x1}x) & \cos(k_y y) \end{pmatrix} e^{-jk_z z}, \quad (2.54)$$

$$\vec{H}_2 = D \begin{pmatrix} 0 \\ -jk_z & e^{-jk_{x2}x} & \sin(k_y y) \\ -k_y & e^{-jk_{x2}x} & \cos(k_y y) \end{pmatrix} e^{-jk_z z}, \quad (2.55)$$

with  $k_y = \frac{n\pi}{h}$ , according to Eqs. (2.22) and (2.23).

Application of the Eqs. (2.52) to (2.55) with the boundary conditions for the tangential electric and magnetic field components, equations (2.22) and (2.23), results in the following two equations:

$$E_t : \quad C \frac{k_{x1}}{\varepsilon_{r1}} \sinh \left( j k_{x1} \frac{w}{2} \right) = -D \frac{k_{x2}}{\varepsilon_{r2}} e^{-j k_{x2} \frac{w}{2}}, \quad (2.56)$$

$$H_t : \quad C \cosh \left( j k_{x1} \frac{w}{2} \right) = D e^{-j k_{x2} \frac{w}{2}}. \quad (2.57)$$

Division of the last two formulae leads to the eigenvalue equations for the propagation constants of the even LSM modes:

$$\rightsquigarrow \frac{k_{x1}}{\varepsilon_{r1}} \tan \left( k_{x1} \frac{w}{2} \right) = j \frac{k_{x2}}{\varepsilon_{r2}}. \quad (2.58)$$

With Eqs. (2.52) and (2.54) or (2.53) and (2.55) an expression for the characteristic impedance can be found:

$$Z_{F,LSM} = \frac{E_x}{H_y} = \frac{k_y^2 + k_{z,LSM}^2}{\omega \varepsilon_0 \varepsilon_{r1} k_{z,LSM}}. \quad (2.59)$$

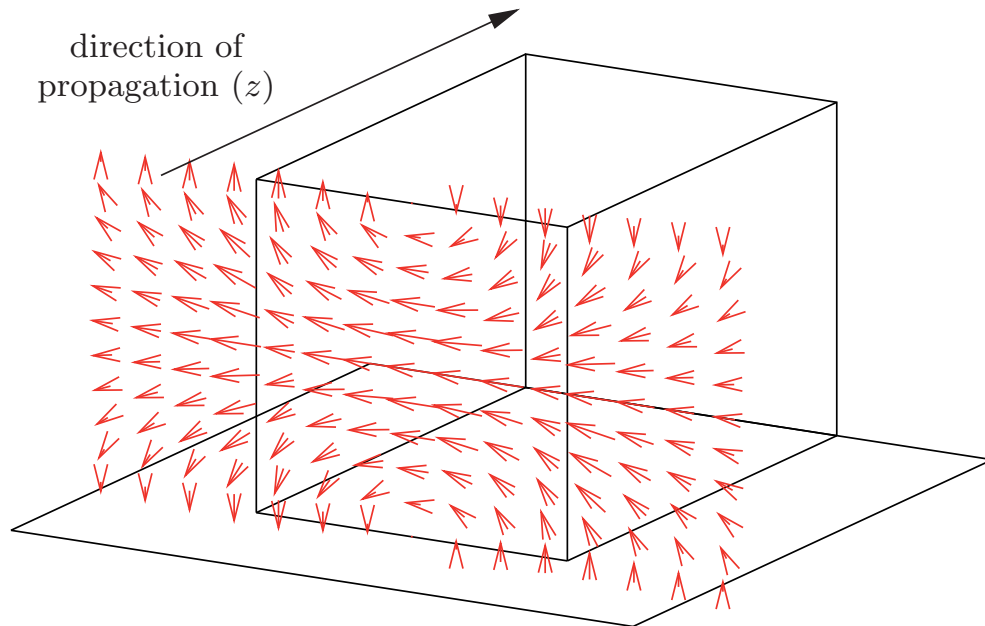
### 2.2.2 LSM Odd Modes

The longitudinal section magnetic (LSM) mode with an odd rank, (i.e. LSM<sub>1n</sub>, LSE<sub>3n</sub>, ...) usually is not so much of interest and thus is not dealt with here in detail. Just the eigenvalue equation shall be stated for the sake of completeness:

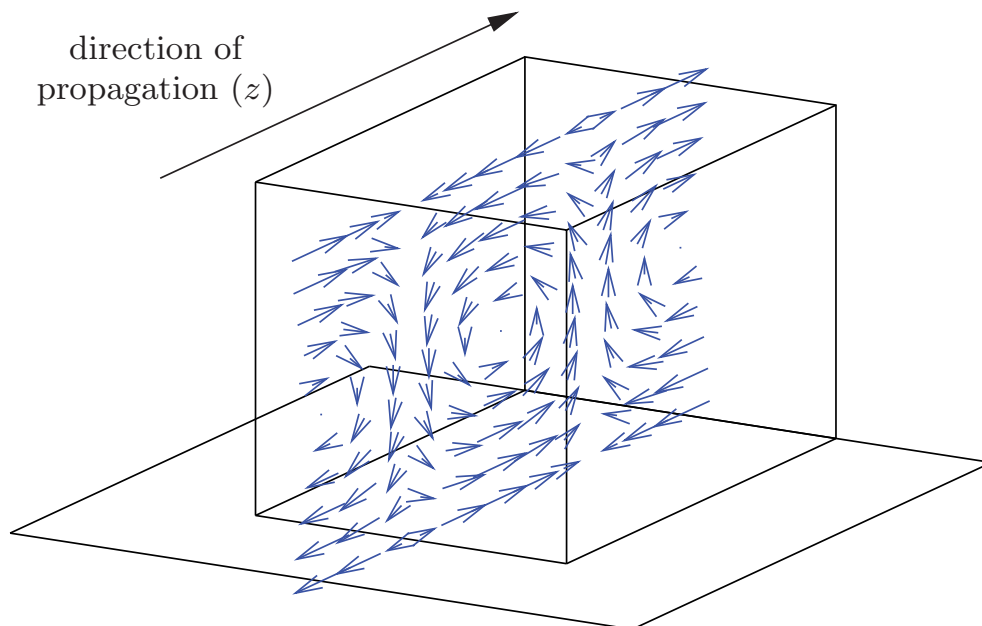
$$\rightsquigarrow \frac{k_{x1}}{\varepsilon_{r1}} \cot \left( k_{x1} \frac{w}{2} \right) = -j \frac{k_{x2}}{\varepsilon_{r2}}. \quad (2.60)$$

## 2.3 Field Solutions for the Fundamental Modes

Exemplary, figures 2.2 and 2.3 illustrate the electric and magnetic fields for the fundamental LSM<sub>01</sub> and LSE<sub>01</sub> modes, respectively. For a comprehensible visualization the field patterns are shown in one cutting plane only and separately for the electric and the magnetic fields. In reality, the electric field of the LSM<sub>01</sub> mode in Fig. 2.2a has an additional component in the  $z$ -direction, and also the magnetic field of the LSE<sub>01</sub> mode in Fig. 2.3b has a component in the  $z$ -direction.

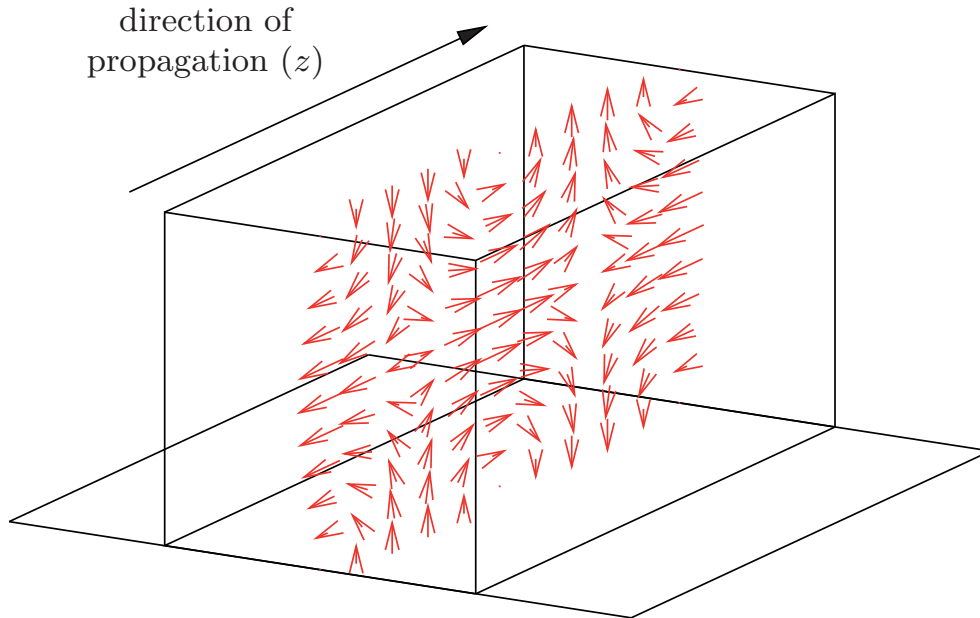


(a) Electric field, for simplification the  $z$ -component is not shown here.

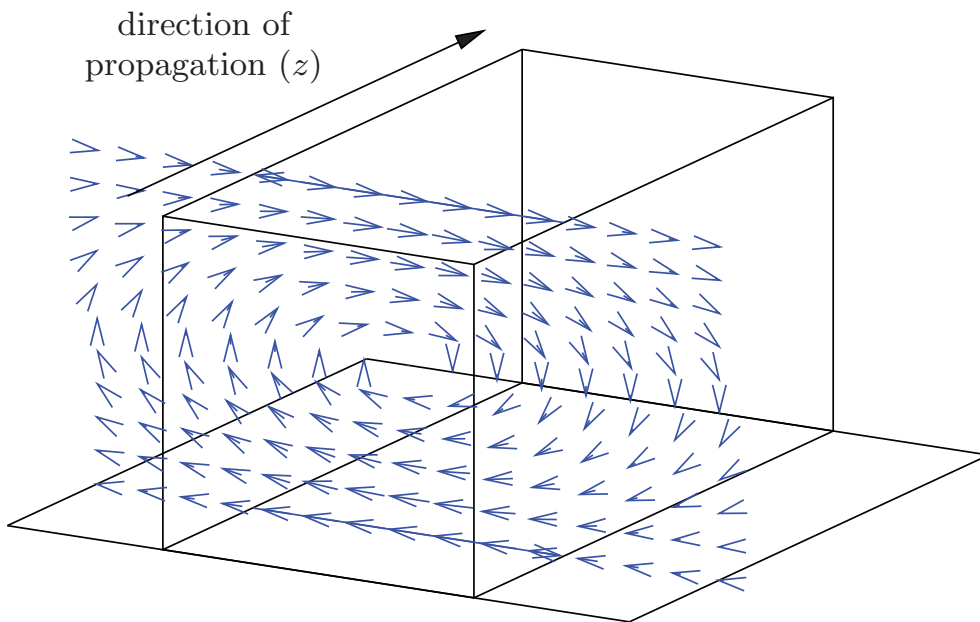


(b) Magnetic field.

**Fig. 2.2:** Field patterns of the  $LSM_{01}$  mode of the NRD-guide.



(a) Electric field.



(b) Magnetic field, for simplification the  $z$ -component is not shown here.

**Fig. 2.3:** Field patterns of the  $LSE_{01}$  mode in the NRD-guide.

## 2.4 A Graphical Method for Solutions of the Eigenvalue Equations and Determination of Cutoff-Frequencies

The eigenvalue equations for the different modes in the NRD-guide, derived in the previous sections, determine one relation between the separation coefficients  $k_{x1}$  and  $k_{x2}$ . A second relation was obtained with Eq. (2.13) by equating the two expressions for the wave number in the direction of propagation in the two different dielectrics. These two relations can be plotted on a  $(k_{x1} \frac{w}{2}) - (jk_{x2} \frac{w}{2})$  plane, yielding a graphical solution at the points of intersection [26]. For this purpose it is convenient to rewrite Eq. (2.13) as follows

$$(\varepsilon_{r1} - \varepsilon_{r2}) \left(k_0 \frac{w}{2}\right)^2 = \left(k_{x1} \frac{w}{2}\right)^2 + \left(jk_{x2} \frac{w}{2}\right)^2. \quad (2.61)$$

This equation determines a circle of radius  $\sqrt{\varepsilon_{r1} - \varepsilon_{r2}} k_0 \frac{w}{2}$ . Now assuming the loss-free case, the cutoff-frequency is where the wave number  $k_z$  approaches zero. Equations for the propagation constant in the two dielectric regions were given in Eqs. (2.11) and (2.12). For  $k_z \rightarrow 0$  these equations can be rewritten to

$$\left(k_{x1} \frac{w}{2}\right)^2 = \varepsilon_{r1} \left(k_0 \frac{w}{2}\right)^2 - \left(k_y \frac{w}{2}\right)^2, \quad (2.62)$$

$$\left(jk_{x2} \frac{w}{2}\right)^2 = \left(k_y \frac{w}{2}\right)^2 - \varepsilon_{r2} \left(k_0 \frac{w}{2}\right)^2. \quad (2.63)$$

These two equations can be combined to yield

$$(\varepsilon_{r1} - \varepsilon_{r2}) \left(k_y \frac{w}{2}\right)^2 = \varepsilon_{r2} \left(k_{x1} \frac{w}{2}\right)^2 + \varepsilon_{r1} \left(jk_{x2} \frac{w}{2}\right)^2, \quad (2.64)$$

which defines an ellipse in the  $(k_{x1} \frac{w}{2}) - (jk_{x2} \frac{w}{2})$  plane. Now the point of interception with the function defined by the eigenvalue equation represents the cutoff-frequency of the mode under consideration.

Considering now even LSM modes, the eigenvalue equation given by Eq. (2.58) can be rewritten as a function of  $k_{x1} \frac{w}{2}$

$$jk_{x2} \frac{w}{2} = \frac{\varepsilon_{r2}}{\varepsilon_{r1}} k_{x1} \frac{w}{2} \tan(k_{x1} \frac{w}{2}) \quad (2.65)$$

which is represented in Fig. 2.4 by the solid, bold curves, for different ratios of strip widths  $w$  to free-space wavelength  $\lambda_0$ , assuming the specific case of a strip made of high density polyethylene (HDPE,  $\varepsilon_{r1}=2.3$ ) surrounded by air ( $\varepsilon_{r2}=1$ ).

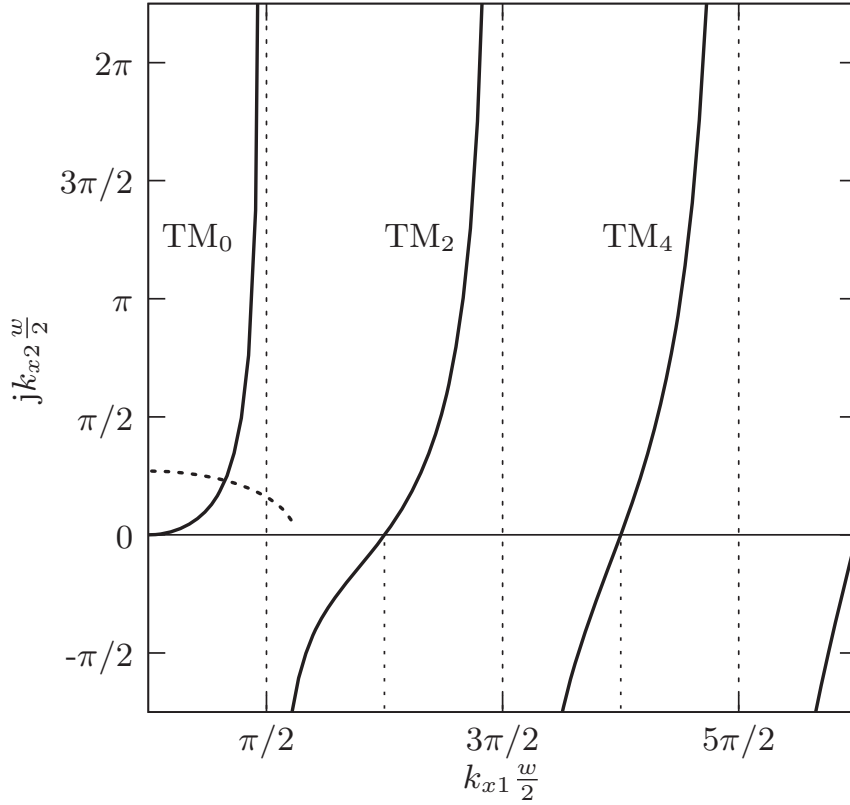


**Fig. 2.4:** Graphical solution for eigenvalues for the even TM modes of surface waves along a dielectric slab ( $\varepsilon_{r1}=2.3$ ) surrounded by air ( $\varepsilon_{r2}=1$ ). Solid, bold curves represent solutions of the eigenvalue equation  $jk_{x2} \frac{w}{2} = \frac{\varepsilon_{r2}}{\varepsilon_{r1}} k_{x1} \frac{w}{2} \tan(k_{x1} \frac{w}{2})$ . The dashed ellipse represents the cutoff-frequencies of the corresponding even LSM modes in an NRD-guide, which is in this example specified by the ratio  $\frac{\sqrt{\varepsilon_{r1}-\varepsilon_{r2}} \cdot w}{h} = 0.94$ .

The dotted curve represents the ellipse defined by Eq. (2.64). The point of intersection between the two curves is the cutoff-frequency of the LSM<sub>01</sub> mode.

The same methodology can be applied to find the cutoff-frequencies for the fundamental mode LSE<sub>01</sub> and the higher order modes LSE<sub>11</sub> and LSM<sub>11</sub> by applying Eqs. (2.32), (2.43), and (2.60), respectively. The cutoff-frequencies for the fundamental and higher order modes can now be plotted in the  $(h/\lambda_0) - (\sqrt{\varepsilon_{r1} - \varepsilon_{r2}} \cdot w/\lambda_0)$  plane as shown in Fig. 2.5 and [27]. This representation has several advantages as compared to Fig. 2.4. First, it shows the regions of single mode, dual mode, and multi mode operation. Second, the fractional bandwidths

of single mode and dual mode operation can be directly determined for a specific setup. A straight line passing through the origin and having the slope  $\frac{\sqrt{\varepsilon_{r1}-\varepsilon_{r2}} \cdot w}{h}$  defined by the material characteristics and geometry of the specific NRD-guide setup, shows intersections  $P_1, P_2, P_3$ , and  $P_4$  with the four curves that represent the cutoff-frequencies for the  $LSE_{01}$ ,  $LSM_{01}$ ,  $LSE_{11}$ , and  $LSM_{11}$ , respectively. The single mode operation fractional bandwidth of the  $LSE_{01}$  mode can now be determined by the ratio of the lengths  $\overline{OP_3}$  and  $\overline{OP_1}$ . From Fig. 2.5 it can be seen, that fractional bandwidths are only dependent on the ratio  $\frac{\sqrt{\varepsilon_{r1}-\varepsilon_{r2}} \cdot w}{h}$ , which determines the slope of the straight line, but not on absolute values of strip width  $w$  or strip height  $h$  nor is it dependent on absolute values of dielectric constants  $\varepsilon_{r1}$  or  $\varepsilon_{r2}$ .

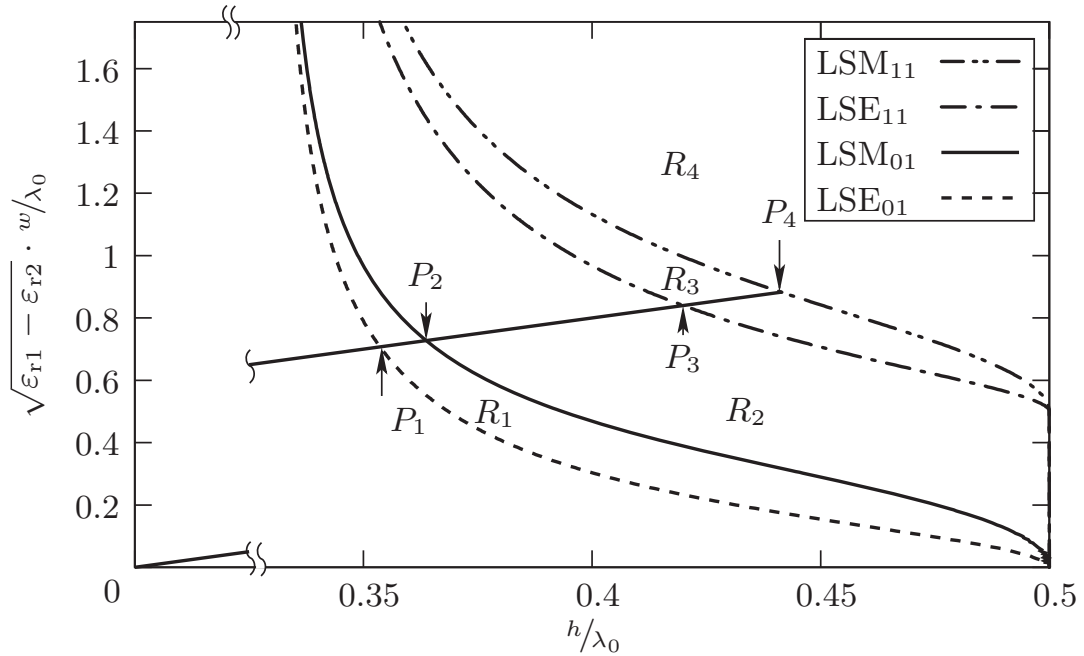


**Fig. 2.5:** Design diagram showing regions of single mode operation in region  $R_1$ , dual mode operation in region  $R_2$ , and multi mode operation in regions  $R_3$  and  $R_4$ , assuming HDPE for the strip material surrounded by air. Intersections  $P_1, P_2, P_3$ , and  $P_4$  can be used to determine fractional bandwidths for each kind of operation.

With this characteristic of the NRD-guide in mind, the fractional bandwidths for single mode operation for the  $LSE_{01}$  and  $LSM_{01}$  modes, respectively, assuming HDPE ( $\varepsilon_{r1}=2.3$ ) for the strip material, which is surrounded by air ( $\varepsilon_{r2}=1$ ), has been plotted in Fig. 2.6. Here, the upper limit of bandwidth  $f_U$  is defined by the cutoff-frequencies of the  $LSE_{11}$  mode or the  $LSM_{11}$  mode, whichever is lower.



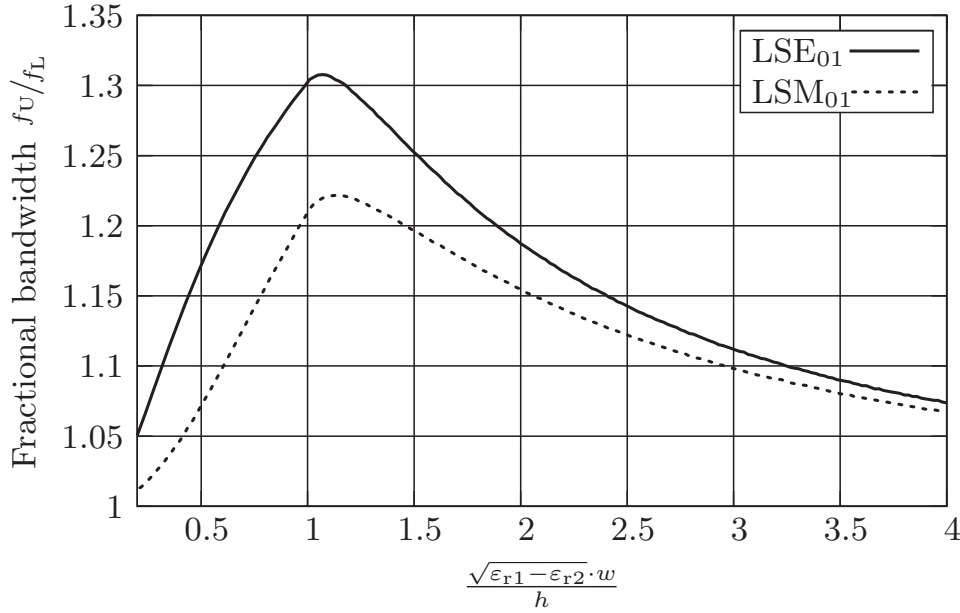


**Fig. 2.6:** Fractional bandwidths of single mode operation for the LSE<sub>01</sub> mode and the LSM<sub>01</sub> mode assuming HDPE ( $\epsilon_{r1}=2.3$ ) for the strip material surrounded by air ( $\epsilon_{r2}=1$ ). The upper limit of bandwidth  $f_U$  is defined by the cutoff-frequencies of the LSE<sub>11</sub> mode or the LSM<sub>11</sub> mode, whichever is lower.

In practical applications though, there are a couple of restrictions in the choice of geometry and material properties with impact on the usable bandwidth. First, in complex NRD-guide feedings with bends, corners, and T-junctions, both fundamental modes, LSE<sub>01</sub> and LSM<sub>01</sub> are required, and sometimes both modes are required on the same section of NRD-guide, as with the dual polarization antennas described in Chapter 4. Second, for ease of construction and assembly, the metal plate distance, i.e. the strip height, should be kept constant all across the feeding. Third, the lower end of frequency band is defined by the cutoff-frequency of the LSE<sub>01</sub>, or the cutoff-frequency of the LSM<sub>01</sub>, whichever is higher, for both fundamental modes are required for proper operation of the feeding. Forth, the upper end of frequency band for the feeding is defined by the cutoff-frequency of the first higher order mode LSE<sub>11</sub> or LSM<sub>11</sub>, or the maximum frequency defined by the non-radiation condition  $f_{\max} = \frac{c_0}{2h\sqrt{\epsilon_{r2}}}$ , whichever is lower.

With these limitations, in order to find the optimum geometry for a given center frequency of 24 GHz, the desired bandwidth has been chosen to 4 GHz. With this, the maximum strip height can be found from  $h_{\max} = \frac{c_0}{2f_{\max}} = 5.8$  mm, according

to the non-radiating condition. Figure 2.7 shows the absolute bandwidths of single mode operation for  $LSE_{01}$  mode and  $LSM_{01}$  mode assuming high density polyethylene (HDPE) for the strip material surrounded by air. The upper limit of bandwidth  $f_U$  is defined by the cutoff-frequencies of the  $LSE_{11}$  mode, the  $LSM_{11}$  mode or the radiating condition  $h=\lambda_0/2$ , which ever is lower. The lower limit of bandwidth  $f_L$  is defined by 22 GHz or the cutoff-frequency of the mode under consideration,  $LSE_{01}$  or  $LSM_{01}$ . The optimum NRD-guide width for either mode has been found from Fig. 2.7 by taking the mean value of upper and lower limits of width  $w$  for maximum bandwidth, i.e.  $w_{LSE}=3.9$  mm and  $w_{LSM}=4.8$  mm.

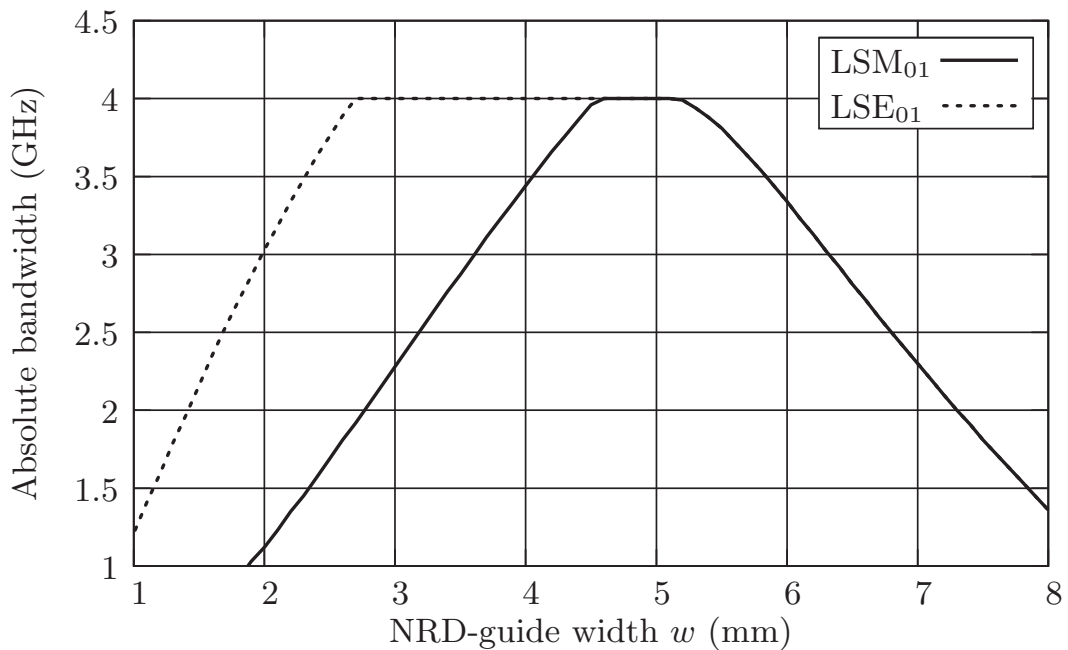


**Fig. 2.7:** Absolute bandwidths of single mode operation for the  $LSE_{01}$  mode and the  $LSM_{01}$  mode assuming HDPE for the strip material surrounded by air. The strip height is chosen to  $h=5.8$  mm.

## 2.5 Loss Calculation

So far the treatment of propagation in the NRD-guide has been confined to the loss-free case, i.e. all materials have been considered ideal. In contrast, real matter shows lossy behavior. Typically, transmission losses can be grouped in three mechanisms. Loss according to imperfect dielectrics, loss according to imperfect conductors, and loss due to surface roughness of boundaries between conductor and dielectric. For planar types of transmission lines, like the microstrip line or triplate line, the latter loss mechanism is a major contribution to the total loss — with those planar transmission line types roughened copper foil can cause an increase of resistivity by a factor of 2 to 3 at frequencies as low as 10 GHz [28, 29]. By contrast, it is a secondary effect for hollow waveguides and the NRD-guide, and is negligible as compared to the first and second loss mechanisms, as will be shown at the end of this section.

The loss mechanisms are derived by the perturbational method [25], where the loss-free solution derived in the previous sections is used to approximate the electric and magnetic fields in the NRD-guide. Assuming the propagation constant to be of the form  $\gamma = \alpha + j\beta$ , with the phase constant  $\beta$  and the attenuation constant  $\alpha$ . Hence a wave traveling in  $+z$ -direction will be of the form  $E, H \propto e^{-(\alpha + j\beta)z}$  and the power flow is given by

$$P_f = P_0 e^{-2\alpha z}$$

or, in terms of time-average powers,

$$\bar{P}_f = \text{Re}(P_f) = \text{Re}(P_0) e^{-2\alpha z}.$$

The rate of decrease in  $\bar{P}_f$  versus  $z$  equals the time-average power dissipated per unit length  $\bar{P}_d$ , or

$$\bar{P}_d = -\frac{\partial \bar{P}_f}{\partial z} = 2\alpha \bar{P}_f.$$

Thus, the attenuation constant is given by

$$\alpha = \frac{\bar{P}_d}{2\bar{P}_f}. \quad (2.66)$$

The time-average power flow  $\bar{P}_f$  can be found from

$$\bar{P}_f = \iint_A \text{Re}(\vec{E} \times \vec{H}^*) \cdot \vec{e}_z \, dx \, dy, \quad (2.67)$$

where  $A$  is the cross section transverse to the direction of propagation  $z$  and bounded by the metal plates.

### 2.5.1 Time-Average Power Flow

With the LSE modes, the electric field  $\vec{E}$  has no  $x$  component and according to the symmetry with respect to the  $y$ - $z$ -plane, the time-average power flow is the same for  $x < 0$  and  $x > 0$ , hence Eq. (2.67) yields

$$\bar{P}_{f,\text{LSE}} = 2 \int_0^h \left\{ \int_0^{w/2} E_{1y} \cdot H_{1x}^* dx + \int_{w/2}^{\infty} E_{2y} \cdot H_{2x}^* dx \right\} dy. \quad (2.68)$$

Applying Eqs. (2.26) through (2.29) for the electric and magnetic fields in the dielectric material with index 1 and index 2 and integration over variables  $x$  and  $y$  leads to

$$\bar{P}_{f,\text{LSE}} = 2 \frac{(k_y^2 + k_z^2) k_z}{\omega \mu} \left\{ \frac{C^2}{4k_{x1}} [wk_{x1} + \sin(wk_{x1})] + \frac{D^2}{2jk_{x2}} e^{-jk_{x2}w} \right\} \frac{h}{2}.$$

According to Eq. (2.31):  $e^{-jk_{x2}w} = \frac{C^2 k_{x1}^2}{D^2 (jk_{x2})^2} \sin^2(k_{x1} \frac{w}{2})$ . This, the identity for trigonometric functions  $\sin^2(\frac{\varphi}{2}) = \frac{1}{2} \sin \varphi \cdot \tan(\frac{\varphi}{2})$ , and the eigenvalue equation for the propagation constants of the even LSE modes Eq. (2.32) leads to a simple equation for the time-average power flow for the even LSE modes

$$\bar{P}_{f,\text{LSE}} = \frac{hC^2 (k_y^2 + k_z^2) k_z}{4k_{x1}\omega\mu} \left\{ wk_{x1} + \sin(wk_{x1}) \left[ 1 + \left( \frac{k_{x1}}{jk_{x2}} \right)^2 \right] \right\}. \quad (2.69)$$

With the LSM modes, the magnetic field  $\vec{H}$  in Eq. (2.67) has no  $x$  component and according to the symmetry with respect to the  $y$ - $z$ -plane, again only half of the structure, e.g.  $x > 0$ , needs to be considered applying the factor 2. Hence the time-average power flow is

$$\bar{P}_{f,\text{LSM}} = 2 \int_0^h \left\{ \int_0^{w/2} E_{1x} \cdot H_{1y}^* dx + \int_{w/2}^{\infty} E_{2x} \cdot H_{2y}^* dx \right\} dy. \quad (2.70)$$

Applying Eqs. (2.52) through (2.55) for the electric and magnetic fields in the dielectric material with index 1 and index 2 and integration leads to

$$\bar{P}_{f,\text{LSM}} = 2 \frac{(k_y^2 + k_z^2) k_z}{\omega \epsilon_0} \left\{ \frac{C^2}{\epsilon_{r1} 4k_{x1}} [wk_{x1} + \sin(wk_{x1})] + \frac{D^2}{\epsilon_{r2} 2jk_{x2}} e^{-jk_{x2}w} \right\} \frac{h}{2}.$$

According to Eq. (2.56):  $e^{-jk_{x2}w} = \frac{C^2 \varepsilon_{r2}^2 k_{x1}^2}{D^2 \varepsilon_{r1}^2 (jk_{x2})^2} \sin^2(k_{x1} \frac{w}{2})$ . This, the identity for trigonometric functions as before, and the eigenvalue equation for the propagation constants of the even LSM modes Eq. (2.58) leads to a simple equation for the time-average power flow for the even LSM modes

$$\bar{P}_{f,\text{LSM}} = \frac{hC^2 (k_y^2 + k_z^2) k_z}{4k_{x1}\omega\varepsilon_0\varepsilon_{r1}} \left\{ wk_{x1} + \sin(wk_{x1}) \left[ 1 + \left( \frac{k_{x1}}{jk_{x2}} \right)^2 \right] \right\}. \quad (2.71)$$

## 2.5.2 Transmission Loss due to Imperfect Conductors

To find the transmission loss due to imperfect conductors, one must first calculate the density of power flow into the conductor, given by the Poynting vector

$$\vec{S} = \vec{E} \times \vec{H}^*. \quad (2.72)$$

The Poynting vector can be expressed in terms of wave impedances with the  $y$  component being

$$S_y = Z_{zx}^+ |H_x|^2 + Z_{xz}^+ |H_z|^2, \quad (2.73)$$

where the wave impedances  $Z_{zx}^+$  and  $Z_{xz}^+$  in a homogeneous conductor are the same and equal to the surface impedance  $\eta_m$  of the metal, see below. The time-average power dissipation per unit area of surface cross section is the real part of the above power flow,

$$\bar{P}_d = |H_0|^2 \cdot R_s \quad \text{in Watts per square meter}, \quad (2.74)$$

where  $R_s = \text{Re}(\eta_m) = \sqrt{\omega\mu_0/(2\kappa)}$  is the surface resistance of the metal.  $H_0$  is the amplitude of the magnetic field at the surface. Equation (2.74) is strictly true only when the wave propagates normally into the conductor. According to [25] this is usually so. An important exception however occurs at sharp corners extending outwards from conductors as with rough surfaces.

To find the power dissipation per unit length in the NRD-guide, this equation must be integrated over both metal plates. But according to symmetries with respect to the plane at  $y = \frac{h}{2}$  and with respect to the  $y$ - $z$ -plane, it is sufficient to integrate only over half of the bottom metal plate at  $x \geq 0$ ,  $y = 0$ , and to apply the factor 4

$$\bar{P}_d = 4R_s \left( \underbrace{\int_0^{w/2} |H_{1x}|^2 + |H_{1z}|^2 dx}_{I_1} + \underbrace{\int_{w/2}^{\infty} |H_{2x}|^2 + |H_{2z}|^2 dx}_{I_2} \right). \quad (2.75)$$

In case of even LSE modes, with Eq. (2.28), page 12 for the magnetic field, the first integral equals

$$\begin{aligned} I_1 &= \frac{C^2}{(\omega\mu)^2} \left\{ \int_0^{w/2} (k_y^2 + k_z^2)^2 \cos^2(xk_{x1}) + k_{x1}^2 k_z^2 \sin^2(xk_{x1}) dx \right\} \\ &= \frac{C^2}{4(\omega\mu)^2 k_{x1}} \left\{ (k_y^2 + k_z^2)^2 [wk_{x1} + \sin(wk_{x1})] + k_{x1}^2 k_z^2 [wk_{x1} - \sin(wk_{x1})] \right\}. \end{aligned} \quad (2.76)$$

The second integral can be simplified using the identity for trigonometric functions as before and the eigenvalue equation for the propagation constants of the even LSE modes Eq. (2.32) and reads

$$\begin{aligned} I_2 &= \frac{D^2}{(\omega\mu)^2} \int_{w/2}^{\infty} \left[ (k_y^2 + k_z^2)^2 + (jk_{x2})^2 k_z^2 \right] e^{-2jk_{x2}x} dx \\ &= \frac{C^2}{2(\omega\mu)^2} \frac{k_{x1}^2}{(jk_{x2})^3} \sin^2\left(\frac{w}{2}k_{x1}\right) \left[ (k_y^2 + k_z^2)^2 + (jk_{x2})^2 k_z^2 \right] \\ &= \frac{C^2}{4(\omega\mu)^2 k_{x1}} \frac{k_{x1}^2}{(jk_{x2})^2} \sin(wk_{x1}) \left[ (k_y^2 + k_z^2)^2 + (jk_{x2})^2 k_z^2 \right]. \end{aligned} \quad (2.77)$$

With the equations for  $I_1$  and  $I_2$  the power dissipation per unit length caused by imperfect conductors can be calculated by

$$\bar{P}_d = \frac{R_s C^2}{(\omega\mu)^2 k_{x1}} \left\{ k_{x1}^3 k_z^2 w + (k_y^2 + k_z^2)^2 \left[ k_{x1} w + \sin(k_{x1} w) \left( 1 + \frac{k_{x1}^2}{(jk_{x2})^2} \right) \right] \right\}. \quad (2.78)$$

The expression  $D_1 = k_{x1} w + \sin(k_{x1} w) \left( 1 + \frac{k_{x1}^2}{(jk_{x2})^2} \right)$  is not only present in the above equation but also in Eq. (2.69) for the power flow of the LSE modes. Hence, the attenuation constant due to imperfect conductors for the even LSE modes can be expressed in a quite simple form

$$\alpha_{c,\text{LSE}} = \frac{\bar{P}_d}{2\bar{P}_f} = \frac{2R_s (k_y^2 + k_z^2)}{hk_z \omega\mu} \left\{ \frac{k_{x1}^3 k_z^2 w + (k_y^2 + k_z^2)^2 D_1}{(k_y^2 + k_z^2)^2 D_1} \right\}. \quad (2.79)$$

The latter equation can be expressed in terms of the wave impedance for the LSE modes defined by Eq. (2.33)

$$\alpha_{c,\text{LSE}} = \frac{2R_s}{hZ_{F,\text{LSE}}} \left\{ \frac{k_{x1}^3 k_z^2 w}{(k_y^2 + k_z^2)^2 D_1} + 1 \right\}. \quad (2.80)$$

With the LSM modes the magnetic field  $\vec{H}$  has no  $x$  component and Eq. (2.75) for the time-average dissipated power simplifies to

$$\bar{P}_d = 4R_s \left( \int_0^{w/2} |H_{1z}|^2 dx + \int_{w/2}^{\infty} |H_{2z}|^2 dx \right). \quad (2.81)$$

With the magnetic fields given in Eqs. (2.54) and (2.55) and integration along the metal plates this reads

$$\bar{P}_d = 4R_s \left\{ \frac{C^2 k_y^2}{4k_{x1}} [wk_{x1} + \sin(k_{x1}w)] + \frac{D^2 k_y^2}{2jk_{x2}} e^{-jk_{x2}w} \right\}.$$

This can be further simplified by applying Eq. (2.56) and the afore mentioned identity for trigonometric functions to yield

$$\bar{P}_d = \frac{4R_s C^2 k_y^2}{4k_{x1}} \left[ k_{x1}w + \sin(k_{x1}w) \left( 1 + \frac{\varepsilon_{r2}}{\varepsilon_{r1}} \frac{k_{x1}^2}{(jk_{x2})^2} \right) \right]. \quad (2.82)$$

With the time-average power flow defined in Eq. (2.71) the attenuation constant due to imperfect conductors for the even LSM modes can be expressed by

$$\alpha_{c,\text{LSM}} = \frac{\bar{P}_d}{2\bar{P}_f} = \frac{2R_s k_y^2 \omega \varepsilon_0 \varepsilon_{r1}}{h (k_y^2 + k_z^2) k_z} \frac{\left[ k_{x1}w + \sin(k_{x1}w) \left( 1 + \frac{\varepsilon_{r2}}{\varepsilon_{r1}} \frac{k_{x1}^2}{(jk_{x2})^2} \right) \right]}{k_{x1}w + \sin(k_{x1}w) \left( 1 + \frac{k_{x1}^2}{(jk_{x2})^2} \right)},$$

which can be expressed in terms of the wave impedance for the LSM modes defined by Eq. (2.59)

$$\alpha_{c,\text{LSM}} = \frac{2R_s}{h Z_{F,\text{LSM}}} \frac{k_y^2}{k_z^2} \frac{\left[ k_{x1}w + \sin(k_{x1}w) \left( 1 + \frac{\varepsilon_{r2}}{\varepsilon_{r1}} \frac{k_{x1}^2}{(jk_{x2})^2} \right) \right]}{k_{x1}w + \sin(k_{x1}w) \left( 1 + \frac{k_{x1}^2}{(jk_{x2})^2} \right)}. \quad (2.83)$$

In practical applications the top and bottom metal plates of an NRD-guide feed are often made of different materials. Most of the antennas described in this thesis use an aluminum base plate, while the common ground metallization between the NRD-guide feed and the planar RF substrate is a copper foil. According to Eq. (2.75) time-average power dissipation can be calculated separately for the top plate and for the bottom plate, or  $\bar{P}_d = \bar{P}_{d,\text{top}} + \bar{P}_{d,\text{bottom}}$ . According to  $\bar{P}_d \propto R_s \propto 1/\kappa$  an equivalent conductivity can be found from

$$\kappa_{\text{eq}} = \frac{4\kappa_{\text{top}}\kappa_{\text{bottom}}}{(\sqrt{\kappa_{\text{top}}} + \sqrt{\kappa_{\text{bottom}}})^2}. \quad (2.84)$$

This leads to an equivalent surface resistance  $R_{s,\text{eq}} = \sqrt{\omega\mu_0/(2\kappa_{\text{eq}})}$  which can be used in Eq. (2.80) and (2.83) to find the attenuation constant due to imperfect conductors if different metals are used for the top plate and bottom plate.

### 2.5.3 Transmission Loss due to Imperfect Dielectrics

In general, the time-average power dissipation in lossy matter is defined as

$$\bar{P}_d = \text{Re} \left\{ \iiint_A \hat{y} |\vec{E}|^2 + \hat{z} |\vec{H}|^2 \, dx \, dy \, dz \right\}, \quad (2.85)$$

where  $\hat{y}(\omega) = j\omega\hat{\epsilon} + \hat{\kappa}$ , and  $\hat{z}(\omega) = j\omega\hat{\mu}$ . In the most general case permittivity  $\hat{\epsilon}$ , permeability  $\hat{\mu}$ , and conductivity  $\hat{\kappa}$  are all complex functions of frequency. In contrast to the response of vacuum, the response of normal matter to external fields generally depends on the rate of change of the field or is dependent on frequency if time-harmonic fields are considered. According to [25], the constitutive relationship for the electric flux density in case of linear matter in the general sense, assuming time-harmonic electromagnetic fields, is the following equation

$$\vec{D} = (\epsilon + j\omega\epsilon_1 - \omega^2\epsilon_2 + \dots) \vec{E} = \hat{\epsilon}(\omega)\vec{E}. \quad (2.86)$$

For this reason, permittivity is often treated as a complex function of frequency,  $\hat{\epsilon}(\omega) = \epsilon'(\omega) + j\epsilon''(\omega)$ , where  $\epsilon'$  is the real part and  $\epsilon''$  the imaginary part of the complex permittivity, or the dielectric loss factor. The dielectric loss factor can be expressed in terms of a dielectric loss angle  $\delta$  by  $\tan \delta = \epsilon''/\epsilon'$ . The corresponding relationship holds also for complex permeabilities and complex conductivities. But for low-loss non-magnetic dielectrics it is common practice to neglect complex conductivity  $\hat{\kappa}$  and to assume permeability to be that of vacuum, so  $\hat{y}(\omega) = j\omega\hat{\epsilon} = j\omega(\epsilon' - j\epsilon'')$ , and  $\hat{z}(\omega) = j\omega\mu_0$ . As a result Eq. (2.85) can be simplified and the transmission loss due to the characteristics of imperfect dielectric materials can be calculated by

$$\bar{P}_d = \iint_A \omega\epsilon'' |\vec{E}|^2 \, dx \, dy = \iint_A \omega\epsilon_0\epsilon_r \tan \delta |\vec{E}|^2 \, dx \, dy. \quad (2.87)$$



With the specific geometry and material characteristics of the NRD-guide given in Fig. 2.1, page 8 and according to the symmetry with respect to the  $y$ - $z$ -plane, the power dissipation can be calculated by

$$\bar{P}_d = 2\omega\varepsilon_0 \left[ \varepsilon_{r1} \tan \delta_1 \int_0^h \int_0^{w/2} |\vec{E}_1|^2 dx dy + \varepsilon_{r2} \tan \delta_2 \int_0^h \int_{w/2}^{\infty} |\vec{E}_2|^2 dx dy \right]. \quad (2.88)$$

With the LSE modes the electric field  $\vec{E}$  has no  $x$  component, so the integral over the electric field  $\vec{E}_1$  in the core material can be expressed as

$$\begin{aligned} & \int_0^h \int_0^{w/2} (|E_{1y}|^2 + |E_{1z}|^2) dx dy \\ &= C^2 \int_0^{w/2} \cos^2(k_{x1}x) dx \left[ k_z^2 \int_0^h \cos^2(k_y y) dy + k_y^2 \int_0^h \sin^2(k_y y) dy \right], \\ &= \frac{C^2}{4k_{x1}} [wk_{x1} + \sin(wk_{x1})] \frac{h}{2} (k_y^2 + k_z^2). \end{aligned}$$

The integral over the electric field  $\vec{E}_2$  in the lateral material equals to

$$\begin{aligned} & \int_0^h \int_{w/2}^{\infty} (|E_{2y}|^2 + |E_{2z}|^2) dx dy \\ &= D^2 k_z^2 \int_{w/2}^{\infty} e^{-2jk_{x2}x} dx \left[ k_z^2 \int_0^h \cos^2(k_y y) dy + k_y^2 \int_0^h \sin^2(k_y y) dy \right], \\ &= \frac{C^2}{4k_{x1}} \left( \frac{k_{x1}}{jk_{x2}} \right)^2 \sin(wk_{x1}) \frac{h}{2} (k_y^2 + k_z^2). \end{aligned} \quad (2.89)$$

With this the time-average dissipation due to dielectric loss in the even LSE modes can be expressed as

$$\begin{aligned} \bar{P}_{d,LSE} &= \frac{h\omega C^2 (k_y^2 + k_z^2) \varepsilon_0 \varepsilon_{r1} \tan \delta_1}{4k_{x1}} \\ &\cdot \left\{ wk_{x1} + \sin(wk_{x1}) \left[ 1 + \frac{\varepsilon_{r2} \tan \delta_2}{\varepsilon_{r1} \tan \delta_1} \left( \frac{k_{x1}}{jk_{x2}} \right)^2 \right] \right\}. \end{aligned} \quad (2.90)$$

With  $D_1$  introduced on page 28 and the time-average power flow defined by Eq. (2.69) the attenuation constant can be stated as follows

$$\begin{aligned} \alpha_{d,\text{LSE}} = \frac{\bar{P}_d}{2\bar{P}_f} = & \frac{\varepsilon_{r1}k_0^2 \tan \delta_1}{2k_z} \cdot \frac{k_{x1}w + \sin(k_{x1}w)}{D_1} \\ & + \frac{\varepsilon_{r2}k_0^2 \tan \delta_2}{2k_z} \cdot \frac{\sin(k_{x1}w) \left(\frac{k_{x1}}{jk_{x2}}\right)^2}{D_1}. \end{aligned} \quad (2.91)$$

With the LSM modes the electric field  $\vec{E}$  shows all three components, so the integral over the electric field  $\vec{E}_1$  in the core material in Eq. (2.88) can be expressed as

$$\begin{aligned} & \int_0^h \int_0^{w/2} (|E_{1x}|^2 + |E_{1y}|^2 + |E_{1z}|^2) dx dy \\ & = \frac{C^2}{\omega^2 \varepsilon_0^2 \varepsilon_{r1}^2} \left\{ (k_y^2 + k_z^2)^2 \cdot \int_0^{w/2} \cosh^2(jk_{x1}x) dx \cdot \int_0^h \sin^2(k_y y) dy \right. \\ & \quad + k_{x1}^2 k_y^2 \cdot \int_0^{w/2} \sinh^2(jk_{x1}x) dx \cdot \int_0^h \cos^2(k_y y) dy \\ & \quad \left. + k_{x1}^2 k_z^2 \cdot \int_0^{w/2} \sinh^2(jk_{x1}x) dx \cdot \int_0^h \sin^2(k_y y) dy \right\} \\ & = \frac{C^2 h}{8\omega^2 \varepsilon_0^2 \varepsilon_{r1}^2} \left\{ (k_y^2 + k_z^2)^2 [wk_{x1} + \sin(wk_{x1})] + k_{x1}^2 (k_y^2 + k_z^2) [wk_{x1} - \sin(wk_{x1})] \right\} \\ & = \frac{C^2 h}{8k_{x1} \omega^2 \varepsilon_0^2 \varepsilon_{r1}^2} (k_y^2 + k_z^2) \varepsilon_{r1} k_0^2 \left\{ wk_{x1} + \sin(wk_{x1}) \left[ 1 - \frac{2k_{x1}^2}{\varepsilon_{r1} k_0^2} \right] \right\}. \end{aligned}$$

The integral over the electric field  $\vec{E}_2$  in the lateral material equals to

$$\begin{aligned} & \int_0^h \int_{w/2}^{\infty} (|E_{2x}|^2 + |E_{2y}|^2 + |E_{2z}|^2) dx dy \\ & = \frac{D^2}{\omega^2 \varepsilon_0^2 \varepsilon_{r2}^2} \left\{ (k_y^2 + k_z^2)^2 \int_{w/2}^{\infty} e^{-2jk_{x2}x} dx \cdot \int_0^h \sin^2(k_y y) dy \right. \end{aligned}$$

$$\begin{aligned}
 & + |k_{x2}|^2 \int_{w/2}^{\infty} e^{-2jk_{x2}x} dx \left[ k_y^2 \int_0^h \cos^2(k_y y) dy + k_z^2 \int_0^h \sin^2(k_y y) dy \right] \Bigg\} \\
 = & \frac{C^2 [(jk_{x2})^2 + k_y^2 + k_z^2]}{\omega^2 \varepsilon_0^2 \varepsilon_{r2}^2 4k_{x1}} \left( \frac{k_{x1}}{jk_{x2}} \right)^2 \frac{\varepsilon_{r2}}{\varepsilon_{r1}} \sin(wk_{x1}) \frac{h}{2} (k_y^2 + k_z^2) .
 \end{aligned} \tag{2.92}$$

With the above equations substituted in Eq. (2.88), the time-average dissipation due to dielectric loss in the even LSM modes can be expressed as

$$\begin{aligned}
 \bar{P}_{d,\text{LSM}} = & \frac{hC^2}{4k_{x1}\omega\varepsilon_0} \left\{ \frac{\tan \delta_1}{\varepsilon_{r1}} \left[ (k_y^2 + k_z^2)^2 (wk_{x1} + \sin(wk_{x1})) \right. \right. \\
 & \left. \left. + k_{x1}^2 (k_y^2 + k_z^2) (wk_{x1} - \sin(wk_{x1})) \right] \right. \\
 & \left. + \frac{\tan \delta_2}{\varepsilon_{r2}} \left[ (k_y^2 + k_z^2)^2 + k_{x1}^2 (k_y^2 + k_z^2) \right] \sin(wk_{x1}) \left( \frac{k_{x1}}{jk_{x2}} \right)^2 \frac{\varepsilon_{r2}}{\varepsilon_{r1}} \right\} \\
 = & \frac{hC^2 \tan \delta_1}{4k_{x1}\omega\varepsilon_0} (k_y^2 + k_z^2) k_0^2 \left\{ wk_{x1} + \sin(wk_{x1}) \left[ 1 - \frac{2}{\varepsilon_{r1}} \left( \frac{k_{x1}}{k_0} \right)^2 \right] \right\} \\
 & + \frac{hC^2 \tan \delta_2}{4k_{x1}\omega\varepsilon_0} \frac{\varepsilon_{r2}}{\varepsilon_{r1}} (k_y^2 + k_z^2) k_0^2 \sin(wk_{x1}) \left( \frac{k_{x1}}{jk_{x2}} \right)^2 \left[ 1 + \frac{2}{\varepsilon_{r2}} \left( \frac{k_{x1}}{k_0} \right)^2 \right] .
 \end{aligned} \tag{2.93}$$

With  $D_1$  introduced on page 28 and time-average power flow defined by Eq. (2.71) the attenuation constant can be stated as follows

$$\begin{aligned}
 \alpha_{d,\text{LSM}} = \frac{\bar{P}_d}{2\bar{P}_f} = & \frac{\varepsilon_{r1} k_0^2 \tan \delta_1}{2k_z} \cdot \frac{k_{x1}w + \sin(k_{x1}w) \left[ 1 - \frac{2}{\varepsilon_{r1}} \left( \frac{k_{x1}}{k_0} \right)^2 \right]}{D_1} \\
 & + \frac{\varepsilon_{r2} k_0^2 \tan \delta_2}{2k_z} \cdot \frac{\sin(k_{x1}w) \left( \frac{k_{x1}}{jk_{x2}} \right)^2 \left[ 1 + \frac{2}{\varepsilon_{r2}} \left( \frac{k_{x1}}{k_0} \right)^2 \right]}{D_1} .
 \end{aligned} \tag{2.94}$$

To verify the equations derived for the attenuation constant for the even LSE<sub>01</sub> mode, calculated values are compared to measured values given by [30]. In this example, the strip was fabricated with ceramic material ( $\varepsilon_{r1}=38$ ,  $\tan \delta_1=2 \cdot 10^{-4}$ ) and with strip height  $h=7$  mm and strip width  $w=2$  mm. The metal plates were made of brass with conductivity  $\kappa=1.8 \cdot 10^7 \frac{\text{S}}{\text{m}}$ . Figure 2.8 shows an excellent

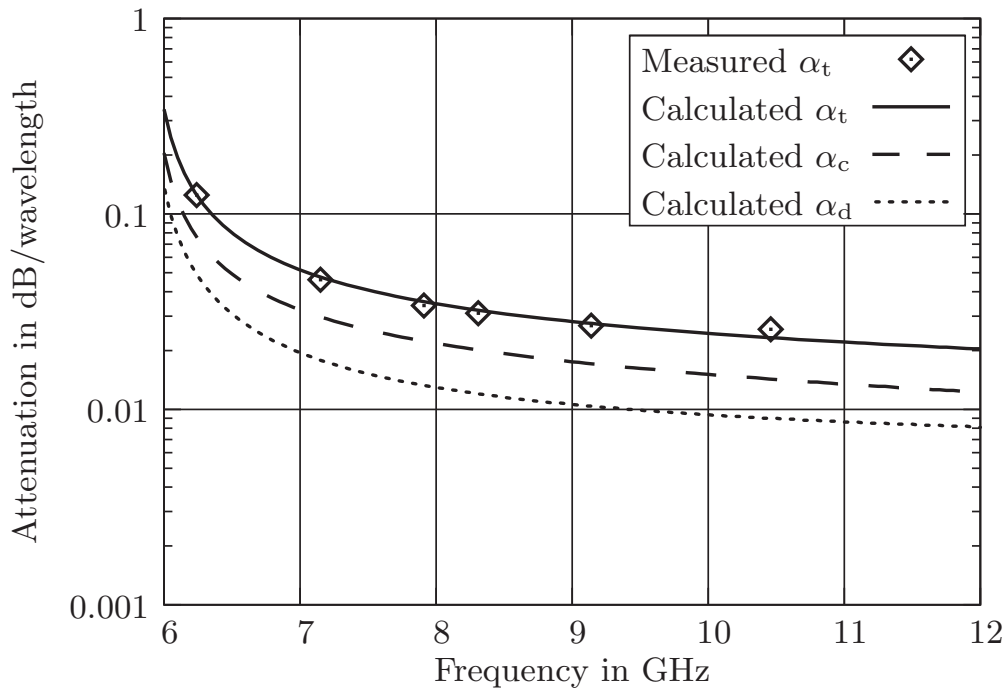


**Fig. 2.8:** Attenuations for the  $LSE_{01}$  mode. Measured values (diamonds) according to [30] versus calculated values (solid curve) using Eqs. (2.80) and (2.91). Contribution by conductor loss (dashed curve) and contribution by dielectric loss (dotted curve).

agreement between the total attenuation constant calculated using above equations (solid curve) and the measured values (diamonds).

This conclusion also validates the initial assumption of negligible loss due to surface roughness. Another conclusion of Fig. 2.8 is that in this case the total loss is dominated by the loss due to the imperfect conductor (dashed line). The loss due to the imperfect dielectric has less yet not insignificant effect.

The same comparison between measurement [31] and calculation is performed for the  $LSM_{01}$  mode, using two different dielectric materials for the NRD-guide strip, but for both using silver-plated metal plates ( $\kappa=6.17 \cdot 10^7 \frac{S}{m}$ ). The first NRD-guide was fabricated with a Teflon strip ( $\epsilon_{r1}=2.04$ ,  $\tan \delta_1=1.5 \cdot 10^{-4}$ ) with height  $h=2.85$  mm and width  $w=3.2$  mm. For this example, the prediction of the attenuation constant in Fig. 2.9 is not as good as for the  $LSE_{01}$  mode. One reason is that the frequency is five times higher than for the example of the NRD-guide with a ceramic strip operated with the  $LSE_{01}$  mode, and therefore, the effect of rough surfaces is not negligible here. When an increase of resistivity

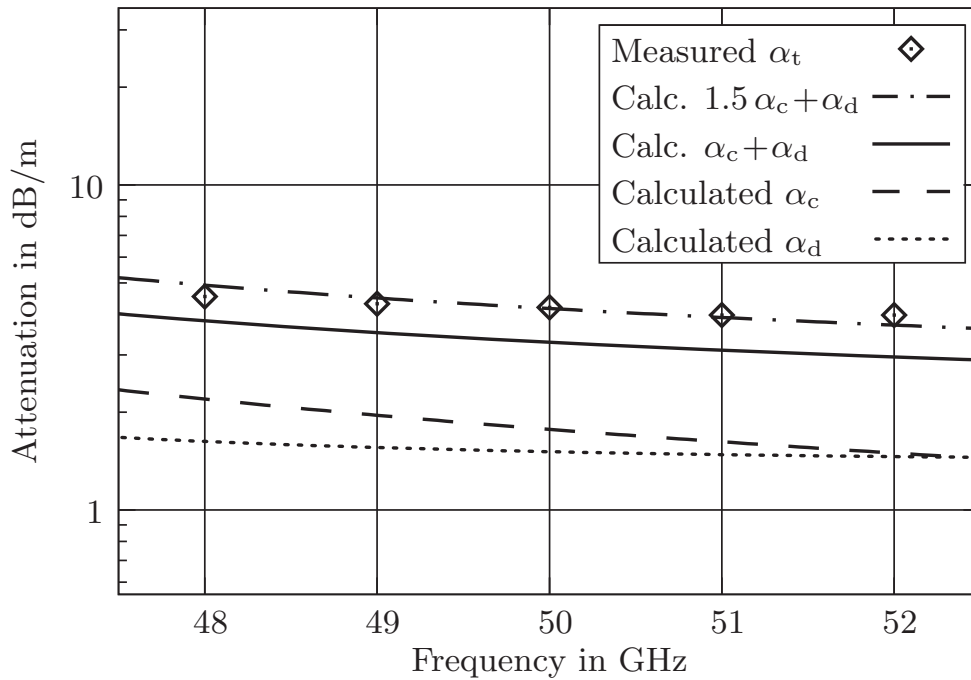


**Fig. 2.9:** Attenuations for the  $\text{LSM}_{01}$  mode on an NRD-guide made of Teflon. Measured values (diamonds) according to [31] versus calculated values (solid curve) using Eqs. (2.83) and (2.94). Contribution by conductor loss (dashed curve) and contribution by dielectric loss (dotted curve). Approximation  $\alpha'_t = 1.5\alpha_c + \alpha_d$  (dash dotted curve) yields better agreement with measured values.

by a factor of 1.5 is taken into account, measured and calculated values show good agreement.

The second NRD-guide with height  $h=2.7$  mm and width  $w=2.4$  mm is fabricated with a Polystyrene strip ( $\epsilon_{r1}=2.56$ ,  $\tan \delta_1=9 \cdot 10^{-4}$ ). Figure 2.10 indicates that for this setup the attenuation constant due to the imperfect dielectric  $\alpha_d$  is 4 to 5 times higher than the attenuation constant due to the imperfect conductor  $\alpha_c$ . As a result, and despite the fact that the frequency range is the same, surface roughness has little impact and  $\alpha_t = \alpha_c + \alpha_d$  (solid line) is a good approximation to the measured values designated by diamonds. The approximation  $\alpha'_t = 1.5\alpha_c + \alpha_d$  (dash dotted curve) yields an even better result at higher frequencies and can be taken as an upper bound.

In summary, the equations for the attenuation constant derived here take into account the effects of imperfect conductors and imperfect dielectrics. They do not account for surface roughness at the interface between different materials,

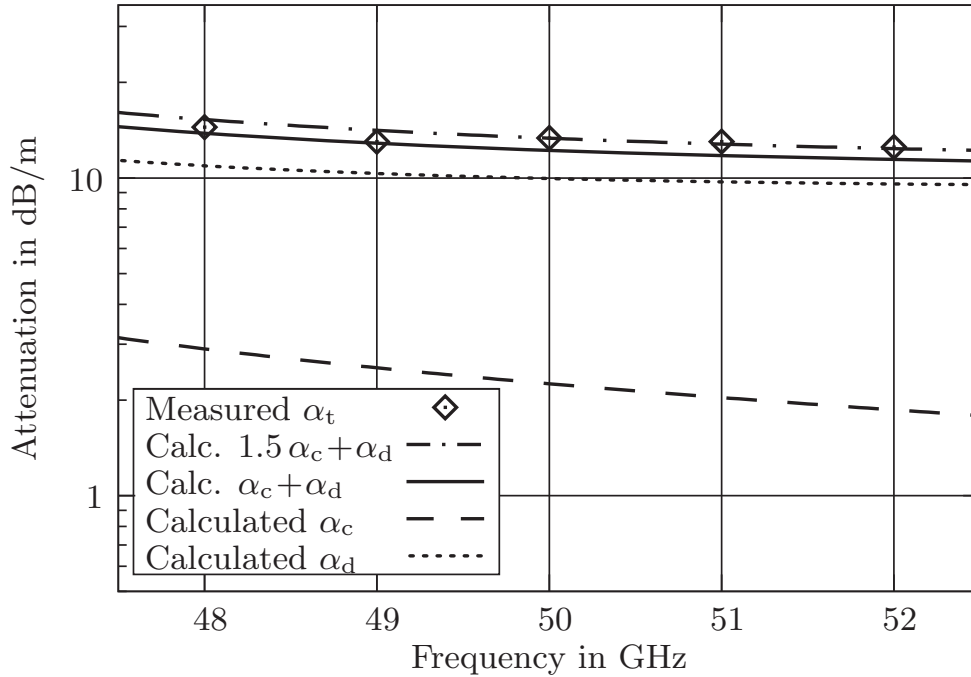


**Fig. 2.10:** Attenuations for the  $\text{LSM}_{01}$  mode on an NRD-guide made of Polystyrene. Measured values (diamonds) according to [31] versus calculated values (solid curve) using Eqs. (2.83) and (2.94). Contribution by conductor loss (dashed curve) and contribution by dielectric loss (dotted curve). From 50 GHz to 52 GHz the approximation  $\alpha'_t = 1.5\alpha_c + \alpha_d$  (dash dotted curve) yields a better agreement with the measured values.

e.g. roughness of conductor surfaces. The latter effect is negligible concerning the topology and frequency range of typical NRD-guide applications. One exception is when conductor losses exceed dielectric losses and in addition the NRD-guide is operated at very high frequencies. This can be the case when using dielectrics with a very low loss angle, e.g. Teflon, at frequencies exceeding 50 GHz. For this case the impact of rough conductor surfaces can be taken into account by an increase of the surface resistivity by a specific factor, which is dependent on the materials and frequency range. For the NRD-guide topologies used in this thesis the losses due to imperfect dielectrics are typically three times higher than the conductor losses, and therefore, the effect of surface roughness is negligible.

At the end of Sec. 2.4, an optimum setup of NRD-guide for a feed network based on high density polyethylene ( $\epsilon_r = 2.3$  and  $\tan \delta(@24 \text{ GHz}) = 5.3 \cdot 10^{-4}$ ) was determined for a desired center frequency at 24 GHz and bandwidth 4 GHz. The strip height is 5.8 mm and strip widths are 3.9 mm and 4.8 mm for the  $\text{LSE}_{01}$  and the  $\text{LSM}_{01}$  mode operation, respectively.

Attenuations for these two setups have been calculated applying the formulae given in Sec. 2.5, assuming an equivalent conductivity  $\kappa_{\text{eq}}$  based on Eq. (2.84), with  $\kappa_{\text{top}} = \kappa_{\text{copper}} = 5.62 \cdot 10^{-8} \frac{\text{S}}{\text{m}}$  and  $\kappa_{\text{bottom}} = \kappa_{\text{aluminum}} = 3.96 \cdot 10^{-8} \frac{\text{S}}{\text{m}}$  and results are shown in Figs. 2.11 and 2.12, respectively.

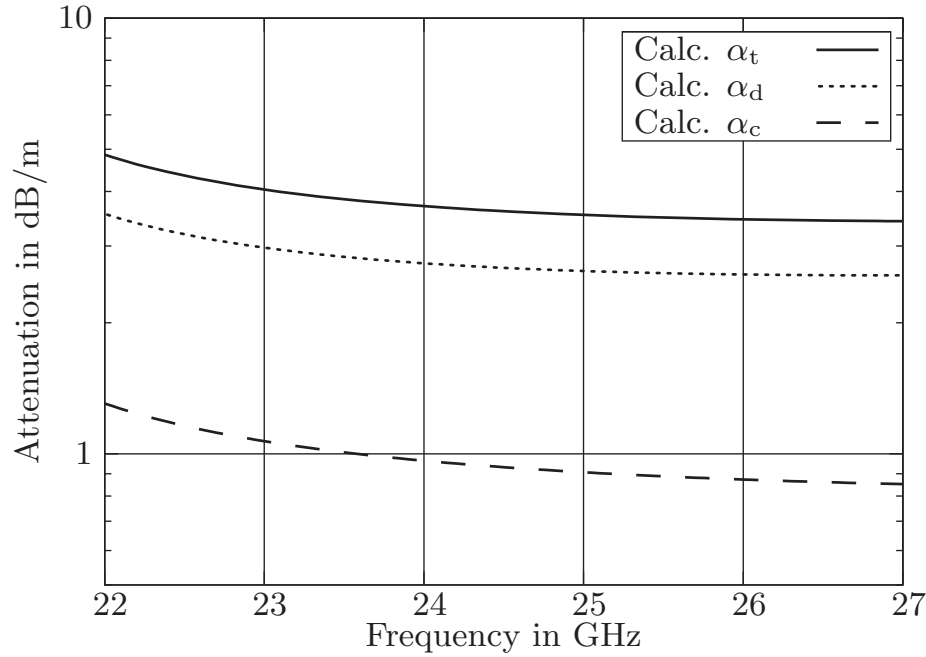


**Fig. 2.11:** Attenuation for the  $\text{LSE}_{01}$  mode on an NRD-guide made of high density polyethylene (HDPE). Calculated values (solid curve) using Eqs. (2.80) and (2.91). Contribution by conductor loss (dashed curve) and contribution by dielectric loss (dotted curve).

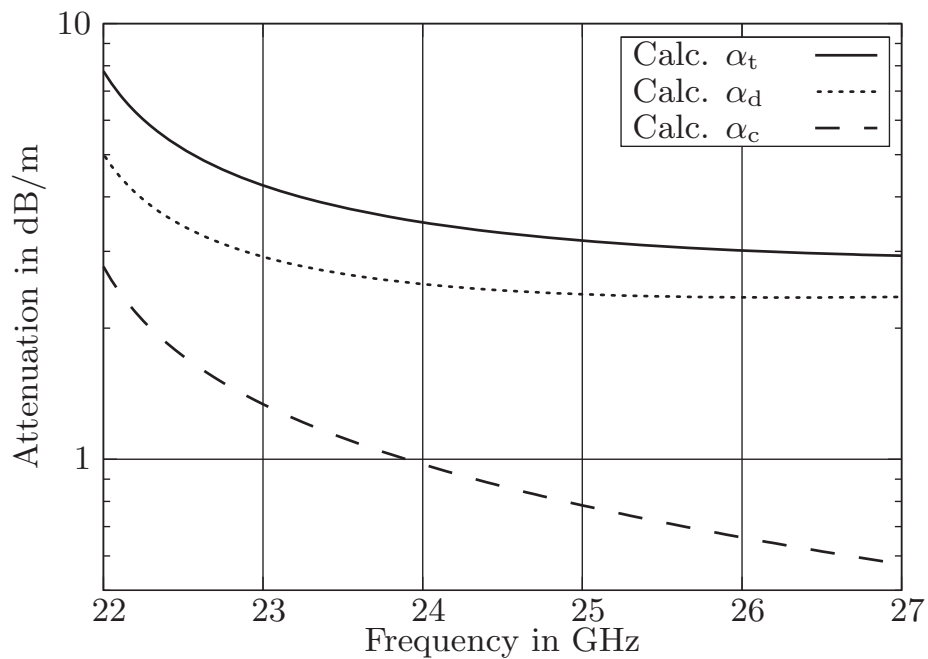


**Fig. 2.12:** Attenuation for the LSM<sub>01</sub> mode on an NRD-guide made of high density polyethylene (HDPE). Calculated values (solid curve) using Eqs. (2.83) and (2.94). Contribution by conductor loss (dashed curve) and contribution by dielectric loss (dotted curve).



### 3 Fixed Beam Antenna for Point-to-Point Applications

The motivation for a new type of mm-wave antennas featuring low loss and low profile characteristics as well as the potential for low cost production has been discussed in the introduction. Antennas for point-to-point applications require high directivity, i.e. a narrow beamwidth of the main beam, in order to concentrate radiated power towards a limited direction without interfering with other radio links which may be located in the immediate vicinity. This requirement of the so-called pencil beam antennas has a direct impact on the aperture size and thus on the length of the feed network. If bandwidth as a limiting factor has to be maintained a parallel type or corporate feed network has to be chosen. Losses in the feed network often limit the gain of pencil beam antennas, which has been demonstrated in the Introduction, Fig. 1.1. With increasing antenna size beamwidth still decreases and thus directivity increases. But as with the increased aperture the feed losses are increased, too, the gain of the antenna reaches its maximum at an optimum size. Further enlargement of the antenna aperture will even result in a lower antenna gain. Hence the attenuation in the feed network is a key parameter of any pencil beam antenna with high directivity.

Comparison of the attenuation for a microstrip line and for the fundamental NRD-guide modes—Fig. 3.1 with the NRD-guide loss calculated applying the formulae stated in Sec. 2.5 and assuming 0.2 dB per wavelength typically experienced with microstrip lines—shows two remarkable facts. By the use of appropriate dielectric materials and geometric dimensions as discussed in Sec. 2.4, the attenuation of both fundamental modes in the NRD-guide is significantly lower than with microstrip line. Furthermore, in contrast to the attenuation in the microstrip line which shows a linear rise over frequency, the attenuation of the NRD-guide declines with increasing frequencies. As a result the NRD-guide lends itself for a low loss feeding, especially for increasing frequencies such as in the millimeter wave range.

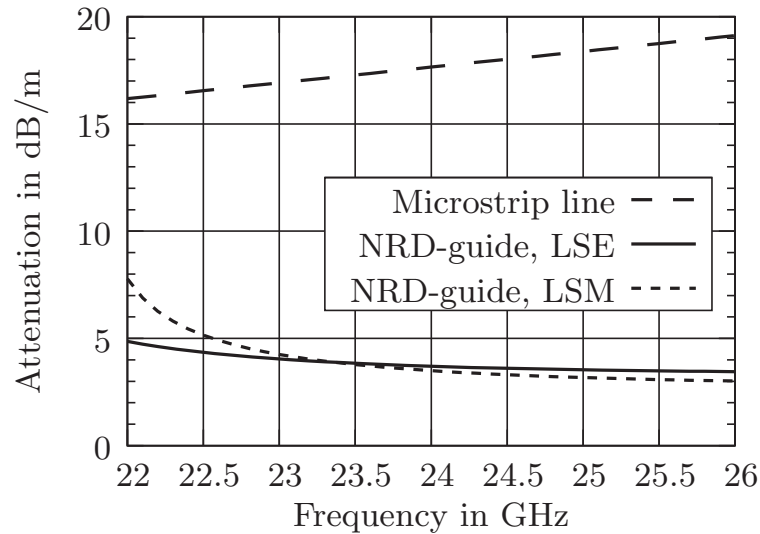


**Fig. 3.1:** Comparison of attenuation for microstrip line and for the two fundamental NRD-guide modes.

### 3.1 Antenna Design

For the antenna described in this chapter a corporate network of engraved NRD(ENRD)-guides (cross section in Fig. 3.3) serves as a feed for planar microstrip patch antenna sub arrays. A top view of the antenna is depicted in Fig. 3.2. Smaller sub arrays of microstrip patch antennas have been used where feed losses still are low [32, 33]. The sub arrays are coupled to the NRD-guides via slots in the ground plane of the planar substrate, as illustrated in Fig. 3.3. Using the planar sub arrays, an NRD-guide network with larger distances between the guides can be used, thus ensuring a considerable reduction of spurious coupling within the feeding network. The total height of the antenna is 6.3 mm only, plus the back sided aluminum plate.

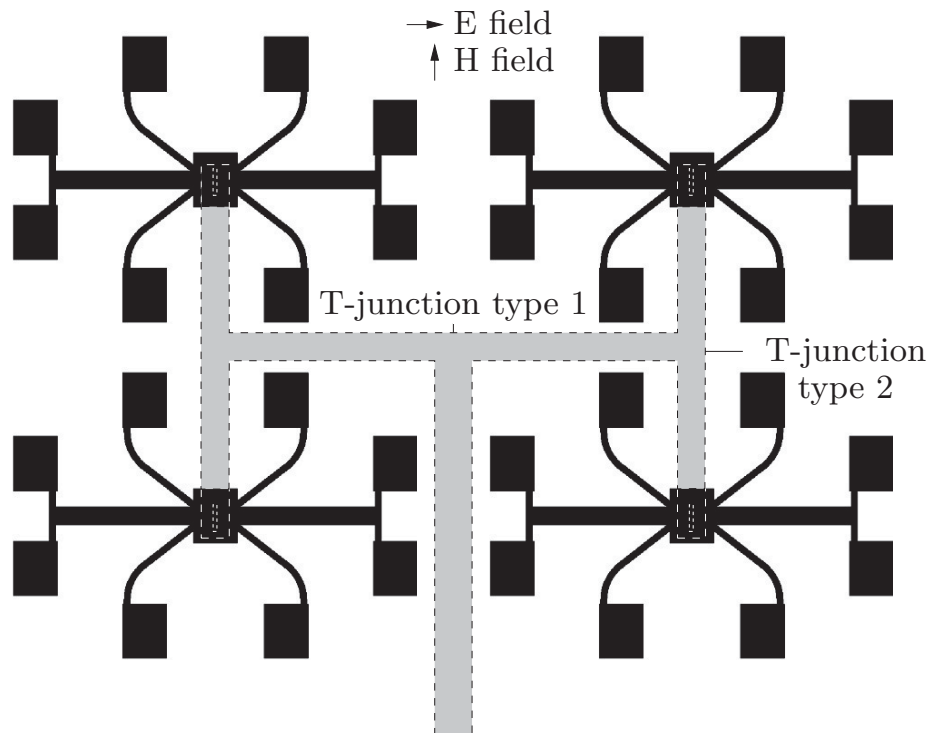


**Fig. 3.2:** Top view of the antenna with the planar microstrip patch subarrays on the front side in solid black filled pattern, and the slot coupled ENRD-guide on the back side in gray filled pattern. T-junctions are used to split the power.

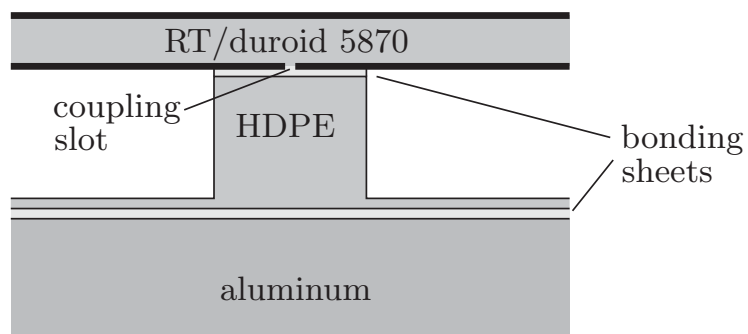


**Fig. 3.3:** Cross section of the antenna with the principle of the ENRD-guide feeding of the planar structure.

## 3.2 Design and Simulation of Components

This section describes the design principle and simulation results for the key components of the fixed beam antenna. Simulations were performed with the commercial electromagnetic field solver for 3 dimensional structures CST Microwave Studio [34]. This simulation tool is based on the Finite Integration Technique (FIT) [35, 36], which is a method in time domain similar to the method of Finite Difference in Time Domain (FDTD). Maxwell's equations are used in the integral form and stated in a form discretized in space and time. As a result, nearly arbitrary 3 dimensional structures can be simulated. A short impulse, usually a modulated Gaussian impulse, is used for excitation and propagates along the structure. Analysis of the electromagnetic field at predefined waveguide ports, and application of the Fourier transform, yields the characteristics of the structure in the frequency domain, such as S-parameters.

### 3.2.1 Configurations for Excitation of an NRD-guide

Basically, there are two possible configurations for the excitation of an NRD-guide. The first configuration is based on a transition from rectangular waveguide to NRD-guide, the other configuration is based on a transition from microstrip line to NRD-guide.

#### 3.2.1.1 Transition from Microstrip Line to NRD-guide

The configuration based on a transition from microstrip line to NRD-guide [37, 38] is depicted in Fig. 3.4. Typically one of the NRD-guide metal layers is replaced by the ground metallization of a planar RF substrate with a coupling slot. This transition allows very simple integration of discrete active and passive devices and thus is mainly used within complex systems. Disadvantages are due to the asymmetry along the height of the NRD-guide which can excite a small portion of power in parallel plate waves. Parallel plate waves are not bound to the dielectric material, but propagate away from the NRD-guide. They may cause spurious coupling within the feeding network and degradation of the radiation pattern due to radiation at the edges of the planar substrate. Additionally, the coupling slot and the open ended microstrip line stub typically used with this kind of transition are a source of spurious emissions, too. For this

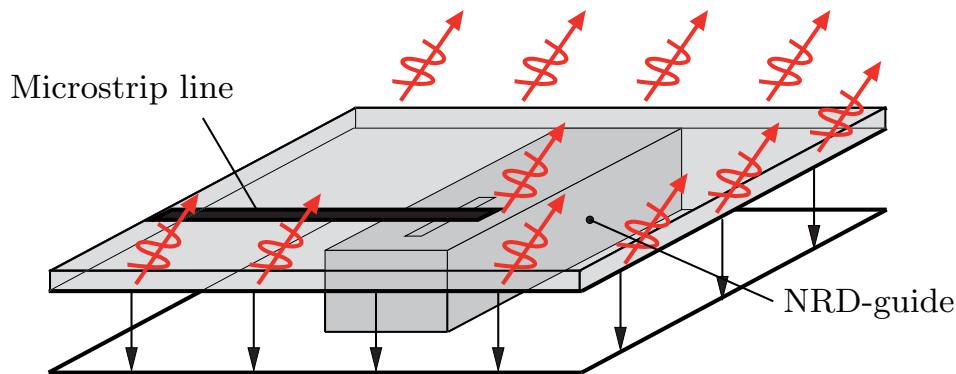


**Fig. 3.4:** Transition from microstrip line to NRD-guide, black arrows indicating the E-field of the parallel plate waves and red arrows indicating potential sources of spurious radiation.

reason, for the antenna described in this chapter, the configuration based on a transition from rectangular waveguide to NRD-guide is preferred. In the next chapters, however, antenna configurations will be presented with special features such as dual polarization capability, which is more complicated to realize with a transition from rectangular waveguide to NRD-guide. Another example for application of the transition from microstrip line to NRD-guide is the scanning receiver array described in Chapter 5, where emphasis is on a simple implementation. Details on the design and performance of these transitions will be given there.

### 3.2.1.2 Transition from Rectangular Waveguide to NRD-guide

The configuration based on a transition from rectangular waveguide to NRD-guide shown in Fig. 3.5, makes use of the field distribution similarity between the  $LSM_{01}$  mode in the NRD-guide and the  $TE_{01}$ -mode in the rectangular waveguide. The rectangular waveguide is set up on edge and placed symmetrically at the end of the NRD-guide. Some tapered metal shielding in the NRD-guide can improve the matching.

Due to the symmetrical alignment between rectangular waveguide and NRD-guide, the excitation of parallel plate waves is not an issue with this type of transition. Radiation of the transition is impossible due to the shielded structure. Test setups in the mm-wave range typically use coaxial cables or rectangular waveguides. Transitions between these two waveguide types are commercially

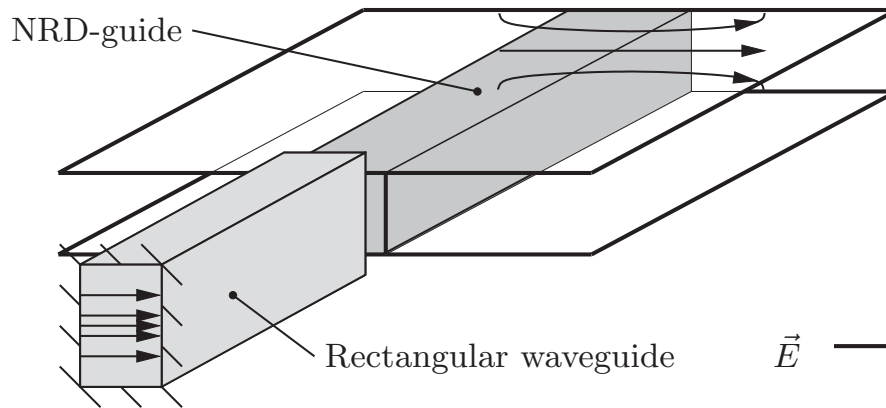


**Fig. 3.5:** Transition from rectangular waveguide to NRD-guide.

available so the excitation by a standard rectangular waveguide is optimum with respect to testability. A minor disadvantage is the mechanical complexity and the higher production cost. Further advantages are mechanical stability and good reproducibility.

In [39] a broadband transition with very high return loss has been presented using an impedance matching technique by tapering both the cross sections of the NRD-guide and of the rectangular waveguide. Compared to the single mode bandwidth of standard rectangular waveguide the single mode bandwidth of the  $LSM_{01}$  mode in the NRD-guide is relatively narrow-band having a maximum of 25% according to [24] and results in Sec. 2.4. Thus the rectangular waveguide taper is not necessary and might be replaced by a rectangular waveguide  $\lambda/4$  transformer [40] leading to a reduced complexity. But still the taper of the shielded NRD-guide to the dielectric filled rectangular waveguide and the  $\lambda/4$  transformer section with reduced width require a complicated milling process which does not lend itself for low cost applications. Another drawback is the overall length of these transitions.

In most antenna applications a much lower bandwidth is sufficient. A sudden transition from standard rectangular waveguide to NRD-guide without matching, depicted in Fig. 3.5, causes reduced return loss which is usually not acceptable. The reason is mainly due to the big difference in the characteristic impedance of the two waveguides but also due to some differences in the field pattern. But the discontinuity introduced by the sudden transition can be effectively used to create a first impedance inverter for a band-pass filter. In [41] a procedure is given for the design of a matching network for transitions between coplanar waveguide and microstrip line consisting of distributed elements. There, impedance inverters are created by short sections of high impedance

lines represented by series inductors, and  $\lambda/2$  transmission lines represent the resonators.

In NRD-guide technique the characteristic impedance is dependent on the permittivity, the height and the width of the dielectric rod, for details see Chapter 2. Ease of production requires the limitation on only one dielectric material and a fixed strip height, i.e. the distance between the metallic ground planes must be kept constant all over the circuit. The strip width has a strong influence on the cutoff-frequency of the fundamental and the higher modes as has been discussed in Chapter 2.4, and can therefore be varied in a small range only, ensuring the mono mode operation. Thus the characteristic impedance is limited to a small range and can not be used for transformation purpose. On the other hand, impedance inverters can be easily created by holes in the dielectric strip represented by shunt inductors as an equivalent circuit.

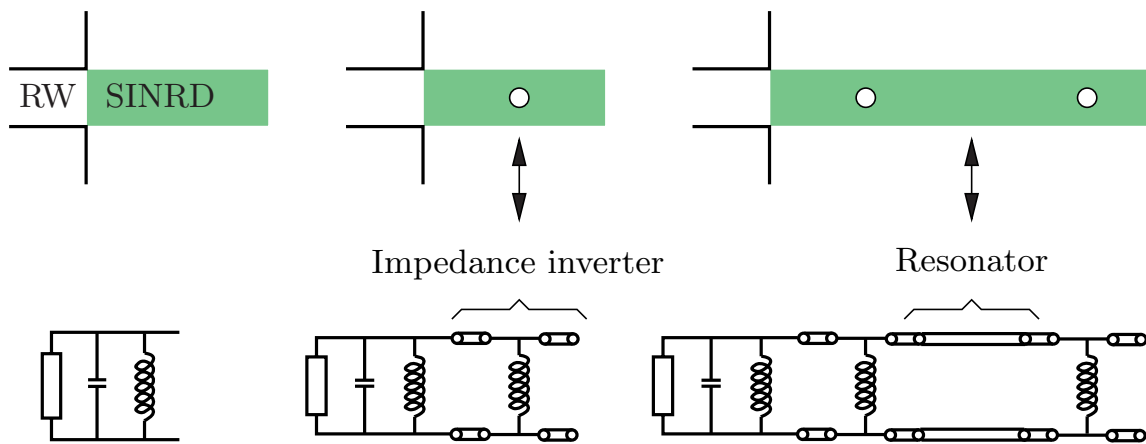


**Fig. 3.6:** Design procedure for the transition rectangular waveguide to SINRD-guide.

In a reduced frequency range the sudden transition from rectangular waveguide to NRD-guide can be described by a strongly untuned shunt resonator, as indicated in Fig. 3.6. Following the design procedure given in [41], but adapted to the equivalent circuits of the sudden transition from rectangular waveguide to NRD-guide and that of the impedance inverter created by the drill hole in the dielectric rod, very compact and easy to fabricate transitions have been developed using different dielectric materials for the NRD-guide. Figure 3.7 shows both the measured and the simulated S-parameters of the back-to-back arrangement of two transitions from rectangular waveguide to SINRD-guide, here Rogers TMM-6 is used as the dielectric material. The measurement data is in good agreement with the simulation. For the fixed beam antenna described in Chapter 3, such a transition also has been developed based on high density polyethylene (HDPE).

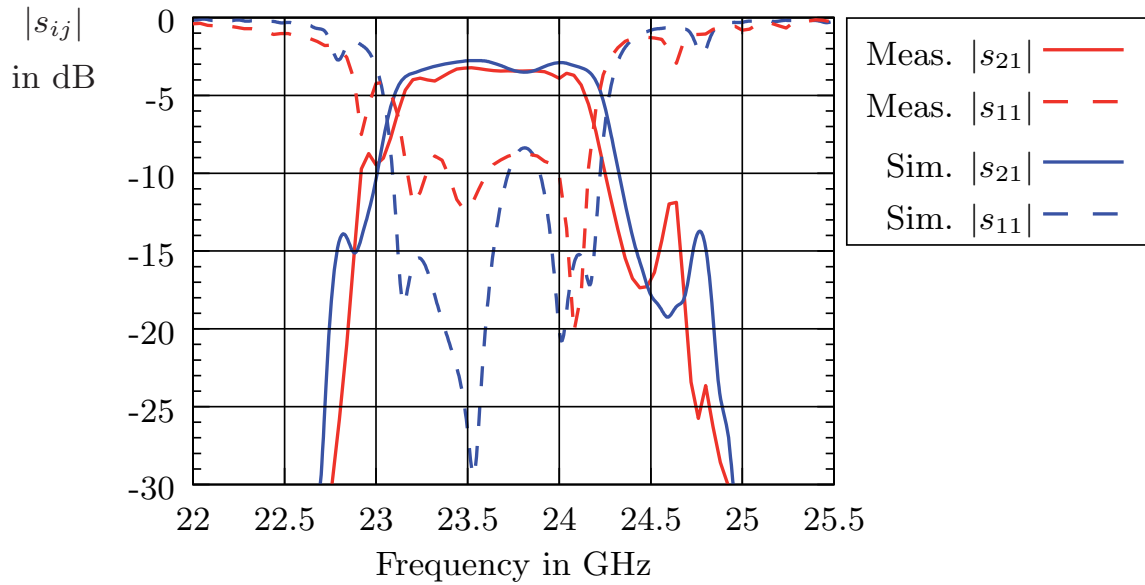


**Fig. 3.7:** S-parameters of a back-to-back transition from rectangular waveguide to SINRD-guide made of TMM-6 material with one inverter hole to rectangular waveguide. Comparison of measured (red curves) versus simulated (blue curves) S-parameters.

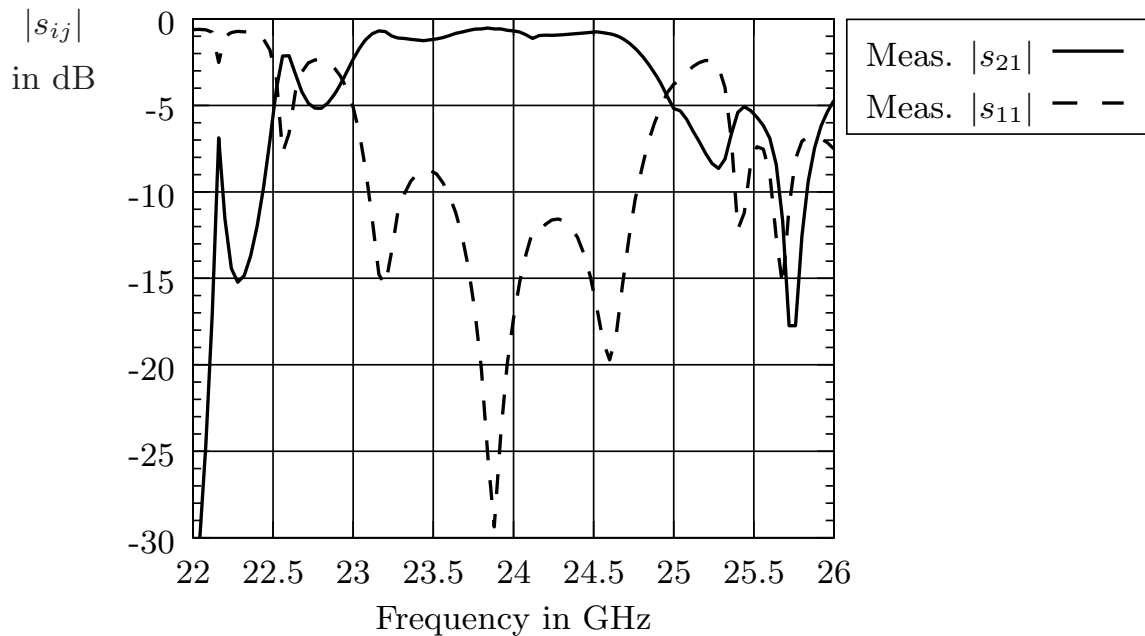


**Fig. 3.8:** Measured S-parameters of the back-to-back transition from rectangular waveguide to SINRD-guide made of HDPE with one inverter hole to rectangular waveguide.



Comparing the measured S-parameters of the back-to-back arrangement with an NRD-guide based on HDPE in Fig. 3.8 with those S-parameters of the back-to-back arrangement with an SINRD-guide based on the TMM-6 material in Fig. 3.7 reveals two facts. First, according to the lower loss tangent and lower permittivity of the HDPE compared to the TMM-6, the insertion loss of approximately 1 dB is much lower compared to the approximately 3 dB of the transition based on the TMM-6 material. Second, the bandwidth is increased from 1 GHz to 1.7 GHz. The transition based on the HDPE material has been used to feed the antenna described in this chapter.

### 3.2.2 Feeding Network

The corporate feeding network in this antenna for point-to-point applications consists of a set of NRD-guides made of high density polyethylene (HDPE) with  $\epsilon_r=2.3$  and  $\tan \delta(@24 \text{ GHz})=5.3 \cdot 10^{-4}$ . At the end of Sec. 2.4, an optimum setup of NRD-guide for such a feed network was determined for a desired center frequency at 24 GHz and bandwidth 4 GHz. The strip height is 5.8 mm and strip widths are 3.9 mm and 4.8 mm for the  $\text{LSE}_{01}$  and the  $\text{LSM}_{01}$  mode sections, respectively. For ease of production and in order to circumvent alignment problems, the feeding network has been realized as engraved NRD-guide (ENRD-guide, Fig. 1.3, page 3 and Fig. 3.3, page 41). A dielectric block of HDPE is glued on an aluminum plate using a bonding sheet. As HDPE is a soft and low surface energy material, it is necessary to use a special adhesive. In this project 50  $\mu\text{m}$  thick high strength bonding adhesive transfer tape 3M 9471 LE [42] was used to glue the HDPE block on top of the aluminum plate.

Then the block is milled to remove the dielectric material around the guide. A small layer of dielectric material (60  $\mu\text{m}$ ) is left below the air region to ensure that the guide is not moved aside by the milling force. Due to the softness of the HDPE material it is important to use the correct revolution speed and form feed to prevent burrs during the milling and drilling process. The planar structure including the microstrip patch antenna sub arrays is glued on top of the NRD-guide feeding network again using the bonding sheet. The back side metallization of the substrate serves, at the same time, as the top metallization of the NRD-guides.

The losses for the two NRD-guide setups have been determined at the end of Sec. 2.5 and results are summarized in Fig. 3.1, page 40. For the NRD-guides with the LSM mode ( $w_{\text{NRD,LSM}}=4.8 \text{ mm}$ ) the expected attenuation is

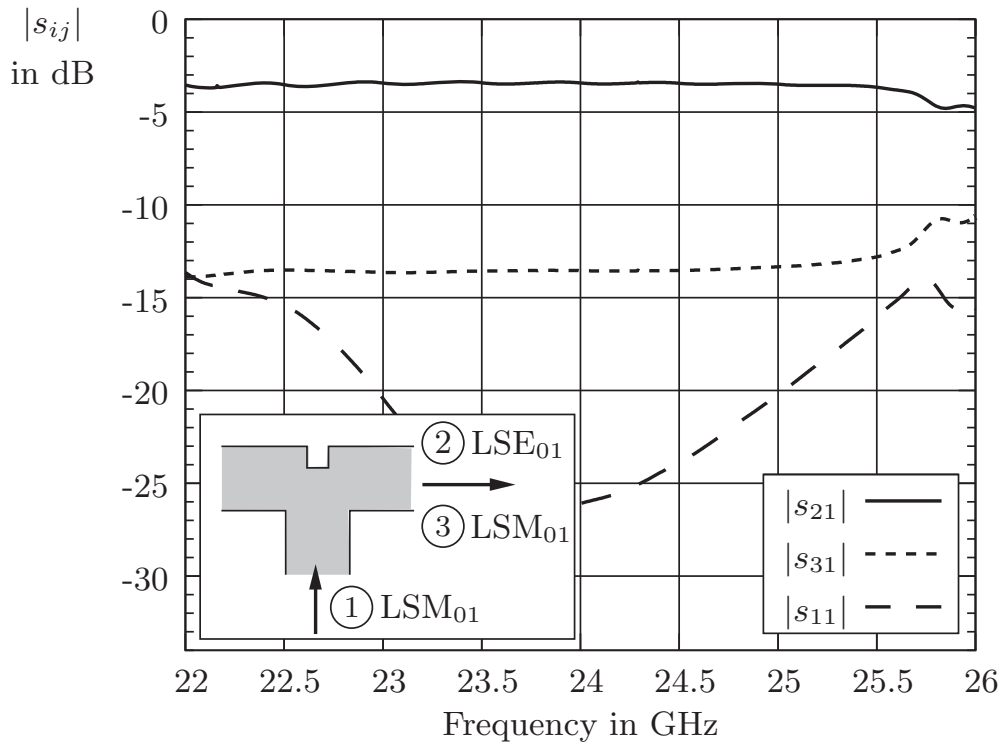
3.5 dB/m. For the NRD-guides with the LSE mode ( $w_{\text{NRD,LSE}}=3.9$  mm) the expected attenuation is 3.7 dB/m. This results in a theoretical insertion loss for the whole feeding network of only 0.3 dB mainly due to dielectric losses in the dielectric rod, to a minor degree due to ohmic losses in the metal plates.

#### 3.2.3 T-junctions

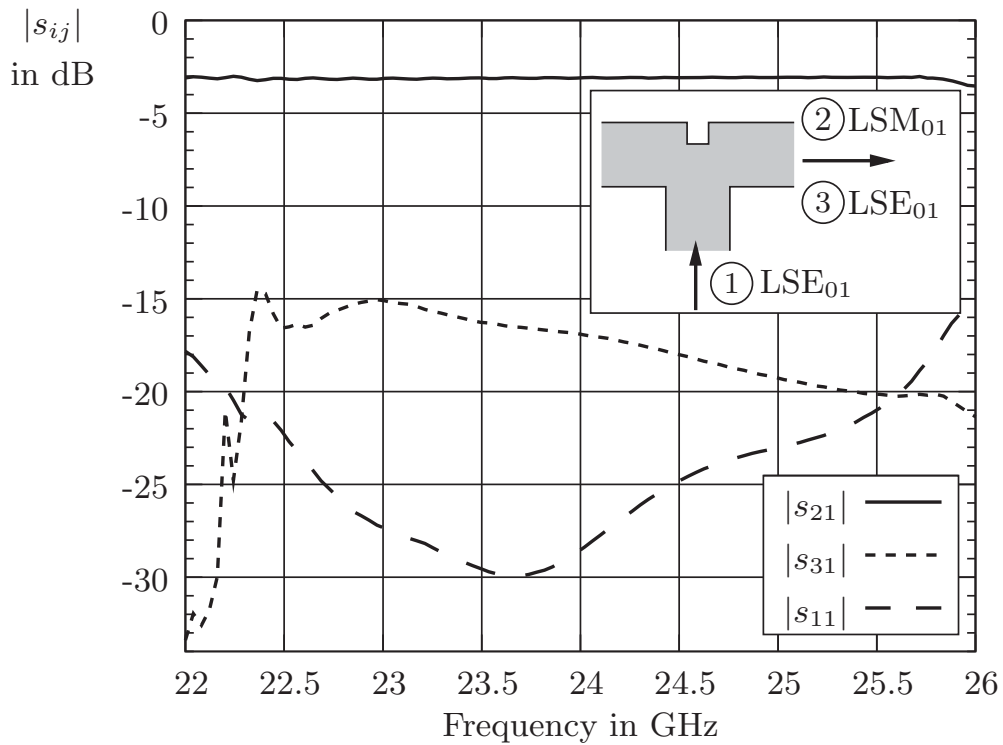
In the feeding network T-junctions are used to split the power. In [43] an NRD-guide T-junction has been presented for the first time, but although metal patches were placed along the branches to suppress spurious modes and improve the impedance matching—the geometry of the output branches were optimized as well—strong variation on the transmission factor dependent on frequency degraded the performance. Experiments and theoretical studies on curved NRD-guide bends [44, 45] showed that losses in these structures can mainly be attributed to mode conversion between the two fundamental modes. According to the abrupt 90° bend of the geometry and due to the similarity of the electromagnetic field patterns with respect to a 90° rotation (Figs. 2.2 and 2.3), NRD-guide T-junctions always produce mode conversion between the LSE mode and the LSM mode [17, 24]. In the feeding network, the T-junctions have been optimized to maximize the conversion. This results in two types of T-junctions (Fig. 3.2). Type 1 is excited by the LSM mode which is converted to the LSE mode at the output branches. Type 2 is excited by the LSE mode which is converted to the LSM mode at the output branches. The widths of the two types of NRD-guide branches is chosen by the following criteria:

- a minimum width guarantees that only the desired modes can propagate along the NRD-guide,
- a larger width reduces dielectric and ohmic losses (see Chapter 2.5).

The simulated S-parameters of the two types of T-junctions are shown in Fig. 3.9. Both T-junctions show good performance with return loss exceeding 10 dB over a broad frequency range of operation from 22 GHz to 25.5 GHz. Another requirement to T-junctions in this application is the mode purity.



(a) Type 1 from LSM mode to LSE mode.



(b) Type 2 from LSE mode to LSM mode.

**Fig. 3.9:** Simulated S-parameters of T-junctions.

At the transition from the NRD-guide feed network to the microstrip sub arrays only the  $\text{LSM}_{01}$  mode is coupled to the planar substrate layer. The  $\text{LSE}_{01}$  mode is totally reflected and bounced back to the input causing mismatch and ripple. With the transition type 1 slightly more ( $|s_{31}| = -14$  dB in Fig. 3.9a) of the inserted power of the  $\text{LSM}_{01}$  mode is conserved and transferred to the output branch. With the transition type 2 the mode purity is better and power transfer from the  $\text{LSE}_{01}$  mode at the input branch to the  $\text{LSE}_{01}$  mode at the output branch,  $|s_{31}|$  in Fig. 3.9b, is lower than  $-15$  dB over the whole bandwidth.

#### 3.2.4 Sub Arrays

Using planar sub arrays of 9 rectangular microstrip patch radiators as indicated in Fig. 3.2 on page 41, an NRD-guide network with larger distances between the guides can be used, thus ensuring a considerable reduction of spurious coupling within the feeding network [46]. The sub arrays are small enough to keep microstrip feed losses low. The sub arrays are coupled to the NRD-guides via slots in the ground plane of the planar substrate. To avoid spurious radiation by the slot coupling, the coupling slots are covered by a microstrip patch. This approach has been first proposed by Duffy and Pozar [33] and later investigated in detail by Engeln [7]. The position of the patches and the feeding microstrip lines are adjusted for equal phase excitation with a compact setup. The substrate is RT/Duroid 5870 with  $\epsilon_r = 2.33$  and thickness  $h = 0.51$  mm. The outer 8 patches are side fed where matching is done by adjusting the position of the feeding point. Figure 3.10 shows the simulated radiation diagrams of the sub array in the E- and H-plane.

Simulated return loss of one sub array fed by an LSM mode excited NRD-guide is shown in Fig. 3.11. According to these simulation results the overall bandwidth of the antenna will be limited by the 400 MHz bandwidth of this sub circuitry.

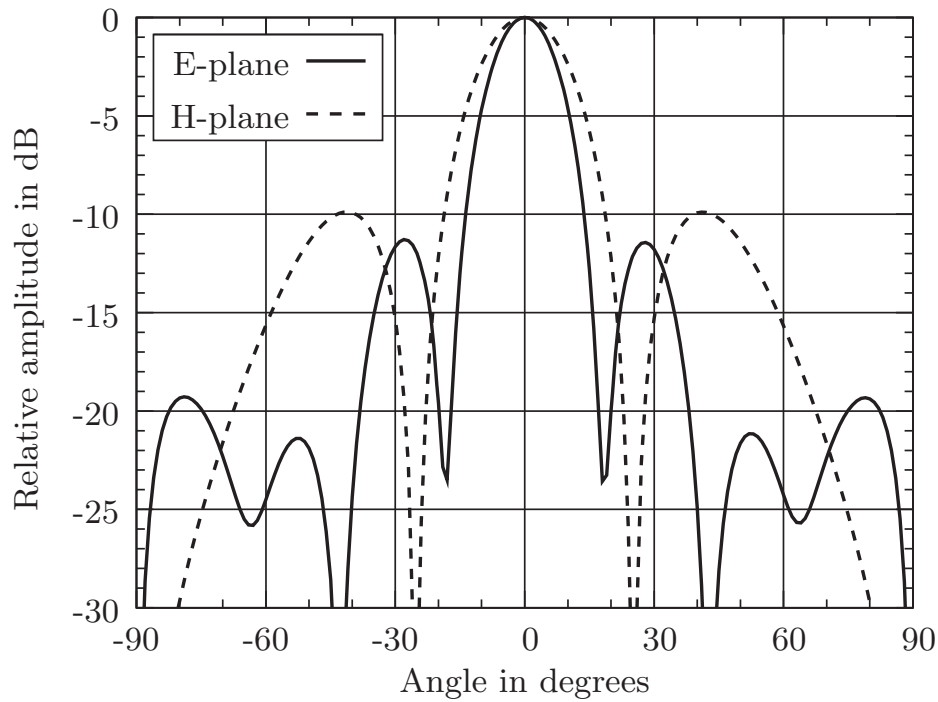


**Fig. 3.10:** Simulated radiation diagrams of the sub array in the E-plane and H-plane.

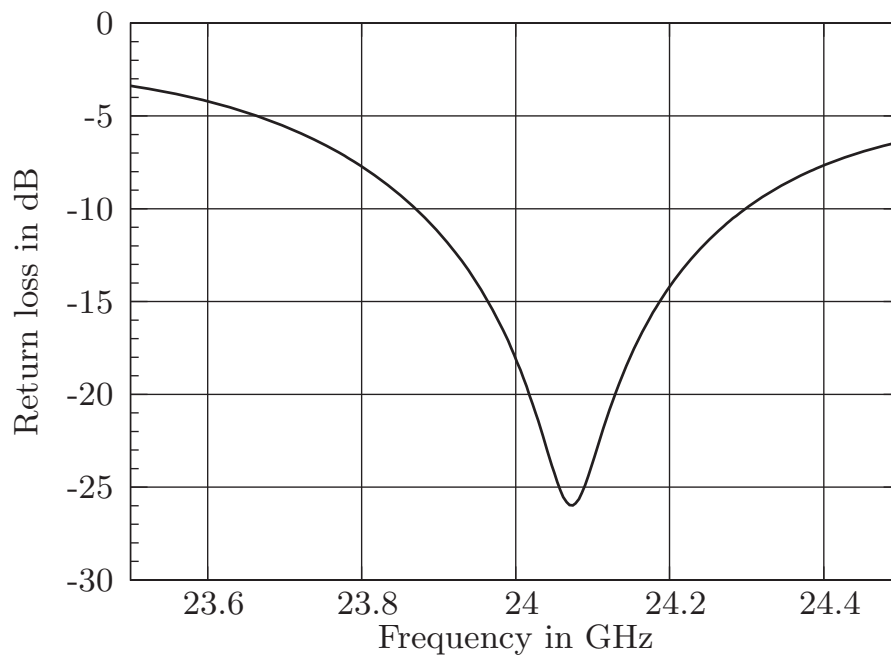


**Fig. 3.11:** Simulated return loss of a sub array fed by an LSM<sub>01</sub> mode excited NRD-guide.

### 3.3 Complete Antenna Array

With the 9 resonators sub array described before, a  $2 \times 2$  antenna array has been designed. Figure 3.12 shows a photo of the pencil beam antenna. In order to circumvent spurious radiation, the antenna is excited by a shielded transition from rectangular waveguide to NRD-guide described in Sec. 3.2.1.2.

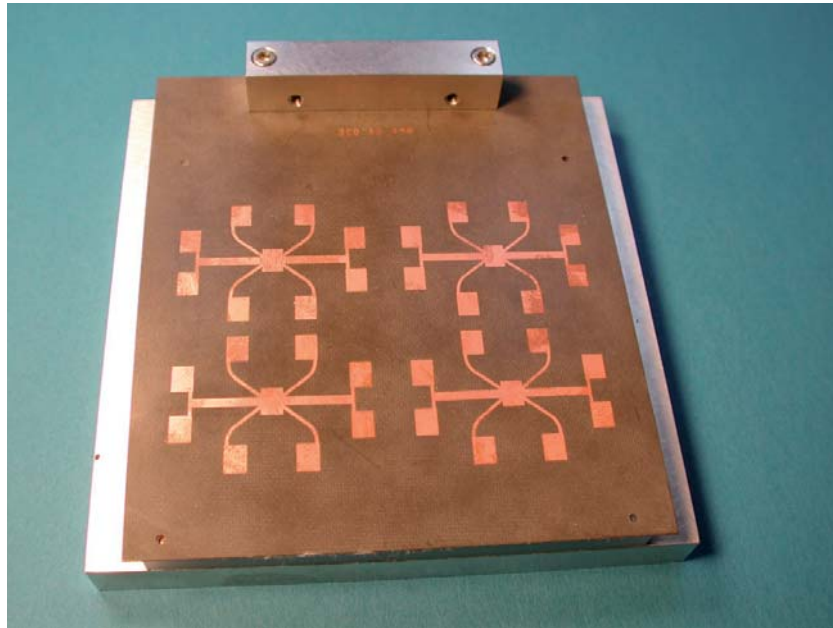
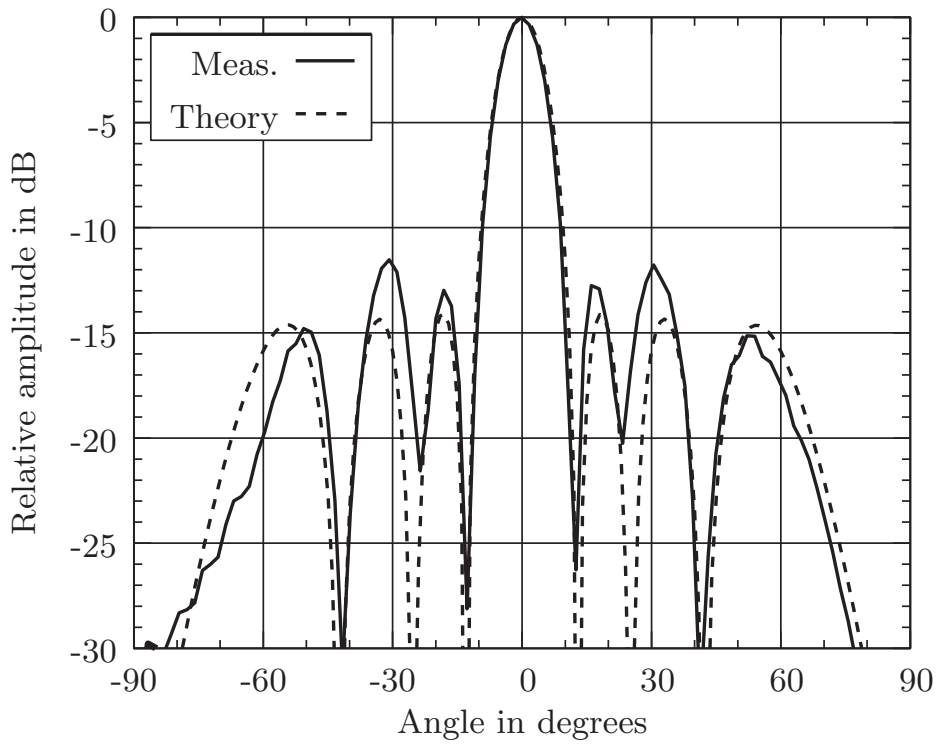


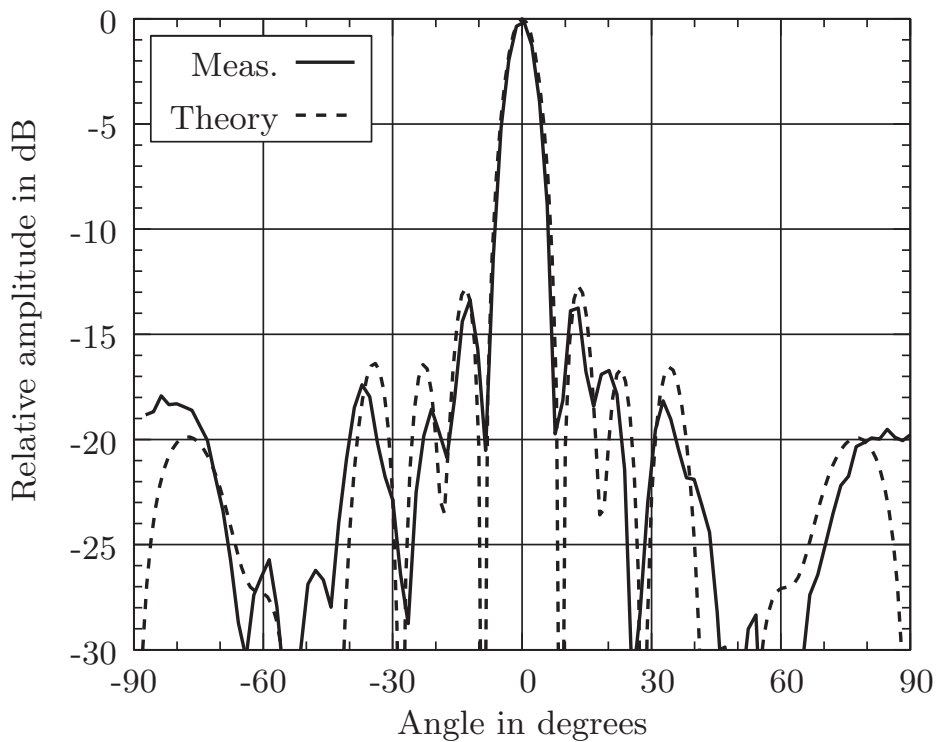
**Fig. 3.12:** Photo of the whole NRD based pencil beam antenna.

The radiation diagrams have been measured in the H-plane and in the E-plane (Fig. 3.13) and compared to the theoretical radiation diagrams, i.e. the radiation pattern of the sub array multiplied by the array factor. The half power beam width is  $7^\circ$  in the E-plane and  $11.2^\circ$  in the H-plane. A  $-11.5$  dB side lobe level is observed at  $\pm 31^\circ$  in the H-plane. This is higher than the value  $-14$  dB, that was expected according to the calculation from the radiation pattern of the single antenna element multiplied by the array factor. In the E-plane there is a very small difference between the measured radiation diagram and theory. The level of the first side lobe is at  $-13.3$  dB, further side lobes are at a level of  $-17$  dB or lower.

The slight differences in the radiation diagrams between theory and measurement are identified to be due to misalignment between the feeding network and the planar structure including the microstrip patch antenna sub arrays.



(a) H-plane.



(b) E-plane.

**Fig. 3.13:** Comparison between measured and theoretical (sub array multiplied by array factor) radiation diagrams.

The measured gain of the antenna array is 21.3 dBi at 24 GHz center frequency including a mismatch loss of 1.3 dB. Exclusive of the mismatch loss, the gain is approximately 22.6 dBi. The theoretical ideal gain for this array based on the aperture area is 24.9 dBi. Thus the aperture efficiency of the antenna array is approximately 59%. The losses can be attributed to dielectric and ohmic losses in the NRD-guide feeding (approximately 0.24 dB according to calculations based on the formulas given in Chapter 2.5), ohmic losses in the small microstrip feeding network of the sub array and the radiating patch elements (approximately 0.25 dB) and radiated power density that is present in the side lobes.

Comparing the aperture efficiency of other low loss antenna approaches in Table 3.1 and Table 3.2 for antennas with rectangular and circular apertures, respectively, shows that only microstrip antenna arrays with a waveguide feed network can provide similar or even greater efficiency numbers.

**Table 3.1:** Examples of high gain, low loss antenna approaches with rectangular apertures.

Citation	[14]	[15]	[2]	[2]	[47]	[48]	this
No. of elements	16×2	8×8	4×4	32×32	8×8	n.s. <sup>†</sup>	2×2×9
Feed type <sup>††</sup>	rw	rw	msl	msl	msl	horn	nrd
Radiator type	patch	patch	patch	patch	patch	patch	patch
Frequency in GHz	12.45	10	35	38	34.7	27.6	24
Aperture in mm <sup>2</sup>	40×366	175×175	18.9×18.9	n.s. <sup>†</sup>	53×51.8	150×150	73.5×53
Meas. gain in dBi	23.0	25.0	16.7	29.0	22.2	30.8	22.6
Efficiency in %	63	74	77	21	36	50	59

A linear array of four sub arrays each consisting of 4×2 circularly polarized microstrip patch elements combined by a small microstrip feed network [14] shows a similar aperture efficiency of 63%, but due to the arrangement of the waveguide feed network the antenna depth is approximately 40 mm and too big for some communication applications. A 2-dimensional array of 4×4 sub arrays each consisting of 2×2 microstrip patch elements [15] has been reported even with a greater efficiency of 74%. The drawback of both solutions is the higher production cost and weight.

---

<sup>†</sup>n.s. is an abbreviation for not specified.

<sup>††</sup>rw indicates a feed based on rectangular waveguides, msl a feed based on microstrip lines, and nrd a feed based on NRD-guides. In this context, horn is a cone-shaped primary feed to a reflector type antenna.



**Table 3.2:** Examples of high gain, low loss antenna approaches with circular apertures.

Citation	[49]	[50]	[11]	[50]	[50]
Feed type <sup>††</sup>	horn	horn	horn	horn	horn
Reflector type	patch	patch	patch	patch	patch
Frequency in GHz	61	58	58.4	58	37.3
Depth in mm	25	20	25	15	14.36
Diameter in mm	100	100	100	100	100
Meas. gain in dBi	34.0	32.8	33	30.7	25.5
Efficiency in %	62	52	53	32	23

Printed reflect arrays are known to be an alternative solution for efficient, high gain antennas with up to 62% aperture efficiency [11, 48–50], but for some applications in the automotive radar field, where design aspects require flat assembly, and in the wireless communications field, where increased antenna depth has a critical impact on wind load, antenna depth of 20 mm to 25 mm is still too high. The depth can be reduced to 15 mm by a multiply folded approach [50], where the electromagnetic waves are reflected multiple times—twice for a single folded, three times for a double folded and four times for a triple folded reflector antenna—between a planar polarizing grid array and a twist and reflect array. But that typically limits the aperture efficiency to 32%. Periodic semi-transparent superstrate layers placed in a close distance to a metal ground plane can be an alternative with a low antenna depth of only 14.4 mm [50], but again aperture efficiency is limited, in this case to 23% only.

When very flat antennas are required, the feeding can be implemented with microstrip lines either on the same substrate on the same side like the radiating elements or on the rear side of a multi layer substrate with coupling slots in a common ground plane. For small arrays of 4×4 radiating microstrip patch elements a great aperture efficiency of 77% has been reported [2], but when this array is expanded to 32×32 patch elements, the aperture efficiency is only 21%. The limitation in aperture efficiency with bigger antenna arrays having a microstrip line feeding was confirmed by another publication [47], where an 8×8 array showed 36% aperture efficiency only.

In conclusion non of the considered approaches offers the same or higher aperture efficiency in the microwave and mm-wave range while being as flat, as lightweight

and as production cost effective as microstrip patch antennas with an NRD-guide feeding network.

In a future version the feeding network could be implemented in substrate integrated NRD (SINRD) waveguide technique further reducing the fabrication cost. The principle of this antenna can easily be extended to a bigger array (e.g.  $4 \times 4$  or  $8 \times 8$ ) of the same 9 patch sub array providing not only high directivity but also high gain and high efficiency. The loss in the larger NRD-guide feeding network for a  $4 \times 4$  array is expected to amount to 0.49 dB. Assuming that all other loss contributions are the same like for the  $2 \times 2$  array the gain should be 28.4 dBi, and aperture efficiency should be 51.3%. Using asymmetric T-junctions an amplitude taper function could be realized for lower side lobe levels.

## 4 Dual Polarization Antennas

In the microstrip antenna field there has been increasing interest in the dual polarization operation of microwave and millimeter-wave antennas. A dual polarization antenna can double the capacity of communications by means of polarization diversity. In multi-path propagation scenarios of suburban areas the diversity gain can even be as high as 6 dB [51–53]. In addition, it can increase the transmit-receive isolation of transceivers or transponders. In imaging radar applications such as collision warning radar, military radar, or weather radar, a dual polarization antenna provides more information on the texture of the target, and the detection and discrimination of a target in the presence of clutter can be enhanced significantly by appropriately processing the information present in both polarizations of the backscatter signal.

One example is the ability to assess the road condition such as determining the surface roughness, surface wetness, and detecting the existence of an ice or snow layer on the road surface. In [54] the polarimetric backscatter responses from an asphalt surface have been measured under three different conditions, dry asphalt surface, wet asphalt surface, and asphalt surface covered with a 1.4 mm thick ice layer. These data sets have been used to determine phase and extinction matrices for co polarization and cross polarization for each condition. By comparing the backscatter signal taken with a polarimetric radar with the theoretical values for the backscatter coefficients described by the phase and extinction matrices, different road conditions can be reliably detected. This information can then be linked to the anti-lock brake or traction control systems of the vehicle. An other approach [55] uses genetic algorithms to determine the optimum polarization states of the transmitter and receiver antennas of a non-polarimetric radar for multiple target discrimination and classification as well as detection of road conditions thus avoiding costly polarimetric radar systems. Using phase shifters and variable power splitters the polarization states of a dual polarization antenna can be easily controlled.

For the dual polarization operation of microstrip antennas a common element is the square patch radiating element fed at dual central points of the orthogonal

edges [56], which excites  $TM_{100}$  and  $TM_{010}$  resonances with orthogonal polarizations. This approach has been applied for the antennas described in this chapter. Alternative feeding structures of planar dual polarization single elements and arrays are corner feeding [57] and slot coupling [58, 59]. While for a small array the feed losses of a microstrip line feed network can be kept relatively low, for bigger arrays the feed losses limit the gain of the antenna, as discussed in the introduction. Also for dual polarization antennas, series feeding to reduce feed losses is not a good solution, because of bandwidth limitations and beam squint with frequency. Radiation towards the rear direction is an additional problem, when slot coupling is used to place the microstrip line feed network on the rear side of the antenna [60].

In the previous chapter the NRD-guide has proven to be a low loss alternative for feeding planar antenna sub arrays making quasi planar high gain antennas feasible. Thanks to its multimode characteristic and thanks to the fact that these modes do not interact unless at a group of asymmetric discontinuities, the NRD-guide can also be used to feed sub arrays of microstrip antenna elements for independent operation in two polarizations. This feature of the NRD-guide is shown in Fig. 4.1 with the aid of the field patterns of the fundamental modes. In this chapter two types of dual polarization antennas are described. For ease of production and in order to circumvent alignment problems, the first antenna is fed by a substrate integrated NRD (SINRD) waveguide as described in Fig. 1.3, page 3. The key components of this kind of dual polarization antennas are transitions from NRD-guide to microstrip line which can excite the two fundamental modes independently. For the  $LSM_{01}$  mode, the commonly used matching technique based on a  $\lambda/4$  long NRD-guide stub [37, 38, 61] was applied. By contrast, slots in the back side ground metallization of the SINRD-guide provide a matching mechanism for the  $LSE_{01}$  mode without interference with the  $LSM_{01}$  mode.

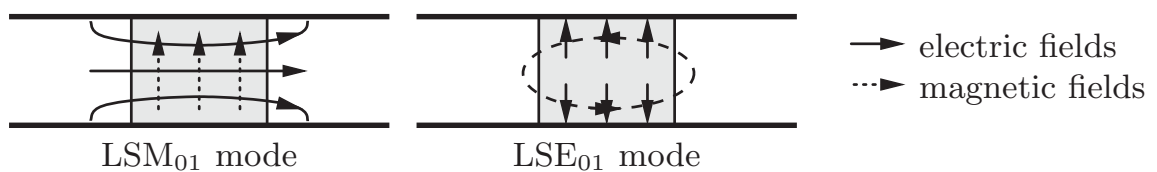


**Fig. 4.1:** Modes in the NRD-guide.

The second type of dual polarization antennas is fed by a conventional NRD-guide. This technique enables the design of dual mode NRD-guide T-junctions, which are required for the implementation of the corporate feed of dual polarization antenna arrays. For this type of antennas positioning forms made of

foam (Rohacell with permittivity similar to air) and dowel pins are used to align the different substrate layers. In contrast to the transitions used in the SINRD-guide dual polarization antenna, the transitions used for the array do not require additional slots in the back side ground metallization. The matching mechanism for the second mode is given by a step in the NRD-guide width. Thus no asymmetry along the height of the NRD-guide is required which would make the transition susceptible to the excitation of parallel plate waves.

#### 4.1 Dual Polarization Antenna Fed by a Dual Mode Substrate Integrated NRD-guide

Usually, the NRD-guide is used only in a single mode configuration ( $LSE_{01}$  or  $LSM_{01}$ ), while the other mode is regarded to be spurious. One example is the antenna described in Chapter 3. But since the modes are orthogonal to each other, they can coexist on the same NRD-guide without interference as long as there is no asymmetric discontinuity that would generate mode conversion problems [24]. Hence the NRD-guide lends itself to feed a dual polarization antenna, where each linear polarization is associated to one mode. Figures 4.3 and 4.4 show the principle of the antenna for horizontal and vertical excitation, respectively. It consists of a two substrate setup (Fig. 4.2). The front side substrate includes the microstrip feedings for radiation in horizontal and vertical polarization, and the antenna array consists of four square patches and a small microstrip line feeding network. The back side substrate includes the SINRD-guide feeding. The layout of the dual polarization antenna can be found in Appendix A.2, page 139.

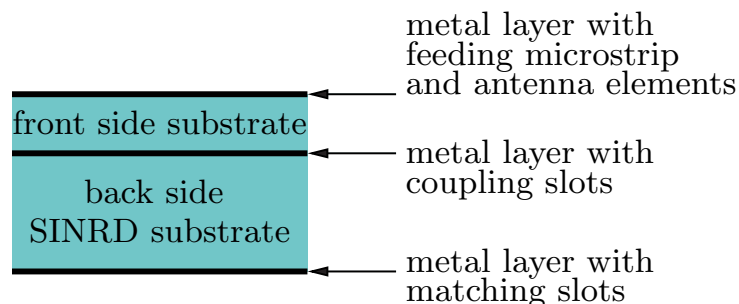


**Fig. 4.2:** Multi-layer setup of the dual polarization antenna (cross section).

The key component of this circuit is a dual mode microstrip to NRD-guide transition which can excite the  $LSE_{01}$  mode and the  $LSM_{01}$  mode independently.

It basically consists of two conventional transitions from microstrip to NRD-guide [37, 38], one for the  $LSE_{01}$  mode, fed by the horizontal microstrip line highlighted brown in Fig. 4.3, the other for the  $LSM_{01}$  mode, fed by the vertical microstrip line highlighted brown in Fig. 4.4. At the other end of the NRD-guide, represented by a dashed rectangle, a transition from dual mode NRD-guide to crossed microstrip lines serves as a feeding for the dual polarization antenna sub array consisting of four square microstrip patch antenna elements. The microstrip sub array including the microstrip feeding network is symmetrical in both planes. This arrangement effectively suppresses radiation in the cross polarization.

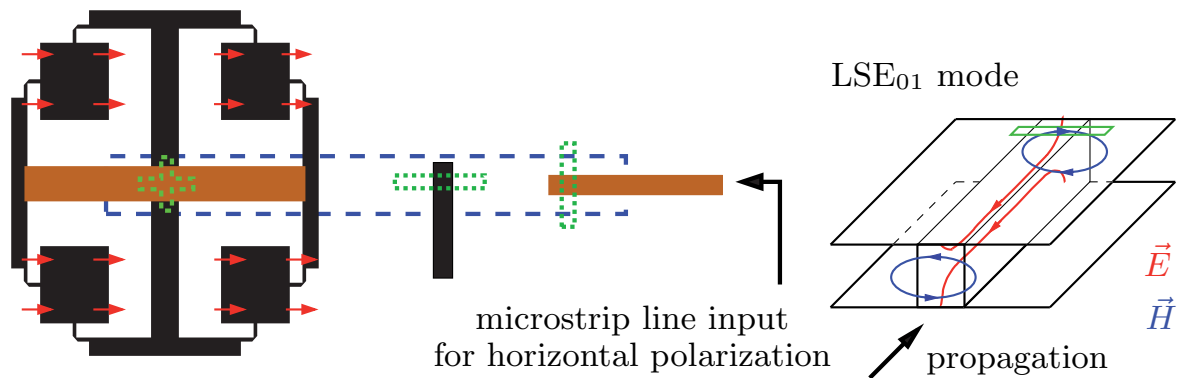


**Fig. 4.3:** Principle of the antenna; excitation of the antenna in the horizontal polarization.

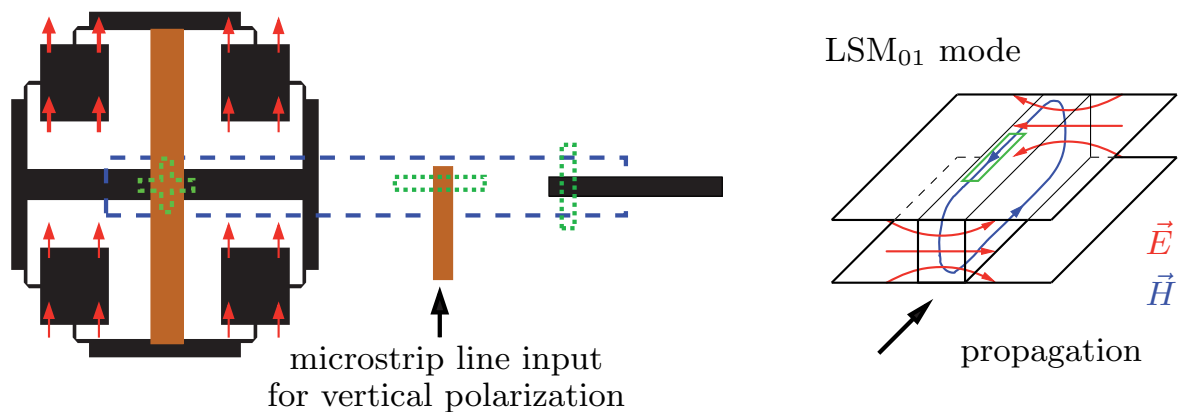


**Fig. 4.4:** Principle of the antenna; excitation of the antenna in the vertical polarization.

Figure 4.3 shows the principle of the antenna for radiation in the horizontal polarization. The power inserted on the horizontal feeding microstrip line is converted to an  $LSE_{01}$  mode wave propagating along the back side NRD-guide. The coupling mechanism via the coupling slot and the field pattern of the  $LSE_{01}$  mode are shown in the three-dimensional inset. At the left-most end of the NRD-guide the power is coupled to the horizontal microstrip line, split by microstrip T-junctions and finally fed to the four square microstrip patch antenna elements for radiation in the horizontal polarization. Figure 4.4 shows the corresponding mechanism with a feeding by the vertical microstrip line via the  $LSM_{01}$  mode on the NRD-guide to the vertical microstrip line for excitation of the patch antenna elements for radiation in the vertical polarization. In the following sections the components are described in detail.

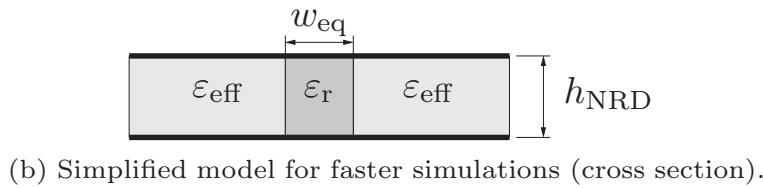
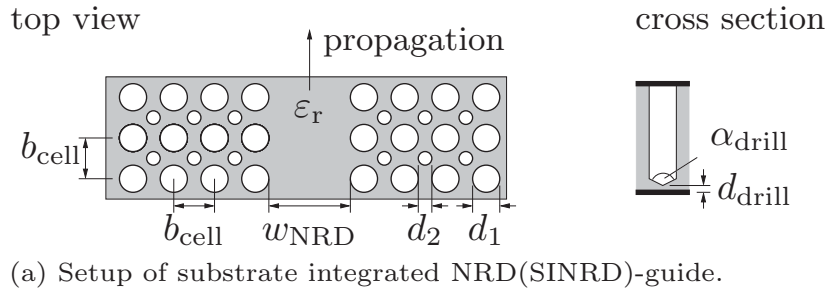


**Fig. 4.5:** SINRD-guide topology: a) drilling hole pattern, b) equivalent NRD-guide for faster simulations.

A common problem of hybrid planar/NRD-guide circuits is related to the mechanical support and the assembly of the planar substrate as well as the alignment between the different layers. For ease of production and in order to circumvent alignment problems, all NRD-guide components for this antenna are implemented in substrate integrated NRD (SINRD) waveguide technique [20], Fig. 4.5a, using TMM-6<sup>†</sup> material with  $\epsilon_r=6$ ,  $\tan \delta(@24 \text{ GHz})=2.1 \cdot 10^{-4}$ ,  $h_{\text{NRD}}=3.18 \text{ mm}$ . A specific air hole pattern ( $d_1=1.5 \text{ mm}$ ,  $d_2=0.5 \text{ mm}$ ,  $b_{\text{cell}}=1.75 \text{ mm}$ )

<sup>†</sup>The TMM-6 material used for the dual polarization antenna is a hydrocarbon ceramic material by Rogers. It is very hard and therefore tricky to process. To prevent overheating of the machining and drilling tools it is important to use the correct revolution speed and form feed dependent on the tool diameter. For the 0.5 mm drill it is necessary to use a thin sheet of a softer material (e.g. FR-2) on top of the TMM-6 to guide the drill and prevent it from breaking when it enters into the TMM-6 material.

is used to effectively lower the dielectric constant of the dielectric substrate regions along the desired NRD-guide, thus creating a wave guiding channel in the substrate, in this case having the width  $w_{\text{NRD}}=5.25$  mm. Using this technique, complex NRD-guide circuits can be implemented in one fabrication step. The NRD-guide layer is sufficiently robust to allow its lamination with other planar substrates. Dowel pins can be used to align the different substrate layers. For this application, all holes in the substrate, except for those which are used for alignment, are blind holes with  $d_{\text{drill}}=60\ \mu\text{m}$  and  $\alpha_{\text{drill}}=118^\circ$  indicated in the cross section in Fig. 4.5a, making sure that the back side metallization is not damaged and can be used for other purposes, e.g. matching slots. This arrangement produces a small asymmetry along the height of the NRD-guide, but is insufficient to generate significant leakage losses [62]. Simulation is done using a simplified NRD-guide model [20], shown in Fig. 4.5b, with  $w_{\text{eq}}=5.1$  mm and  $\epsilon_{\text{eff}}=2.79$ . With the formulae given in Sec. 2.5 the attenuation constants have been calculated for the  $\text{LSE}_{01}$  and the  $\text{LSM}_{01}$  mode (Figs. 4.6 and 4.7).

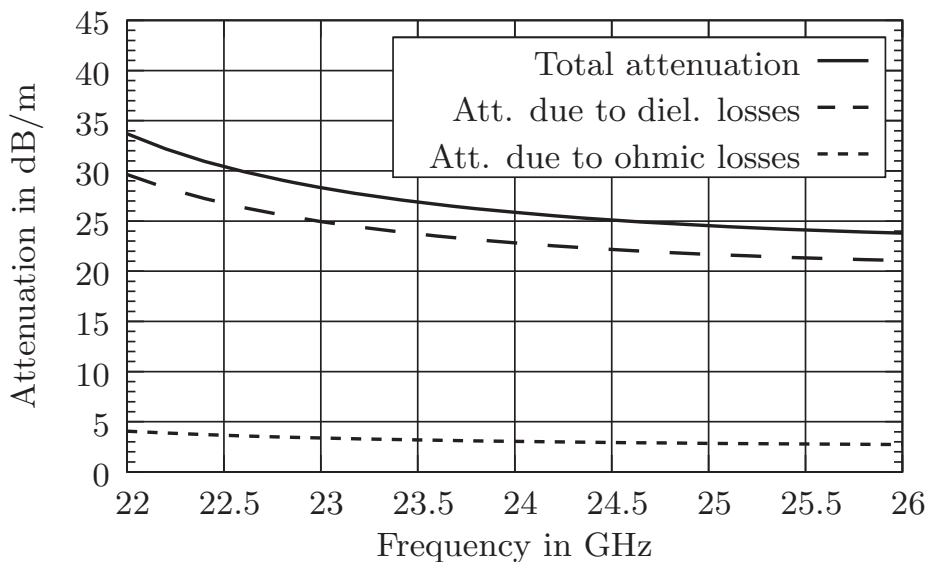


**Fig. 4.6:** Calculated attenuation of the  $\text{LSE}_{01}$  mode.

#### 4.1.1 Design and Characterization of a Dual Mode Transition

The dual mode transition from NRD-guide to microstrip line shown in Fig. 4.8a is a combination of two separate conventional transitions from NRD-guide to microstrip line [37, 38] with one important modification. The quarter-wave NRD-guide stub of the transition from the  $\text{LSM}_{01}$  mode to microstrip line is replaced



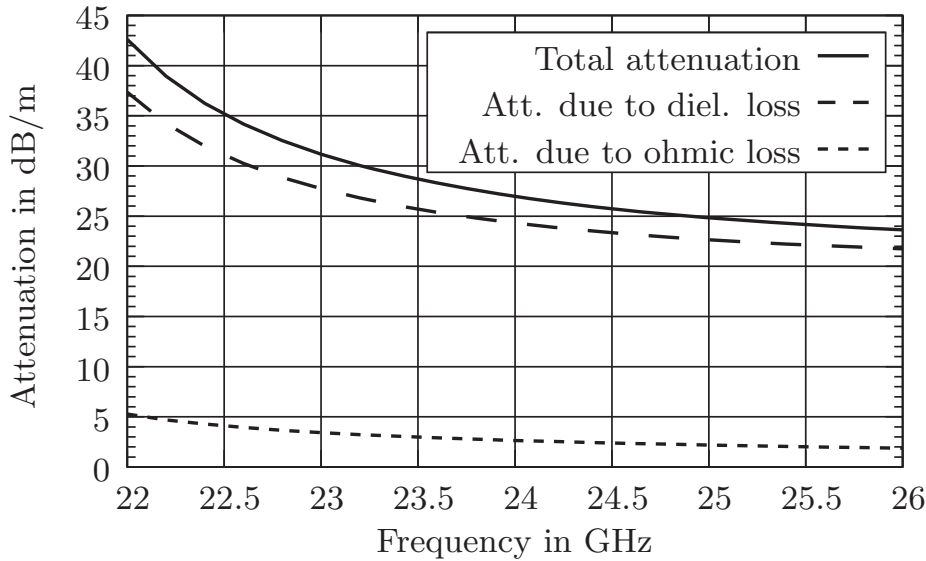
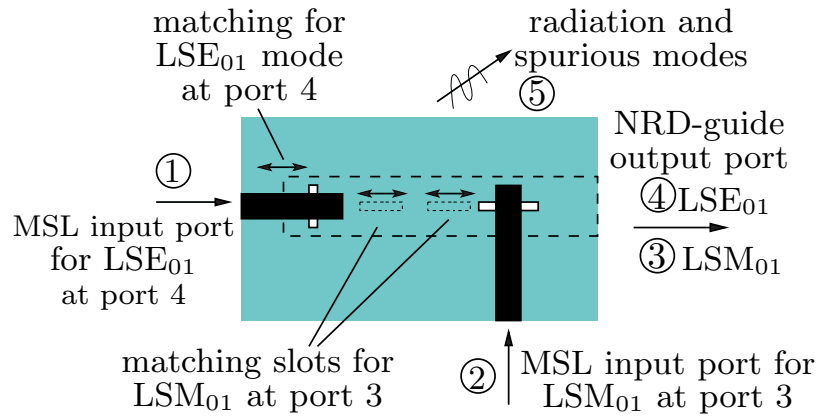


**Fig. 4.7:** Calculated attenuation of the  $\text{LSM}_{01}$  mode.

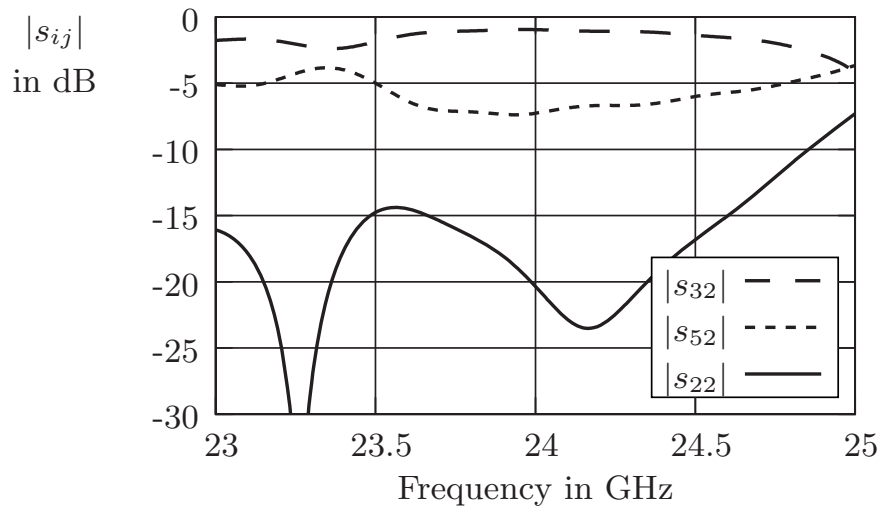
by a set of longitudinal slots—represented by dashed rectangles in Fig. 4.8a—in the back side metallization of the NRD-guide which do not affect the  $\text{LSE}_{01}$  mode, but act as a highly reflective discontinuity for the  $\text{LSM}_{01}$  mode. Figures 4.8b and 4.8c show the simulated S-parameters of the dual mode transition from NRD-guide to microstrip line for excitation of the  $\text{LSM}_{01}$  mode (port 3) and for excitation of the  $\text{LSE}_{01}$  mode (port 4), respectively. Port 5 is defined as the power that is lost by radiation through the coupling slots and the matching slots as well as excitation of parallel plate waves caused by the asymmetry introduced by the matching slots in the NRD-guide substrate. Comparing the two figures the broadband characteristic of the  $\text{LSE}_{01}$  mode excitation with nearly constant insertion loss of 0.9 dB is obvious, whereas the  $\text{LSM}_{01}$  mode excitation works well only in a limited frequency range from 23.6 GHz to 24.6 GHz, where the insertion loss varies between 1 dB minimum and 1.5 dB maximum. Below 23.5 GHz and above 24.7 GHz a non-negligible part of the input power exceeding  $-5$  dB is lost by radiation and excitation of the parallel plate mode due to the matching slots. Above 24.7 GHz also the return loss is limited to less than 15 dB. Especially the excitation of the parallel plate mode is critical. This mode is not bound to the afore-mentioned wave guiding channel in the substrate, but can also propagate in the areas of the lower permittivity defined by the air hole pattern. In a more complex array setup as presented in the next section of this chapter, the parallel plate mode leads to spurious coupling within the feeding network. Additionally, without further precautions, the parallel plate mode causes radiation at the edges of the front side substrate. Hence both

parallel plate mode and spurious radiation of the transitions can cause severe degradation of the radiation diagram.

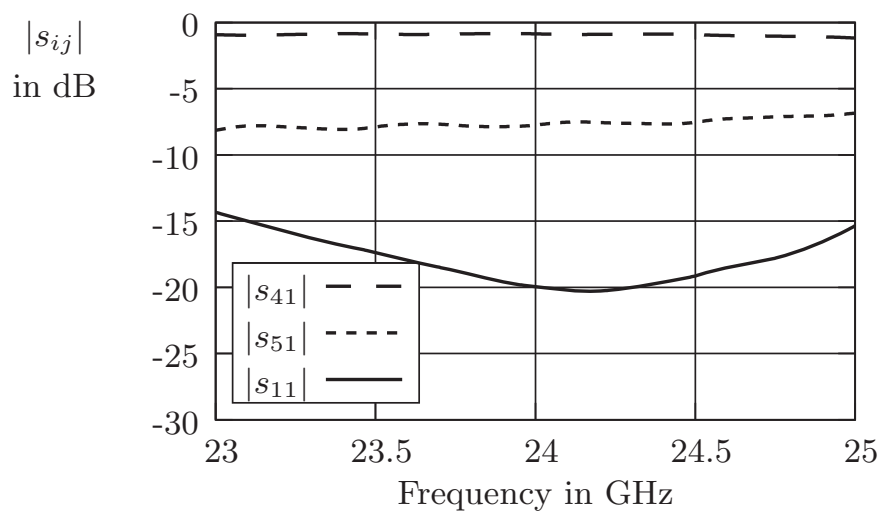
A test transition has been fabricated as a back-to-back transition with the overall dimensions indicated in Fig. 4.9a. The length of the NRD-guide section operated with the  $LSE_{01}$  mode is 53.8 mm. The length of the NRD-guide section operated with the  $LSM_{01}$  mode is 27.8 mm. The total length of all microstrip lines for the  $LSE_{01}$  mode excitation amounts to 22 mm, and the total length of all microstrip lines for the  $LSM_{01}$  mode excitation amounts to 32 mm. The wavelength at 24 GHz for a  $50\ \Omega$  microstrip line made of RT/Duroid 5870 ( $\epsilon_r=2.33$ , thickness=0.51 mm) is about 9 mm.



(a) Setup with port naming convention and principle of matching.

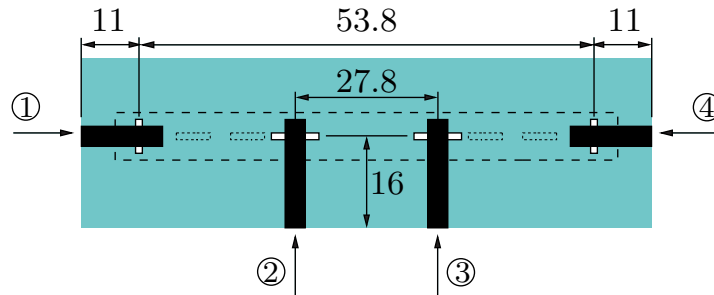


(b) Simulated S-parameters for  $LSM_{01}$  mode excitation.

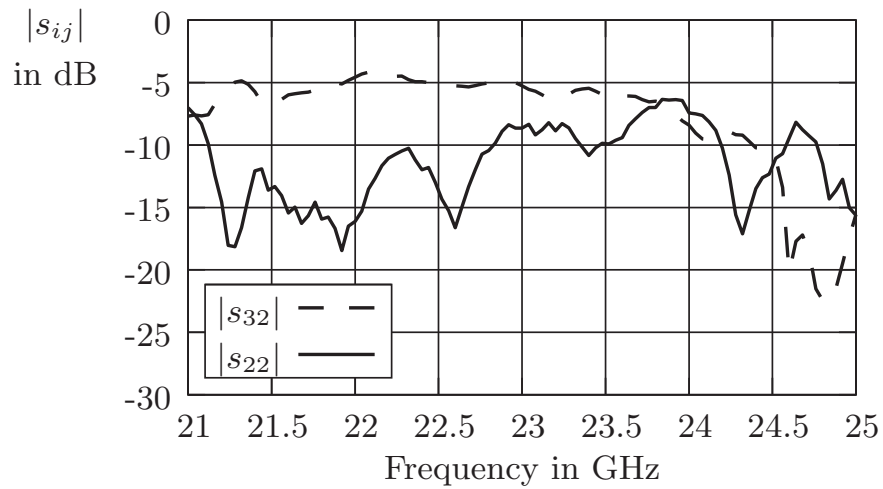


(c) Simulated S-parameters for  $LSE_{01}$  mode excitation.

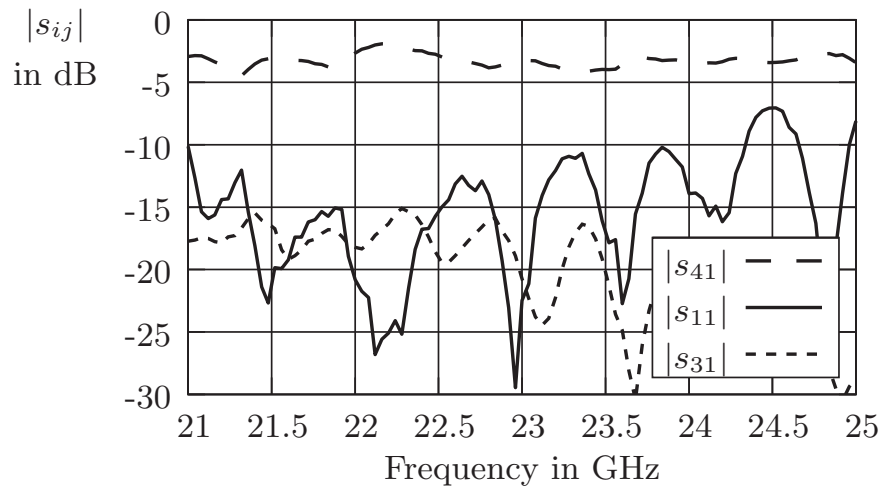
**Fig. 4.8:** Principle structure and simulation results of the dual mode transition NRD-guide to microstrip line.



(a) Setup with port naming convention.



(b) Measured S-parameters for  $LSM_{01}$  mode excitation.



(c) Measured S-parameters for  $LSE_{01}$  mode excitation including cross talk between the two channels (dotted curve).

**Fig. 4.9:** Structure of the back-to-back transition and measurement results of the dual mode transition microstrip line to NRD-guide (two transitions back-to-back).

Since the attenuation of the microstrip line is about 0.2 dB per wavelength, the expected insertion loss amounts to 0.7 dB for the  $\text{LSM}_{01}$  mode excitation microstrip feeding lines and 0.5 dB for the  $\text{LSE}_{01}$  mode excitation microstrip feeding lines.

Figure 4.9 shows the measured S-parameters of the dual mode back-to-back transition. Comparing Fig. 4.9b with Fig. 4.9c shows a higher insertion loss of the  $\text{LSM}_{01}$  mode excitation in general and a strong increase of insertion loss for frequencies higher than 23.5 GHz. This cutoff-frequency is lower than the 24.7 GHz predicted by the simulation. According to simulation results demonstrated in Fig. 4.8b at 23 GHz, about  $-5$  dB of the inserted power is lost at each transition microstrip line to NRD-guide in  $\text{LSM}_{01}$  mode operation due to radiation and excitation of spurious modes. Thus per transition only  $-1.8$  dB of the inserted power is really transferred to the  $\text{LSM}_{01}$  mode on the NRD-guide. Taking into account the losses on the NRD-guide section with the calculated attenuation according to Fig. 4.7 the attenuation along the NRD-guide section can be estimated to  $27.0 \text{ dB/m} \cdot 27.8 \text{ mm} = 0.8 \text{ dB}$ . The attenuation in the microstrip lines amounts to 0.7 dB. As a result the expected insertion loss between port 2 and port 3 in the setup given in Fig. 4.9a amounts to 5.1 dB. This is in good agreement with the measurement result given in Fig. 4.9b. When the power is inserted at port 1 in Fig. 4.9a, the  $\text{LSE}_{01}$  mode is excited on the NRD-guide and the longitudinal matching slots are ineffective. Therefore less power is being lost due to radiation and excitation of spurious modes and more power ( $-0.9$  dB compared to  $-1.8$  dB) per transition is transferred to the  $\text{LSE}_{01}$  mode on the NRD-guide. Now with the calculated attenuation according to Fig. 4.6 taking into account  $25.9 \text{ dB/m} \cdot 53.8 \text{ mm} = 1.4 \text{ dB}$  attenuation along the NRD-guide section and 0.5 dB attenuation in the microstrip lines the expected insertion loss between port 1 and port 4 amounts to 3.7 dB. This is again in good agreement with the measurement result given in Fig. 4.9c.

The dotted curve in Fig. 4.9c represents the cross talk between the  $\text{LSE}_{01}$  mode and the  $\text{LSM}_{01}$  mode. Ideally, interference should vanish completely due to the absence of transverse asymmetries along the SINRD-guide transmission line. Here a peak level of approximately  $-15$  dB indicates a minor misalignment of the front side planar microstrip layer relative to the back side SINRD-guide substrate layer. With dual polarization antennas, cross talk within the feeding structure results in an increased level of cross polarized radiation.

### 4.1.2 Design and Simulation of a Transition from Dual Mode NRD-guide to Crossed Microstrip Lines

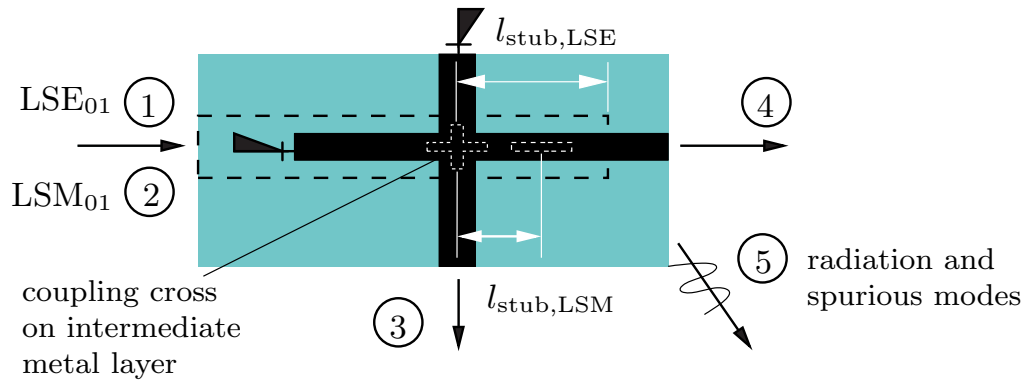
As indicated above, the coupling from the NRD-guide to the dual polarization antenna array is done by crossed coupling slots, Fig. 4.10a. The dimensions of the crossed coupling slots are the same as the dimensions for the coupling slots of the dual mode transition in Fig. 4.8a. Matching of the  $\text{LSM}_{01}$  mode is achieved by a longitudinal slot in the back side metallization of the SINRD-guide substrate represented by a dashed rectangle at the distance  $l_{\text{stub,LSM}}$  from the center of the crossed coupling slots in Fig. 4.10a. Again this longitudinal slot does not affect the  $\text{LSE}_{01}$  mode. The resonance in the  $\text{LSE}_{01}$  mode matching is tuned by the NRD-guide stub length  $l_{\text{stub,LSE}}$ . Figure 4.10c shows the simulated S-parameters of the transition from dual mode NRD-guide to crossed microstrip lines. Power in the  $\text{LSE}_{01}$  mode injected at port 1 and propagating along the NRD-guide is transferred onto the horizontal microstrip line, and approximately half of the power appears at port 4. Power in the  $\text{LSM}_{01}$  mode injected at port 2 is transferred onto the vertical microstrip line, and approximately half of it appears at port 3. As before, port 5 is defined as the power that is lost by radiation and the excitation of spurious modes in the NRD-guide substrate.

For measurement purposes the transitions for dual mode excitation, depicted in Fig. 4.8a, and the transition from dual mode NRD-guide to crossed microstrip lines, shown in Fig. 4.10a, have been combined to form the circuit depicted in Fig. 4.11a. Compared to theory, the measured S-parameters in Fig. 4.11b and Fig. 4.11c show a slight shift towards lower frequencies. As expected, the bandwidth of the circuit, defined by a maximum insertion loss of 6.7 dB, is wider reaching 1.3 GHz (from 22.2 GHz to 23.5 GHz) when driven with the  $\text{LSE}_{01}$  mode compared to 1 GHz bandwidth (from 23 GHz to 24 GHz) when driven with the  $\text{LSM}_{01}$  mode.

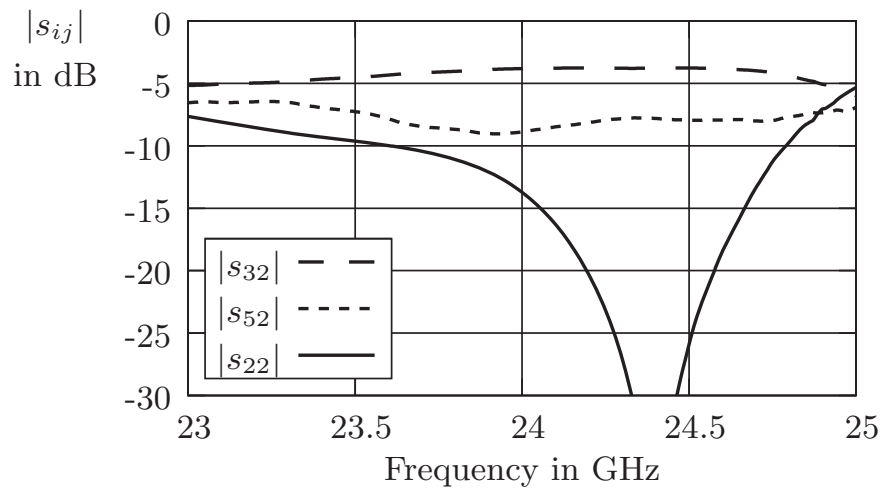
Like with the back-to-back arrangement of the transition from microstrip line to NRD-guide, the measured insertion loss of the setup in Fig. 4.11a can be compared to the corresponding value estimated by simulations and loss calculations. According to the simulation depicted in Fig. 4.8c, page 65 at 23.5 GHz the insertion loss of the transition microstrip line to NRD-guide exciting the  $\text{LSE}_{01}$  mode is 0.9 dB. Figure 4.10c indicates 4.3 dB insertion loss between port 1 on the NRD-guide and port 4 on the microstrip line. Assuming  $25.9 \text{ dB/m} \cdot 41.0 \text{ mm} = 1.1 \text{ dB}$  of attenuation due to NRD-guide losses and 0.5 dB of attenuation due to microstrip line losses results in 6.8 dB insertion loss which is in excellent agreement with the measured 6.7 dB insertion loss shown in Fig. 4.11c.

Also the 6.4 dB measured insertion loss at 24 GHz between port 2 and port 3 in Fig. 4.11b corresponds very well to the estimated value of 6.3 dB when taking 1.0 dB insertion loss from Fig. 4.8b, 3.8 dB insertion loss from Fig. 4.10b and assuming  $27.0 \text{ dB/m} \cdot 28.5 \text{ mm} = 0.8 \text{ dB}$  and 0.7 dB for the attenuation due to NRD-guide and microstrip line losses, respectively.

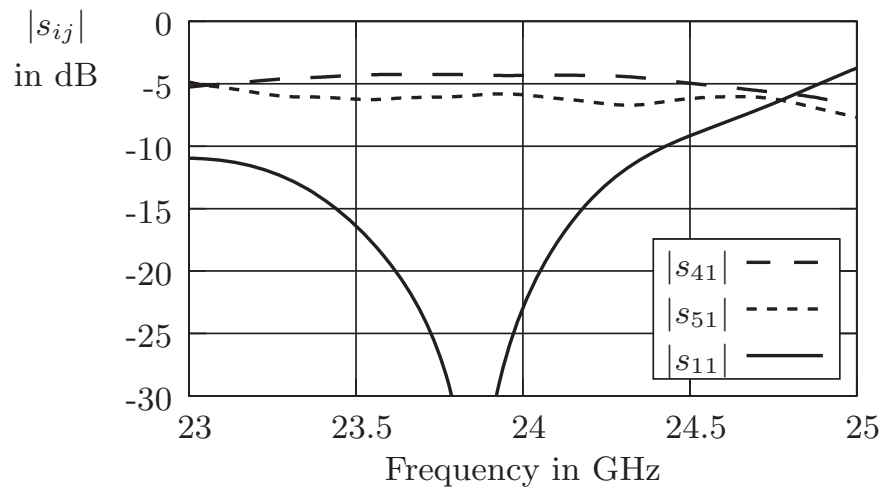
From 23 GHz to 23.5 GHz, the setup works well for both excitations.



(a) Setup with port naming convention and principle of matching.



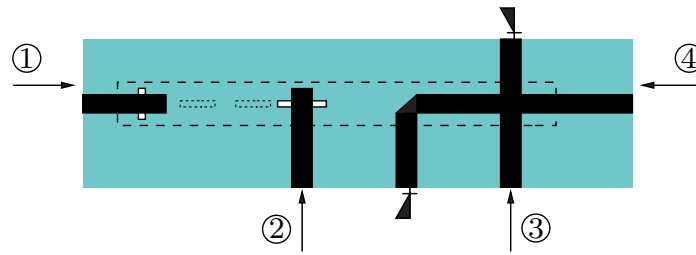
(b) Simulated S-parameters with  $LSM_{01}$  mode excitation.



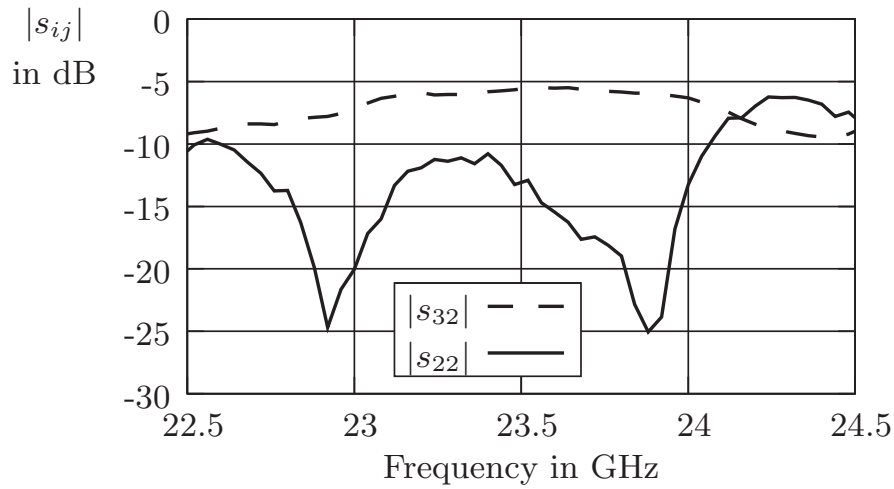
(c) Simulated S-parameters with  $LSE_{01}$  mode excitation.

**Fig. 4.10:** Structure and simulation results of the transition from dual mode NRD-guide to crossed microstrip lines.

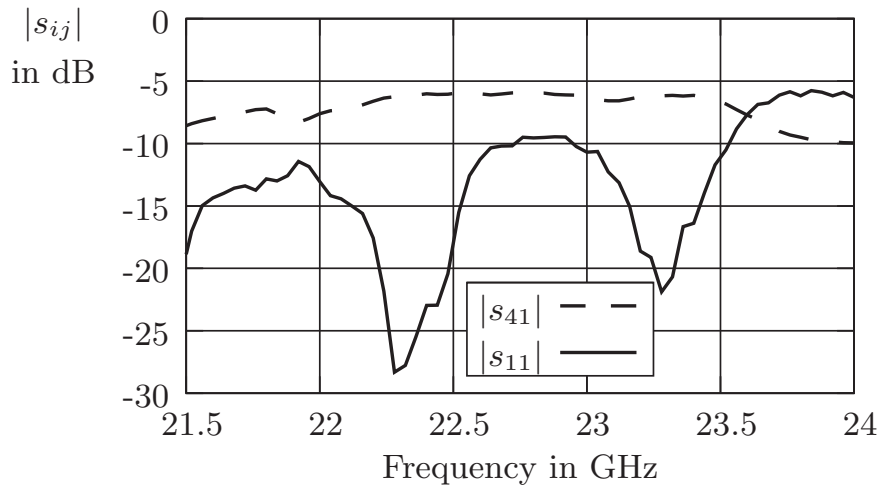




(a) Setup for measurement.



(b) Results for excitation of vertical microstrip line via  $LSM_{01}$  mode.



(c) Results for excitation of horizontal microstrip line via  $LSE_{01}$  mode.

**Fig. 4.11:** Structure and measured S-parameters of the transition from dual mode NRD-guide to crossed microstrip lines.

### 4.1.3 Design of the Dual Polarization Radiating Element

The radiating structure in Fig. 4.12 consists of four square microstrip patch radiating elements and is excited by a network including the transition from dual mode NRD-guide to crossed microstrip lines described in the previous section.

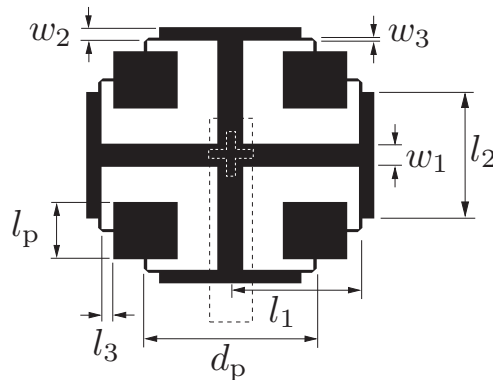


**Fig. 4.12:** Setup of the dual polarization radiating element.

The input impedance of a feeding point at the edge of patch antenna elements in general, and especially of square patches needed for dual polarizable antennas, is very high compared to the characteristic impedance of common microstrip lines. Usually, matching towards a lower characteristic impedance can be achieved by two measures. Either the position of the feeding point along the edge of the patch is optimized as indicated in Fig. 4.13, left. But this results in a strong excitation of the cross polarization and is therefore not suitable for dual polarization antennas. Alternatively, the feeding point could be moved towards the center of the patch as indicated in Fig. 4.13, right.



**Fig. 4.13:** Common techniques of impedance matching used for the feeding of a microstrip patch radiating element.

Also this method does not work with dual polarized antenna elements as the slots would disturb the orthogonal polarization. Here, matching to the characteristic impedance of the output branches of the microstrip T-junctions, in this

case  $100\ \Omega$ , is done by a  $\lambda/4$  impedance transformer. Due to space limitations in the array applications described later in this work, the microstrip line transformer section includes an optimum mitered  $90^\circ$  bend [63]. The planar structure is symmetrical with regard to both planes perpendicular to the substrate surface. The dimensions due to Fig. 4.12 are  $l_1=7.6\ \text{mm}$ ,  $w_1=1.5\ \text{mm}$ ,  $l_2=8.4\ \text{mm}$ ,  $w_2=0.9\ \text{mm}$ ,  $w_3=0.2\ \text{mm}$ ,  $l_p=3.8\ \text{mm}$ ,  $d_p=10\ \text{mm}$ . Using one single antenna element, minor excitation of the cross polarization can be observed due to the small distance  $l_3=0.7\ \text{mm}$ , between the patch and the feeding at the  $90^\circ$  bend. In the sub array consisting of four single antenna elements, in the E-plane and in the H-plane, this effect is compensated due to the symmetric setup.

#### 4.1.4 Measurements on the Dual Polarization Antenna

Finally, the circuit in Fig. 4.11a has been used to feed a dual polarization array of four square patch antenna elements (Fig. 4.14). A test fixture transition with a coaxial Sub-Miniature version A (SMA) connector has been used for a quick and easy to handle interconnect to the measurement setup. The matching of the dual polarization antenna (Fig. 4.15) for both excitations is best between 21.8 GHz and 22.5 GHz.

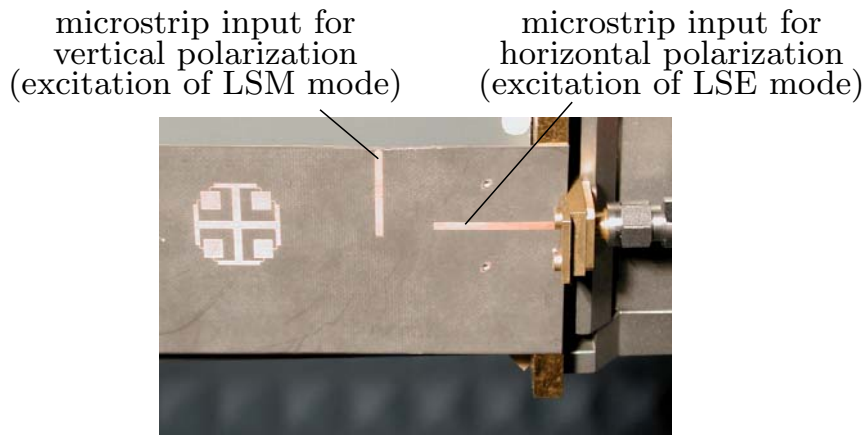


**Fig. 4.14:** Photo of the dual polarization antenna.

The radiation diagrams of the antenna have been measured in the E-plane and in the H-plane for both excitations, excitation with the  $LSE_{01}$  mode is shown in Fig. 4.17, excitation with the  $LSM_{01}$  mode in Fig. 4.18. They partly show strong amplitude variations in the main lobe, especially in the E-plane. Investigations showed that this distortion is mainly due to spurious radiation of the

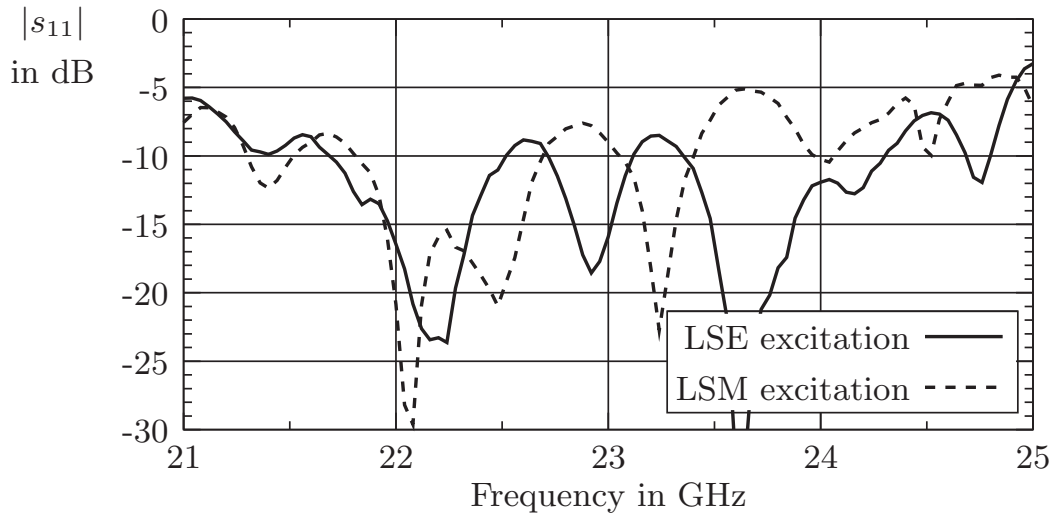


**Fig. 4.15:** Measured return loss of the antenna.

feeding microstrip lines, the interconnect between the test fixture and the feeding microstrip line, and the transitions from the feeding microstrip line to the NRD-guide. The degree of perturbation is influenced by several factors. First of all, it depends on the relative phase of the spurious radiation with respect to the wanted radiation. But even for completely destructive superposition, it still depends strongly on the location of the spurious radiation with respect to the axes of rotation, as indicated in Fig. 4.16. Sources of spurious radiation close to the axis of rotation are less critical than sources of spurious radiation located far away. As a simple approximation, the closely located spurious radiation affect primarily the gain of the antenna element, compared to the spurious radiation located far away there is less influence on the shape of the radiation diagram. For excitation with the  $LSE_{01}$  mode, this can be seen comparing the radiation diagrams of co-polarization in Fig. 4.17b—the position of the feeding microstrip line for  $LSE_{01}$  mode excitation in Fig. 4.16a corresponds to the axis of rotation in the H-plane, resulting in a smooth radiation diagram—with Fig. 4.17a—the position of the feeding microstrip line is far away from the axis of radiation, leading to a strong ripple. The same explanation holds for excitation with the  $LSM_{01}$  mode, but here the positions of the sources of spurious radiation in neither of the cutting planes coincide with the axis of rotation, see Fig. 4.16b, therefore in both planes, E-plane in Fig. 4.18a and H-plane in Fig. 4.18b the radiation diagram shows some amplitude ripple in the main lobe and asymmetries in the side lobes.

For the  $LSE_{01}$  mode excitation, the cross-polarization and the side lobes of the co-polarization are below  $-16$  dB in the H-plane. In the E-plane the spurious radiation of the feeding causes an asymmetry of the side lobes with  $-15$  dB at  $-70^\circ$  and  $-13$  dB at  $+70^\circ$ , and also the cross-polarization is asymmetrical but always lower than  $-16$  dB. For the  $LSM_{01}$  mode excitation, the cross-polarization and the side lobes of the co-polarization are below  $-11$  dB in the H-plane. In the E-plane the side lobe level is asymmetrical and at a level of  $-9$  dB, again due to the spurious radiation of the feeding.

Table 4.1 summarizes the measured half power beam widths of the antenna for both excitations.

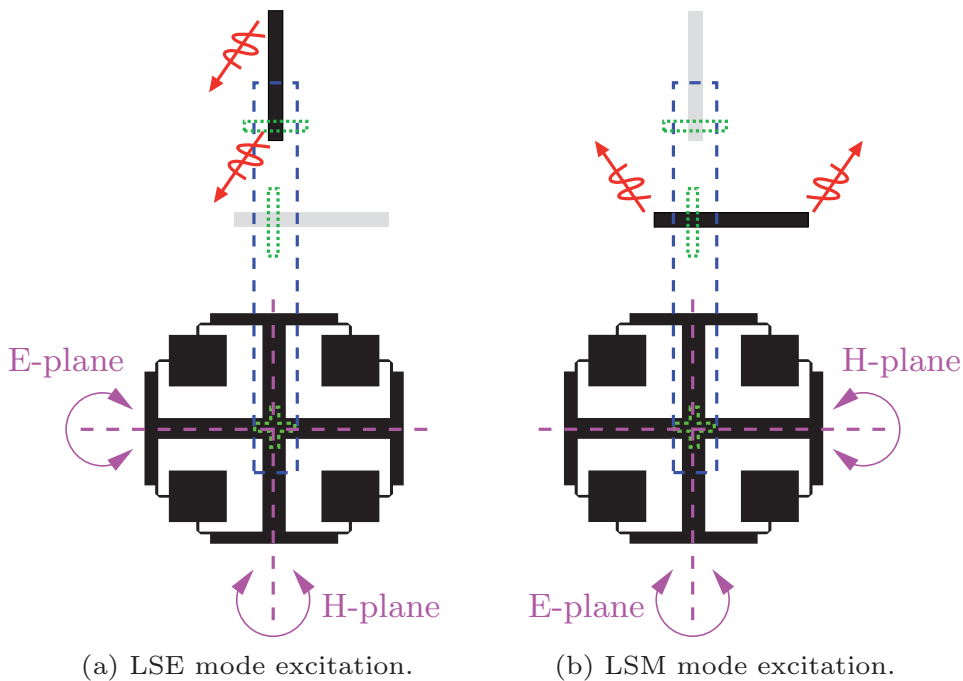
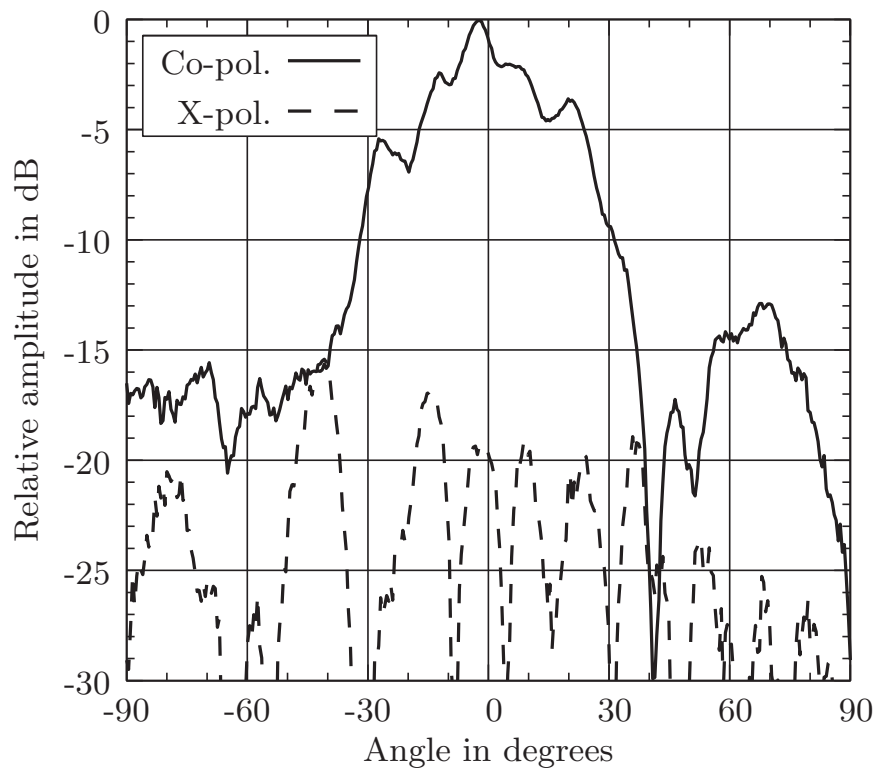


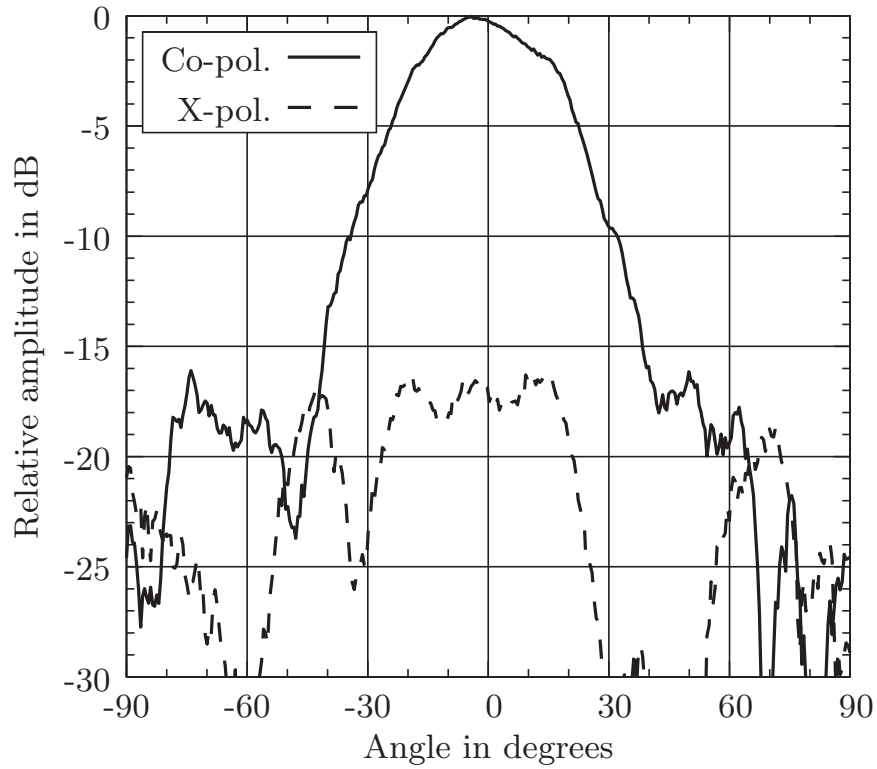
**Fig. 4.16:** Setup of the dual mode antenna element including the sources of spurious radiation.

**Table 4.1:** Measured half power beam width of the antenna

	E-plane	H-plane
LSE mode excitation	$25^\circ$	$38^\circ$
LSM mode excitation	$37^\circ$	$30^\circ$

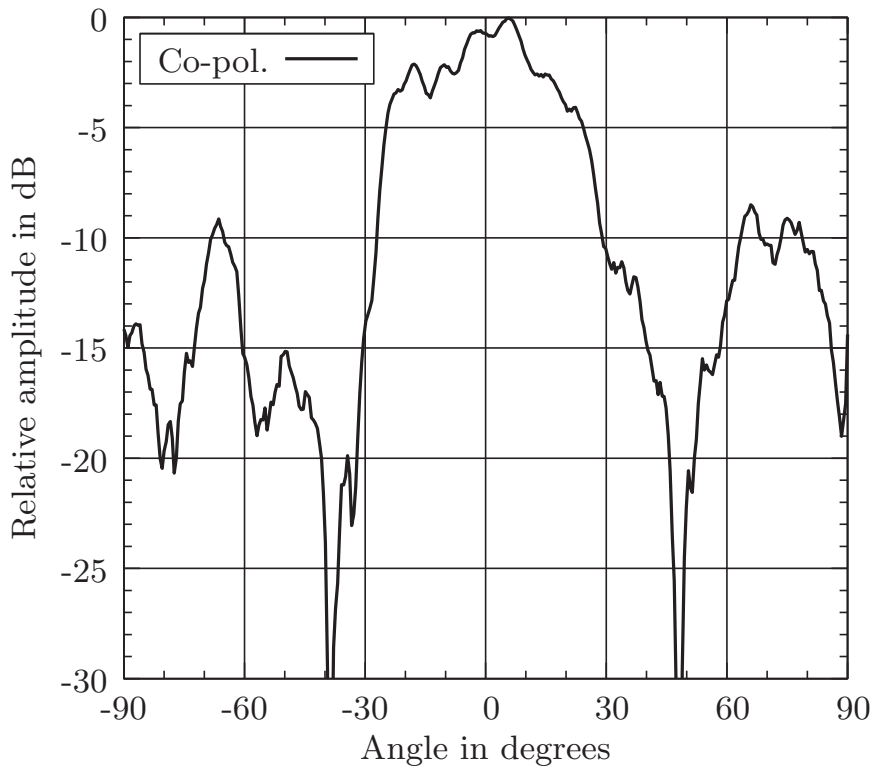


(a) E-plane.

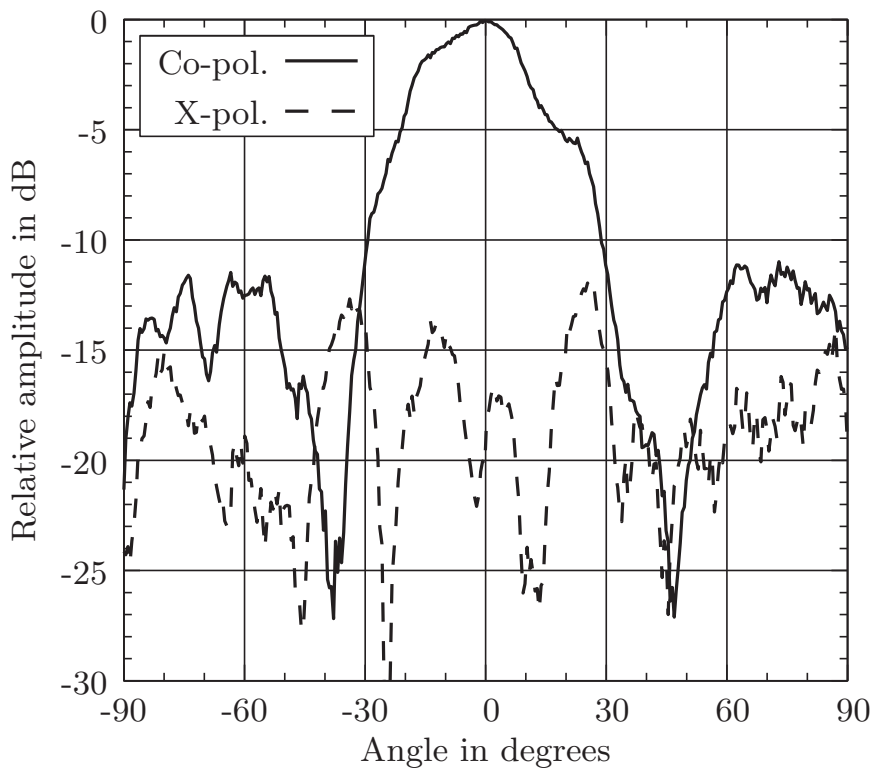


(b) H-plane.

**Fig. 4.17:** Measured radiation diagrams with  $LSE_{01}$  excitation.



(a) E-plane.



(b) H-plane.

**Fig. 4.18:** Measured radiation diagrams with  $LSM_{01}$  excitation.

### 4.1.5 A Transition Microstrip Line to NRD-guide for Simultaneous Excitation of Both Modes

With the antennas described in this chapter, the nonradiative dielectric (NRD) waveguide is used as a dual mode waveguide for feeding a dual polarization antenna array.  $LSE_{01}$  and  $LSM_{01}$  modes are excited independently by separate transitions from microstrip line to NRD-guide. Each of the modes causes the planar patch array to radiate in one linear polarization. By properly choosing the driving amplitude and the phase at the two input ports, the antenna can not only operate in linear polarizations, vertical and horizontal or  $\pm 45^\circ$  slanted, but also in circular or elliptical polarizations, left and right hand. Radiation in circular and elliptical polarization can even be achieved with a modified transition using a single microstrip line and exciting both modes in the necessary phase relation.

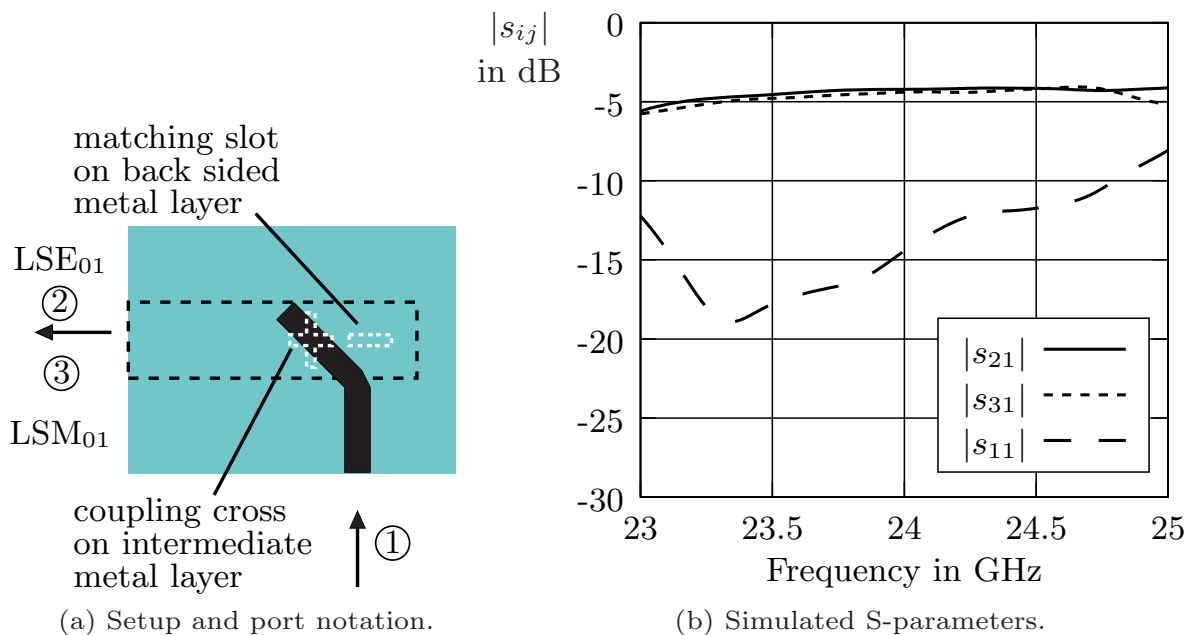


**Fig. 4.19:** Transition from microstrip line to NRD-guide for simultaneous excitation of both modes.

Figure 4.19a shows such a transition. Here, the feeding microstrip line is oriented under a  $45^\circ$  angle with respect to the crossed coupling slots resulting in an equal power distribution, of both modes,  $LSE_{01}$  and  $LSM_{01}$ , see Fig. 4.19b. For elliptical polarization the angle can be varied in order to obtain an unequal power distribution between the two modes. The matching mechanism is the same like the one of the transition from dual mode NRD-guide to crossed microstrip lines



in Fig. 4.10a. As the wavelength is different for the two modes, it is important to carefully adjust the length between the transition and the radiating element for an exact  $90^\circ$  phase shift between the two modes.

## 4.2 Dual Polarization Antenna Array with Optimized Feeding Network

The general motivation for dual polarization antennas has been discussed in the beginning of Chapter 4, and an implementation with a feeding based on substrate integrated NRD-guide was given in Chapter 4.1, where the transitions from NRD-guide to microstrip line and the transition from NRD-guide to crossed microstrip lines make use of slots in the back side metallization to provide a matching mechanism for the excitation of the  $LSM_{01}$  mode. With the matching slots only present in the back side metallization but not in the common metallization between the front side substrate and the back side SINRD substrate, another asymmetry was introduced along the NRD-guide height causing an increased level of parallel plate waves. Both, the increased level of parallel plate waves and the radiation of the matching slots are root causes for a degradation of the radiation diagrams.

The dual polarization antenna described in this chapter works without additional slots in the back side metallization and thus provides better radiation diagrams.

Figure 4.20 shows the setup of the antenna array with two microstrip feedings—one for radiation in the horizontal polarization and one for radiation in the vertical polarization. It consists of two substrate layers mounted on an aluminum plate serving as a support, see Fig. 4.21. The front side substrate (RT/Duroid 5870,  $\epsilon_r=2.33$ , thickness 0.51 mm) includes the microstrip feedings and two antenna sub arrays consisting of four square microstrip patch radiating elements and a small microstrip feeding network. The intermediate substrate (TMM-6,  $\epsilon_r=6$ ,  $\tan \delta(@24 \text{ GHz})=0.0021$ , thickness 3.18 mm) includes the corporate NRD-guide feeding network. It is milled out of a solid block and then glued onto the supporting aluminum plate using the same type of bonding sheet that was also used with the other antennas and described in Sec. 3.2.2. The layout of the entire antenna can be found in Appendix A.2, page 140. A positioning form made of a polymethacrylimide- (PMI-) rigid foam (Rohacell [64] with permittivity similar to air) and dowel pins are used to align the different substrate layers. The planar front side substrate including the microstrip patch antenna

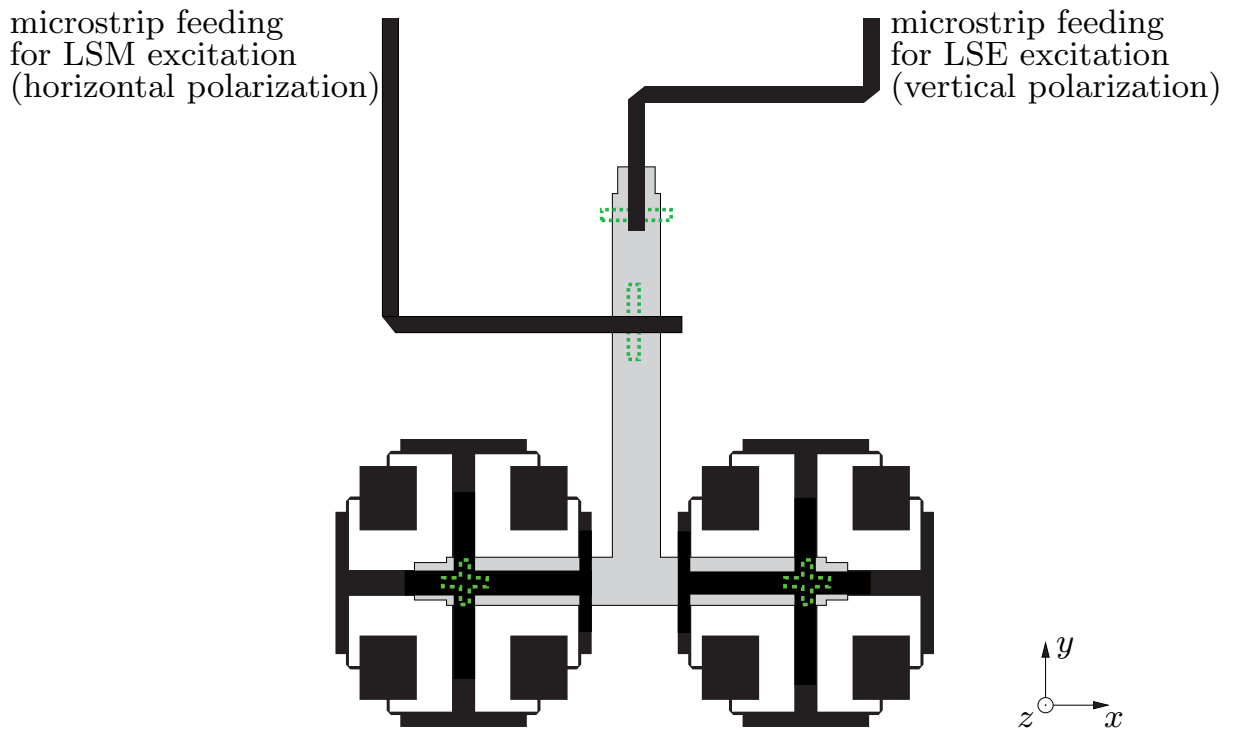


**Fig. 4.20:** Top view of the dual polarization antenna array with slot coupled NRD-guide feeding network on the back side (grey).

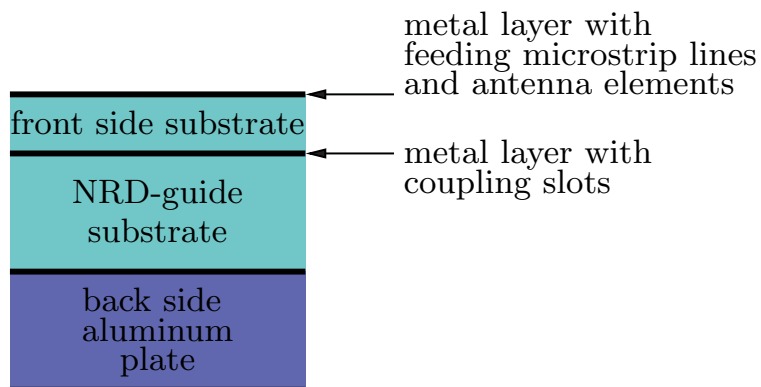


**Fig. 4.21:** Cross section of the antenna array.

sub arrays is glued on top of the NRD-guide feeding network using the same type of bonding sheet. The back side metallization of the substrate serves, at the same time, as the top metallization of the NRD-guides. The total height of the antenna is 3.5 mm only, plus the back side aluminum plate.

### 4.2.1 NRD-guide Circuit Elements

The dual polarization antenna array consists of several NRD-guides and hybrid circuit elements. The design principles and detailed simulation results for these components are given in this section. Sketches of the components including naming conventions and values for the geometrical dimensions are given in Appendix A.1, page 135 et seq. The key component of the antenna is a microstrip to NRD-guide transition which can excite the  $LSE_{01}$  mode and the  $LSM_{01}$  mode independently. For matching the transitions from NRD-guide to microstrip line, it is necessary to influence the propagation of the  $LSE_{01}$  mode and  $LSM_{01}$  mode independently. In the previous chapter this was done by additional longitudinal slots in the back side metallization of the NRD-guide leading to spurious radiation and a more complicated, costlier setup including an additional small asymmetry along the height of the NRD-guide. With the antenna described in this section, results are improved by a step in width of the NRD-guide which has a strong influence on the  $LSM_{01}$  mode, but virtually no influence on the  $LSE_{01}$  mode. This matching technique is the subject of a patent application (see footnote<sup>†</sup>, page 5).

#### 4.2.1.1 Transition from Dual Mode NRD-guide to Microstrip Line

The dual mode transition from NRD-guide to microstrip line, Fig. 4.22, is a combination of two separate conventional transitions from NRD-guide to microstrip line [37, 38] with one important modification. The matching for the  $LSM_{01}$  mode excitation is controlled by a setup which influences the  $LSM_{01}$  mode but not the  $LSE_{01}$  mode. With the antenna described in Sec. 4.1 this has been realized by a set of longitudinal slots in the back side metallization of the NRD-guide, which caused some problems of radiation and was rather narrow band.

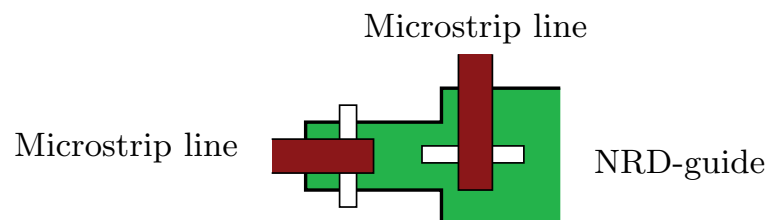


**Fig. 4.22:** Principle structure of the the transition from microstrip line to the NRD-guide with a step in NRD-guide width.

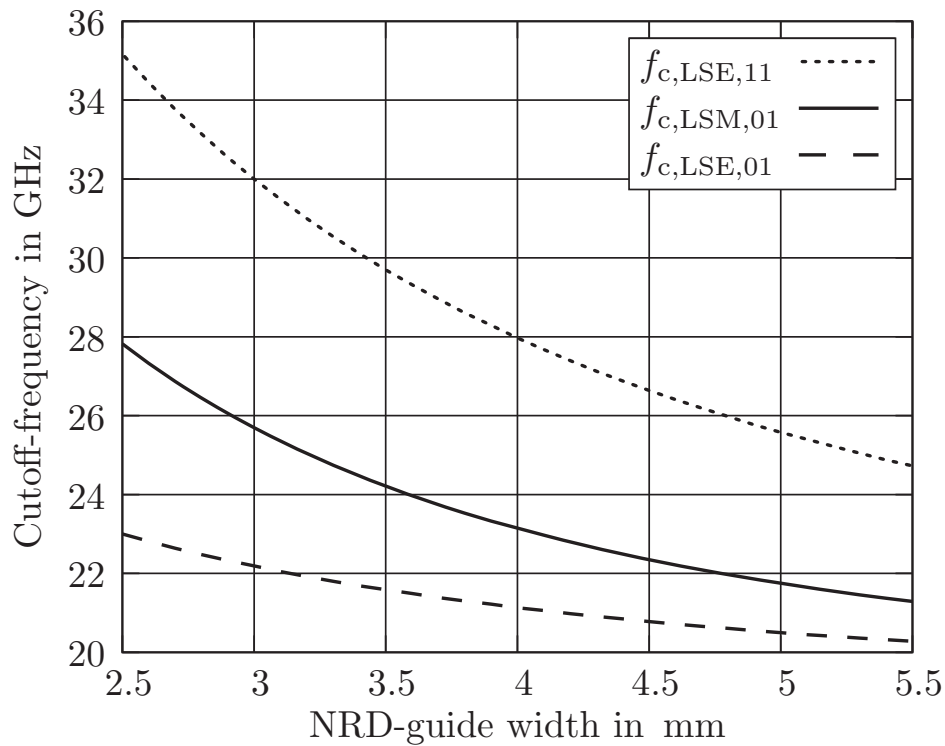


**Fig. 4.23:** Cutoff-frequency for the fundamental modes depending on the NRD-guide width.

The antenna presented in this section works without additional slots. Analysis of the eigenvalue equations derived in Chapter 2 leads to the cutoff-frequencies of the different modes in the NRD-guide. The cutoff-frequency of the NRD-guide modes is strongly dependent on the NRD-guide width (Fig. 4.23). Using an NRD-guide width  $w_{\text{NRD}}=5$  mm provides a wide band of operation where both fundamental modes  $\text{LSE}_{01}$  and  $\text{LSM}_{01}$  are operated above the cutoff-frequency, but the first higher order mode  $\text{LSE}_{11}$  is well suppressed due to its high cutoff-frequency. If the NRD-guide width is reduced to  $w_{\text{NRD}}=3$  mm, we observe a wide frequency range of operation from 22.5 GHz to 25.5 GHz (3 GHz bandwidth or 12.5% fractional bandwidth) where the  $\text{LSM}_{01}$  mode can not propagate due to its high cutoff-frequency and the  $\text{LSE}_{01}$  mode propagates as frequency is well above the related cutoff-frequency, see Fig. 4.24. Thus the step in the NRD-guide width acts as a strong discontinuity for the  $\text{LSM}_{01}$  mode; the dashed curve in Fig. 4.25 indicates that an  $\text{LSM}_{01}$  wave inserted at port 2 is completely reflected. The step can be used to create a  $\lambda/4$  stub for the  $\text{LSM}_{01}$  mode but has virtually no effect on the propagation of the  $\text{LSE}_{01}$  mode, which is indicated by the dotted curve in Fig. 4.25 representing the return loss of the discontinuity when excited with the  $\text{LSE}_{01}$  mode.

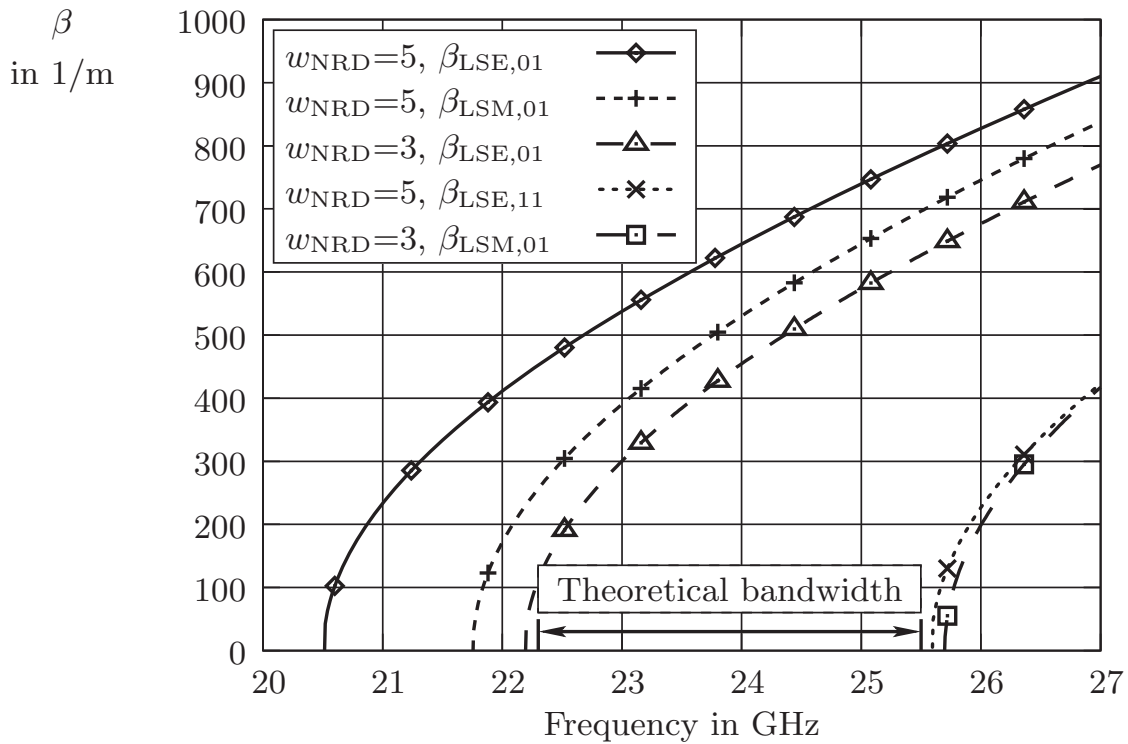


**Fig. 4.24:** Propagation constant for the fundamental modes depending on the NRD-guide width. The frequency range from 22.5 GHz to 25.5 GHz indicates the theoretical bandwidth of a dual mode transition based on a step in NRD-guide width.

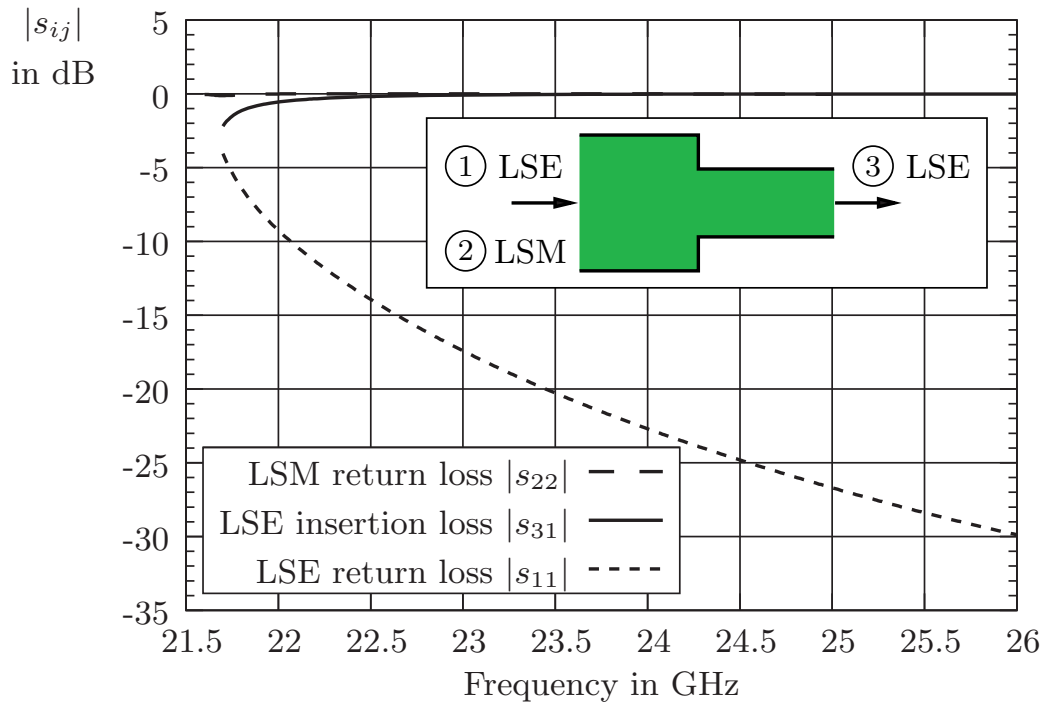


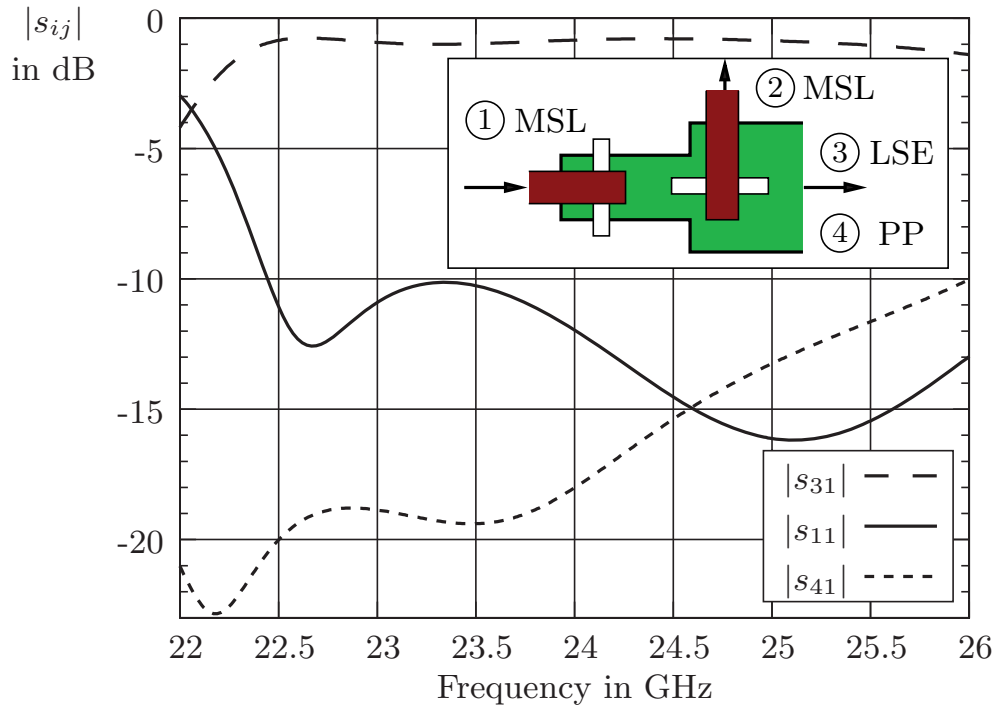
**Fig. 4.25:** Simulation of a step in the NRD-guide width ( $w_{NRD,1}=5$  mm,  $w_{NRD,2}=3$  mm).

Requirements for the transition are a good matching, a high level of isolation between the LSE mode excitation and the LSM mode excitation, and a low level of the parallel plate (PP) mode excitation between the ground metallization layer of the front side substrate and the back side aluminum plate. The isolation can be expected to be noncritical, as the transition is quasi-symmetrical along the width of the NRD-guide; only the microstrip line stub of the LSM<sub>01</sub> mode feeding contributes to a slight asymmetry. Nevertheless, the excitation of the parallel plate mode is of a great concern. It is not guided by the NRD-guide and can therefore cause both spurious coupling within the feeding network and distortion of the radiation diagrams due to spurious radiation.

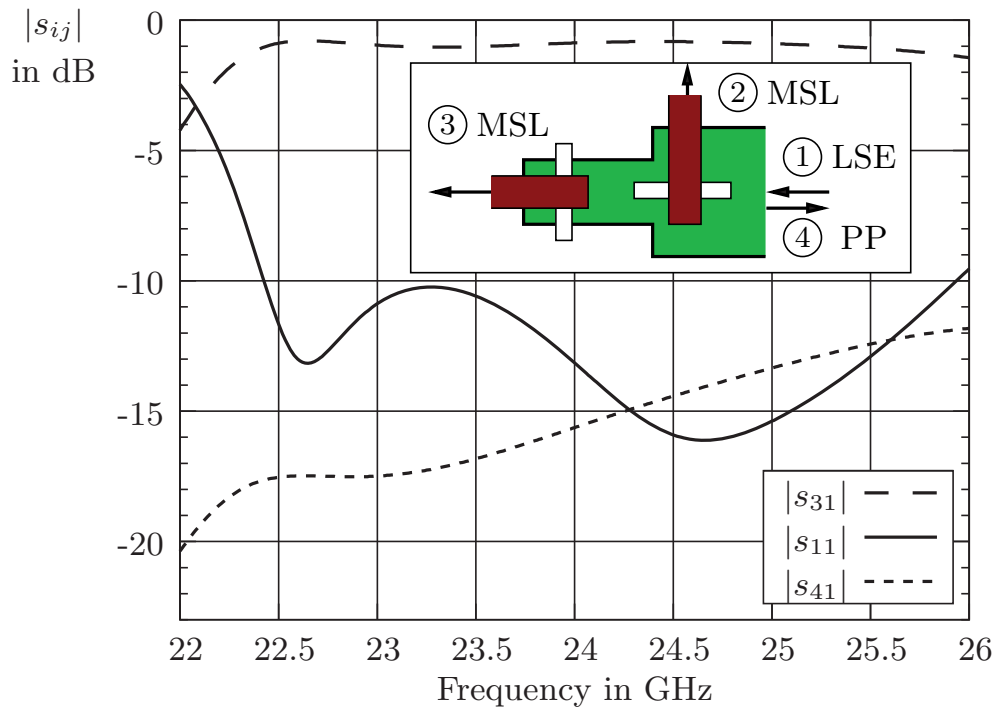
Simulations with the commercial finite integration time domain simulator CST Microwave Studio [34] (Fig. 4.26 and Fig. 4.28) of such a transition from dual mode NRD-guide to microstrip line show a good performance in the frequency range from 23 GHz to 25 GHz.

For the LSE<sub>01</sub> mode excitation in Fig. 4.26, the bandwidth of the transition is limited at the lower frequency end by the cutoff-frequency in the reduced NRD-guide,  $f_{c,LSE,01}=22.2$  GHz. The additional resonance is due to minor reflections at the step of the NRD-guide width and can be used to improve the bandwidth or the level of matching, e.g. by optimizing the offset distance between the two transitions as indicated in Fig. 4.27 for a distance 8.5 mm and 10 mm, respectively. For increasing frequencies the excitation of the parallel plate mode (PP, dotted curve in Fig. 4.26a) gets more and more critical and together with a reduced return loss, sets the band limit at the upper frequency end.

Assuming that a minimum return loss of 10 dB is required, the frequency range of operation of the transition with the LSE<sub>01</sub> mode excitation is 22.5 GHz to 26 GHz (3.5 GHz bandwidth or 14.4% fractional bandwidth).



(a) Excitation by the microstrip line.



(b) Excitation by the NRD-guide with the  $LSE_{01}$  mode.

**Fig. 4.26:** Simulated S-parameters (insertion loss  $|s_{31}|$ , return loss  $|s_{11}|$ , excitation of the parallel plate (PP) mode  $|s_{41}|$ ) of the transition microstrip line to the NRD-guide ( $LSE_{01}$  mode).

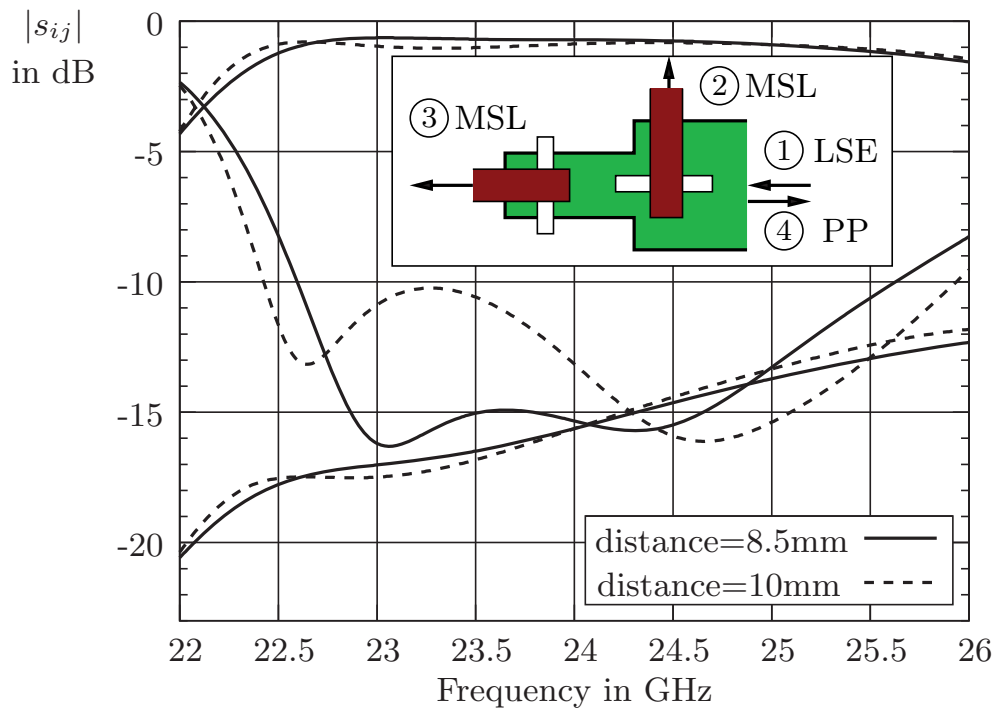
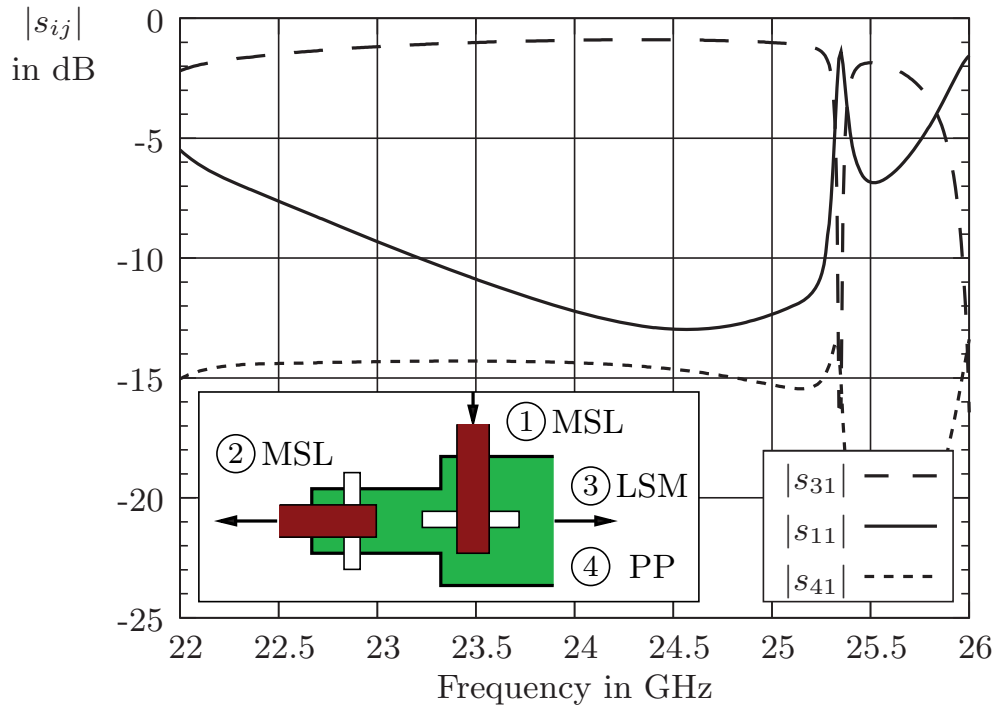


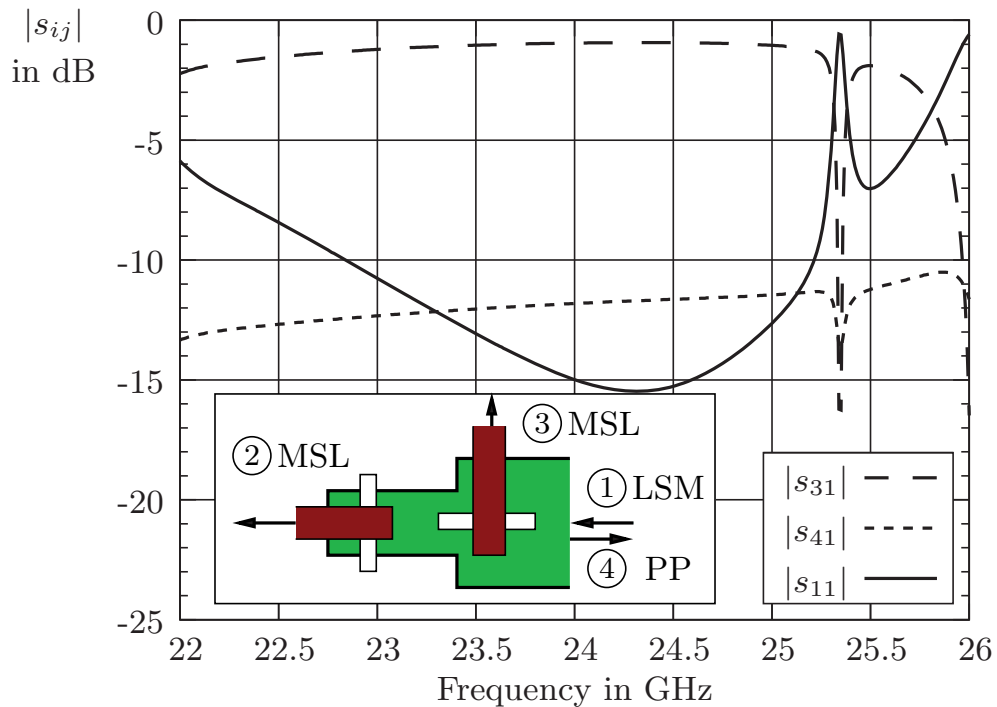
**Fig. 4.27:** Simulated S-parameters (insertion loss, return loss, excitation of the parallel plate (PP) mode) of the transition microstrip line to the NRD-guide ( $LSE_{01}$  mode), the offset distance between the two coupling slots being 8.5 mm (solid curve) and 10 mm (dotted curve), respectively.

For the  $LSM_{01}$  mode excitation in Fig. 4.28 the bandwidth of the transition is limited at the higher frequency end by both the cutoff-frequency of the  $LSE_{11}$  mode in the full width NRD-guide (dotted curve with cross symbols in Fig. 4.24), and the cutoff-frequency of the  $LSM_{01}$  mode in the reduced width NRD-guide stub (long dashed curve with square symbols) causing a transmission zero at 25.3 GHz. With the 10 dB return loss definition the frequency range of operation of the transition with  $LSM_{01}$  mode excitation is 23 GHz to 25 GHz (2 GHz bandwidth or 10.4% fractional bandwidth).





(a) Excitation by the microstrip line.



(b) Excitation by the NRD-guide with the  $LSM_{01}$  mode.

**Fig. 4.28:** Simulated S-parameters (insertion loss  $|s_{31}|$ , return loss  $|s_{11}|$ , excitation of the parallel plate (PP) mode  $|s_{41}|$ ) of the transition microstrip line to the NRD-guide ( $LSM_{01}$  mode).

## 4.2.1.2 Transition from Dual Mode NRD-guide to Crossed Microstrip Lines

The same idea serves for the development of a transition from dual mode NRD-guide to crossed microstrip lines via crossed coupling slots (insert of Fig. 4.29).

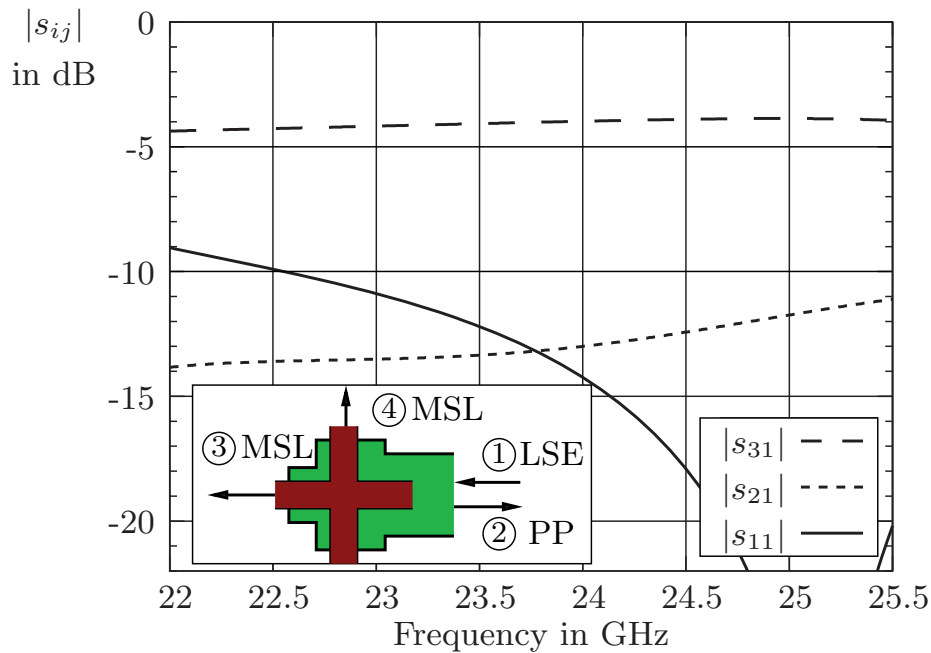


**Fig. 4.29:** Simulated S-parameters of dual mode transition NRD-guide to crossed microstrip lines excited with the  $LSE_{01}$  mode.

An extensive parameter study showed that by having a section of wider NRD-guide width  $w_{NRD}=6.6$  mm and thus allowing the propagation of the  $LSE_{11}$  mode, Fig. 4.1, page 58 in the region of the coupling cross, the operational bandwidth of the transition can be extended. Simulation with excitation with the  $LSE_{01}$  mode shows good and, with 3 GHz bandwidth, also broadband performance. Below 22.5 GHz return loss gets lower than 10 dB and transmission is limited by mismatch. The asymmetry caused by the crossed coupling slots produces a parallel plate wave that gets stronger with increasing frequencies and reaches  $-11$  dB at 25.5 GHz. According to the problems related to parallel plate waves, which have been described earlier in this chapter, it is not recommended to use this transition at frequencies higher than 25.5 GHz. In case of excitation with the  $LSM_{01}$  mode (Fig. 4.30), the parallel plate mode is negligible. The bandwidth is limited to 1.4 GHz. Below 23.2 GHz and above 24.6 GHz return loss is lower than 10 dB and transmission is limited by mismatch.

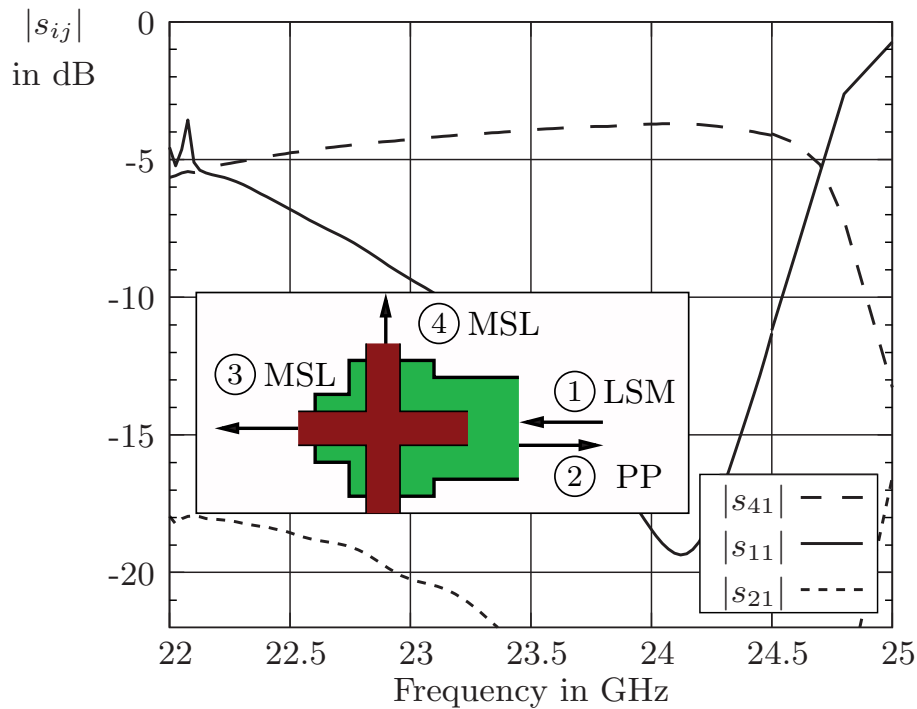


**Fig. 4.30:** Simulated S-parameters of dual mode transition NRD-guide to crossed microstrip lines excited with the  $\text{LSM}_{01}$  mode.

#### 4.2.1.3 Dual Mode NRD-guide T-junction

In order to extend bandwidth a parallel type feeding topology has been chosen for the antenna array presented in this chapter. Symmetrical NRD-guide T-junctions are used to equally split the power implementing a constant power distribution between all sub arrays. NRD-guide T-junctions always produce mode conversion between the fundamental  $\text{LSE}_{01}$  mode and the  $\text{LSM}_{01}$  mode [17, 24]. With the fixed beam antenna with single polarization in Chapter 3, only one mode is desired on each NRD-guide section of the feeding network, and the two types of T-junctions can be optimized separately for optimum mode conversion. In the dual mode feeding network for the dual polarization antenna the T-junctions must distribute both modes simultaneously. As a consequence, they have been optimized to maximize the conversion for both modes. If the T-junctions are excited by the  $\text{LSM}_{01}$  mode, the power is converted to the  $\text{LSE}_{01}$  mode at the output branches. If the T-junctions are excited by the  $\text{LSE}_{01}$  mode, the power is converted to the  $\text{LSM}_{01}$  mode at the output branches.

In a first step, the T-junction is optimized by a variation of the dimensions of a center notch opposite to the input branch (Fig. 4.31 left) to obtain a good

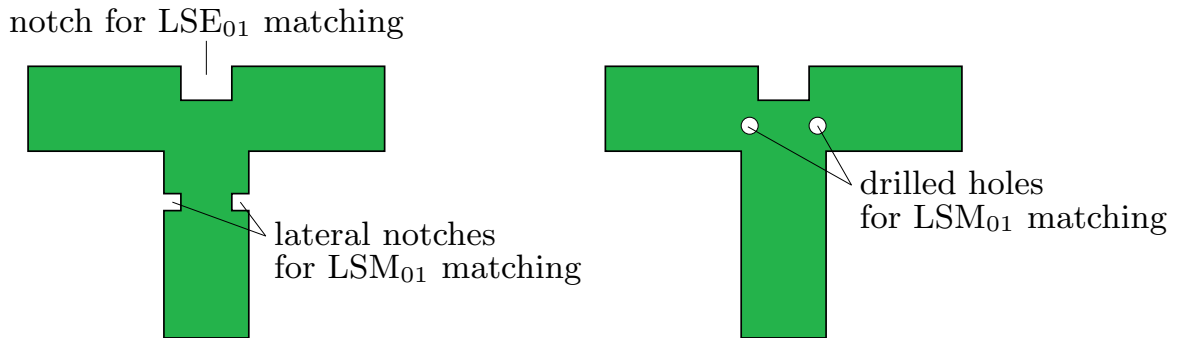


**Fig. 4.31:** Design of the dual mode NRD-guide T-junctions with lateral notches (left), with drilled holes (right) for  $\text{LSM}_{01}$  matching.

matching for an excitation with the  $\text{LSE}_{01}$  mode. This results in a strong mismatch for an excitation with the  $\text{LSM}_{01}$  mode. To prevent this, a discontinuity with the same return loss for an  $\text{LSM}_{01}$  excitation is inserted at a half a wavelength distance to the T-junction to form a resonator. This discontinuity should not influence the propagation of the  $\text{LSE}_{01}$  mode. So a reduction of the NRD-guide width in form of small lateral notches has proven to be the right choice (Fig. 4.31 left). In the final version of the T-junction the lateral notches were replaced by drilled holes depicted in Fig. 4.31 right. This gives a number of electrical and mechanical advantages including simplification of production, better mechanical stability and broader bandwidth. These matching techniques both with lateral notches and with drilled holes are the subject of a patent application (see footnote<sup>†</sup>, page 5). It is worth to note that the T-junction does not add any contribution to the parallel plate mode excitation as it is symmetrical along the height of the NRD-guide, and simulation can be accelerated significantly by making use of the symmetry plane. The simulated S-parameters of the T-junction for  $\text{LSE}_{01}$  mode and  $\text{LSM}_{01}$  mode excitation (Figs. 4.32 and 4.33, respectively) show good and broadband performance between 22.5 GHz and 25 GHz, with matching of the  $\text{LSM}_{01}$  mode being slightly better concerning both level and bandwidth.

Also the spurious conversion is higher (nearly constantly  $-15$  dB compared to typically less than  $-20$  dB) when the input NRD-guide is excited with the  $\text{LSE}_{01}$  mode ( $|s_{21}|$  in Fig. 4.32). This will lead to a higher level of cross polarization of the antenna array. When the input NRD-guide is excited with the  $\text{LSM}_{01}$  mode, the spurious conversion is negligible ( $|s_{31}|$  in Fig. 4.33), and the level of cross polarization is expected to be low, too.

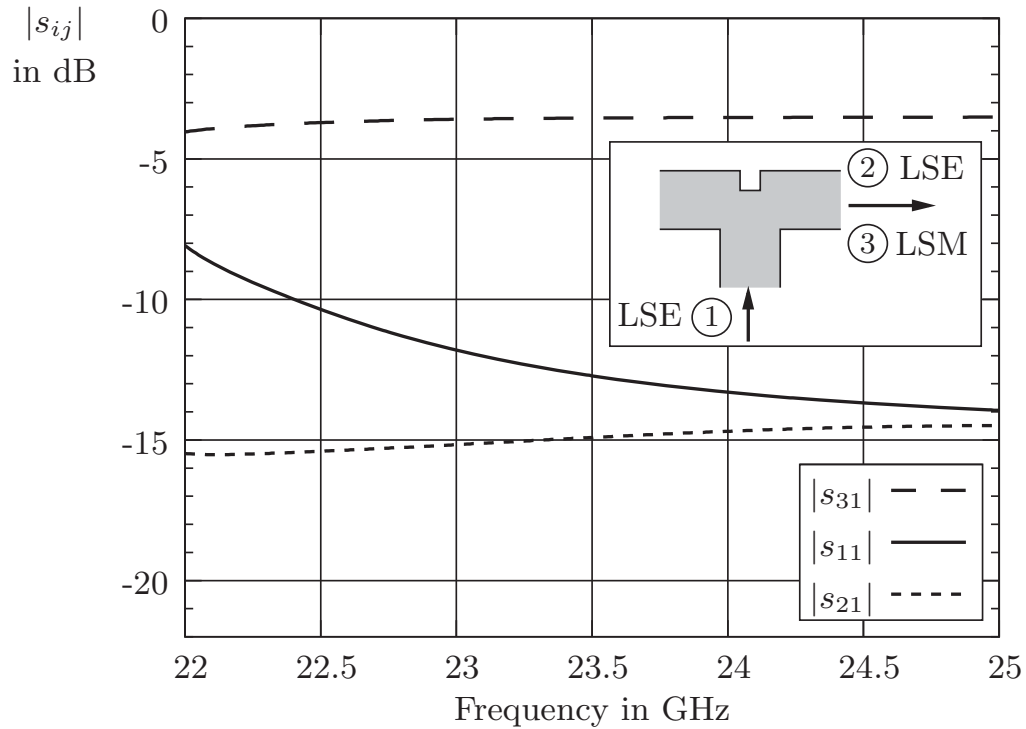


**Fig. 4.32:** Simulated S-parameters of the dual mode T-junction excited with the  $LSE_{01}$  mode.

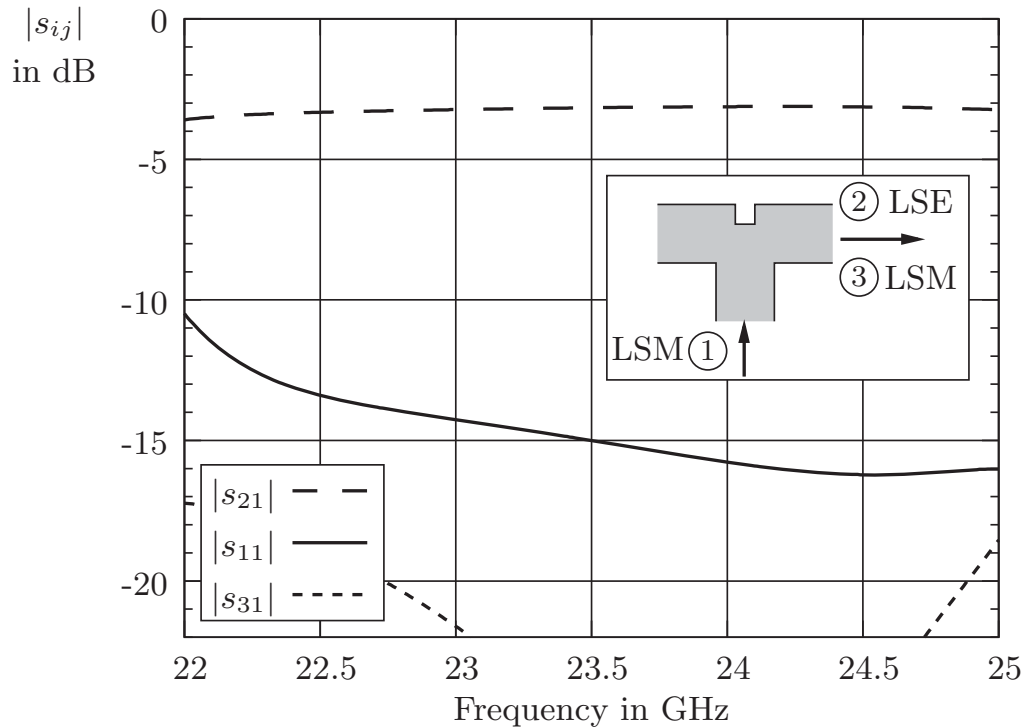


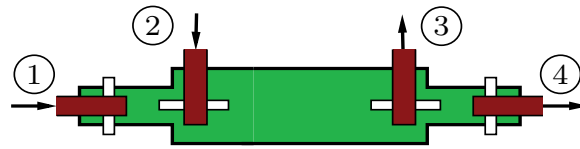
**Fig. 4.33:** Simulated S-parameters of the dual mode T-junction excited with the  $LSM_{01}$  mode.

## 4.2.2 Measurements of Dual Mode NRD-guide Test Circuits

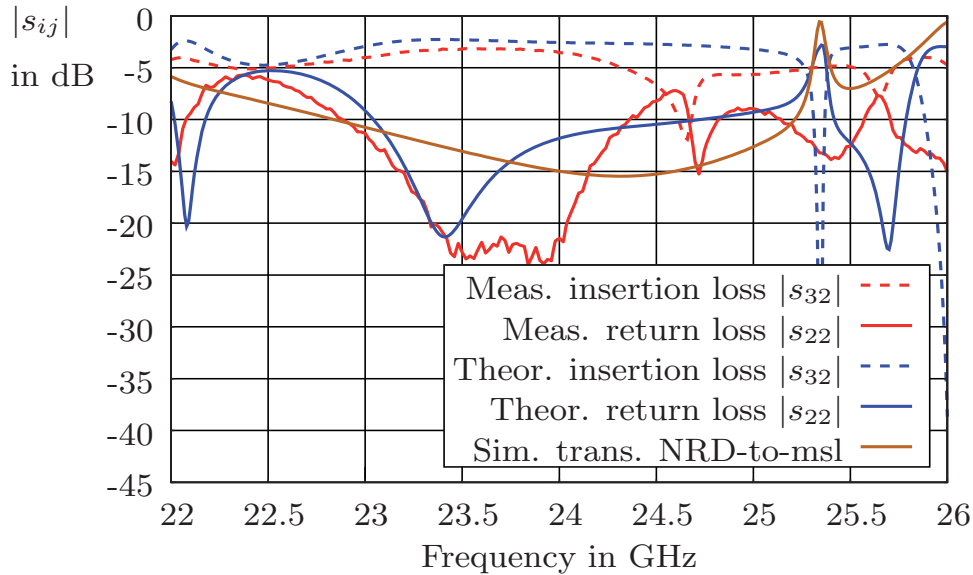
### 4.2.2.1 Test Circuit for Dual Mode Excitation

In order to prove the functionality of the dual mode feeding of the antenna, the transitions and T-junctions described in Sec. 4.2.1 have been implemented in a back-to-back arrangement with 13.2 mm distance. The simulated S-parameters of the single components have been combined analytically using the propagation properties and length of the NRD-guide section between the reference planes of the respective subcircuits. The resulting S-parameters serve as a reference in the following comparison to the measurement results of the back-to-back arrangement.

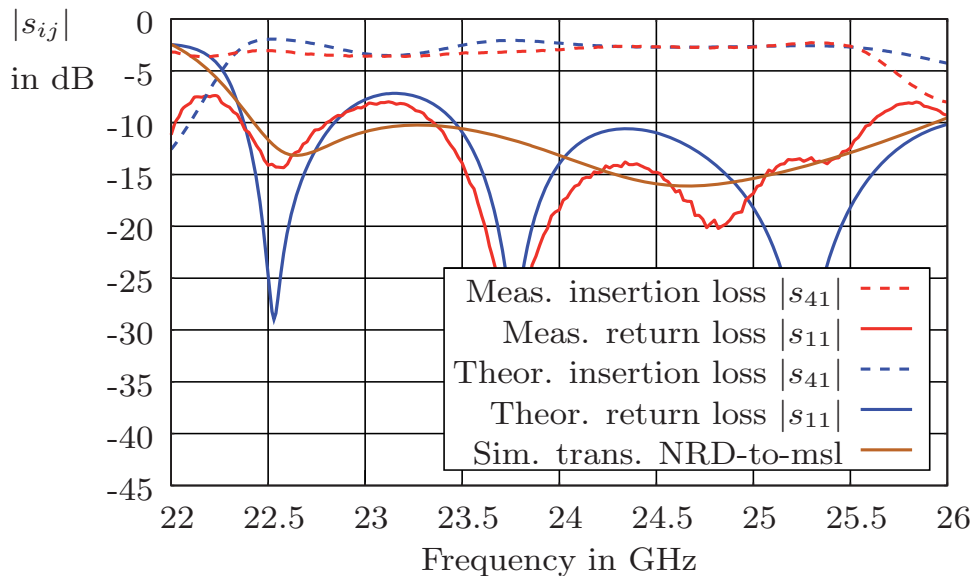
The first circuit analyzed accordingly is the back-to-back arrangement depicted in Fig. 4.34a consisting of two transitions from microstrip line to NRD-guide for dual mode excitation. In Fig. 4.34 the solid brown curves represent the simulated return loss of a single transition NRD-guide to microstrip line as given in Fig. 4.26a and Fig. 4.28a, for excitation with the  $LSE_{01}$  mode and with the  $LSM_{01}$  mode, respectively. The blue curves represent the S-parameters resulting from the back-to-back combination of the S-parameters from the simulation of the single transitions here referred to as theoretical S-parameters. The red curves display the measured S-parameters of the back-to-back arrangement. For the excitation with the  $LSM_{01}$  mode from 22 GHz to 23.5 GHz the theoretical S-parameters (blue curves in Fig. 4.34b) are in excellent agreement with the measured S-parameters (red curves). From 23.5 GHz to 24 GHz the mismatch of a single transition is not correctly anticipated by the simulation, and thus multiple reflections between the slot couplings of the two transitions result in a different course of the return loss (solid red and blue curves). A transmission zero in the measured transmission coefficient (sharp drop of the dotted red curve at 24.7 GHz) indicates the cutoff-frequency of the  $LSM_{01}$  mode in the NRD-guide section with reduced width  $w_{NRD}=3$  mm. Instead of being completely reflected, the  $LSM_{01}$  mode wave leaks into the NRD-guide section with reduced width, is partly attenuated, partly reflected, and causes strong mismatch at the coupling slot. According to the simulation the cutoff-frequency is located at 25.3 GHz (sharp drop of the dotted blue curve). This indicates that in fact the electrical and mechanical properties of the materials are different to the assumed values.



(a) Measurement setup.



(b) Results for excitation with the LSM<sub>01</sub> mode.



(c) Results for excitation with the LSE<sub>01</sub> mode.

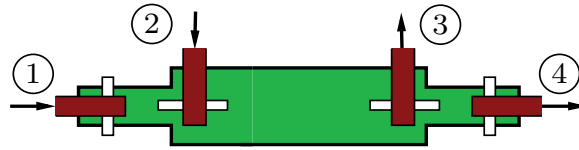
**Fig. 4.34:** Measured (red) versus theoretical (blue) S-parameters of the dual mode back-to-back transition microstrip line to NRD-guide to microstrip line (dotted: insertion loss; solid: return loss), and simulated return loss of a single transition NRD-guide to microstrip line (solid brown), simulations assuming  $\epsilon_{r,tape}=2$  and  $h_{tape}=50\ \mu\text{m}$ .

For the excitation with the  $\text{LSE}_{01}$  mode from 22.4 GHz to 25.5 GHz the theoretical S-parameters (blue curves in Fig. 4.34c) are in good agreement with the measured S-parameters (red curves). Below 22.4 GHz the theoretical transmission coefficient shows a steep slope according to the limited return loss of the single transition indicated by the brown curve. The measurement does not confirm this mismatch, the measured transmission coefficient is nearly constant with frequency. Above 25.5 GHz the measured transmission coefficient drops with a steep slope according to the excitation of higher order modes, while the theoretical transmission coefficient stays nearly constant with frequency. The last two observations again indicate that the assumptions concerning the properties of the materials used in the NRD-guide implementation are not exact and have to be reviewed.

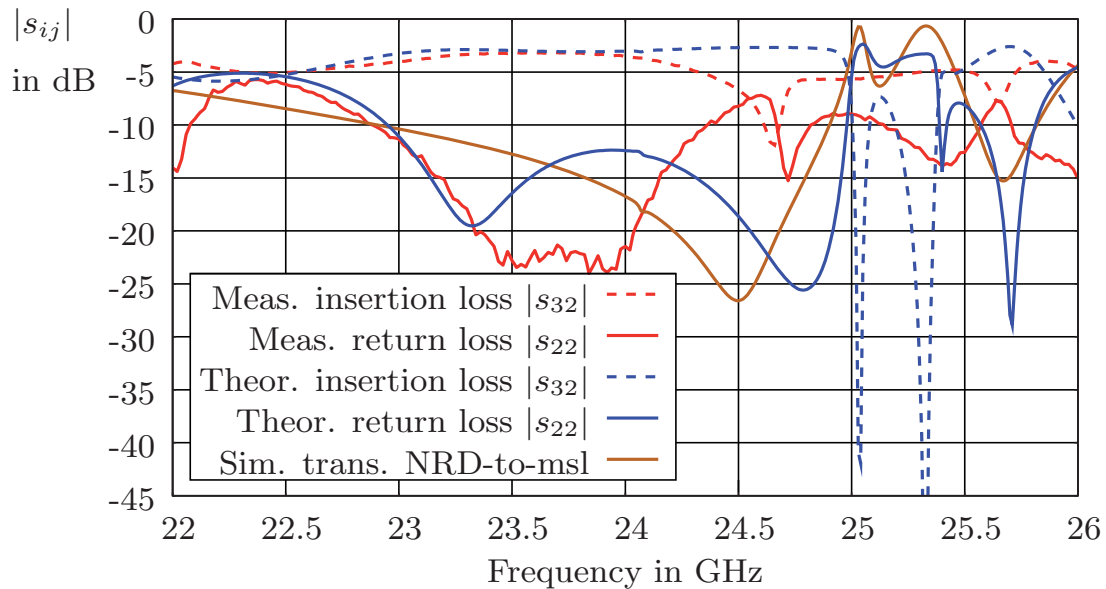
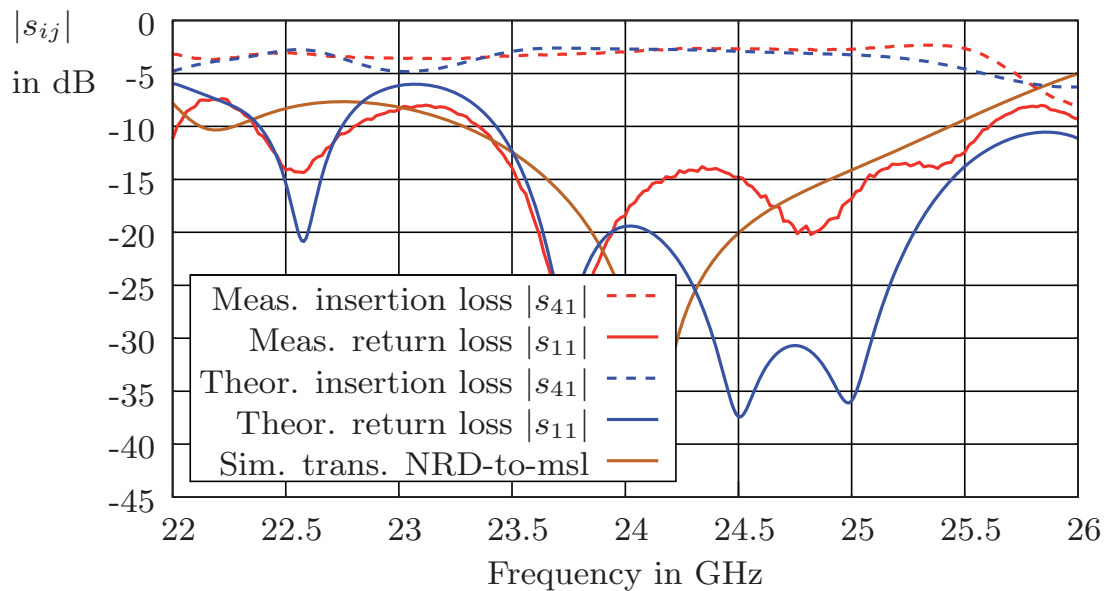
The electrical properties of the dielectric material TMM-6 have been determined by a 2-port characterization of a rectangular waveguide section filled with this material. The height and width of the TMM-6 parts are controlled very well during the milling process and confirmed by measurements. On the other hand, there was only little information about the electrical and mechanical properties of the bonding sheet. Due to the manufacturer the thickness is  $50\ \mu\text{m}$ , but in fact the sheet is soft and thus the thickness can not be controlled very well during production. Another effect related to the softness of the bonding sheet, is that after the assembly of the distinct layers the bonding sheet extends again, when the pressure of the gluing process is released. The dielectric constant of the bonding sheet can not be directly measured due to the consistency of the material.

In conclusion, there is a great inaccuracy due to the bonding sheet. According to a parameter study both thickness and dielectric constant of the bonding sheet have a strong impact on the propagation constant of the fundamental modes as well as on the cutoff-frequency of the higher order modes. Thus the properties of the bonding sheet have been optimized to fit the simulated cutoff-frequency to the cutoff-frequency observed with the measurement results leading to  $\varepsilon_{r,\text{tape}}=5$  and  $h_{\text{tape}}=80\ \mu\text{m}$ . Simulations of the transition from NRD-guide to microstrip line have been repeated assuming the corrected properties of the bonding sheet. In the comparison of the measured S-parameters versus the theoretical S-parameters based on the new simulations in Fig. 4.35b, the frequency of the transmission zero with 25 GHz comes closer to but is still higher than the 24.7 GHz observed with the measurement. This indicates that  $\varepsilon_{r,\text{tape}}$  is even higher than 5 and that due to the softness of the material  $h_{\text{tape}}$  should be assumed to be greater than  $80\ \mu\text{m}$ .





(a) Measurement setup.


 (b) Results for excitation with the  $LSM_{01}$  mode.

 (c) Results for excitation with the  $LSE_{01}$  mode.

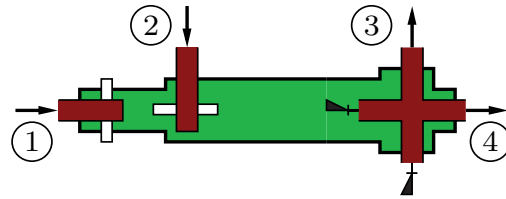
**Fig. 4.35:** Measured (red) versus theoretical (blue) S-parameters of the dual mode back-to-back transition microstrip line to NRD-guide to microstrip line (dotted: insertion loss; solid: return loss), and simulated return loss of a single transition NRD-guide to microstrip line (solid brown), simulations assuming  $\epsilon_{r,tape}=5$  and  $h_{tape}=80\ \mu\text{m}$ .

By increasing both thickness and permittivity of the bonding sheet the propagation constant of the  $LSE_{01}$  mode in the NRD-guide section with reduced width is increased, and with it the electrical length of the NRD-guide stub. As a consequence, the lower end of the frequency range of matching of the single transition excited with the  $LSE_{01}$  mode (brown curve in Fig. 4.35c) is now shifted down in frequency to nearly 22 GHz resulting in a better fit between measurement and theory between 22 GHz and 23.3 GHz. On the other hand, the level of return loss of the single transition is increased and results in a maximum mismatch of  $-8$  dB between 22.5 GHz and 23 GHz, which is not confirmed by the measured S-parameters. Some deviation between theoretical and measured return loss (solid red and blue curves) between 24 GHz and 25.5 GHz indicates that the slot coupling is not yet perfectly modeled with the assumptions on the electrical properties of the bonding sheet. Yet another cause of deviation is that the coupling slot in the common ground metallization is partly filled with the soft bonding sheet and partly filled with air. This has an influence on the resonance frequency of the coupling slot. In addition, deviations might also be an indication for irregularities in the assembly of the structure, e.g. an air gap between the TMM-6 material and the planar substrate, which particularly in the vicinity of the coupling slot has a major impact on the performance of the transition.

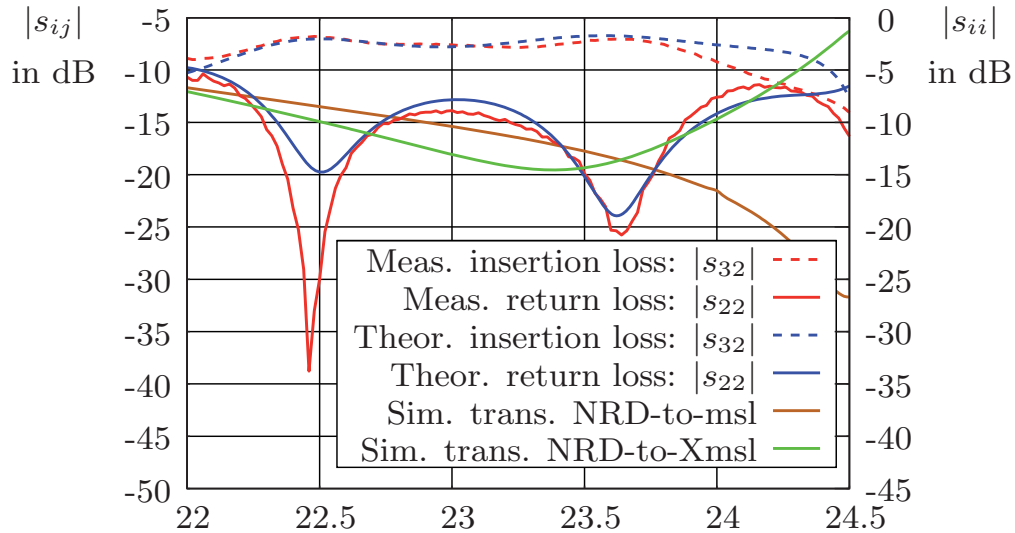
#### 4.2.2.2 Test Circuit for Dual Mode Transition to Crossed Microstrip Lines

The circuit depicted in Fig. 4.36a is a combination of the dual mode excitation shown in the inset of Fig. 4.28 and the transition from dual mode NRD-guide to crossed microstrip lines shown in the inset of Fig. 4.29. To avoid reflections at the ports which are not connected, absorber wedges are placed on top of those microstrip lines. They are made of the two-component absorber material C-RAM 369 by Cuming Microwave Corporation [65].

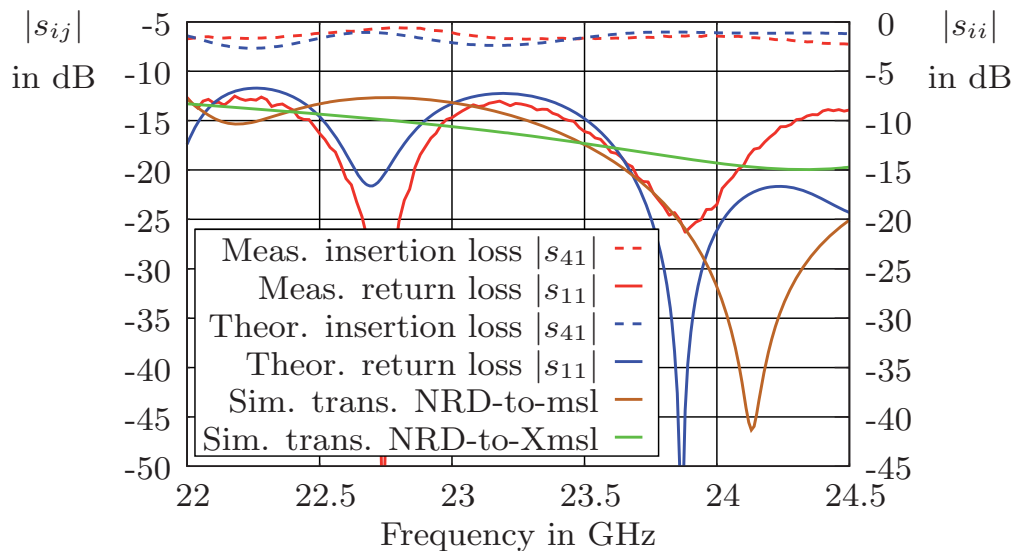
As expected, the bandwidth for an  $LSM_{01}$  mode excitation (Fig. 4.36b) suffers from the reduced cutoff-frequency of the  $LSE_{11}$  mode. Above 23.8 GHz the insertion loss strongly increases with frequency. For the  $LSE_{01}$  mode excitation (Fig. 4.36c) the circuit works well in the whole frequency range though there is some amplitude ripple due to minor reflections at the transitions. As expected by symmetry considerations, the measured isolation between the two channels is noncritical and is measured to below  $-25$  dB for both excitations in the whole band of operation.



(a) Measurement setup.



(b) Results for excitation with the  $LSM_{01}$  mode.



(c) Results for excitation with the  $LSE_{01}$  mode.

**Fig. 4.36:** Measured (red) versus theoretical (blue) S-parameters of the dual mode back-to-back transition microstrip line to NRD-guide to crossed microstrip lines (dotted: insertion loss, left  $y$ -axis; solid: return loss, right  $y$ -axis), simulated return loss of a single transition NRD-guide to microstrip line (solid brown), and simulated return loss of a single transition NRD-guide to crossed microstrip lines (solid green).

### 4.2.2.3 Test Circuit for Dual Mode NRD-guide T-junction

In order to validate the proper operation of the dual mode T-junction, the circuit described in Fig. 4.37 has been fabricated and measured.

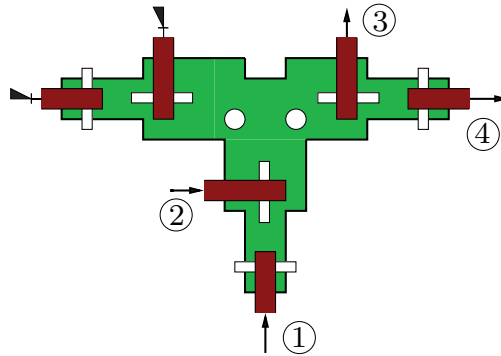
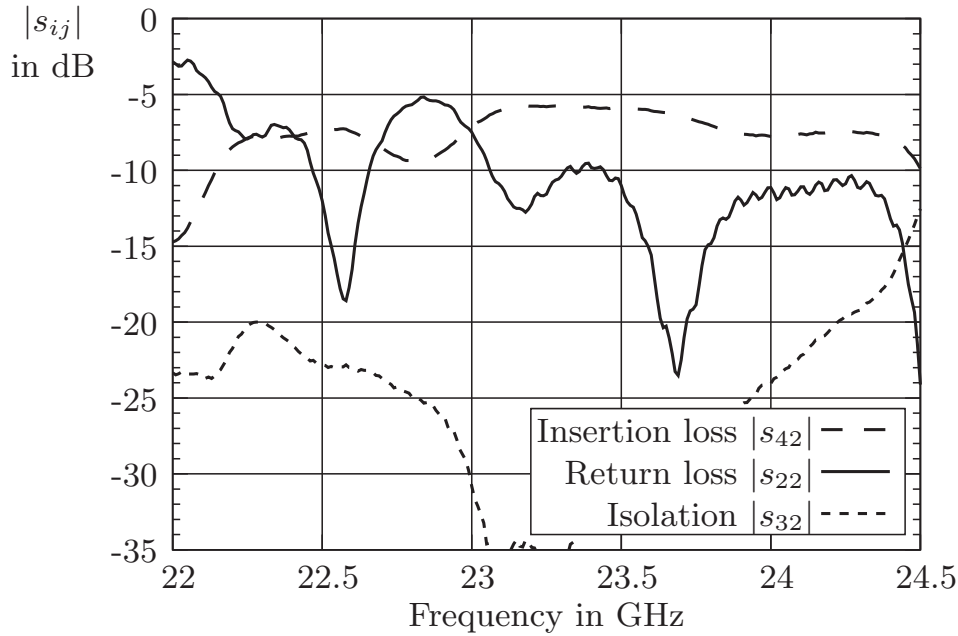


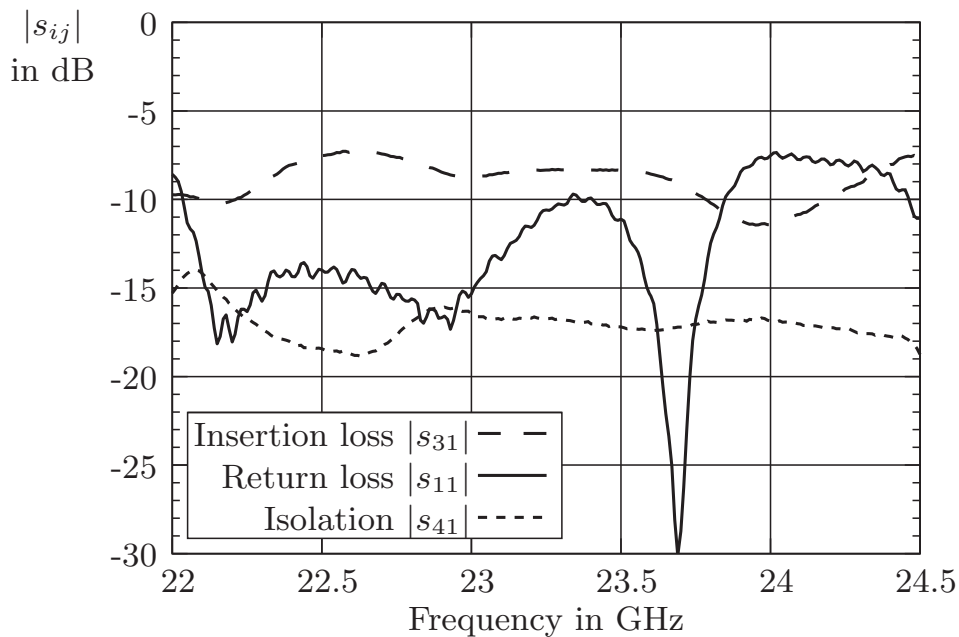
**Fig. 4.37:** Measurement setup of the dual mode T-junction.

Again, absorber wedges have been placed on the microstrip lines to avoid reflections at the ports which are not connected. The analysis of the measured S-parameters is difficult as it includes effects of five different components: the three transitions from NRD-guide to microstrip line ( $LSM_{01}$  mode and  $LSE_{01}$  mode), the dual mode T-junction, and the mismatch of the absorber wedges. In the results for the excitation with the  $LSM_{01}$  mode shown in Fig. 4.38a the bandwidth limitation is in agreement with the bandwidth limitation of the single transition from the microstrip line to the NRD-guide at the input branch of the T-junction. Below 23 GHz the strong mismatch of the single transition causes multiple reflections with the mismatch of the T-junction and thus a strong amplitude ripple on the transmission coefficient. Above 23.8 GHz the insertion loss is increased due to the reduced cutoff-frequency of the  $LSM_{01}$  mode in the NRD-guide section with reduced width  $w_{NRD}=3$  mm and agrees well with the increased insertion loss in the measurement results of the back-to-back arrangement of two single transitions in Fig. 4.35b. In Fig. 4.38b the insertion loss for an excitation with the  $LSE_{01}$  mode on the input branch of the T-junction is lowest between 22.4 GHz and 22.8 GHz, where also the return loss is best. According to the simulation results in Fig. 4.32 and Fig. 4.35, the circuit should work best between 23.5 GHz and 24.5 GHz, because this is the frequency range where all subcircuits show the highest return loss. The frequency shift between theory and measurement can be only explained by inaccuracies in the assembly of the circuit, e.g. air gaps between the dielectric rod and the ground metallization of the microstrip line and tolerances in the position of the coupling slots. In coincidence with the simulations the crosstalk between the fundamental modes for an excitation with the  $LSE_{01}$  mode at the input branch is nearly constant with frequency at a level of  $-16$  dB. For an excitation with the  $LSM_{01}$  mode at

the input branch the cross talk in general is much lower and shows a deep notch between 22.8 GHz and 24 GHz.



(a) Results for excitation with the LSM<sub>01</sub> mode.



(b) Results for excitation with the LSE<sub>01</sub> mode.

**Fig. 4.38:** Measured S-parameters of the dual mode T-junction.

### 4.2.3 Measurements of the Linear Array of $2 \times 2$ Sub Arrays

Using the components described before, an antenna array consisting of two  $2 \times 2$  sub arrays has been implemented (Fig. 4.20, page 80). A photograph of the antenna array is given in Fig. 4.39. For a quick and easy handling the antenna has been placed on a test fixture with a coaxial SMA connector.

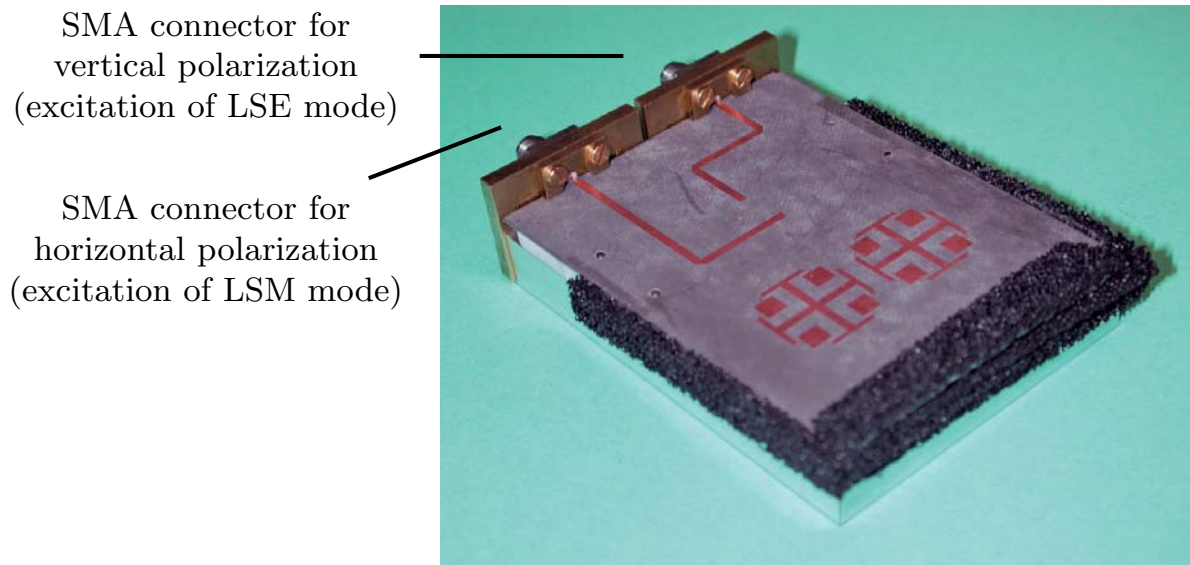


**Fig. 4.39:** Photo of the dual polarization antenna consisting of two  $2 \times 2$  sub arrays.

The radiation diagrams of the antenna array have been measured at 22.7 GHz in the E-plane and in the H-plane for both excitations (Figs. 4.40 and 4.41). The notation with  $x$ - $y$ - $z$  coordinates is according to the definition in Fig. 4.20.

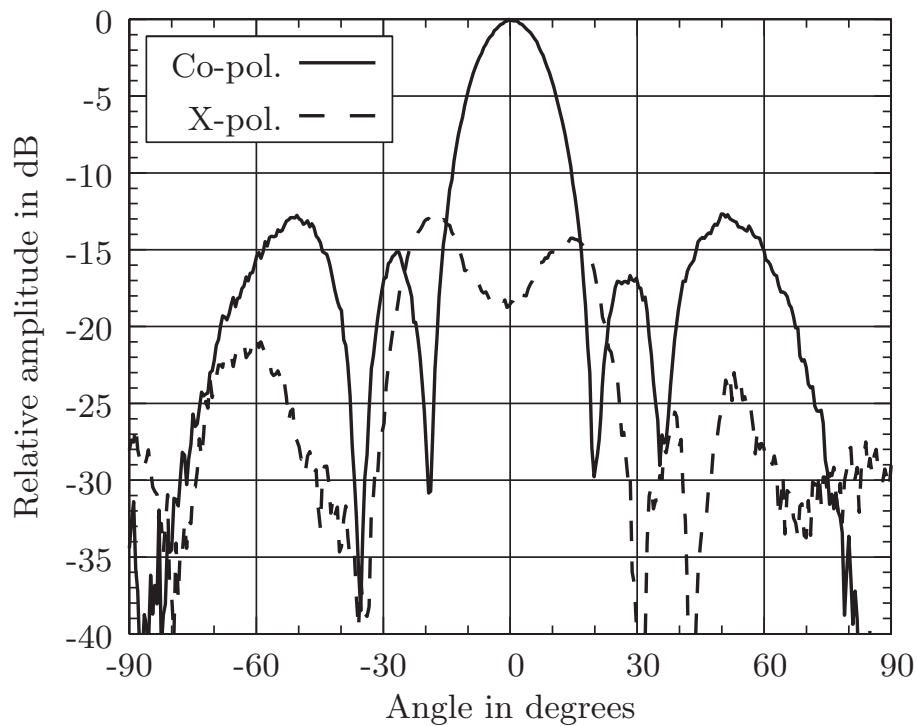
When the array is excited with the  $LSE_{01}$  mode, the first side lobes in the  $x$ - $z$ -plane (H-plane) are below  $-15$  dB and the second side lobes are below  $-12$  dB. Cross polarization is  $-18$  dB at boresight and reaches a peak value of  $-13$  dB at the notches of the main lobe where cross polarization is usually not as critical. One part of the high level of cross polarization can be attributed to the reduced mode purity at the output branches of the NRD-guide T-junctions when the input branch is excited with the  $LSE_{01}$  mode (dotted curve in Fig. 4.32). But having in mind the symmetry of the assembly with respect to the  $y$ -axis, any radiation due to the spurious mode transfer from the  $LSE_{01}$  mode at the input branch to the  $LSE_{01}$  mode at the output branches must result in an anti-phase excitation of the radiating square patch elements with opposite  $x$ -components

of the electric field. In the far field at boresight, the electric field would cancel resulting in a perfect cancellation of the cross polarization. As a consequence the  $-18$  dB cross polarization at boresight and also part of the increased cross polarization in other directions must be caused by radiation of the feed. Another possible cause for the increased level of cross polarization at boresight is a slight angular missalignment between the reference antenna and the dual polarization antenna under test.

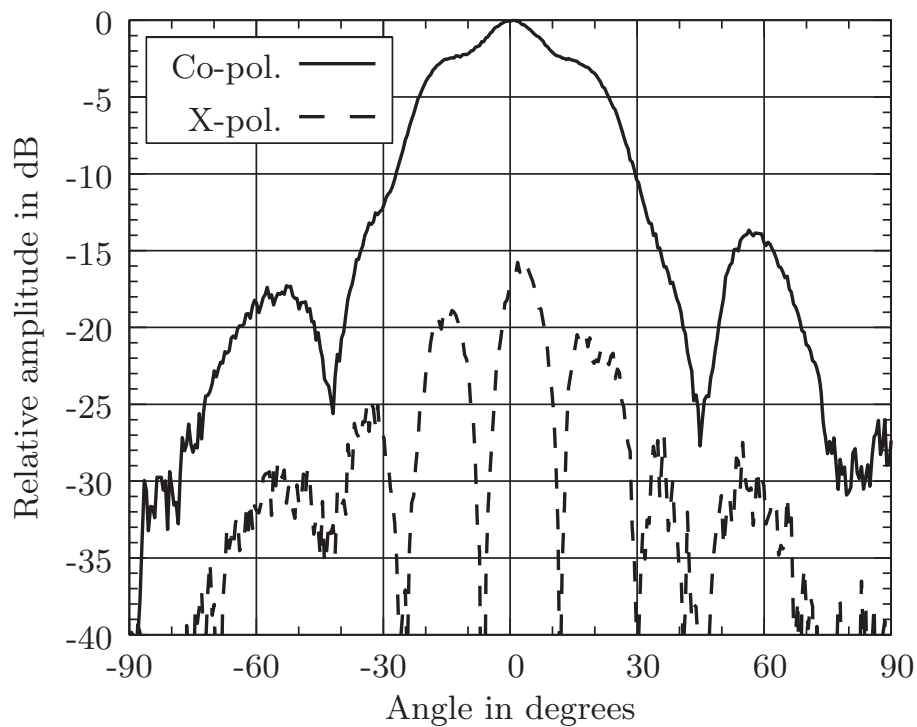
In the  $y$ - $z$ -plane (E-plane) the radiation diagram shows an amplitude ripple in the main lobe (Fig. 4.40b). This distortion is also due to spurious radiation of the feeding microstrip lines. The degree of perturbation of the radiation diagram strongly depends on the location of the sources of spurious radiation (mainly radiation of the open ended microstrip stubs and the coupling slots of the transitions from the feeding microstrip line to the NRD-guide), and on its distance to the axis of rotation, as discussed in Sec. 4.1.4. For a rotation in the  $x$ - $z$ -plane (Figs. 4.40a and 4.41a) the transitions from the feeding microstrip line to the NRD-guide are laying on the axis of rotation and thus spurious radiation has no effect on the shape of the radiation diagram. The spurious radiation is also the root cause for the asymmetry of the radiation diagram in the  $y$ - $z$ -plane. The level of the side lobe at  $-60^\circ$  is  $-17$  dB while the side lobe at  $+60^\circ$  is  $-14$  dB.

When the array is excited with the  $\text{LSM}_{01}$  mode, the first side lobes in the  $x$ - $z$ -plane (E-plane, Fig. 4.41a) are below  $-11$  dB and the second side lobe at  $-75^\circ$  is at  $-24$  dB. Again spurious radiation of the feed is the cause for a slight asymmetry of the radiation diagram. The cross polarization is in accordance with the simulation results of the NRD-guide T-junction excited with the  $\text{LSM}_{01}$  mode (Fig. 4.33) lower than when the array is excited with the  $\text{LSE}_{01}$  mode. At boresight cross polarization is below  $-20$  dB and reaches a peak value of  $-17$  dB at the edge of the main lobe.

In the  $y$ - $z$ -plane (H-plane) the radiation diagram is asymmetrical with the side lobe at  $-60^\circ$  with a level of  $-17$  dB and the side lobe at  $+60^\circ$  with a level of  $-12$  dB. In contrast to the excitation with the  $\text{LSE}_{01}$  mode there is virtually no amplitude ripple in the main lobe. The reason is that the source of spurious radiation, i.e. the transition from microstrip feeding to the NRD-guide for excitation with the  $\text{LSM}_{01}$  mode is much closer to the radiating square patch elements and thus the impact on the radiation diagram is shifted towards the side lobes, resulting in the asymmetry concerning their amplitude level.



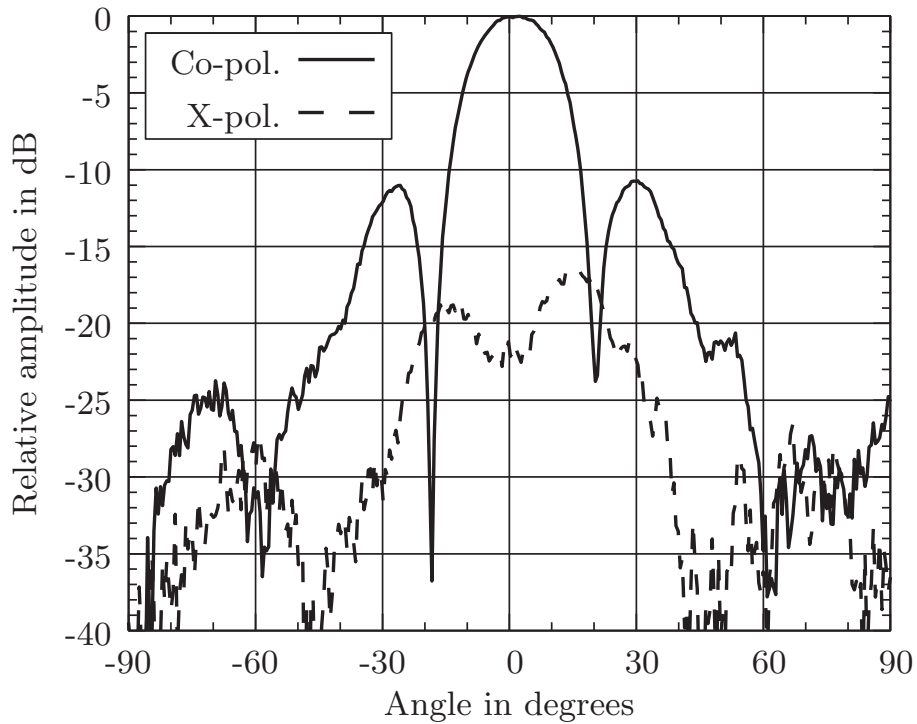
(a) Radiation diagrams in the  $x$ - $z$ -plane (H-plane).



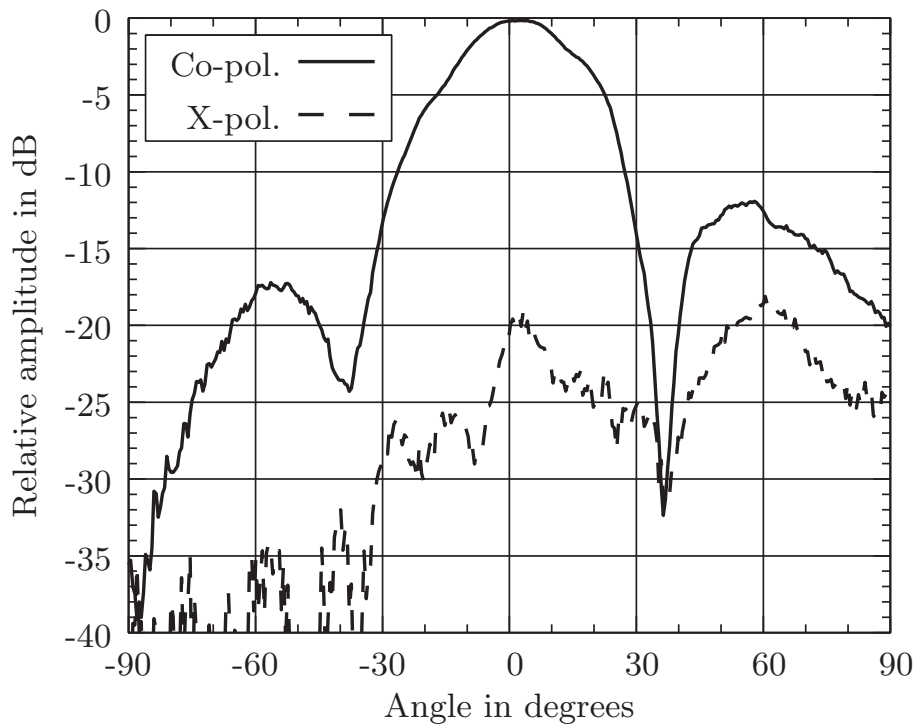
(b) Radiation diagrams in the  $y$ - $z$ -plane (E-plane).

**Fig. 4.40:** Measured radiation diagrams of the antenna array excited with the  $LSE_{01}$  mode.





(a) Radiation diagrams in the  $x$ - $z$ -plane (E-plane).



(b) Radiation diagrams in the  $y$ - $z$ -plane (H-plane).

**Fig. 4.41:** Measured radiation diagrams of the antenna array excited with the  $LSM_{01}$  mode.

**Table 4.2:** Measured half power beam width of the antenna array

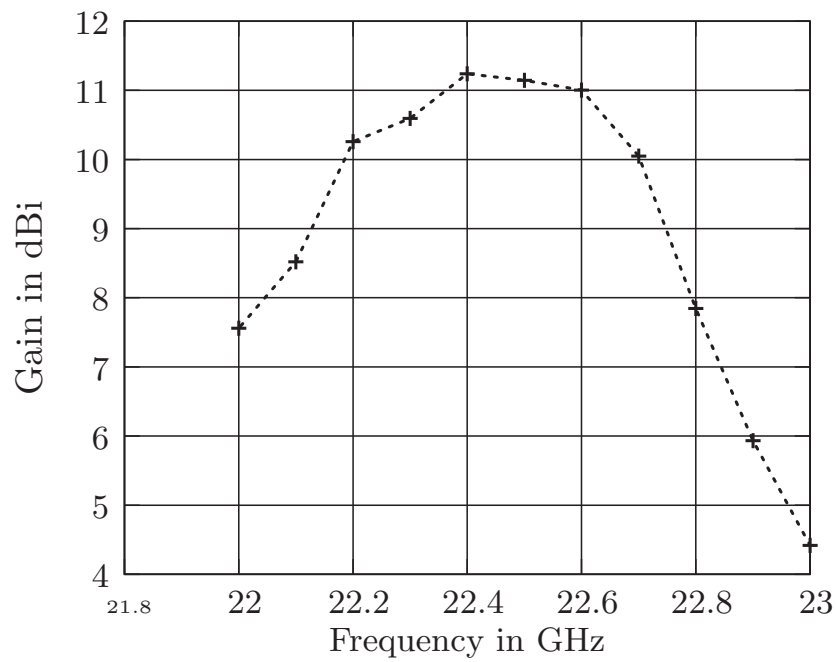
	$x$ - $z$ -plane	$y$ - $z$ -plane
LSE mode excitation	17°	35°
LSM mode excitation	21°	31°

Table 4.2 summarizes the measured half power beam widths of the antenna array for both excitations.

Much of the distortion in the radiation diagrams is attributed to the spurious emissions of the microstrip feedings and the transitions to the NRD-guide. The results can be improved considerably by removing those transitions from the front side. One alternative could be to replace the back side aluminum plate by an other planar RF substrate with the two transitions integrated. A metal shielding could be used to prevent radiation from back side. Another option is the use of co-layered interconnects between the NRD-guide corporate feeding network and planar circuits as proposed in [66]. However, this approach introduces another asymmetry along the height of the NRD-guide and is therefore susceptible to excitation of parallel plate waves and leakage [67]. Another challenge is the implementation of the dual mode transitions with the co-layered topology.

The antenna gain of the dual polarization antenna array when excited with the LSE<sub>01</sub> mode was measured over a frequency range from 22 GHz to 23 GHz as indicated in Fig. 4.42. The peak value is 11.24 dBi at 22.4 GHz including microstrip line feed loss (0.88 dB) and mismatch loss (0.12 dB). The half power bandwidth is 0.8 GHz, i.e. 3.6% fractional bandwidth. Exclusive of the above losses, the gain is approximately 12.2 dBi. The theoretical directivity for this array based on the aperture area is 15.1 dBi at 22.4 GHz. Thus the array and feed network efficiency is approximately 51% (measured gain minus ideal gain).

When excited with the LSM<sub>01</sub> mode, the maximum measured gain of this array is 10.2 dBi at 22.7 GHz including microstrip line feed loss (1.1 dB) and mismatch loss (0.82 dB). Exclusive of the above losses, the gain is approximately 12.1 dBi. The theoretical ideal gain for this array based on the aperture area is 15.3 dBi at 22.7 GHz. Thus the array and feed network efficiency is approximately 49% (measured gain minus ideal gain). The remaining losses are partly due to spurious emissions of the microstrip feeding, partly due to ohmic and dielectric losses



**Fig. 4.42:** Measured gain of the antenna array excited with the  $LSE_{01}$  mode.

in the NRD-guide feeding (approximately 1.1 dB for  $LSM_{01}$  mode excitation, 1.4 dB for  $LSE_{01}$  mode excitation).



# 5 A Low Cost Low Profile Scanning Receiver Array

## 5.1 Introduction

### 5.1.1 Motivation for Automotive Sensors

In recent years car manufacturers and their suppliers have shown an increasing interest in safety and comfort applications for the automotive sector. These applications ask for environmental sensors which scan the surrounding of the car and provide information about obstacles to a micro-controller or digital signal processing unit. With more conventional applications, e.g. for navigation and control in the aeronautical field, reliability and performance have highest priority, and cost typically is not the main issue. But for automotive applications, cost usually decides on success or failure of one approach or the other. Other, general requirements are robustness against severe weather conditions, high reliability, long lifetime, fast scanning capability, and agility.

### 5.1.2 Comparison of Sensor Types

While some of these requirements can be handled quite well by approaches based on light detection and ranging (LIDAR) [68, 69], also referred to as laser scanners, ultrasonic sensors, infrared devices and video cameras, those approaches tend to be sensitive to bad weather conditions like fog, snow, heavy rain and spray water caused by cars driving in front. In addition, video cameras do not work well in darkness. Collision warning and driver assistant comfort systems based on radio detection and ranging (RADAR) are of special interest because they work well in all weather conditions [70] and provide detection ranges from within a few centimeters of the vehicle to several hundred meters. Another advantage of radar sensors is the capability to directly measure relative radial speed of one

or many targets by analyzing the Doppler frequency offset of the received versus the transmitted signal.

### 5.1.3 Applications of Radar Sensors

Applications of radar sensors include extended versions of parking assistant, e.g. fully automated parallel parking, detection and tracking of obstacles or pedestrians in front of the vehicle, speed adaption to the specific traffic situation known as adaptive cruise control (ACC), stop and go functionality or in a more complex and complete manner autonomous intelligent cruise control (AICC), and pre-crash safety functionalities like seat-belt tighteners, preconditioning of head restraints or the activation of airbags for the driver and passengers as well as for pedestrians. Another application that is typically based on radar sensors yet not as well known is the lane change assistant (LCA) and blind spot surveillance [70, 71]. It permanently scans the adjacent lanes on expressways or other multilane highways and gives an acoustic or optical warning or even starts vibration of the steering wheel when the driver starts to change to the adjacent lane while another car is approaching on that lane from behind. Another similar example is the warning against vehicles which drive on adjacent lanes in front and suddenly start to cut into the lane used by the vehicle equipped with the sensor.

### 5.1.4 System Requirements

The afore mentioned applications have different implications on the requirements for the sensors. Forward looking sensors for AICC systems require a long range radar (LRR) sensor with highest gain for good detection capability over a large range up to 150 meters, sharpest antenna beam width of  $2^\circ$  to  $3^\circ$  in azimuth in order to distinguish targets on different lanes far ahead, and measurement of relative radial velocity. Usually there is no need for a wide angular view and a  $\pm 7^\circ$  total scanning range is enough for AICC to follow smooth curves on expressways.

Short range radar (SRR) systems such as detection of near-by rear and side obstacles, and early warning of side crash impact are performed typically in the range of a few meters and thus beamwidth and gain are not that important but the call for observation of the full surrounding of the vehicle requires a large

angular view, possibly 180°. High angular resolution is required in order to distinguish closely spaced targets or to perform target or obstacle recognition for detection of road boundaries and early warning of side crash impact. Good angular resolution can be achieved or with antennas with beam switching [72] or beam steering capability or with a set of different sensors applying the multilateration approach [73] or the monopulse approach [72]. Both multilateration and monopulse tend to be ambiguous for several targets being located at similar distances. With the monopulse approach, tolerances in the alignment of the antennas limit the angular point accuracy. And some part of the dynamic range is used for angular resolution which reduces the maximum range for a given antenna aperture. Multilateration only gives good angular point accuracy for short range. Beam steerable antennas can provide both, high angular resolution over a large scan range and maximum dynamic range.

But not only for sensor applications for the car industry, antennas with electronic scanning facilities are becoming increasingly important. Also in communication systems, e.g. mobile phone networks like Global System for Mobile Communications (GSM) and Universal Mobile Telecommunications System (UMTS), wireless local area networks (W-LAN), and wireless multiple access (WiMAX) systems of the IEEE 802.11-xx standard, beam steerable and smart antennas provide a wide field of improvements.

Another potential field of application are the ground and the satellite terminals of low orbit satellite (LEO) systems. One example is the Iridium satellite network [74, 75].

### **5.1.5 Beam Switching and Steering Approaches with Increased Angular Resolution**

In the past years several beam steerable antenna approaches have been investigated with the goal to increase both angular resolution and scan range (angular view) enabling at the same time fast scan sweeps. In the beginning the antenna beams of surveillance radar and communication systems have been mechanically rotated or electronically controlled by phased arrays using phase shifters. Usually mechanical scanning systems do not meet the requirement of the aforementioned sensor and communication systems for fast scanning. Phased array antennas or Electronically Steerable Arrays (ESA) using electronic phase shifters [76] offer distinct advantages over mechanically rotated antennas. A nearly flat setup is possible and electronic beam scanning provides an inertia-less steering

system with superior life expectancy and allowing faster scanning. But those approaches are by far too complex and with a per module cost of approximately US\$1000 they are also way too expensive to be used for automotive applications. In a first approach to increase the scanning agility of sensors based on mechanical steering, the much smaller and lighter reflector was moved instead of the complete antenna. One example to increase the scan rate of antennas based on mechanical steering is a high gain Cassegrain-type antenna with low side lobes, enabling e.g. the detection of a motorcycle in one lane at the same range as a heavy truck in another lane, that has been made steerable by mechanically rotating the main reflector [77]. The same approach has been applied to a low profile folded reflect array antenna [78] consisting of a fixed planar polarizing grid and a planar twisting and focusing reflect array, the latter being tilted without moving the whole antenna. The downside of all mechanical scanning approaches, even though substantially reduced by rotating only the lighter reflector, is the limitation in angular scan rate also referred to as update rate according to inertia. Other issues of mechanical scanning are long term precision and life time.

An alternative solution has been found in beam switching. One solution to the multibeam approach is to apply several feeds to one reflector antenna [10], another solution is to use several primary antennas to one dielectric lens [72]. A similar approach [79] makes use of a beam forming network, in this case a Rotman lens [80, 81] based on microstrip technology to feed several rows of serially fed microstrip patch antenna arrays. But all those approaches require a fast and low loss switching network that operates reliably over a long period of time of 10 years and more with about  $10^9$  cycles per year. A low loss solution at mm-waves can be a non-contact cylindrical NRD-guide switch [82]. A polyhedral cylinder, in this case with a square cross section, with four outer surfaces each consisting of one NRD-guide which serves as a dielectric resonator. The four dielectric resonators are located at different lateral offsets to the focus of a dielectric lens. Hence rotation of the polyhedral cylinder makes the antenna switch between four beams. The main advantage of this approach is a very low switch insertion loss with less than 0.1 dB at 60 GHz. The main disadvantages are an increased production cost due to a complicated mechanical arrangement, a limited switching speed, and the potential for a beam offset in elevation caused by limited accuracy in the rotation of the polyhedral cylinder.

Leaky wave antennas are well known to enable high gain and low loss antennas with beam steering capability [83–85]. But as with other types of traveling wave antennas, they show limitations concerning the scan range, especially in the broadside direction. Leaky-wave antennas can be grouped in two kinds, the uniform type with a uniform aperture along the leaky waveguide structure and



the periodic type which is periodically modulated along the wave guiding structure. Leaky-wave antennas of the uniform type can only radiate in the forward quadrant but not in the backward quadrant. Also, they cannot approach broadside too closely, and depending on geometry they are limited towards end fire, too. Leaky-wave antennas of the periodic type can scan from backward end-fire through broadside into part of the forward quadrant, except for a narrow region around broadside called *open stop band*, where reflections from all perturbations in the wave guiding structure superimpose in-phase at the input port resulting in a large voltage standing wave ratio (VSWR) and a typical dip in gain for broadside radiation [85]. There are techniques [86] which permit periodic leaky wave antennas to scan through broadside with nearly constant gain by using pairs of radiating elements with a spacing of  $\lambda_{g0}/4$ , where  $\lambda_{g0}$  is the guide wavelength at broadside frequency. This configuration allows the reflected wave from one radiating element to be canceled by that of the other radiating element. But typically those techniques also degrade the performance of the antenna with respect to scan range, side lobe level, and radiation efficiency. Another general issue of the periodic leaky wave antenna is the dependency of beamwidth on frequency, and an even more critical problem is the need for variation of the radiation frequency (RF) to control the scan angle. A frequency sweep of the RF typically has a negative impact on system parameters like e.g. the degradation of range resolution in a frequency modulated continuous wave (FM/CW) radar sensor. Therefore some investigations have been driven by the goal to implement leaky-wave antennas that work at a fixed RF. PIN diodes have been used to electronically control the propagation characteristics of a switchable leaky wave antenna in [87] and thus switch the main beam between two states,  $+13^\circ$  and  $-22^\circ$ , but that approach does not work for a continuous sweep from backward to forward quadrant. Another approach that enables leaky-wave antennas for beam scanning at fixed RF has been found in the beam scan controlled by the grating of the wave guiding structure. With a mechanically movable grating film with variable element-to-element spacings [88], the scan angle could be modified directly over a wide scanning range  $\pm 50^\circ$  at 35 GHz or 40 GHz. In [89] a similar approach has been presented using a spinning grating for operation at 94 GHz. But as with the frequency controlled leaky-wave antennas, both approaches must circumvent the *open stop band* issue. Another drawback is according to the mechanical scanning that again limits the angular scan rate and causes potential problems of point-inaccuracy. And the spinning grating with parabolic reflectors is a rather bulky construction that can not easily be integrated in the car front. In order to simultaneously circumvent all three problems, that of *open stop band*, that of RF fixed scanning, and limitations due to movable parts and inertia, composite right/left-handed (CRLH) transmission lines have recently been investigated in detail applying both the periodic and

the uniform leaky-wave antenna approach. Earlier implementations [90–92] of a periodic leaky wave antenna were based on a multiplicity of lumped LC unit cells and resulted in a complicated design that does not lend itself to low cost mass production. A more recent approach [93] uses a uniform ferrite-loaded open waveguide structure with composite right/left-handed (CRLH) response. Thanks to a gapless nonzero group velocity transition between the left- and right-handed bands, this antenna overcomes the problem of the *open stop band* yet providing the possibility for scanning at a fixed frequency but by biasing. This method of creating a balanced structure is comparable to the method of reflection cancellation of the periodic type leaky-wave antenna. Although simulation results for this approach are very promising, the variation of antenna gain with scan angle with approximately 4 dB is still too high, and for increasing frequency in the microwave and mm-wave range the losses of the ferrite material become prohibitively large.

Another approach [94, 95] is a reflect array based on ferroelectric phase shifters. This approach eliminates feed losses by applying quasi optical feeding. But ferroelectric phase shifters exhibit relatively high RF losses of 3 dB to 4 dB at 24 GHz. One advantage though is continuous phase shift over DC bias voltage. But this is at the cost of very high supply voltages of typically 350 V, which makes the control circuitry complicated and error-prone.

Liquid crystal reflectarrays are an other interesting approach that showed beam steering capabilities in the mm-wave region at 35 GHz [96] and at 77 GHz [97]. Biasing voltage is typically limited to the range from 0 V to 25 V, and control circuitry can be easily implemented using common SMD components. Scanning range capability with  $-35^\circ$  to  $+25^\circ$  at 35 GHz and  $-10^\circ$  to  $+25^\circ$  at 77 GHz is quite good. But first implementations showed only poor side lobe level behavior as high as  $-4.2$  dB with the main beam at broadside and  $-6$  dB for the steered beams. The poor radiation pattern characteristic is mainly due to amplitude and phase errors of the reflector unit cells. The amplitude and phase errors are caused by losses in the unit cells which can be as high as 20 dB in the resonance region thus limiting the usable phase range of the complex reflection coefficient. As a result also the gain variation as a function of steering angle is very high and with 4 dB too high for practical applications.

In addition, in the last years there was a big interest in reducing cost and complexity of phased arrays and their key component the phase shifter. Microelectromechanical systems (MEMS) [76, 98] can be a low loss solution at microwave (0.5 dB per bit or 1.4 dB insertion loss for a 3-bit K-band phase shifter) and mm-wave frequencies (0.8 dB per bit and 0.9 dB per bit for a V-band and W-band phase shifter, respectively) for discrete phase shifts. Typical approaches include

switching between different delay lines and, for smaller phase increments, stub-loaded line phase shifters [79], with the latter being a constant phase type phase shifter that is inherently narrow-band and produces beam squint when used for phased arrays. RF MEMS phase shifters have been first reported in 1999 [99] and since then many circuits have been developed covering the frequency range from 8 GHz to 94 GHz [100, 101]. But the MEMS technology is still in a rather premature state and the lifetime of MEMS switches is of concern for long term applications especially for the high switching rates required for beam scanning antennas. The lifetime of today's MEMS phase shifters is in the range of several billion ( $10^9$ ) cycles. For automotive radar the required lifetime is in the range of 10 billion cycles assuming a scan rate of 20 Hz with eight antenna beams, i.e. a 3-bit phase shifter and accordingly higher for more beams, 4 hours operation per day over a 10 years period. So for automotive radar sensors as for ground terminals of satellite high-data-rate communication systems, the MEMS phase shifter technology starts to become an interesting alternative, but more tests are required to prove long term reliability. Moreover, to avoid charging of the insulator between the cantilever and the lower metal contact, the bias voltage is varied between positive and negative pulses. Thus, MEMS circuits consume negligible DC power, but require complicated bias control circuits.

In conclusion, non of the approaches described so far provides a one-fits-all solution to the applications given in Secs. 5.1.4 and 5.1.5 meeting all the requirements the most important of which are low profile, low loss, high gain, high angular resolution, fast scanning rates, wide angular view, long term reliability, and low cost. For those applications antennas with continuous electronic beam scanning are the best solution. In the higher frequency range, this typically is associated with increasing loss and cost using conventional phased array techniques. Moreover, phase shifters experience temperature-sensitivity, hysteresis and quantization errors, and are limited to the microsecond phase shifting time range [102]. A possible solution is the use of frequency scanned arrays, as it is demonstrated for automotive radar applications, e.g. in [103], where simple series-fed frequency-scan arrays are used for beam steering with no phase shifter components except for fixed delay lines. In [104] a wide scanning range was achieved with a frequency scanned antenna array using a suspended stripline negative index transmission line. In [105–107] alternative approaches have been presented using heterodyne principles with a frequency sweep in the local oscillator (LO) path. Thus, radio frequency (RF) can be kept constant, and available bandwidth can be fully exploited for other purposes. In order to keep the LO and, consequently, the intermediate frequency (IF) variation small, long delay lines between the tapping points of the LO feed line have been selected [108], leading to a rather bulky and costly setup as rectangular waveguide was cho-

sen for low loss behavior. The nonradiative dielectric (NRD) waveguide on the other hand is known to be a low loss waveguide especially for increased frequencies, while allowing for low profile and low cost applications [109]. Therefore, for this chapter a 19 GHz receiver array using an NRD-guide LO feed line was investigated.

## 5.2 Antenna Design

A block diagram of the scanning array is given in Fig. 5.1. The RF signal is received by an array of four microstrip antenna elements. Each antenna element is connected to a mixer. The LO signal is distributed via a serial NRD-guide feeding providing the frequency dependent phase shift for beam scanning. A bandpass topology of the tapping points ensures good matching and solves the *open stop band* problem. In the mixers the RF signals are down-converted to the IF band including the phase shift. The IF signals finally are combined in-phase by a four-to-one Wilkinson power combiner network. A stronger weighting of the inner two channels is used for reduction of the side lobe level and in order to compensate for the deviation of the power distribution along the LO feeding. The layout of the low cost low profile scanning array can be found in Appendix A.2, page 141.

An LO frequency variation of 2.0 GHz in the 22.8 GHz to 24.8 GHz range allows for a 28° scan. In order to have a wide scanning range while maintaining the circuit rather small, the LO frequency is chosen to be higher than the RF frequency (high-frequency injection). The receiver array consists of two layers. Antenna elements, mixers, filters and the IF power combination are implemented as planar structures on Ultralam 2000 ( $\epsilon_r=2.48$ , thickness=0.26 mm). The LO feeding network is made of an NRD-guide with Rogers TMM-6 ( $\epsilon_r=6$ ,  $\tan \delta(@24 \text{ GHz})=2.1 \cdot 10^{-3}$ ,  $w_{\text{NRD}}=6 \text{ mm}$ ,  $h_{\text{NRD}}=3.18 \text{ mm}$ ). The total height of the antenna is 3.5 mm only, plus the back sided aluminum plate.

The following sections describe first the design of all components, and detailed simulation and measurement results of those sub-circuits are given. Section 5.4 deals with the characterization and the performance of the complete receiver array. In Sec. 5.5 an alternative approach to the conventional NRD-guide feeding network is proposed, and simulation results are compared to the original feeding. This feeding provides a steeper phase increment with frequency and hence a

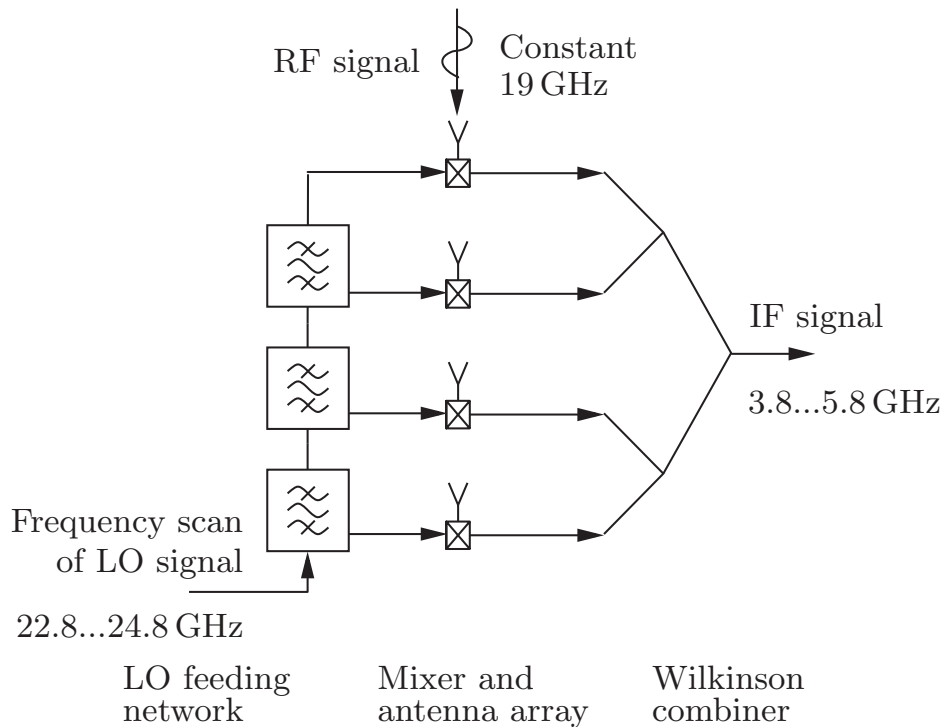


**Fig. 5.1:** Block diagram of the scanning array.

greater angular scan with less LO frequency variation.

## 5.3 Design and Simulations of the Components

### 5.3.1 Design and Simulations of Hybrid Couplers

The serial LO feeding consists of a simple straight line of an NRD-guide saving space compared to other approaches, and meandering of the feed line is not required. Coupling between the planar mixers and the feeding is done by a slot in the common ground metallization. The distance between the tapping points, i.e. the coupling slots, is set by the condition that for optimum suppression of the secondary main lobes the antenna elements must be placed at a half a free space wavelength distance with respect to the RF. For given NRD-guide dimensions the wavelength of the  $LSE_{01}$  mode is shorter than the wavelength of the  $LSM_{01}$  mode, hence, the NRD-guide feeding has been designed for operation in the longitudinal section electric (LSE) mode. Another good reason is the transverse orientation of the coupling slots with respect to the feeding, this makes the implementation of the balanced mixer circuit very compact. The coupling

slot in one of the ground planes introduces a discontinuity to the NRD-guide. The coupling coefficient and the degree of mismatch of this discontinuity are both increased with the length of the slot, thus the slot length is used to optimize the coupling coefficient to a given value. In order to limit the required LO bandwidth while maintaining the scan range, a steep phase increment over frequency is one of the goals for the feeding. In this regard band-pass filters can provide an improvement compared to a simple NRD-guide. With NRD-guide band-pass filters typically an air gap discontinuity between the resonator sections has been used [110, 111] to form an impedance inverter. For ease of production and in order to circumvent alignment problems between the adjacent resonator sections, an alternating width approach was introduced in [110]. The width of the NRD-guide sections that represent the inverters was fixed to a value assuring the operation below the cutoff-frequency. The inverter coefficient was set by optimizing the length of these sections. Although this approach solves the alignment issue, it is still rather complicated in production and sensitive to the milling accuracy. With the NRD-guide feeding for the scanning receiver array an alternative approach has been investigated using drill holes with optimized diameter values, thus providing a very simple yet accurate solution to the alignment problem. In Fig. 5.2 the design steps for the hybrid couplers are depicted. First, a three resonator NRD-guide band-pass is designed, where the four impedance inverters are implemented by drill holes in the dielectric material with different diameters. Then one of the smaller holes is replaced by the coupler NRD-guide to microstrip line including the coupling slot in the common ground metallization between the planar structure and the back side LO feeding network.

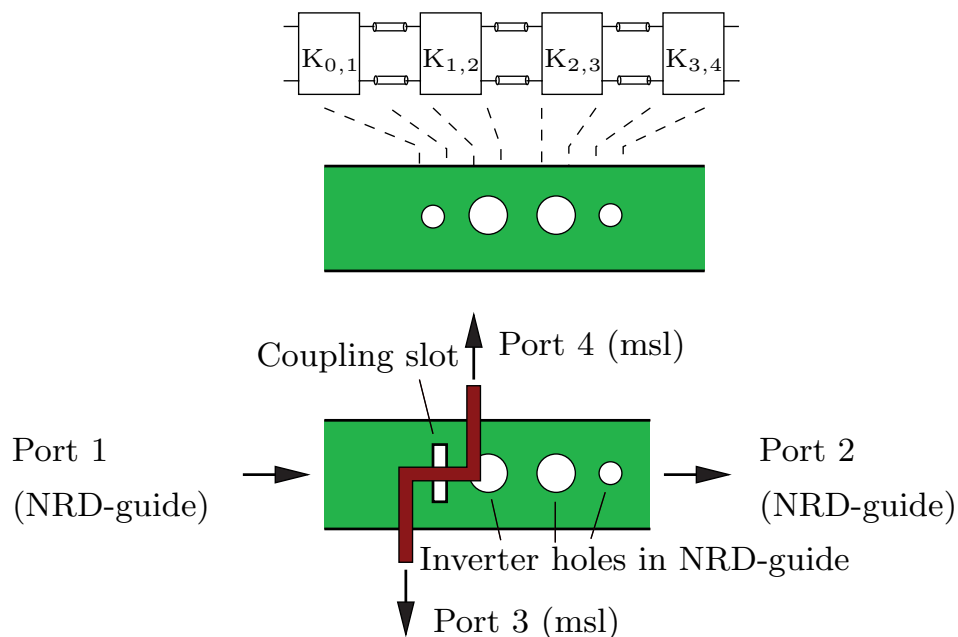


**Fig. 5.2:** Design steps of the couplers NRD-guide to microstrip line.

One task of the LO feeding network is to provide the same LO power level to all mixer circuits. The slot coupling between the NRD-guide and the microstrip line in general is non-ideal and thus generates some amount of radiation. Due to its non-symmetric property also parallel plate waves are generated. A typical value for losses due to radiation is  $-10$  dB relative to the power injected to the coupler at port 1 in Fig. 5.3.

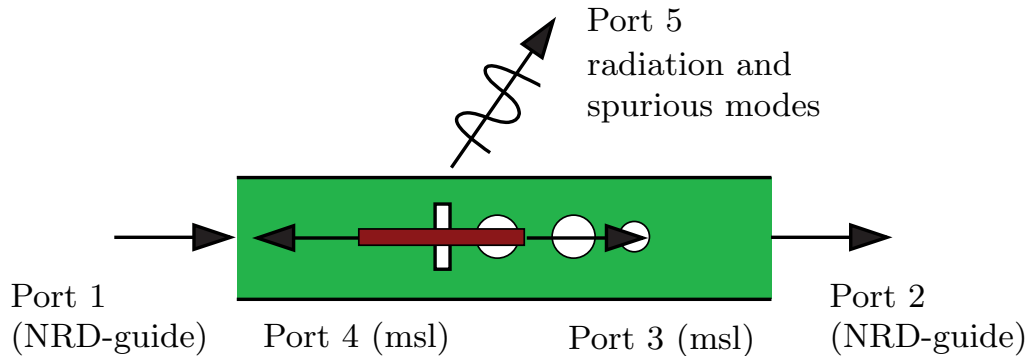


**Fig. 5.3:** Port naming convention of the couplers NRD-guide to microstrip line.

According to the formulae given in Sec. 2.5 the total attenuation coefficient in the NRD-guide including both ohmic and dielectric losses is  $\alpha_t=2.6$  1/m which equals to 22.4 dB/m for the wave attenuation. The signal flow diagram given in

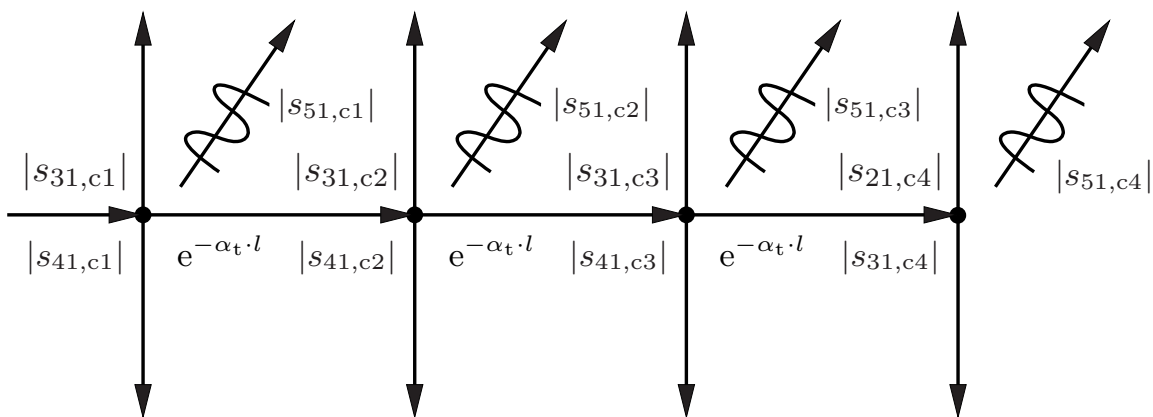


**Fig. 5.4:** Signal flow diagram of the LO feeding network describing the power transfer coefficients, the coupling coefficients, and the attenuation in the NRD-guide.

Fig. 5.4 summarizes the effects that have an impact on the calculation of the optimum coupling coefficients, with

$|s_{21,ci}|$  being the power transfer coefficient (NRD-guide to NRD-guide) of the coupler with index  $i$ ,  
 $|s_{31,ci}| = |s_{41,ci}|$  being the coupling coefficient (NRD-guide to microstrip line) of the coupler with index  $i$ ,  
 $|s_{51,ci}|$  being the coefficient of radiation and excitation of spurious modes.

The power balance equation for each coupler

$$|s_{21,ci}|^2 = 1 - 2 \cdot |s_{31,ci}|^2 - |s_{51,ci}|^2 \quad (5.1)$$

with the criteria for equal power distribution to all mixer circuits

$$|s_{31,ci}|^2 = |s_{21,ci}|^2 \cdot e^{-\alpha_t \cdot l} \cdot |s_{31,ci+1}|^2 \quad (5.2)$$

$$= (1 - 2 \cdot |s_{31,ci}|^2 - |s_{51,ci}|^2) \cdot e^{-\alpha_t \cdot l} \cdot |s_{31,ci+1}|^2 \quad (5.3)$$

can be solved for the coupling coefficient of the coupler  $|s_{31,ci}|^2$  and results in

$$|s_{31,ci}|^2 = \frac{(1 - |s_{51,ci}|^2) \cdot e^{-\alpha_t \cdot l} \cdot |s_{31,ci+1}|^2}{1 + 2 \cdot e^{-\alpha_t \cdot l} \cdot |s_{31,ci+1}|^2}. \quad (5.4)$$

Starting with the last coupler with index 4 and successive application of equation (5.4) leads to the optimum coupling coefficient values for the hybrid NRD-guide/microstrip line couplers given in Table 5.1.

**Table 5.1:** Optimum coupling coefficients for the four couplers.

	$ s_{31,c1} $	$ s_{31,c2} $	$ s_{31,c3} $	$ s_{31,c4} $
$ s_{31,ci} $ [dB]	-10.2	-8.7	-6.4	-3.5

Figures 5.5 through 5.8 show the simulated S-parameters of the four hybrid couplers with the coupling coefficients agreeing well with the optimum values given in Table 5.1. Typically, the coupling coefficient is nearly constant between 22 GHz and 25 GHz with only small amplitude variations. With the first coupler the coupling coefficient shown in Fig. 5.5 is slightly increasing beyond 24.5 GHz resulting in some deviation from the equal power distribution to all mixers.



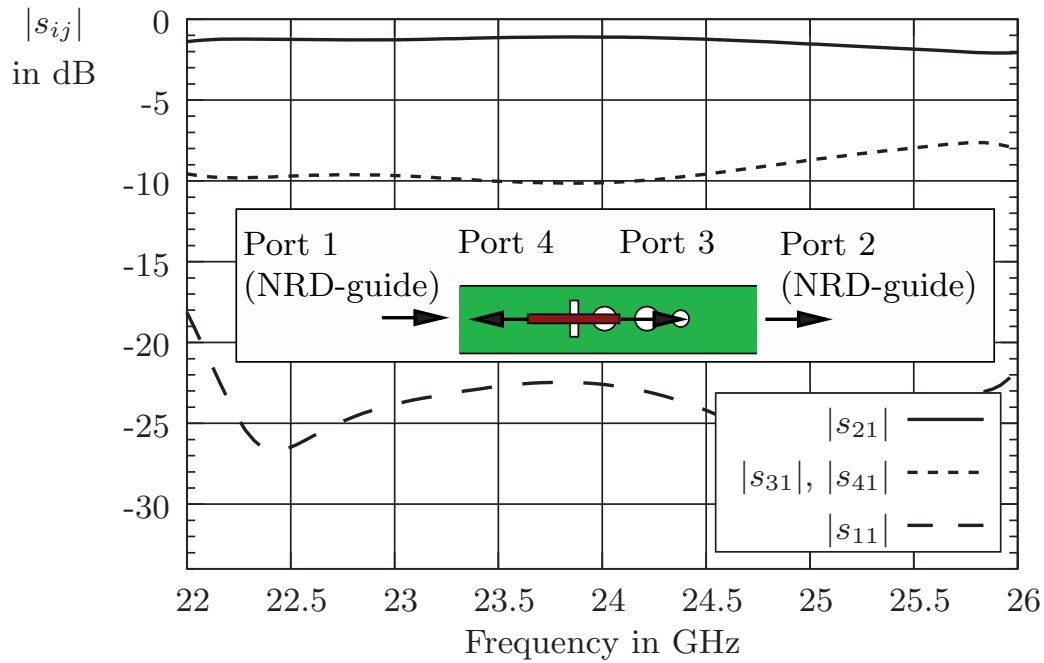


**Fig. 5.5:** Simulated S-parameters of the first coupler.

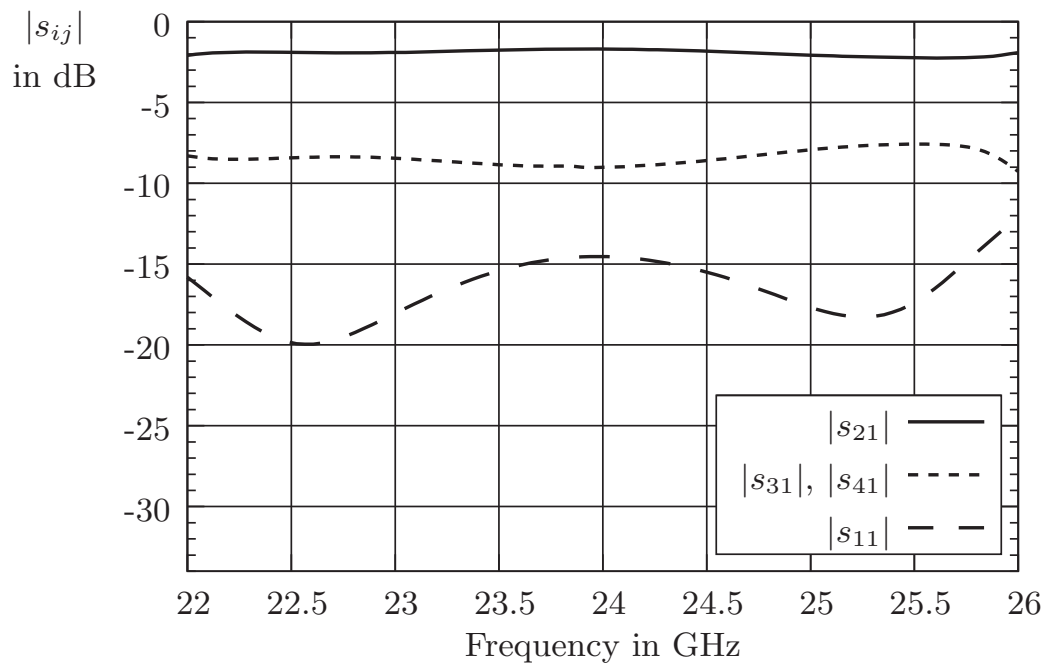


**Fig. 5.6:** Simulated S-parameters of the second coupler.

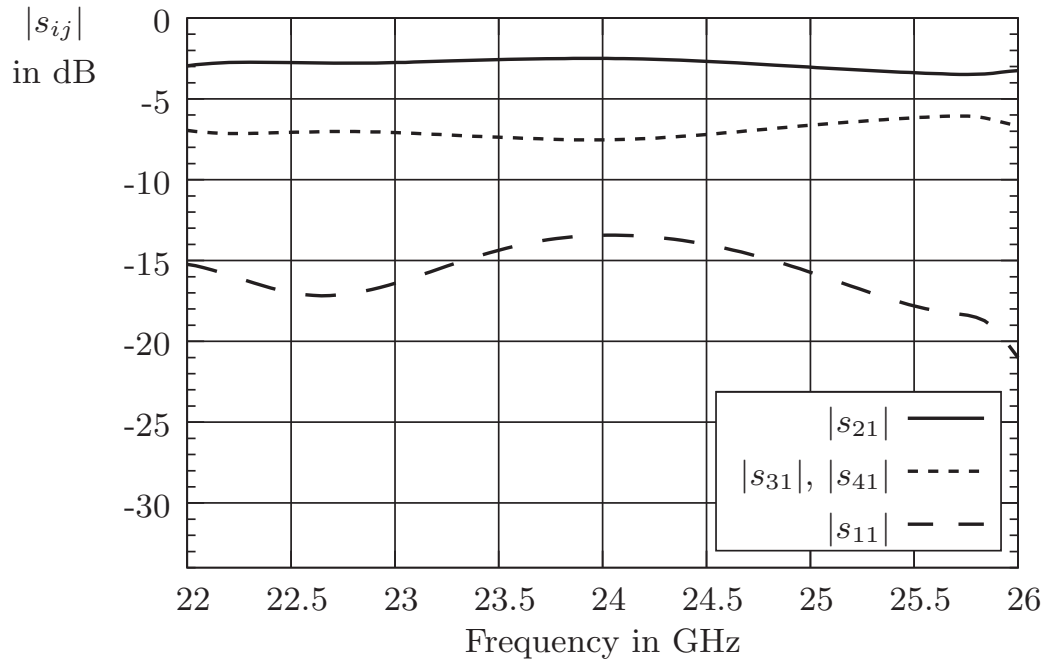


**Fig. 5.7:** Simulated S-parameters of the third coupler.

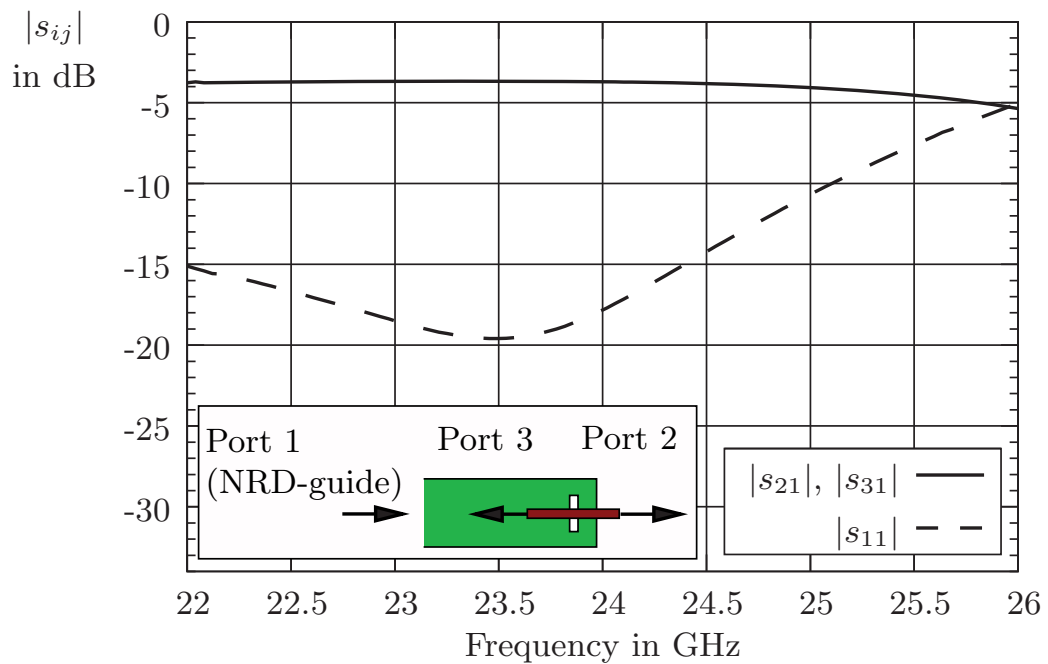


**Fig. 5.8:** Simulated S-parameters of the fourth coupler.

Due to the fact that the drill hole diameters are kept the same for the first three couplers and are not matched to the length of the coupling slot, i.e. the degree of discontinuity, the return loss is more and more limited with increasing coupling coefficients. But still in the worst case being the third coupler, the return loss exceeds 13 dB over the complete operational bandwidth.

The last coupler (insert in Fig. 5.8) has a different topology. The complete power should be transferred to the microstrip line, thus the matching mechanism is the same like for a conventional transition between NRD-guide and microstrip line with a short NRD-guide stub. The bandwidth is limited by the reduced return loss above 25 GHz, but again between 22 GHz and 25 GHz the coupling coefficient is nearly constant.

#### 5.3.2 Design of a Balanced Mixer with an NRD-guide LO Feed

The mixers designed for the scanning receiver array are implemented as single balanced mixers, using Skyworks' low barrier silicon beam-lead Schottky diode pairs DMF 2828-000 [112] in a series configuration. This diode pair with a forward voltage  $V_F(I_F=1\text{ mA})=270\text{ mV}$  to  $350\text{ mV}$  requires a relatively low drive level. A commercial large signal model of the diode was not available at the time, but had to be set up using the standard diode model in the circuit simulator within Agilent's Advanced Design System (ADS) [113]. The parameters within the model have been optimized step by step to fit simulation results to the measurement results of the diode pair. Details about measurements of the DC and RF characteristics and modeling of the diodes can be found in [114]. According to [115] advantages of a balanced mixer topology shown in Fig. 5.9 over a single diode configuration are

- systematic suppression of certain spurious intermodulation products,
- inherent LO to RF isolation without additional filters,
- suppression of amplitude modulation (AM) noise in the balanced signal.

A disadvantage of balanced mixers is their greater LO power requirement. Which intermodulation products are suppressed is dependent on whether the RF drive or the LO drive to the two diodes is anti-phase (balanced). The signal injected to the  $\Delta$  port of the  $180^\circ$  hybrid appears to be an anti-phase drive to the diodes and is canceled at the IF port without additional filtering. Typically, the LO

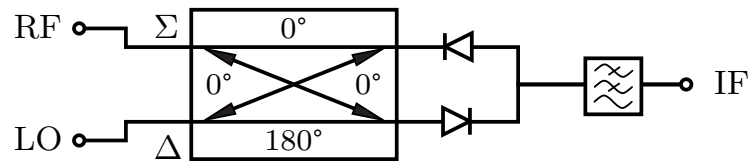


**Fig. 5.9:** Block diagram of a single-balanced mixer.

drive is much higher than the RF power level and shall thus be strongly suppressed by the mixer, so with this implementation the LO signal is injected to the  $\Delta$  port of the  $180^\circ$  hybrid, and the RF signal is injected to the  $\Sigma$  port. As a consequence, if the mixing products are at  $f_{\text{mix}} = m \cdot f_{\text{RF}} \pm n \cdot f_{\text{LO}}$ , the mixer will reject all products where  $m$  is even. A detailed discussion on the suppression of intermodulation products with different mixer configurations can be found in [115].

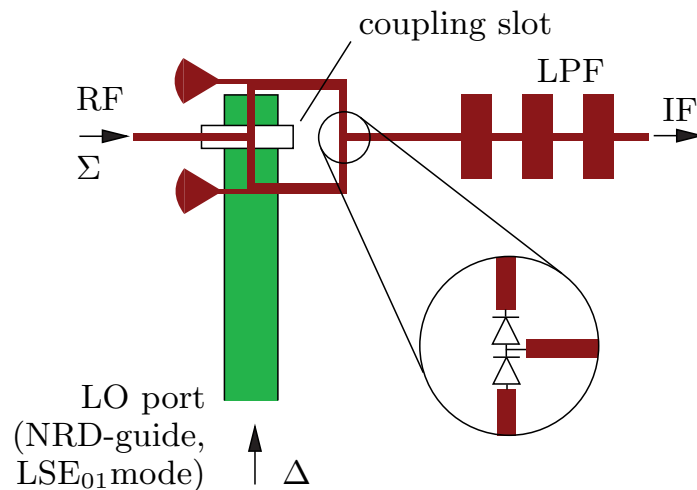


**Fig. 5.10:** Setup of the balanced mixer.

For the beam steerable antenna described in this chapter a special type of a single balanced mixer has been developed using the NRD-guide as an LO feed. The principle of the mixer is shown in Fig. 5.10. The  $180^\circ$  hybrid is implemented by a modification of the couplers described in Sec. 5.3.1, page 115 et seq. The NRD-guide excited by the  $\text{LSE}_{01}$  mode represents the  $\Delta$  input terminal causing an anti-phase drive of the antipodal diodes pair located at either end of the microstrip line ring which represents the output terminals of the  $180^\circ$  hybrid. Assuming that the diodes are identical, the common node between the diodes is a virtual ground to the LO signal. An additional microstrip line branch attached perpendicular to the microstrip line ring, provides the  $\Sigma$  input terminal fed

by the RF signal. For a low conversion loss the RF impedance level at the common node between the diodes must be low, too, i.e., the circuit must not only provide a short for the LO but also for the RF signal. This is accomplished by the distributed low-pass filter (LPF in Fig. 5.10), which starts with a shunt capacitance implemented by a low impedance microstrip line section. The length of the microstrip line section between the diode pair and the LPF is adjusted to provide this RF short to the diodes. Another task of the LPF is to reject remaining spurious intermodulation products. In order to suppress IF signal leakage to the RF port and to guarantee low conversion loss, the diodes should be also IF short circuited at their input leads. This is achieved by radial stubs which are attached to the microstrip ring via a short high impedance microstrip line.

For evaluation purposes the balanced mixer configuration has been implemented and characterized as a stand alone test circuit. The  $LSE_{01}$  mode on the NRD-guide is excited with a typical transition from microstrip line to NRD-guide using a transverse coupling slot. A transition of this kind is part of the dual mode transition that has been used for feeding the dual polarization antenna in Chapter 4. The principle of the transition has been discussed on page 60, and simulation results have been given in Sec. 4.2.1.1, page 85 et seq. Figures 5.11 and 5.12 show the measured conversion loss versus LO power level and LO frequency when the mixer operates as a down converter with  $f_{RF}=19$  GHz and  $P_{RF}=-8$  dB. Optimum LO frequency range is 22.3 GHz to 24.1 GHz with conversion loss lower than 9 dB.

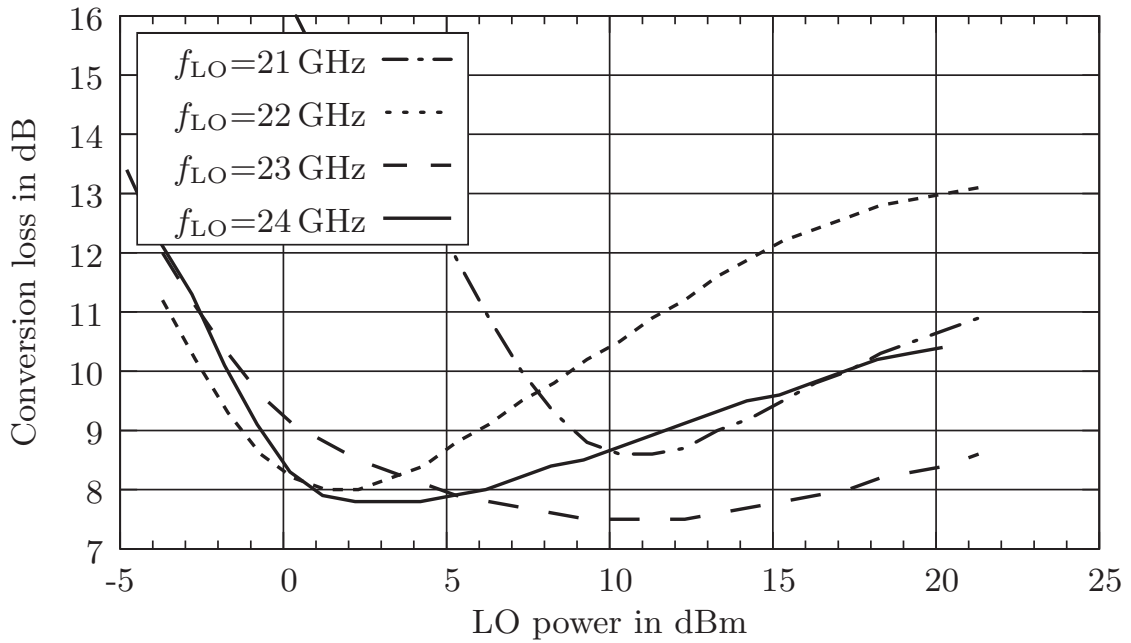


**Fig. 5.11:** Measured conversion loss as a function of the LO power level with different LO frequencies ( $f_{RF}=19$  GHz,  $P_{RF}=-8$  dBm).

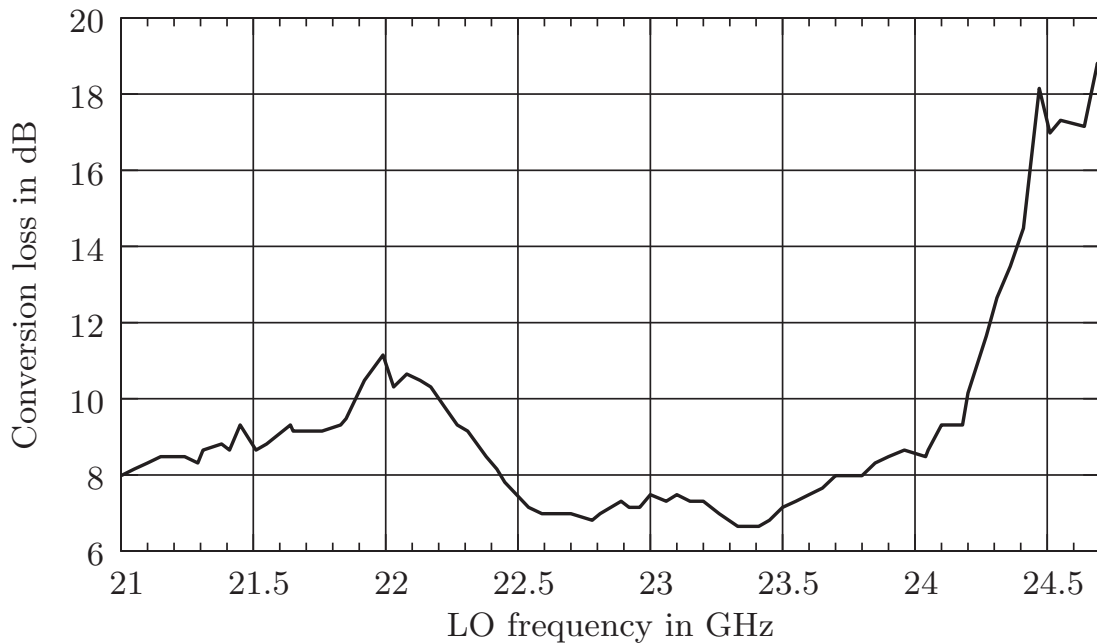


**Fig. 5.12:** Measured conversion loss as a function of the LO frequency with constant RF frequency ( $f_{RF}=19$  GHz,  $P_{LO}=11.3$  dB,  $P_{RF}=-8$  dBm).

## 5.4 Performance of the Scanning Receiver Array

A photo of the complete receiver array is shown in Fig. 5.13. A detailed layout of all parts can be found in Appendix A.2, page 141. The IF output signals of the mixers are filtered by distributed low-pass filters (LPF) and then combined in-phase by a four-to-one Wilkinson combiner network. A stronger weighting of the inner two channels is used for reduction of the side lobe level and in order to compensate for the deviation of the power distribution of the LO feeding network described in Sec. 5.3.1.

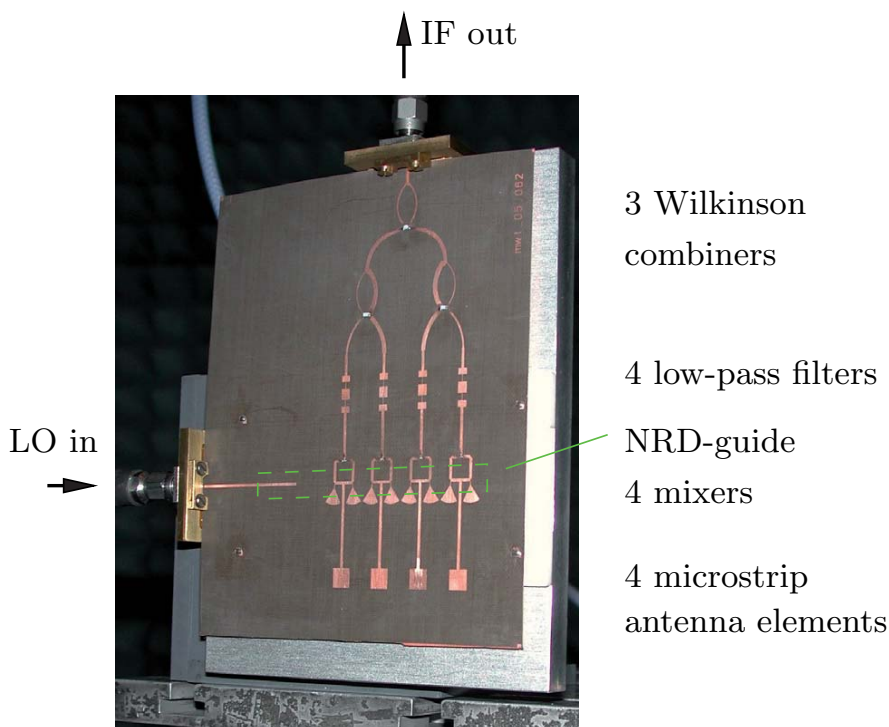


**Fig. 5.13:** Photo of the complete antenna.

A block diagram of the measurement setup for the radiation diagrams of the antenna is given in Fig. 5.14. Some part of the transmit signal is fed to another mixer providing a reference signal. Both reference (IF) signal and receiver array output are fed to the down-converter of a network analyzer operated in a dual frequency mode. In this way, a coherent and sensitive measurement setup could be achieved [116].

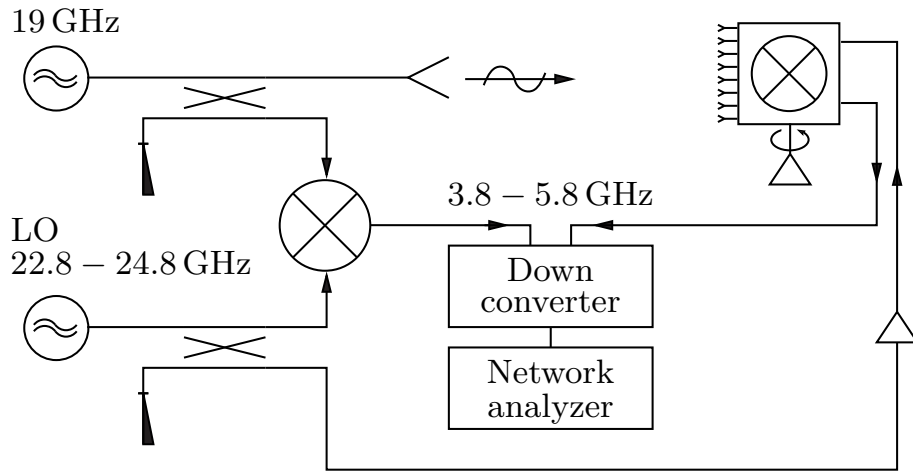


**Fig. 5.14:** Block diagram of the antenna measurement setup.

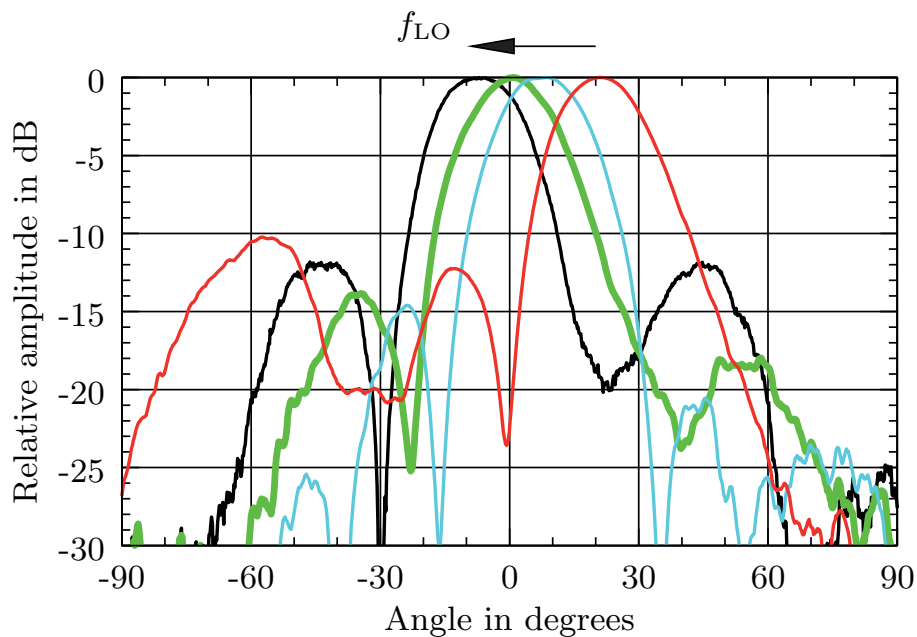


**Fig. 5.15:** H-plane radiation diagrams of the antenna array operated in the receive mode at 19 GHz (LO frequency  $f_{LO}=22.8$  GHz ... 24.8 GHz, IF frequency  $f_{IF}=3.8$  GHz ... 5.8 GHz, all diagrams normalized to 0 dB).

Figure 5.15 shows the H-plane radiation diagrams of the receiver arrangement with the RF frequency fixed at 19 GHz and the LO frequency varied from 22.8 GHz to 24.8 GHz, resulting in a scan range from  $-7^\circ$  to  $+21^\circ$ . The dotted



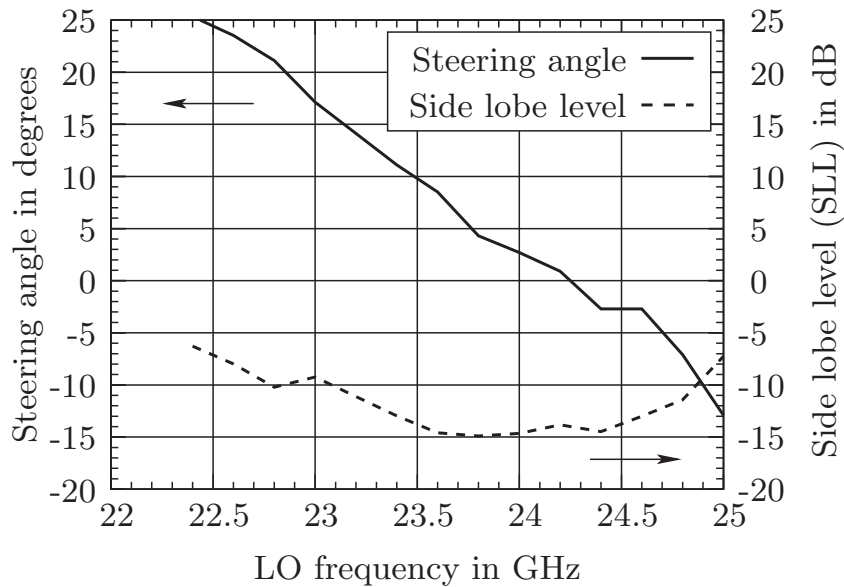


**Fig. 5.16:** Measured steering angle and side lobe level of the radiation diagram of the receiver array as function of the LO frequency.

curve in Fig. 5.16 shows that in the frequency range from 22.8 GHz to 24.8 GHz the side lobe level is below  $-10$  dB. Measurement of the radiation diagrams for a wider range of LO frequencies indicated that allowing a slightly higher side lobe level of  $-8$  dB, the scan range is extended to  $-11.8^\circ$  to  $+23.5^\circ$ .

In [108] it was shown that by injecting a 3.8 GHz to 5.8 GHz signal at the IF port and a 22.8 GHz to 24.8 GHz signal at the LO input port in Fig. 5.13, the antenna can also be operated in a transmit mode with a constant RF signal at 19 GHz.

## 5.5 Two-path Band-pass Filters for a Steeper Phase Increment

In [117] a class of two-path multimode band-pass filters using the NRD-guide was proposed, providing an additional pole of attenuation close to the cut-off frequency thus offering steeper slopes in the filter characteristic than one-path NRD-guide band-pass filters.

A similar setup depicted in Fig. 5.17 provides a steep phase increment over frequency to allow for a wide scanning range with a low LO frequency variation.

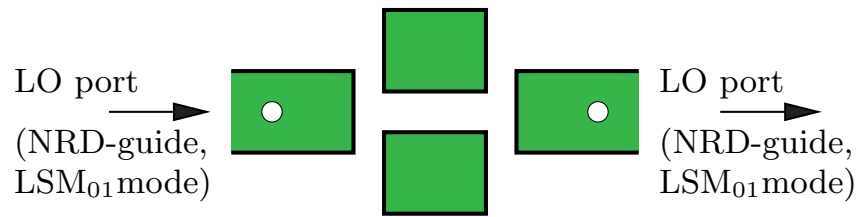


**Fig. 5.17:** Setup (top view) of the two-path NRD-guide band-pass filter.

In this approach, the center section of the three resonator band-pass filter in Fig. 5.2, page 116 is replaced by two parallel dielectric strips, and the gap between the two-path section in the center and the single-path sections at either end is carefully adjusted for providing the proper inverter coefficient.

The step from the one-path NRD-guide to the two-path NRD-guide excites both the  $LSE_{01}$  and the  $LSM_{01}$  mode in the two-path NRD-guide section. This increases the order of the band-pass filter by one. So actually the two-path NRD-guide band-pass filter is of order four and has therefore a steeper phase increment compared to a one-path NRD-guide band-pass filter with identical physical length. The symmetry along the NRD-guide prevents the excitation of the  $LSE_{01}$  mode in the one-path NRD-guide sections. In Fig. 5.18 two of the four expected resonances are falling on the same frequency and thus only three reflection zeros can be observed. The rectangle in this figure indicates the frequency range from 23.92 GHz to 24.64 GHz where return loss exceeds 15 dB.

Comparison of the phase increments in Fig. 5.19 of a two-path NRD-guide band-pass filter and of a one-path NRD-guide band-pass filter shows the big advantage of the first. In the 0.72 GHz range from 23.92 GHz to 24.64 GHz indicated by the rectangle, where according to Fig. 5.18 return loss exceeds 15 dB, a variation of the phase increment by  $188^\circ$  is achievable, leading to a wider scanning range compared to the 2 GHz range from 23 GHz to 25 GHz, where only a variation of the phase increment by  $145^\circ$  is achievable with the one-path NRD-guide band-pass filter.

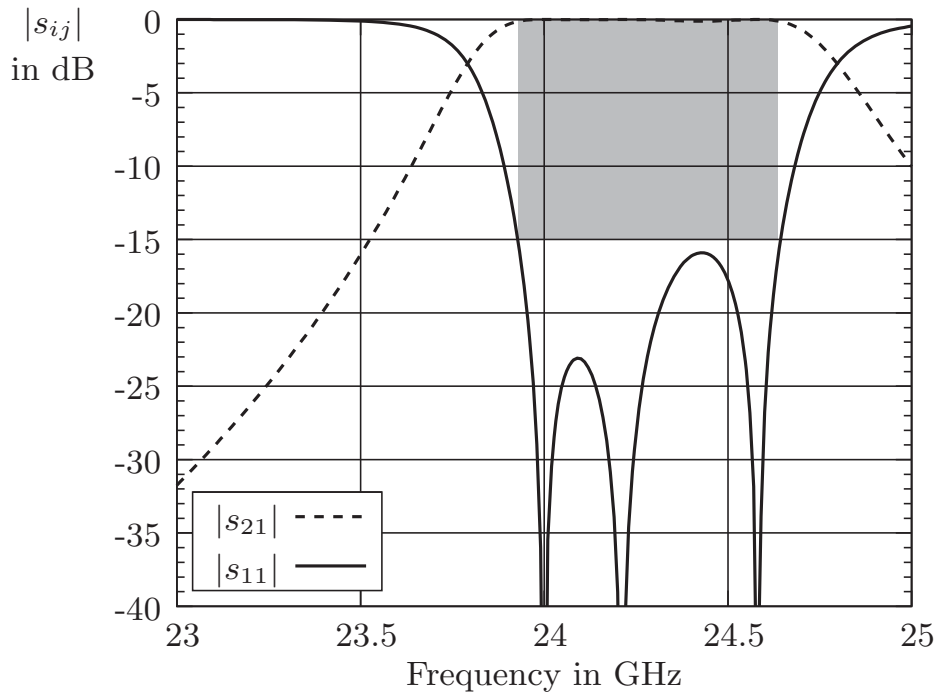


**Fig. 5.18:** Simulated S-parameters of the two-path NRD-guide band-pass filter.

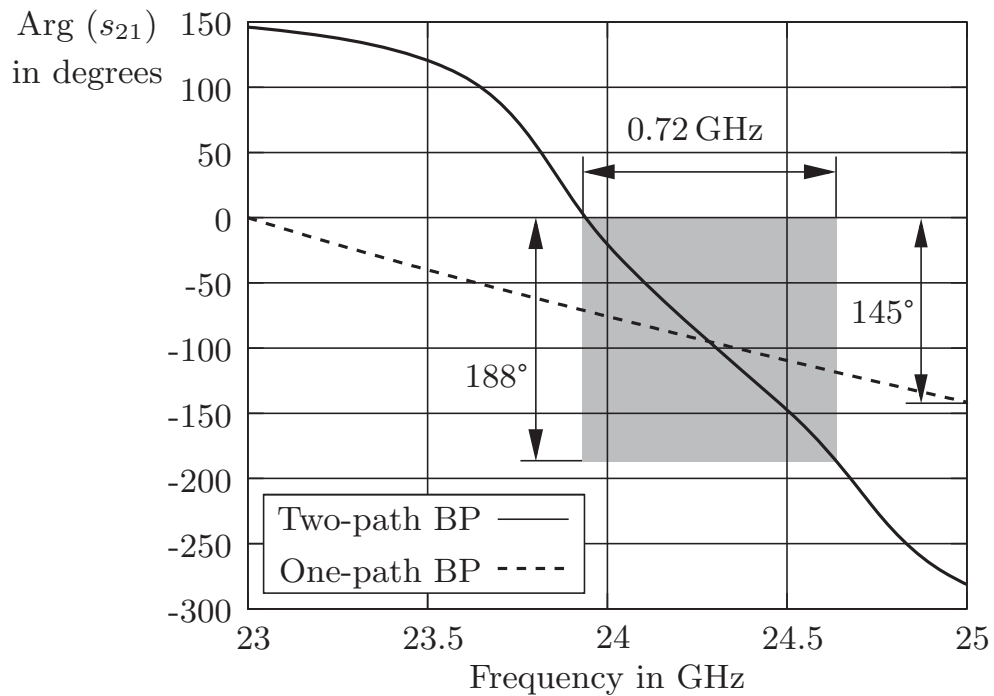


**Fig. 5.19:** Phase behavior of the two-path NRD-guide band-pass filter (Fig. 5.17) and of the one-path NRD-guide band-pass filter (Fig. 5.2, middle), showing the steeper characteristic of the first.

Considering the phase and amplitude characteristics of couplers with two-path NRD-guide sections, expected radiation patterns have been calculated for control signals with different frequencies. The calculated radiation diagrams have been analyzed in terms of steering angle of the main lobe in azimuth and side lobe levels. Figure 5.20 plots both values (solid curves) versus the control signal frequency. For comparison the measured values (dashed curves) are given for the receiver array with the conventional NRD-guide feeding, too. Allowing a side lobe level of  $-8$  dB the main lobe can be steered between  $\pm 45^\circ$  with an LO frequency variation of only 0.72 GHz.

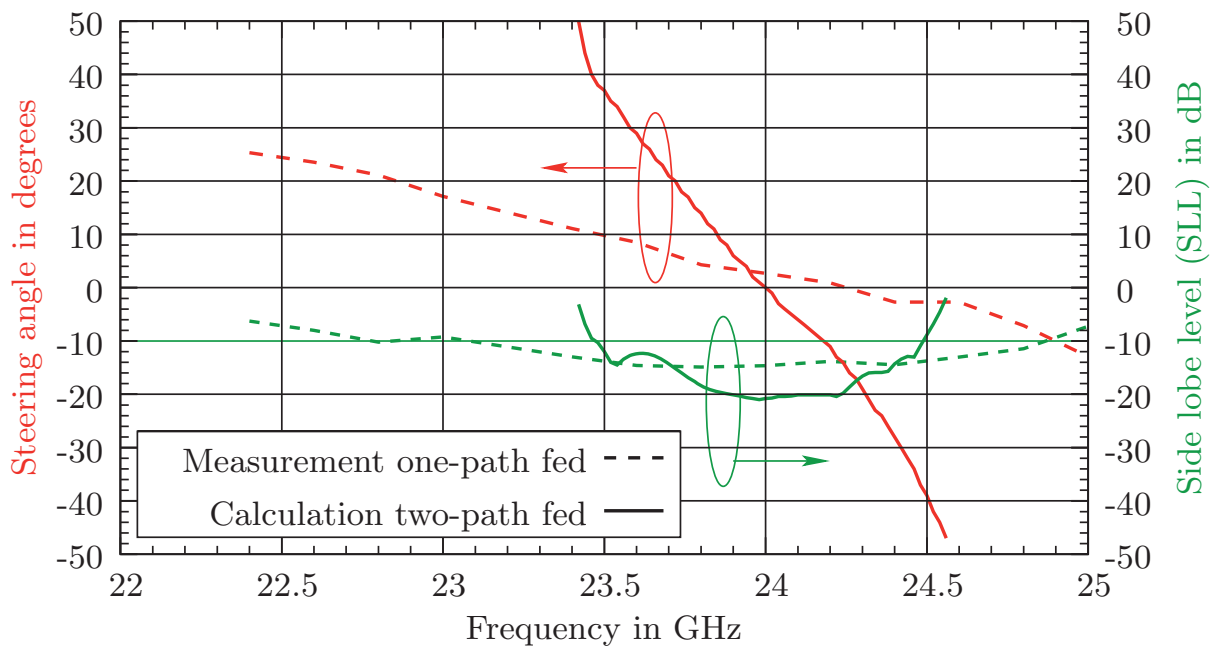


**Fig. 5.20:** Measured steering angle and side lobe level (dashed curves) of the radiation diagram of the receiver array dependent on the LO frequency versus calculated values (solid curves) based on a feeding with two-path sections.

## 6 Summary

This thesis deals with the investigation and development of low profile, low loss antennas with emphasis on reduced cost implementations for different communication and radar applications in the microwave and millimeter-wave region. All antennas investigated in this work are implemented in the K-band (18 GHz–26.5 GHz) as for this frequency range measurement facilities and power amplifiers were readily available, but actually they lend themselves for applications in the mm-wave range where the low loss characteristic of the NRD-guide is even more pronounced.

In the first part, Chapter 3 a **fixed beam antenna for point-to-point applications** is presented. The focus for this antenna is to implement a low cost solution for high gain antennas with high efficiency and a flat setup. To meet this goal, a planar antenna array is combined with an NRD-guide feeding structure. The NRD-guide provides a low loss, lightweight and easy to fabricate alternative to conventional rectangular waveguide techniques. This antenna shows a depth of only 6.3 mm. Such a low profile can otherwise only be achieved with purely planar techniques like microstrip antennas fed by a microstrip line feeding network, but then at the cost of increased loss and reduced efficiency. The half power beam width of this antenna array is  $7^\circ$  in the E-plane and  $11.2^\circ$  in the H-plane. Maximum gain is 22.6 dBi at 24 GHz and aperture efficiency is 59%. A comparison with values given in literature reveals that only microstrip antenna arrays with waveguide feed network can provide similar or even greater efficiency numbers. But this is at the cost of a more complex feeding network with increased production cost and a bulkier and heavier setup. In a future version the feeding network could be implemented in *substrate integrated NRD (SINRD) waveguide* technique further reducing the fabrication cost. The principle of this antenna can easily be extended to a bigger array of the same 9 patch sub array providing not only higher directivity but also higher gain. Side lobe levels can be further reduced applying an amplitude taper function by using asymmetric T-junctions in the NRD-guide feed network.

The second part, Chapter 4 deals with the implementation of **dual polarization antennas**. The NRD-guide is used as a dual mode waveguide for feeding a dual polarization antenna array. Thanks to its multimode characteristic and the fact that these modes do not interact unless at a group of asymmetric discontinuities, the NRD-guide can be used to feed sub arrays of microstrip antenna elements for independent operation in two polarizations. The longitudinal section electric (LSE) mode and the longitudinal section magnetic (LSM) mode are excited independently by separate transitions from microstrip line to NRD-guide. Each of the modes causes the planar patch array to radiate in one linear polarization. In a first implementation of the **dual polarization antenna** the feeding network is implemented in the *substrate integrated NRD (SINRD) waveguide* technique. With this antenna the production process of the feed network only includes drilling and no machining. This has two major advantages over a conventional NRD-guide implementation. First, the production cost is reduced substantially and, second, it solves the alignment issue between the distinct layers because some of the drill holes in the dielectric material together with dowel pins can be used to align the NRD-guide feeding structure with the planar radiating structure. With this antenna the dual mode transitions are implemented by a set of slots in the ground metallization. For the  $LSM_{01}$  mode, the commonly applied matching technique based on a  $\lambda/4$  long NRD-guide stub is used. By contrast, slots in the back side ground metallization of the SINRD-guide provide a matching mechanism for the  $LSE_{01}$  mode without interference with the  $LSM_{01}$  mode. The dual polarization antenna consisting of four square patch radiators shows a half power beamwidth between  $25^\circ$  and  $38^\circ$  in the E- and H-plane for excitation with both modes.

The second antenna described in Chapter 4 is a **dual polarization antenna array of two sub arrays**. In contrast to the transitions used in the SINRD-guide dual polarization antenna, the transitions used for the array works without additional slots in the back side ground metallization. A reduction in the width of the NRD-guide is used to control the matching of the transitions for both modes independently. Thus no asymmetry along the height of the NRD-guide is required which would make the transition susceptible to the excitation of parallel plate waves. The dual polarization antenna array consisting of two identical sub arrays with  $2 \times 2$  square patch radiators shows half power beamwidths of  $17^\circ$  and  $35^\circ$  when excited with the  $LSE_{01}$  mode and  $21^\circ$  and  $31^\circ$  when excited with the  $LSM_{01}$  mode. The gain of the antenna array when excited with  $LSE_{01}$  mode is 12.2 dBi, that is the array and feed network efficiency is 51%. When the array is excited with the  $LSM_{01}$  mode, gain is 12.1 dBi and efficiency is 49%. This antenna array can be easily extended to a bigger array with higher gain by duplicating the existing structure. All necessary sub circuits are described in detail. Both implementations of dual polarization antennas show with 3.5 mm antenna depth a very flat and compact setup.

---

The third part, Chapter 5 describes the design and implementation of a **low cost low profile scannable receiver array**. Possible applications include radar sensors in the automotive field, ground terminals of low earth orbit (LEO) satellite communication systems and smart antennas for wireless communication networks. The antenna beam scanning is achieved by a frequency scan of the LO signal. In this array, scan range was limited to  $-11.8^\circ$  to  $+23.5^\circ$  due to a phase offset of the couplers and a limited phase increment over the LO frequency. The couplers are key components to this kind of scanning antenna. Two-path NRD-guide band-pass filters feature a steeper phase increment with frequency as compared to conventional NRD-guide band-pass filters. A scanning receiver array with reduced LO frequency variation and wider scanning range using two-path NRD-guide band-pass filters has been proposed and investigated in detail. Simulation results of those two-path NRD-guide band-pass filters indicate the potential for a scanning range of the antenna of  $\pm 45^\circ$  within an LO frequency variation of only 0.72 GHz. For a smaller beamwidth in the H-plane, the array can be easily extended to more antenna elements. In the E-plane the beam might be narrowed by using a set of serial fed patches. The total height of the antenna is only 3.5 mm plus the back side aluminum plate and thus the scannable receiver array suits very well to automotive sensor applications where space requirements are typically critical and low profile setups are required. The lateral dimensions of the antenna ( $120\text{ mm} \times 95\text{ mm}$ ) have not been optimized and could be further reduced by the use of smaller designs of the planar parts including approved and low cost MMIC mixers. The possibility to drive this type of antenna arrays in a transmit mode was shown with a similar antenna and presented in [108]. The scan range in transmit mode operation has been proven to be identical to the scan range in receive mode operation but inverse over LO frequency.





# A Appendix

## A.1 Design Details on the Components of the Dual Polarization Antenna

This appendix gives the layouts and lists the dimensions of all the components of the dual polarization antenna described in chapter 4.2.

### A.1.1 Dual Mode Transition from NRD-guide to Microstrip Line

This dual mode transition from microstrip lines to an NRD-guide is used to independently excite the  $LSE_{01}$  mode and the  $LSM_{01}$  mode on the same NRD-guide section in the dual polarization antennas. The setup with the naming of the dimensions is given in Fig. A.1 and specific values for the dimensions are stated in Table A.1. Simulation results and measurement results are given in section 4.2.1.1, page 81 and section 4.2.2, page 92, respectively.

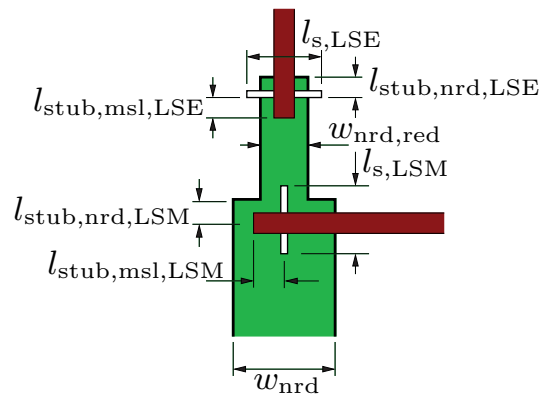


**Fig. A.1:** Setup (top view) of the dual mode transition NRD-guide to microstrip line.

stub length microstrip line, LSE-Mode	$l_{\text{stub,msl,LSE}}$	2.3 mm
stub length microstrip line, LSM-Mode	$l_{\text{stub,msl,LSM}}$	2.0 mm
stub length NRD-guide, LSE-Mode	$l_{\text{stub,nrd,LSE}}$	3.4 mm
stub length NRD-guide, LSM-Mode	$l_{\text{stub,nrd,LSM}}$	0.8 mm
slot length, LSE-Mode	$l_{\text{s,LSE}}$	5.0 mm
slot length, LSM-Mode	$l_{\text{s,LSM}}$	4.6 mm
width of reduced NRD-guide	$w_{\text{nrd,red}}$	3.0 mm
width of NRD-guide	$w_{\text{nrd}}$	5.0 mm

**Table A.1:** Dimensions of the dual mode transition NRD-guide to microstrip line (Fig. A.1).

### A.1.2 Dual Mode NRD-guide T-junction

This NRD-guide T-junction is a 3 dB power divider with good matching performance for both modes,  $LSE_{01}$  and  $LSM_{01}$ . The T-junction is optimized for maximum power conversion to the  $LSE_{01}$  mode at the output branches when excited with  $LSM_{01}$  mode at the input branch and vice versa. The setup with the naming of the dimensions is given in Fig. A.2 and specific values for the dimensions are stated in Table A.2. Details on the matching and optimization principle and on simulation results can be found in section 4.2.1.3, page 89.

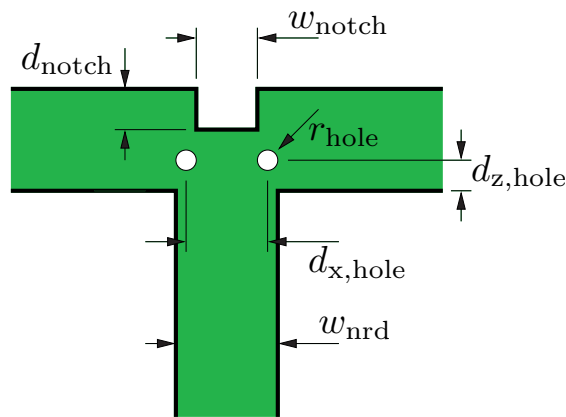


**Fig. A.2:** Setup (top view) of the dual mode NRD-guide T-junction with matching holes.

notch depth	$d_{\text{notch}}$	1.5 mm
notch width	$w_{\text{notch}}$	3.0 mm
distance of drill in x-direction	$d_{x,\text{hole}}$	3.8 mm
distance of drill in z-direction	$d_{z,\text{hole}}$	1.5 mm
radius of drill	$r_{\text{hole}}$	0.6 mm
width of NRD-guide	$w_{\text{nrđ}}$	5.0 mm

**Table A.2:** Dimensions of the dual mode NRD-guide T-junction with matching holes (Fig. A.2).

### A.1.3 Dual Mode Transition from NRD-guide to Crossed Microstrip Lines

This transition is used for feeding the dual polarization antenna sub arrays described in section 4.2.3, page 100. The setup with the naming of the dimensions is given in Fig. A.3 and specific values for the dimensions are stated in Table A.3. Simulation results and measurement results are given in section 4.2.1.2, page 88 and section 4.2.2.2, page 96, respectively.

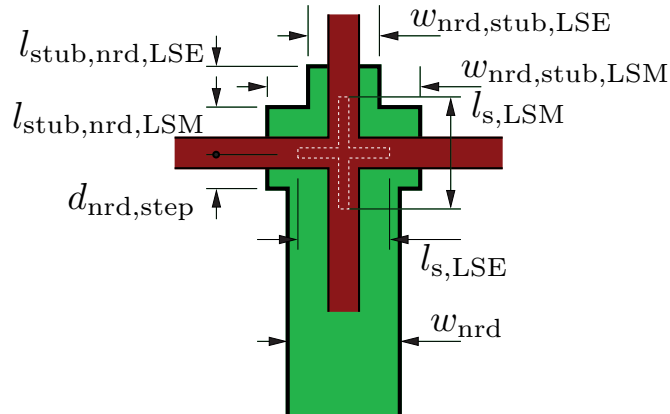


**Fig. A.3:** Setup (top view) of the dual mode transition NRD-guide to crossed microstrip lines.

stub length NRD-guide, LSE-Mode	$l_{\text{stub,nrd,LSE}}$	3.2 mm
stub length NRD-guide, LSM-Mode	$l_{\text{stub,nrd,LSM}}$	1.4 mm
slot length, LSE-Mode	$l_{\text{s,LSE}}$	4.2 mm
slot length, LSM-Mode	$l_{\text{s,LSM}}$	5.0 mm
distance of step in width NRD-guide, LSM-Mode	$d_{\text{nrd,step}}$	2.0 mm
stub width, NRD-guide, LSE-Mode	$w_{\text{nrd,stub,LSE}}$	3.0 mm
stub width, NRD-guide, LSM-Mode	$w_{\text{nrd,stub,LSM}}$	6.6 mm
width of NRD-guide	$w_{\text{nrd}}$	5.0 mm

**Table A.3:** Setup (top view) of the dual mode transition NRD-guide to crossed microstrip lines (Fig. A.3).

## A.2 Layouts of the NRD-guide Fed Antennas

This appendix gives the detailed layouts of the antennas described in Chapter 4 and Chapter 5.

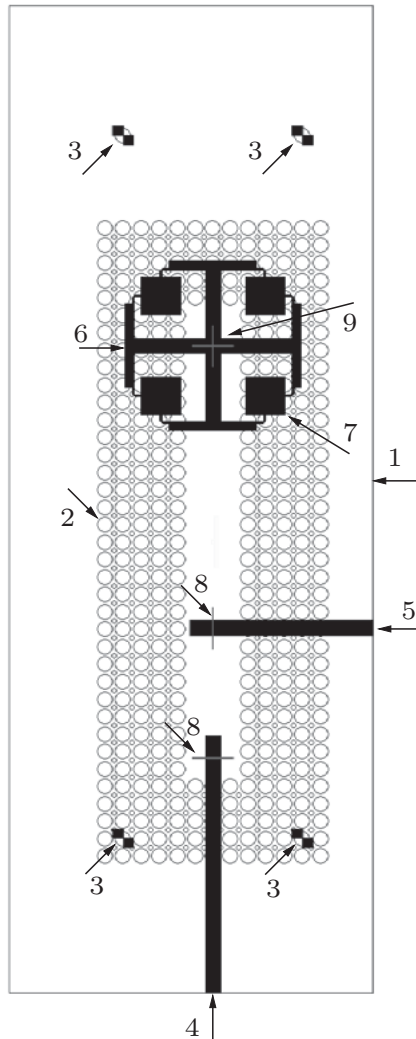


**Fig. A.4:** Layout of the dual polarization antenna fed by an SINRD-guide: 1: SINRD-guide feeding made of Rogers TMM-6, 2: drill hole pattern in the Rogers TMM-6 material, 3: dowel pins, 4: input for radiation in the vertical polarization, 5: input for radiation in the horizontal polarization, 6: small microstrip line feeding network, 7: square microstrip patch antenna elements, 8: coupling slots in the back side metallization of the front side substrate RT/Duroid 5870, 9: crossed coupling slots.

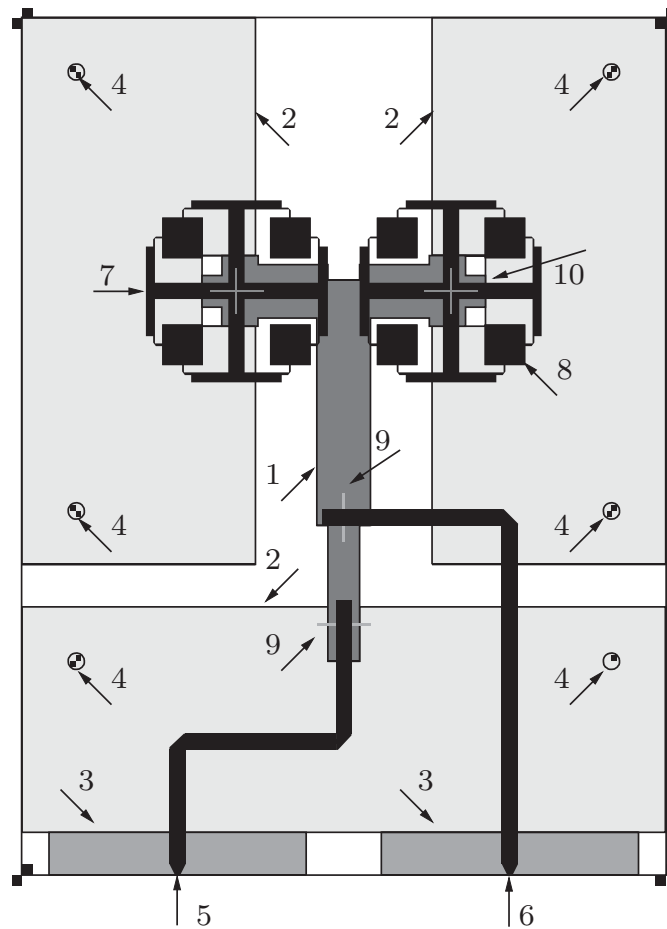


**Fig. A.5:** Layout of the dual polarization antenna array: 1: corporate NRD-guide feeding network made of Rogers TMM-6, 2: positioning forms made of Rohacell foam, 3: fixing plates for the SMA connectors, 4: dowel pins, 5: input for radiation in the vertical polarization, 6: input for radiation in the horizontal polarization, 7: small microstrip line feeding network, 8: square microstrip patch antenna elements, 9: coupling slots in the back side metallization of the front side substrate RT/Duroid 5870, 10: crossed coupling slots.

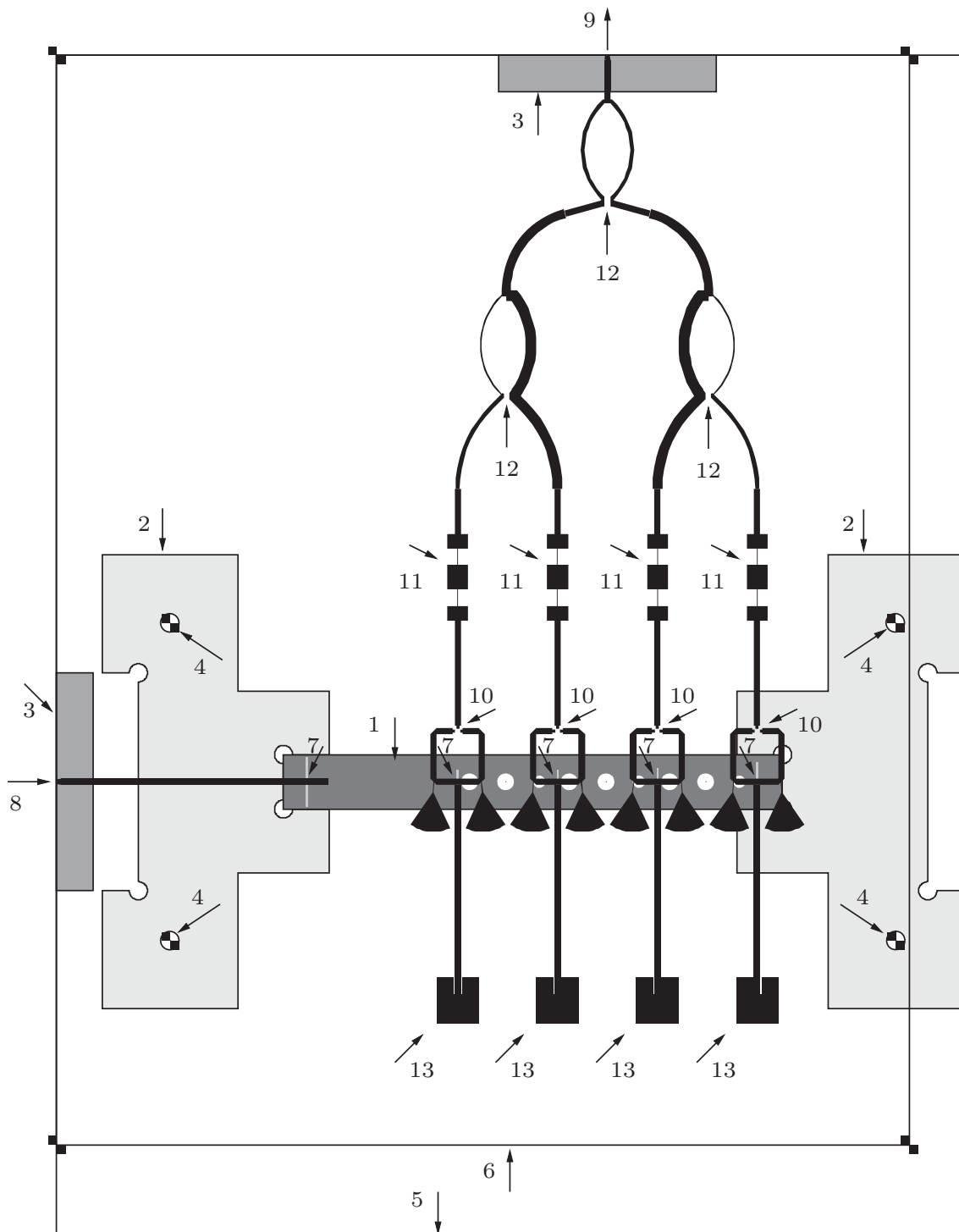


**Fig. A.6:** Layout of the scanning receiver array: 1: dielectric rod made of Rogers TMM-6, 2: positioning form made of Rohacell foam, 3: fixing plates for the SMA connectors, 4: dowel pins, 5: back side aluminum plate, 6: planar substrate RT/Duroid 5870, 7: coupling slots in the back side metallization of the front side substrate, 8: LO input, 9: IF output, 10: diode pairs, 11: low pass filters, 12: SMD resistors  $100\ \Omega$ , 13: antenna elements receiving the RF signal.





## Bibliography

- [1] MANSEN, D. ; VILLINO, G.: Planar Microstrip Antennas for MMDS Application at 40 GHz. In: *European Microwave Conference* Vol. 3, 1999, pp. 9–12
- [2] WEISS, M.: Microstrip antennas for millimeter waves. In: *IEEE Transactions on Antennas and Propagation* 29 (1981), January, No. 1, pp. 171–174
- [3] MENZEL, W. ; SCHREINER, M. ; MACK, R. ; NAVARRO VERA, P. J.: Millimeter-Wave Microstrip Antenna Arrays with Waveguide Feed Network. In: *Frequenz* 55 (2001), November/December, pp. 278–282
- [4] SEHM, T. ; LEHTO, A. ; RÄISÄNEN, A. B.: A high-gain 58 GHz box-horn array antenna with suppressed grating lobes. In: *IEEE Transactions on Microwave Theory and Techniques* 47 (1999), Juli, No. 7, pp. 1125–1130
- [5] ANDERSON, T. ; HOU, J. L. ; MICHALSKI, J.: Design and manufacturing techniques for planar slot array antennas for a variety of radar application. In: *IEEE Radar Conference (RADARCON)*, 1998, pp. 337–342
- [6] ANDO, M. ; HIROKAWA, J. ; YAMAMOTO, T. ; AKIYAMA, A. ; KIMURA, Y. ; GOTO, N.: Novel single-layer waveguides for high-efficiency millimeter-wave arrays. In: *IEEE Transactions on Microwave Theory and Techniques* 46 (1998), June, No. 6, pp. 792 – 799
- [7] ENGELN, C.: *Broadband, Planar mm-Wave Antennas for Radio in the Local Loop*. PhD thesis (in German), Technical University of Aachen, 2000
- [8] DOLP, R. ; MAYER, W. ; GRABHERR, W.: Industrialization of a 58 GHz High Gain Flat Panel Antenna for High Volume Production. In: *European Microwave Conference* Vol. 3, 1999, pp. 267–270
- [9] KASSNER, J.: *Untersuchungen zur Aufbau- und Verbindungstechnik von komplexen Millimeterwellen-Modulen*. PhD thesis (in German), University of Ulm, 2000

- [10] MENZEL, W. ; AL-TIKRITI, M. ; LEBERER, R.: A 76 GHz multiple-beam planar reflector antenna. In: *European Microwave Conference* Vol. 3, 2002, pp. 977–980
- [11] PILZ, D. ; MENZEL, W.: Printed mm-wave folded reflector antennas with high gain, low loss, and low profile. In: *IEEE Int. Symposium on Antennas and Propagation* Vol. 2, 2000, pp. 790–793
- [12] MENZEL, W. ; NAVARRO VERA, P. J.: A 24 GHz Microstrip Antenna Array Incorporating a Ridge Waveguide Feed Network. In: *European Microwave Conference* Vol. 3, 1999, pp. 267–270
- [13] MENZEL, W. ; SCHREINER, M.: A 38 GHz microstrip array with an E-plane waveguide feeding network. In: *European Microwave Conference* Vol. 3, 2000, pp. 24–27
- [14] SHAHABADI, M. ; BUSUIOC, D. ; BORJI, A. ; SAFAVI-NAEINI, S.: Low-cost, high-efficiency quasi-planar array of waveguide-fed circularly polarized microstrip antennas. In: *IEEEAP* 53 (2005), No. 6, pp. 2036–2043
- [15] MENZEL, W. ; MACK, R.: Eine verlustarme Mikrostreifenleitungs-Gruppenantenne mit Hohlleiterspeisenetzwerk. In: *Kleinheubacher Berichte* Vol. 42, 1999, pp. 206–210
- [16] WU, K. ; DALLAIRE, J. ; BOONE, F.: Channalized non-radiative dielectric guide for hybrid and monolithic integration technology. In: *Asia-Pacific Microwave Conference Proceeding*, 1998, pp. 265–268
- [17] YONEYAMA, T.: Properties of Guided Waves and Leaky Waves in NRD-Guide. In: *Asia-Pacific Microwave Conference Proceeding*, 1998, pp. 257–264
- [18] ZHANG, W. X. ; ZHU, L.: New leaky-wave antenna for millimetre waves constructed from groove NRD waveguide. In: *Electronics Letters* 23 (1987), October, No. 22, pp. 1191–1192
- [19] MA, Z. ; YAMASHITA, E.: Wave leakage from groove NRD structures. In: *IEEE Microwave and Guided Wave Letters* 3 (1993), June, No. 6, pp. 170–172
- [20] CASSIVI, Y. ; WU, K.: Substrate Integrated Non-Radiative Dielectric (SINRD) Waveguide. In: *IEEE Microwave and wireless components letters* 14 (2004), March, No. 3, pp. 89–91

- 
- [21] CASSIVI, Y. ; WU, K.: Substrate integrated NRD (SINRD) guide in high dielectric constant substrate for millimetre wave circuits and systems. In: *IEEE Transactions on Microwave Theory and Techniques Symposium*, June 2004
- [22] WU, K. ; BOONE, F.: Guided-wave properties of synthesized non-radiative dielectric waveguide for substrate integrated circuits (SICS). In: *IEEE Transactions on Microwave Theory and Techniques Symposium*, 2001
- [23] CASSIVI, Y. ; DESLANDES, D. ; WU, K.: Engraved NRD-Guide for Millimeter-Wave Integrated Circuits. In: *IEEE Transactions on Microwave Theory and Techniques Symposium* Vol. 2, 2000, pp. 605–608
- [24] BOONE, F. ; WU, K.: Mode Conversion and Design Consideration of Integrated Nonradiative Dielectric (NRD) Components and Discontinuities. In: *IEEE Transactions on Microwave Theory and Techniques* 48 (2000), April, No. 4, pp. 482–491
- [25] HARRINGTON, R. F.: *Time-Harmonic Electromagnetic Fields*. New York : McGraw-Hill, 1987
- [26] COLLINS, R. E.: *Field theory of guided waves*. New York : McGraw-Hill, 1991
- [27] YONEYAMA, T. ; NISHIDA, S.: Nonradiative Dielectric Waveguide for Millimeter-wave Integrated circuits. In: *IEEE Transactions on Microwave Theory and Techniques* 29 (1981), November, No. 11, pp. 1188–1192
- [28] TANAKA, H. ; OKADA, F.: Precise measurements of dissipation factor in microwave printed circuit boards. In: *IEEE Transactions on Instrumentation and Measurement* 38 (1989), April, No. 2, pp. 509–514
- [29] DEUTSCH, A. ; SUROVIC, C. W. ; KRABBENHOFT, R. S. ; KOPCSAY, G. V. ; CHAMBERLIN, B. J.: Prediction of Losses Caused by Roughness of Metallization in Printed-Circuit Boards. In: *IEEE Transactions on Advanced Packaging* 30 (2007), May, No. 2, pp. 279–287
- [30] KUROKI, F. ; IKEDA, K. ; MATSUKAWA, T.: Transmission characteristics of LSE<sub>01</sub> mode in high permittivity NRD guide. In: *Asia-Pacific Microwave Conference Proceeding* Vol. 2, 1997, pp. 593–596
- [31] YONEYAMA, T. ; TOZAWA, N. ; NISHIDA, S.: Loss Measurements of Non-radiative Dielectric Waveguide. In: *IEEE Transactions on Microwave Theory and Techniques* 32 (1984), August, No. 8, pp. 943–946

- [32] LEGAY, H. ; SHAFAI, L.: A high performance spider subarray of five microstrip patches. In: *IEEE Int. Symposium on Antennas and Propagation* Vol. 3, 1993, pp. 1394–1397
- [33] DUFFY, S. M. ; POZAR, D. M.: Aperture coupled microstrip subarrays. In: *Electronics Letters* 30 (1994), November, No. 23, pp. 1901–1902
- [34] CST: *CST Microwave Studio, Version 4.3*. CST-Computer Simulation Technology, 2003
- [35] WEILANDS, T.: Eine Methode zur Lösung der Maxwellschen Gleichungen für sechskomponentige Felder auf diskreter Basis. In: *Archiv für die Elektrotechnik und Übertragungstechnik* 31 (1977), No. 3, pp. 116–120
- [36] CLEMENS, M. ; WEILAND, T.: Discrete Electromagnetism with the Finite Integration Technique. In: *Progress in Electromagnetic Research PIER* 32 (2001), pp. 65–87
- [37] BACHA, A. ; WU, K.: LSE-Mode Balun for Hybrid Integration of NRD-Guide and Microstrip Line. In: *IEEE Microwave and Guided Wave Letters* (1998), pp. 199–201
- [38] BACHA, A. ; WU, K.: Toward an Optimum Design of NRD-Guide and Microstrip-Line Transition for Hybrid-Integrated Technology. In: *IEEE Transactions on Microwave Theory and Techniques* 46 (1998), November, pp. 1796–1800
- [39] MALHERBE, J. A. A. G. ; CLOETE, J. H. ; LÖSCH, I. E.: A Transition from Rectangular to Nonradiating Dielectric Waveguide. In: *IEEE Transactions on Microwave Theory and Techniques* (1985), pp. 539–543
- [40] CASSIVI, Y. ; WU, K.: Compact Transition from Non-Radiating Dielectric (NRD) to Rectangular Waveguides. In: *Personal Communications* (2004)
- [41] STRAUSS, G.: *Häusungs- und Verbindungstechniken von monolithisch integrierten Millimeterwellenschaltungen mittels elektromagnetischer Feldkopplung*. PhD thesis (in German), University of Ulm, 1996
- [42] <http://matls.com/search/SearchProperty.asp>
- [43] YONEYAMA, T. ; NISHIDA, S.: Nonradiative Dielectric Waveguide T-Junctions for Millimeter-Wave Applications. In: *IEEE Transactions on Microwave Theory and Techniques* 33 (1985), November, No. 11, pp. 1239–1241

- 
- [44] YONEYAMA, T. ; YAMAGUCHI, M. ; NISHIDA, S.: Bends in nonradiative dielectric waveguides. In: *IEEE Transactions on Microwave Theory and Techniques* 30 (1982), December, No. 12, pp. 2146–2150
- [45] YONEYAMA, T. ; TAMAKI, H. ; NISHIDA, S.: Analysis and Measurements of Nonradiative Dielectric Waveguide Bends. In: *IEEE Transactions on Microwave Theory and Techniques* 34 (1986), August, No. 8, pp. 876–882
- [46] YONEYAMA, T. ; TOZAWA, N. ; NISHIDA, S.: Coupling Characteristics of Nonradiative Dielectric Waveguides. In: *IEEE Transactions on Microwave Theory and Techniques* 31 (1983), August, No. 8, pp. 648–654
- [47] EFANOV, A. A. ; THIM, H. W.: Corporate-fed  $2 \times 2$  planar microstrip patch sub-array for the 35 GHz band. In: *IEEE Aerospace and Electronic Systems Magazine* 37 (1995), October, No. 5, pp. 49–51
- [48] AL-TIKRITI, M. ; MENZEL, W.: A Folded Reflectarray Antenna with Sidelobe Reduction. In: *European Microwave Conference* Vol. 3. Milano, Italy, September 2002, pp. 973–976
- [49] MENZEL, W. ; AL-TIKRITI, M. ; LEBERER, R.: Low-profile folded reflectarray antennas for communication applications (invited). In: *European Workshop on Integrated Radio Communication Systems*. Chateâu de Pignerolles, Angers, France, May 2002
- [50] AL-TIKRITI, M.: *Multifunctional, quasi-planar antennas*. PhD thesis, University of Ulm, 2005
- [51] VAUGHAN, R. G.: Polarization diversity in mobile communications. In: *IEEE Transactions on Vehicular Technology* 39 (1990), August, No. 3, pp. 177–186
- [52] EMMER, D. ; HUMBURG, E. ; WEBER, P. ; WECKERLE, M.: Measurements of base station two-branch space and polarization diversity reception and a comparison of the diversity gain based on the CDF of signal level and simulations of BER in a GSM system. In: *Vehicular Technology Conference* Vol. 1, 1998, pp. 5–10
- [53] HAJIAN, M. ; VON DER ZWAN, F. ; LIGTHART, L. P.: Branch correlation measurements in an indoor rayleigh fading channel for polarization diversity using a dual polarized patch antenna. In: *7th European Conference on Wireless Technology*, 2004, pp. 225–228

- [54] SARABANDI, Kamal ; LI, Eric S. ; NASHASHIBI, Adib: Modeling and measurements of scattering from road surfaces at millimeter-wave frequencies. In: *IEEE Transactions on Antennas and Propagation* 45 (1997), November, No. 11, pp. 1679–1688
- [55] SARABANDI, Kamal ; LI, Eric S.: Characterization of optimum polarization for multiple target discrimination using genetic algorithms. In: *IEEE Transactions on Antennas and Propagation* 45 (1997), December, No. 12, pp. 1810–1817
- [56] VALLECCHI, A.: Planar square and diamond microstrip patch array antennas for dual-polarization operation. In: *IEEE Int. Symposium on Antennas and Propagation* Vol. 3, 2004, pp. 2472–2475
- [57] ZHONG, Shun-Shi ; YANG, Xue-Xia ; GAO, Shi-Chang ; CUI, Jun-Hai: Corner-fed microstrip antenna element and arrays for dual-polarization operation. In: *IEEE Transactions on Antennas and Propagation* 50 (2002), October, No. 10, pp. 1473–1480
- [58] EDIMO, M. ; SHARAIHA, A. ; TERRET, C.: Optimised feeding of dual polarised broadband aperture-coupled printed antenna. In: *Electronics Letters* 28 (1992), September, No. 19, pp. 1785–1787
- [59] YAMAZAKI, M. ; RAHARDJO, E. T. ; HANEISHI, M.: Construction of a slot-coupled planar antenna for dual polarisation. In: *Electronics Letters* 30 (1994), October, No. 22, pp. 1814–1815
- [60] VALLECCHI, A. ; GENTILI, G. B.: Design of dual-polarized series-fed microstrip arrays with low losses and high polarization purity. In: *IEEE Transactions on Antennas and Propagation* 53 (2005), May, No. 5, pp. 1791–1798
- [61] TANG, J. ; WU, K.: Integrated Microstrip to NRD-Guide Transition Using a Spurious Mode Suppressing Technique. In: *IEEE Transactions on Microwave Theory and Techniques Symposium* Vol. 3, June 2000, pp. 1805–1808
- [62] LEE, J. Y. ; LEE, J. H. ; IM, C. H. ; KIM, H. S. ; CHOI, K. ; JUNG, H.-K.: Selection of proper modes of an NRD guide using a perturbing boundary. In: *IEEE Transactions on Magnetics* 39 (2003), May, No. 3, pp. 1246–1249

- 
- [63] DOUVILLE, R. J. P. ; JAMES, D. S.: Experimental Study of Symmetric Microstrip Bends and Their Compensation. In: *IEEE Transactions on Microwave Theory and Techniques* 26 (1978), January, No. 3, pp. 175–181
- [64] <http://www.rohacell.com>
- [65] [http://www.cumingmw.com/micro\\_rf.html](http://www.cumingmw.com/micro_rf.html)
- [66] TANG, J. ; WU, K.: Co-layered integration and interconnect of planar circuits and nonradiative dielectric (NRD) waveguide. In: *IEEE Transactions on Microwave Theory and Techniques* 48 (2000), April, No. 4, pp. 519–524
- [67] TANG, J. ; ZENG, X. ; XU, S. ; WU, K.: Low-loss millimeter-wave propagation characteristics of NRD-guide surface-mounted on planar substrate for hybrid integrated circuit. In: *IEEE Transactions on Microwave Theory and Techniques Symposium* Vol. 3, 2000, pp. 1679–1682
- [68] GERN, A. ; FRANKE, U. ; LEVI, P.: Robust vehicle tracking fusing radar and vision. In: *International Conference on Multisensor Fusion and Integration for Intelligent Systems MFI*, 2001, pp. 323–328
- [69] SKUTEK, M. ; LINZMEIER, D. T. ; APPENRODT, N. ; WANIELIK, G.: A precrash system based on sensor data fusion of laser scanner and short range radars. In: *International Conference on Information Fusion* Vol. 2, 2005, pp. 1287–1294
- [70] JONES, T. O. ; GRIMES, D. M.: Automotive radar: A brief review. In: *Proceedings of the IEEE* 62 (1974), June, No. 6, pp. 804–822
- [71] ROLLMANM, G. ; KNOLL, P. ; MEKHAIEL, M. ; SCHMID, V. ; BLÖCHER, H.-L.: Short Range Radar (SRR)-System for Automotive Applications. In: *IEEE-MTT/AP German Newsletter* 8 (2004), June, No. 1, pp. 4–7
- [72] DÄMBKES, H. ; LUY, J.F.: Millimetrewave Components and Systems for Automotive Applications. (Dec./Jan. 1996), pp. 43–48
- [73] MICHAEL, B. ; MENZEL, W. ; GRONAU, A.: A Real-Time Close-Range Imaging System with Fixed Antennas. In: *IEEE Transactions on Microwave Theory and Techniques* 48 (2000), December, No. 12, pp. 2736–2741

- [74] MAINE, K. ; DEVIEUX, C. ; SWAN, P.: Overview of IRIDIUM satellite network. In: *IEEE WESCON/'95. Conference record. 'Microelectronics Communications Technology Producing Quality Products Mobile and Portable Power Emerging Technologies'*, 1995, pp. 483–490
- [75] Iridium satellite constellation. In: [http://en.wikipedia.org/wiki/Iridium\\_satellite\\_constellation](http://en.wikipedia.org/wiki/Iridium_satellite_constellation)
- [76] ROMANOFSKY, R. R.: *Antenna Engineering Handbook*. Chapter 21 Array Phase Shifters: Theory and Technology. New York : McGraw-Hill, 2007
- [77] ERIKSSON, L. H. ; BRODÉN, S.: High performance automotive radar. In: *Microwave Journal* (1996), October, No. 10, pp. 24–38
- [78] MENZEL, W. ; PILZ, D. ; LEBERER, R.: A 58 GHz FM/CW radar frontend with a low-profile, low-loss printed antenna. In: *IEEE Transactions on Microwave Theory and Techniques* 47 (1999), December, No. 12, pp. 2237–2241
- [79] SCHOEBEL, J. ; BUCK, T. ; REIMANN, M. ; ULM, M. ; SCHNEIDER, M. ; JOURDAIN, A. ; CARCHON, G. J. ; TILMANS, H. A. C.: Short Range Radar (SRR) -System for Automotive Applications. In: *IEEE Transactions on Microwave Theory and Techniques* 53 (2005), June, No. 6, pp. 1968–1975
- [80] HANSEN, R. C.: Design trades for Rotman lenses. In: *IEEE Transactions on Antennas and Propagation* 39 (1991), April, No. 4, pp. 464–472
- [81] CHAN, K. K. ; MARTIN, R.: Design of an octave band wide scan dual polarized phased array. In: *Asia-Pacific Microwave Conference Proceeding* Vol. 3, WD6\_06, 2003
- [82] TANIZAKI, T. ; NISHIDA, H. ; NISHIYAMA, T. ; YAMADA, H. ; SAKAMOTO, K. ; ISHIKAWA, Y.: Multi-Beam Automotive Radar Front End using Non-contact Cylindrical NRD Switch. In: *IEEE Transactions on Microwave Theory and Techniques Symposium* Vol. 2, 1998, pp. 521–524
- [83] OLINER, A. A. ; JACKSON, D. R.: *Antenna Engineering Handbook*. Chapter 11 Leaky-Wave Antennas. New York : McGraw-Hill, 2007
- [84] ITOH, T.: Leaky-Wave Antenna and Band-Reject Filter for Millimeter-Wave Integrated Circuits. In: *IEEE Transactions on Microwave Theory and Techniques Symposium* Vol. 77, 1977, pp. 538–541



- 
- [85] SOLBACH, K.: E-Band Leaky Wave Antenna Using Dielectric Image Line with Etched Radiating Elements. In: *IEEE Transactions on Microwave Theory and Techniques Symposium* Vol. 79, 1979, pp. 214–216
- [86] SOLBACH, K. ; ADELSECK, B.: Dielectric image line leaky wave antenna for broadside radiation. In: *Electronics Letters* 19 (1983), August, No. 16, pp. 640–641
- [87] HUANG, L. ; CHIAO, J.-C. ; DE LISIO, M. P.: An Electronically Switchable Leaky Wave Antenna. In: *IEEE Transactions on Antennas and Propagation* 48 (2000), November, No. 11, pp. 1769–1772
- [88] RODENBECK, Christopher T. ; LI, Ming-yi ; CHANG, Kai: A Novel Multi-beam Grating Antenna with Applications to Low-Cost Millimeter-Wave Beam-Steering. In: *IEEE Transactions on Microwave Theory and Techniques Symposium*, Seattle 2002, pp. 57–60
- [89] MANASSON, V. ; SADOVNIK, L. ; MINO, R.: MMW scanning antenna. In: *IEEE Antennas and Propagation Magazine* 11 (1996), October, No. 10, pp. 29–33
- [90] LIU, L. ; CALOZ, C. ; ITOH, T.: Dominant mode leaky-wave antenna with backfire-to-endfire scanning capability. In: *Electronics Letters* 38 (2002), November, No. 23, pp. 1414–1416
- [91] LIM, S. ; CALOZ, C. ; ITOH, T.: Electronically-controlled metamaterial-based transmission line as a continuous-scanning leaky-wave antenna. In: *IEEE Transactions on Microwave Theory and Techniques Symposium* Vol. 1, June 2004, pp. 313–316
- [92] SUNGJOON, L. ; CALOZ, C. ; ITOH, T.: Metamaterial-based electronically controlled transmission-line structure as a novel leaky-wave antenna with tunable radiation angle and beamwidth. In: *IEEE Transactions on Microwave Theory and Techniques* 53 (2005), January, No. 1, pp. 161–673
- [93] KODERA, T. ; CALOZ, C.: Uniform Ferrite-Loaded Open Waveguide Structure With CRLH Response and Its Application to a Novel Backfire-to-Endfire Leaky-Wave Antenna. In: *IEEE Transactions on Microwave Theory and Techniques* 57 (2009), April, No. 4, pp. 784–795
- [94] ROMANOFSKY, R. R. ; BERNHARD, J. T. ; VAN KEULS, F. W. ; MIRANDA, F. A. ; WASHINGTON, G. ; CANEDY, C.: K-band phased array antennas based on  $\text{Ba}_{0.60}\text{Sr}_{0.40}\text{TiO}_3$  thin-film phase shifters. 48 (2000), December, No. 12, pp. 2504–2510

- [95] ROMANOFSKY, R. R.: Advances in Scanning Reflectarray Antennas Based on Ferroelectric Thin-Film Phase Shifters for Deep-Space Communications. In: *Proceedings of the IEEE* 95 (2007), October, No. 10, pp. 1968–1975
- [96] MOESSINGER, A. ; DIETER, S. ; JAKOBY, R. ; MENZEL, W. ; MUELLER, S.: Reconfigurable LC-reflectarray setup and characterisation. In: *European Conference on Antennas and Propagation EuCAP 2009*, pp. 2761–2765
- [97] MOESSINGER, A. ; DIETER, S. ; MENZEL, W. ; MUELLER, S. ; JAKOBY, R.: Realization and characterization of a 77 GHz reconfigurable liquid crystal reflectarray. In: *13th International Symposium on Antenna Technology and Applied Electromagnetics and the Canadian Radio Science Meeting, ANTEM/URSI 2009*, pp. 1–4
- [98] SCHOEBEL, J. ; BUCK, T. ; REIMANN, M. ; ULM, M. ; SCHNEIDER, M.: W-band RF-MEMS Subsystems for Smart Antennas in Automotive Radar Sensors. In: *European Microwave Conference* Vol. 3, 2004, pp. 1305–1308
- [99] MALCZEWSKI, A. ; ESHELMAN, S. ; PILLANS, B. ; EHMKE, J. ; GOLDSMITH, C. L.: X-band RF MEMS phase shifters for phased array applications. In: *IEEE Microwave and Guided Wave Letters* 9 (1999), December, No. 12, pp. 517–519
- [100] SCARDELLETTI, M. C. ; PONCHAK, G. E. ; ZAMAN, A. J. ; LEE, R. Q.: RF MEMS phase shifters and their application in phase array antennas. In: *IEEE Wireless and Microwave Technology Conference (WAMICON)*, 2005, pp. 191–194
- [101] REBEIZ, G. M. ; GUAN-LENG, T. ; HAYDEN, J. S.: RF MEMS phase shifters: design and applications. In: *IEEE Microwave Magazine* 3 (2002), June, No. 2, pp. 72–81
- [102] SKOLNIK: *Introduction to Radar Systems*. Chap. 8 The electronically directed phased array antenna in radar, pp. 278–342, McGraw-Hill Publishing Co., 1980
- [103] RELPH, P. M. ; GRIFFITHS, H. D.: An Electronically Scanning Antenna for Automotive Radar Systems. In: *IEEE Colloquium on Automotive Radar and Navigation Techniques* (1998), pp. 535–537
- [104] MENZEL, W. ; SATHIASEELAN, M.: Frequency Scanned Antenna Array Using a Suspended Stripline Negative Index Transmission Line. In: *European Microwave Conference*, 2005, pp. 253–256

- 
- [105] NISHIMURA, T. ; ISHII, N. ; ITHO, K.: Beam Scan Using the Quasi-Optical Antenna Mixer Array. In: *IEEE Transactions on Antennas and Propagation* 47 (1999), Juli, No. 7, pp. 1160–1165
- [106] KIM, M. ; HACKER, J. B. ; SAILER, A. L. ; HONG, J. H.: A Heterodyne-Scan Phased-Array Antenna. In: *IEEE Microwave and Guided Wave Letters* (1999), pp. 7/1–7/7
- [107] HONG, John H.: Electronically scanned phased array antenna system and method with scan control independent of radiating frequency. In: *United States Patent No. US 6,266,011 B1, Date of Patent July 24, 2001*
- [108] SCHMID, U. ; MENZEL, W.: A 24 GHz Scanning Receiver Array. In: *Symposium on Antenna Technology and Applied Electromagnetics, ANTEM 2002*, pp. 319–322
- [109] SCHMID, U. ; MENZEL, W.: A 24 GHz Microstrip Antenna Array With A Non-Radiative Dielectric Waveguide (NRD-Guide) Feeding Network. In: *Symposium on Antenna Technology and Applied Electromagnetics, ANTEM 2005*, pp. 266–267
- [110] YONEYAMA, T. ; TAMAKI, H. ; NISHIDA, S.: Design of Nonradiative Dielectric Waveguide Filters (Short Papers). In: *IEEE Transactions on Microwave Theory and Techniques* 32 (1984), December, No. 12, pp. 1659–1662
- [111] JEDRZEJEWSKI, P. ; MROZOWSKI, M.: Design of NRD-guide bandpass filters. In: *12th International Conference on Microwaves and Radar MIKON '98* Vol. 1, May 1998, pp. 3–7
- [112] <http://www.skyworksinc.com/Product.aspx?ProductID=186>
- [113] AGILENT: *Advanced Design System 2002C*. Agilent Technologies, Inc., Palo Alto, CA., 2002
- [114] WENZEL, E.: *Design of a slot coupled planar balanced mixer*. Prefinal project (in German), University of Ulm, Institute for Microwave Techniques, August 2004
- [115] MAAS, S. A.: *Microwave Mixers*. Artech House, London, 1986
- [116] MENZEL, W. ; WERNER, R.: A High Dynamic Range Extension for Antenna Measurements in the mm-Wave Range. In: *Proc. 11th Conf. on Microwaves and Optronics (MIOP '01), Stuttgart, Germany, 2001*, pp. 194–197

- [117] HUANG, J. ; WU, K.: A Two-Path Multimode Bandpass Filters Using the Nonradiative Dielectric (NRD) Waveguide Technology. In: *IEEE Transactions on Microwave Theory and Techniques Symposium* Vol. 3, 1995, pp. 1547–1550

## Publications and Patent

- SCHMID, Ulf ; MENZEL, Wolfgang: A 24 GHz Microstrip Antenna Array With A Non-Radiative Dielectric Waveguide (NRD-Guide) Feeding Network. In: *Symposium on Antenna Technology and Applied Electromagnetics, ANTEM Proceedings*, July 2005, pp. 266–267
- SCHMID, Ulf ; MENZEL, Wolfgang ; CASSIVI, Yves ; WU, Ke: Dual polarization antenna fed by a dual mode substrate integrated NRD-guide. In: *IEEE Int. Symposium on Antennas and Propagation Proceedings*, July 2004, pp. 4348–4351
- SCHMID, Ulf ; MENZEL, Wolfgang: A Low Cost Low Profile 19 GHz Scanning Receiver Array with a Nonradiative Dielectric Waveguide Feeding Network. In: *German Microwave Conference (GeMiC) Proceedings*, Karlsruhe, Germany, March 2006, Session 3b-3
- SCHMID, Ulf ; MENZEL, Wolfgang: Planar Antenna Arrays Using a Feed Network with Nonradiative Dielectric (NRD) Waveguide (invited). In: *EuCAP*, November 2006
- SCHMID, Ulf: *AZ 10 2011 107 128.1 - Anordnung für einen nichtstrahlenden dielektrischen Rechteckwellenleiter zur unabhängigen Nutzung zweier oder mehrerer Moden zur Signal-Übertragung*. Date of filing: July 12, 2011



# Lebenslauf

Name: Ulf Schmid  
Geburtsdatum: 26.09.1973  
Geburtsort: Calw

## Schulausbildung

Sep. 1980–Aug. 1984 Grundschole in Ebhausen  
Sep. 1984–Aug. 1990 Otto-Hahn-Gymnasium in Nagold  
Sep. 1990–Jun. 1993 Technisches Gymnasium in Nagold  
Abschluss: Abitur

## Studium

Okt. 1993–Nov. 2001 Studium der Elektrotechnik an der Universität Ulm,  
Studienmodell Hochfrequenztechnik  
Abschluss: Diplom-Ingenieur

## Berufstätigkeit

Jan. 2002–Dez. 2005 Wissenschaftlicher Mitarbeiter in der Abteilung  
Mikrowellentechnik an der Universität Ulm  
Jul. 2006–Jan. 2009 Entwicklungsingenieur bei Ubidyne in Ulm  
seit März 2009 Entwicklungsingenieur bei EADS in Ulm







